THICK-FILM PIEZOELECTRIC SLIP SENSORS FOR A PROSTHETIC HAND

By

Darryl Paul James Cotton

A thesis submitted for the degree of Doctor of Philosophy

School of Electronics and Computer Science,

University of Southampton,

United Kingdom.

December, 2007

UNIVERSITY OF SOUTHAMPTON

ABSTRACT

FACULTY OF ENGINEERING

SCHOOL OF ELECTRONICS AND COMPUTER SCIENCE

Doctor of Philosophy

THICK-FILM PIEZOELECTRIC SLIP SENSORS FOR A PROSTHETIC HAND

By: Darryl Paul James Cotton

This thesis details an investigation into using thick-film piezoelectric sensors to detect slip for a hand prosthesis application. The investigation focuses on the slip characteristics produced from the sensor, the effects of device fabrication parameters on d_{33} sensitivity and the enhancement of piezoelectric thick-film devices.

Prototype fingertips incorporating a thick-film piezoelectric slip sensor were tested on purpose built slip test apparatus for their viability to be used as slip sensors. The results demonstrated that the devices can be used to detect slip and they can do this even with a cosmesis material placed between the sensor and object surface. The stoichiometry and d_{33} sensitivity of thick-film devices were investigated, where the film was subjected to multiple firing cycles at 850°C. An XRF analysis of the films suggested that there was no change in stoichiometry during firing and the d_{33} sensitivity of all devices remained unchanged. A binderless paste was investigated to fabricate piezoelectric thick-film devices at peak processing temperatures of 150°C, 720°C, 850°C and 950°C and showed an increase in d_{33} sensitivity of 28% over glassy thick-film devices processed at the same peak temperature of 950°C, (168pC/N compared to 131pC/N) and 33% over polymer based thick-films processed at a peak temperature of 150°C (20pC/N compared to 15pC/N).

Finally, future work is suggested for further characterisation of piezoelectric thick-film slip sensors and the enhancement of other piezoelectric thick-film devices.

Contents

List of Figures

List of Tables

Acknowledgements

I would like to thank my supervisors Paul Chappell and Neil White for their support throughout my studies. Special thanks to Andy Cranny for answering endless questions and always being willing to help when things were going wrong (which was quite often)! I would also like to thank the group secretaries Lesley and Lucina for their help, and the workshop crew Mark, Eric and Ken for their advice on designing apparatus and for bringing my drawings to life.

I have been fortunate to have the opportunity to work within a large multidisciplinary group amongst good friends and colleagues including: Cheryl Metcalf, Scott Page, Neil Grabham, Andrew Frood, Geoff Merit, Alex Weddell, Russell Torah, Mathew Swabey, Steven Kok, Siti Ahmed. Thank you all and best wishes for the future.

Throughout my 21 years of education and temporary work I have been very fortunate to have had the guidance and support of a number of excellent teachers, in particular I would like to thank; Gary Hickson of Yorkshire Wold Commercials, Driffield, for encouraging me to continue in my studies, Mr. Dyson from Driffield Secondary School for always making time to answer my mathematical questions and Jack Hale from Newcastle University for introducing me to piezoelectric devices and providing me with invaluable support in the final year of my undergraduate degree.

Finally I would like to thank, Lucy, Mum, Dad, Conn and my sister Suellen for their endless love and support.

Definitions and Abbreviations Used

Abduction	Pull away from the median axis of the body.
Adduction	Pull towards the median axis of the body.
Afferent	Bringing or directing inwards to a part or organ of the body.
Anisotropic	Having a different magnitude or properties when measured in different directions.
Anthropomorphic	Resembling the human form.
Divalent	Having a valency of two.
Efferent	Pushing or directing outwards away from a part or organ of the body.
Electromyography	The monitoring of the electrical signals used to activate muscles with electrodes (EMG).
Extension	Straightening or extending a limb.
Flexion	Bending a limb.
Glabrous	Without hair.
Mechanoreceptor	A sensory receptor which is sensitive to mechanical stimulus such as pressure.
Myelin	Insulating tissue formed around certain nerve fibres.
Myoelectric	A type of prosthesis that uses electromyography (EMG) signals from the user's muscles to control it.
Nociceptive	Responds to pain.
Nociceptor	A type of receptor which responds to pain.
Phalangeal Joints	The three joints in the finger.
Stoichiometry	The process of calculating atomic proportions, combining weights and other numerical relations of chemical elements and their compounds.
Tetravalent	having a valency of four.
Valency	The combining power of an element.
Volar	Of or relating to the palm of the hand or the sole of the foot.

ADL	Activities of daily living.
Avg	Average.
d_{33}	The charge produced from a piezoelectric material for a force applied in the same direction (pC/N) or the strain produced for an applied electric field in the same direction (in both cases with the direction being defined as direction 3). Refer to section 3.1.4.
DARPA	Defense advanced research projects agency.
DIP	Dual in line package.
DOF	Degrees of freedom.
EDX	Energy Dispersive X-ray.
EMG	Electromyography.
ESL	Electroscience Laboratories.
FA	Fast adapting.
FBD	Free body diagram.
FEA	Finite element analysis.
FFT	Fast fourier transform.
IMES	Implantable myoelectric sensor.
ISPO	International Society for Prosthetics and Orthotics.
MEMS	Micro Electro Mechanical Systems
PMN	Lead magnesium niobate.
PT	Lead titanate.
PVDF	Polyvinylidene fluoride.
PVF2	Polyvinylidene fluoride.
PZT	Lead Zirconate Titanate.
SA	Slow Adapting.
SAMS	Southampton adaptive manipulation scheme.
UNB	University of New Brunswick.
VI	Virtual Instrument.
XRD	X-ray Diffraction.
XRF	X-ray Florescence.

Chapter 1 Introduction

1.1 Contributions

This thesis documents several novel contributions made to the fields of upper limb prosthetics and thick-film piezoelectric devices including:

- The first experimental evidence that a thick-film piezoelectric device fabricated on a stainless steel substrate can be used to detect slip and it can do this with a cosmesis material between the sensor and object surface (chapters 7+8).
- The effects on stoichiometry and d_{33} of multiple firing cycles at a peak temperature of 850°C, on piezoelectric thick-films (chapter 4).
- Enhancement of piezoelectric d_{33} sensitivity with a binderless thick-film piezoelectric paste (chapter 5).

1.2 Declaration

This thesis describes the research undertaken by the author while working within a collaborative research environment. This report documents the original work of the author except in the following sections.

Chapter 6

- Design of screens for all three prototype fingertips.
- Fabrication of prototype fingertips 1 and 2 (including poling of piezoelectric sensors).

1.3 Document Structure

Chapter 2 reviews current prototype and commercially available upper limb prosthetics along with the sensors used for automatic grip control to prevent objects slipping from the grasp of a prosthesis. Potential new human to prosthesis interfaces are also reviewed and control strategies proposed for a six degree of freedom hand with slip, force and temperature sensors.

Chapter 3 describes the piezoelectric effect, the thick-film fabrication technique and the processes, equipment and materials used to fabricate and test piezoelectric thick-films throughout this thesis.

Chapter 4 introduces the theory of X-ray spectrometry and details the use of an X-ray fluorescence (XRF) technique to investigate the stoichiometry of piezoelectric thick-film devices when fired one to four times at a peak temperature of 850°C. The d_{33} sensitivity of devices (fabricated from PZT-5H and PZT-Pz29) processed under the same conditions are also evaluated when fabricated with several different electrode materials.

Chapter 5 presents an investigation into a screen printable piezoelectric paste formulated from a blend of PZT-Pz29 powders of different mean particle size mixed in an organic vehicle. In order to enhance d_{33} properties of the thick-film, no binder material was mixed into the paste. The d_{33} coefficient and maximum applied electrical field of devices processed at peak temperatures of 150°C, 200°C, 720°C, 850°C and 950°C were measured and the film adhesion assessed using an SEM and scratch and tape tests.

Chapter 6 describes the integration of thick-film force, temperature and slip sensors onto the Southampton Hand. The design and fabrication of several prototype fingertips and finger linkage slip sensors are detailed. The design and mechanical analysis of slip test apparatus, used to characterise the slip sensors, is detailed along with an amplifier circuit and software for data collection and analysis.

Chapter 7 describes the experimental testing of the piezoelectric slip sensor on prototype fingertip 2, using a signal thresholding method. The results of slip detection

are then given in terms of object velocity and the distance travelled before slip was detected.

Chapter 8 describes the experimental testing of the piezoelectric slip sensor on prototype fingertip 3, using a cosmesis covering and two different surface textures. The results of slip detection are then given in terms of object velocity and the distance travelled before slip was detected.

Chapter 9 discusses the conclusions from testing the thick-film slip sensors, the effects on d_{33} sensitivity of a number of firing cycles a thick-film is subjected too and the binderless piezoelectric paste. Future work is also proposed.

Chapter 2 Literature review

2.1 Overview of prosthetic hands

2.1.1 History of prosthetic hand development

Throughout history mankind has fabricated upper limb prosthetic devices in order to replace defective or lost limbs. One of the earliest hands found on an Egyptian mummy dates back to 330 B.C. A number of other surviving hands date back from the 15th century, some with documentation of their designs. These devices were commonly made from steel or wood and examples of both passive and adaptive hands have been found. A good overview these devices along with later developments can be found in [1].

In 1863 the first rubber hand was produced allowing the amputee to interchange the hand with other tools and implements such as knives or a hook [2]. This type of prosthesis is still widely used today although there is a much greater range of tools available [3].

The American civil war (1861-1865) was the first real example of modern warfare resulting in a large number of amputees, and an increase in the number of new mechanical prosthesis designs to suit the different injuries of patients were made available. The end of World War I saw an increase in the European development of prosthetics to supply the demand of the British amputee casualties estimated at around 42,000 and the 100,000 amputees from European armies [4]. The end of World War II produced an even larger amount of amputees in America and in 1946 the American Orthotics and Prosthetics Association was set up in order to develop new types of

prosthesis, followed by the International Society for Prosthetics and Orthotics (ISPO) in 1970 [5].

In the 1960s a new type of prosthesis was developed in Russia which used electromyography signals from a muscle extensor/tenser pair to control an electrical hand. This type of control is still commonly used in commercial hands today and is referred to as a myoelectric device.

The trend of investment in the development of upper limb prosthetics still continues today. As a result of the recent conflicts in Iraq and Afghanistan a large number of American soldiers have lost limbs. This has encouraged the US government to invest $70 million in developing new upper limb prosthetic devices and interfaces [6-8].

2.2 Commercially available prosthetic hands

2.2.1 Touch Bionics iLimb Hand

The iLimb Hand is the only commercially available prosthetic hand with individually actuated digits. It was first demonstrated at the myoelectric control (MEC) conference in Canada, August 2005 [9] and after successfully undergoing clinical trials was made available to patients in 2007. The prosthesis has a motor in each finger and the thumb, which actuates the extension/flexion movements of each digit, with the thumb rotation being manually operated by the user. Currently, the prosthesis is interfaced to the patient using traditional two input myoelectric signals. The fingers and thumb are therefore actuated simultaneously. To take advantage of the extra motors in the prosthesis, the fingers are controlled by monitoring the stall currents in the motors during actuation. This allows the hand to adapt to the surface profile of a grasped object effectively causing the motors to stall until all the digits have contacted the object, or reached full flexion, before applying a larger force. The rotating thumb also allows a number of useful grasp patterns to be used. The control strategy for this prosthesis may be adapted in the future, depending on the number of inputs available from future human to prosthesis interfacing techniques (a number of which are described in section 2.5) and also the inclusion of tactile feedback from sensors.

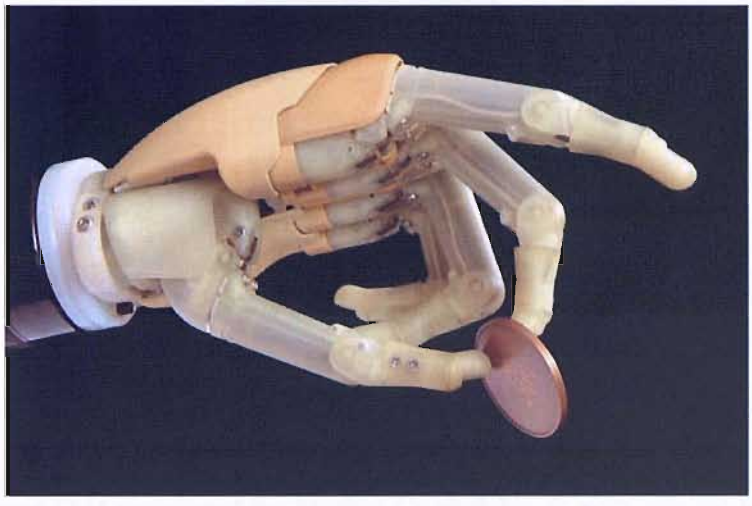

Figure 2.1: Touch Bionics iLimb Hand.

The grip force produced from this prosthesis is less than that quoted for the OttoBock SensorHand Speed and other similar devices, however, the extra functionality provided by the adaptive grasp means that higher grip forces are not required for manipulating most objects. The extension flexion speed of the fingers is approximately 1s and the weight is also comparable to other commercially available devices.

2.2.2 Otto Bock SensorHand Speed

The Otto Bock SensorHand Speed [10] is one of the most commonly used, commercially available, prosthetic hands. It has 1 DOF and utilises a three digit grip between the thumb, index and middle fingers producing a maximum grip force of approximately 100N. The ring and little fingers are passive and move in unison with the other two fingers in an anthropomorphic manner, making the prosthesis more aesthetically pleasing to the user. Figure 2.2 shows a picture of the hand's skeletal structure. A single motor drives the digits through an automatic gearbox, producing an open/closing time of less than 1/3 of a second, nearly three times the speed of other conventional devices. The hand weighs approximately 520g and is the first commercially available device to incorporate an auto grasp feature, which is described in section 2.4.4.

Figure 2.2: Otto Bock SensorHand Speed.

2.2.3 Pro-Hand

The pro-hand [11] developed by Motion Control Inc is very similar to the Otto Bock hand, using the same tri-digital grip also having a maximum pinch force of 100N. The hand is integrated to use the same batteries and myoelectric sensors as the Otto Bock hand and can be attached to a flexional wrist for increased mobility. However, it does not have the slip prevention feature.

There are a number of similar commercially available prosthetic hands including the CENTRI hand and a range of VASI children's hands [12] all incorporating a similar tri-digital grip with comparable grip forces and opening and closing speeds.

2.3 Prototype myoelectric upper limb prosthetics

2.3.1 The Southampton Hand

The Southampton Hand project has been ongoing since its beginning in the 1960s investigating a range of potential improvements to prosthetic hands. These improvements include the control system [13-15], mechanical functionality[16,17] and the integration of sensors for automatic control [18-22]. The current mechanical design of the hand is based on the Southampton REMEDI Hand [23,24] and can be seen in Figure 2.3.

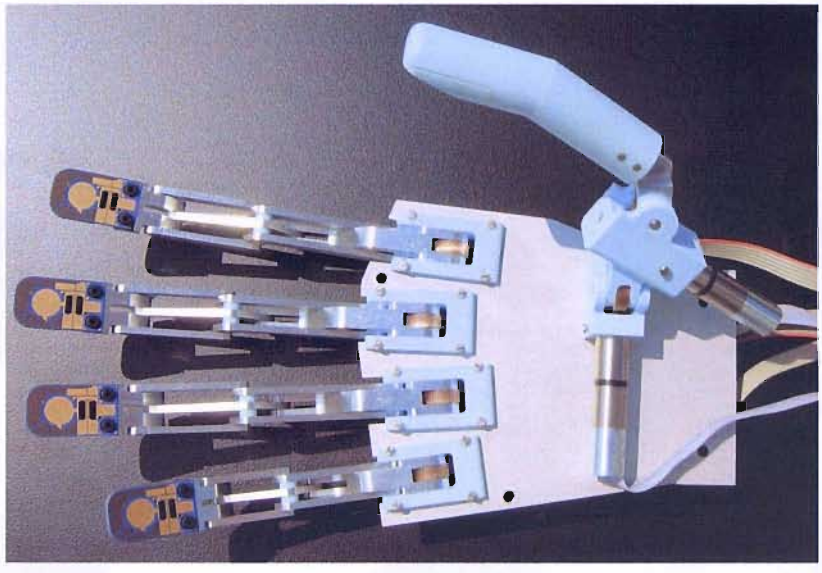

Figure 2.3: The Southampton Hand with prototype 3 fingertips.

The hand consists of six small electrical motors, two of which are used to actuate the extension-flexion and rotation movements of the thumb, with each of the remaining four motors being assigned to individual fingers. Each finger unit is made from six bar linkages, which when extended or flexed curl in a fixed anthropomorphic trajectory. To reduce the power used to hold an object, the fingers are driven via a worm wheel gear configuration thus preventing the finger being back driven after power is removed from the motor. The worm wheel drive also increases the torque produced from the small motors to provide approximately 9 Newton's of grip force at the end of each finger. The increased dexterity of this prosthesis is designed to allow a number of activities of daily living (ADL) to be easily accomplished without the need to compensate for the lack of functionality of a single degree of freedom prosthesis with unnatural body movements. This is achieved by producing a number of prehensile grasp patterns, which can be used to accomplish a range of different activities. Figure 2.4 illustrates the hand in six commonly used prehensile grasp patterns [25].

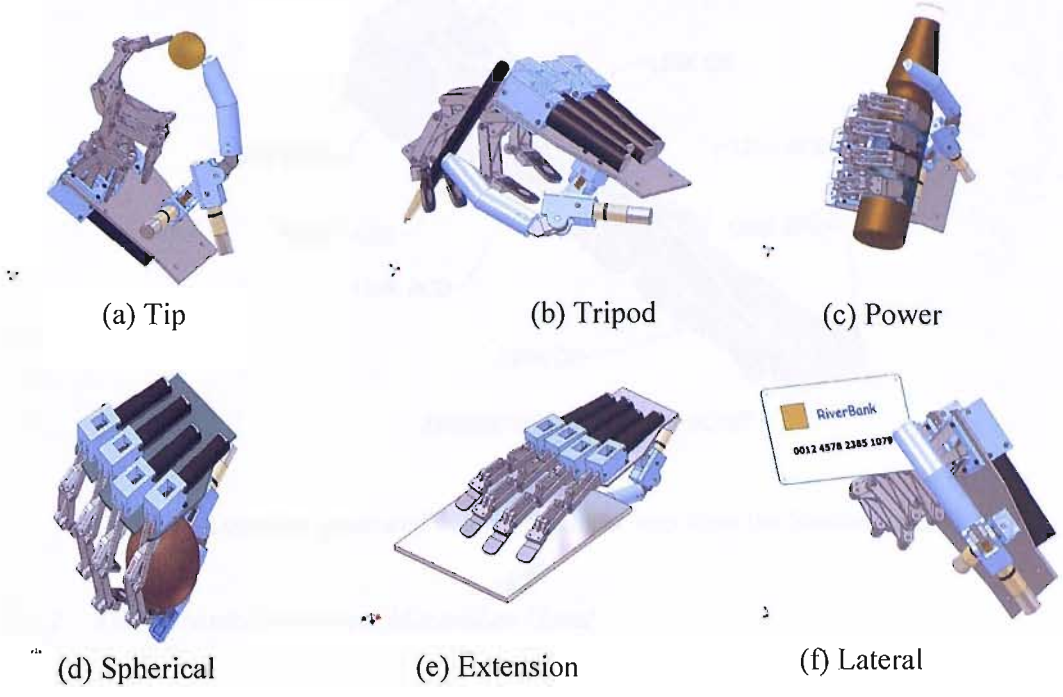

Figure 2.4: Computer generated model of the Southampton Hand in six prehensile grasp patterns, used in activities of daily living.

Prototype finger design

The major changes in the current mechanical design of the Southampton Hand, from its predecessor the Southampton REMEDI Hand lie in the design of the finger unit. The fingertip attachment link (EFG) shown in Figure 2.5 has been added to provide an easy method to attach the prototype fingertips (described in section 6.1) with 2 bolts. The linkages have also been redesigned in order to produce a symmetrical arrangement around the centre of the longitudinal axis of the finger. This evolutionary step was deemed necessary to provide a stable platform for the prototype fingertips by reducing the effects of torsion loads on the fingertips. The other major enhancement was the inclusion of a ball bearing within the knuckle block as part of the mechanical drive system to support the distal end of the worm, reduce friction and decrease radial loading on the motor shaft.

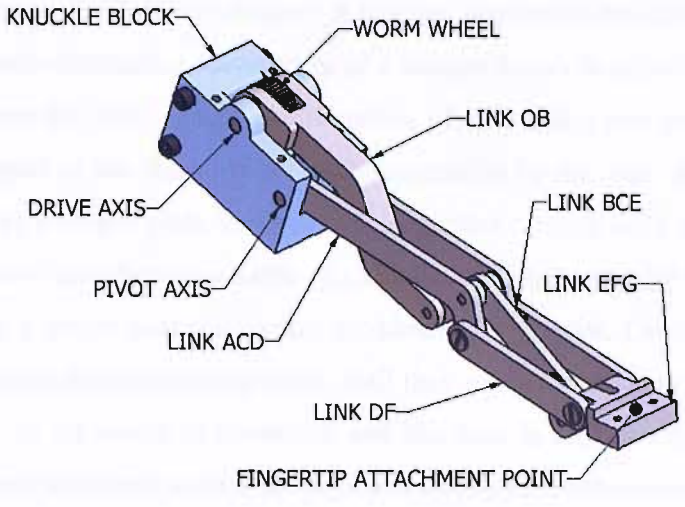

Figure 2.5: Computer generated model of a finger unit from the Southampton Hand.

2.3.2 The Toronto/Bloorview Macmillan Hand

The Toronto/Bloorview Macmillan Hand (TBM) [26-28] is a prototype prosthesis developed at the University of Toronto and the Bloorview MacMillan centre in Canada. The hand is specifically designed for children in the 7-11 year age group but could potentially be scaled up to produce an adult sized prosthesis. The designers of the hand have adopted an under actuated mechanical approach to produce an adaptive grasp hand, utilising the existing controller and battery of a VASI 7-11 prosthetic device [12]. This mechanical approach is designed to eliminate the need for sensors and a control system for positioning of independent fingers during the grasp action.

The TBM hand has been used as a test bed to investigate a number of mechanical design adaptations of the hand including: a cable driven finger, which was reported to suffer instability problems, an extension spring actuation system to drive the fingers with a counterbalance mechanism to reduce imbalance during a pinch grip.

Presently the TBM hand consists of four identically sized fingers made from six bar linkages similar to that of the Southampton Hand, with an anthropomophical finger trajectory. The bar linkages are also arranged to bend at the approximate position of the phalangeal joints of a natural finger.

The thumb is made from a four bar linkage system to simulate the two phalangeal joints of the human hand during flexion. It has two degrees of freedom simulating the rotation and flexion/extension movements of a human thumb to allow a range of grasp patterns. To meet the hand design specifications of only using one electric motor, the rotation movement of the thumb is manually controlled by the user. All of the fingers are connected to a single plate via individual cylinder springs with the thumb being directly coupled to the plate via a cable. To actuate the fingers and the thumb, the plate is driven along a single axis, distal and proximal to the wrist. During actuation the fingers curl in their pre-defined trajectory until they reach full flexion or make contact with an object. If an object is contacted and the user is still closing the hand, the contacting fingers will apply a force to the object through the compression springs.

The TBM hand demonstrates the potential of a mechanically orientated adaptive grasp prosthesis with a lightweight design of 280g including gearbox and motors. Currently, however, the TBM hand still suffers from instability in the initial stages of grasping an object, it has a very low efficiency consuming 3-4 times more energy per open/close cycle than a conventional prosthesis, and the closing cycle time (from full finger extension to flexion) is 4-5 seconds compared to 0.3-1.5 seconds for conventional devices.

2.3.3 The Cyberhand Project

The Cyberhand project [29] has investigated a number of different mechanical designs of prosthetic hands, including two which were constructed from three digits, to test alternative actuating strategies. The three digits in each case were the index and middle fingers, and the thumb.

The RTR I hand [30,31] incorporated two of the most advanced micro motors (with the highest torque available in such a size of motor at the time) in each of the digits, one located in the palm of the hand and the second in the proximal phalange of each finger. This design allowed a more adaptable grip around an object, however, the force generated by the motors was reported to be very low, with the increased dexterity not being able to compensate for this factor in all the activities required by a prosthesis user. This research therefore shows that the micro motors on the market at the time were not adequate to provide the force required to power the phalangeal joints of a

prosthetic hand. This could potentially change in the future, however, it is likely to be driven by the requirements of other applications, where the financial reward to the designers is much higher.

The RTR II Hand [32-34] is actuated by two individual motors, one for the abduction/adduction of the thumb and the other motor the extension flexion of the three digits. Each digit is tendon driven and is constructed from a number of pulleys at the phalangeal joints with springs in the phalanges to return the digits to their extended positions. In order to flex the digits with a single motor, the tendons are connected to a linear slider, (in a similar manner to that described for the TBM hand in the above section) which acts like a differential mechanism allowing both fingers to contact an object with an uneven surface. Unfortunately the published literature reveals little information on the success of the hand when grasping objects. The hand was also later re-designed with three motors to actuate the flexion of each of the digits individually [35].

The latest prosthesis unveiled by the group is the CyberHand, which is constructed from four underactuated fingers and a thumb. The fingers and thumb units have a similar architecture to those described for the RTR II hand also being driven by tendons with springs to return the digits to their extended positions. Details of the construction and mechanics of the finger units can be found in [36]. The hand has six motors housed in a 250cc socket below the hand (in place of the forearm) to actuate each digit individually and is capable of applying approximately 70N of force in a power grip. The hand has been shown to have an adaptive grasp and can simulate all six of the prehensile grasp patterns illustrated in Figure 2.4.

However, the weight of the prosthesis including motors is quoted at 1800g, approximately 3½ times that of a conventional prosthesis. The use of the forearm to contain the motors also limits the number of amputee patients, which could use this type of device. This is where a trade off exists in upper limb prosthetic design between the force, weight, actuation speed and the number of actuators.

2.4 Review of slip prevention sensors for prosthetic hands

2.4.1 Introduction

Although today there is still no real slip sensors included in any commercially available prosthetic hand, a number of researchers have continuously investigated different designs since the 1960's [37].

There are a range of applications throughout industry for slip detection devices, such as vehicle anti-lock braking systems (ABS), traction control, robotic grippers and object handling (specifically with hazardous materials). Some of the existing solutions to these industrial problems include a magnetic roller ball sensor or rotating encoder [38]. However, the majority of these solutions are not suitable for inclusion in a prosthetic hand device due to the need for an anthropomorphical appearance, low weight and low power consumption. The sensor must also be small enough to fit onto a prosthetic finger and be capable of detecting slip through a cosmesis.

2.4.2 Slip sensors

A number of researchers have identified piezoelectric sensors as a candidate for detecting slip. The majority of the investigative work done with this type of sensor has used polyvinylidene fluoride strips (PVDF) [39-41]. This is most likely because they are cheap, easily available and come ready to use. There are, however, a number of limitations with this type of sensor, such as a low sensitivity of around 20-30 pC/N and a high sensitivity to temperature change [42]. The sensor activity changes by approximately 0.5% per °C, which in the operating temperature range of a prosthetic hand of -30°C in cold conditions to 50°C (or potentially higher) when holding a hot object means a 40% change in the activity of the sensor would occur. Although a number of researchers report on the inclusion of these devices in prototype fingertips, there is very little informative data on the successful detection of slip.

Kyberd et al [18] investigated using a microphone embedded in a rubber tube chamber, which is mechanically coupled to a grasped object through the hands cosmesis. The frequency range from the microphone was restricted to a range of 150Hz – 1kHz. The slip sensor was attached to a prosthetic hand and a number of objects with

different surface textures were allowed to slip past it. The results showed that the device could successfully detect slip.

Cutkosky and Howe et al [41,43] developed a slip sensor using accelerometers mounted on the inside of a silicone rubber skin. To allow the accelerometers to vibrate, a dome shaped piece of foam bulks out the skin producing a fingertip shape. The foam and the side of the rubber skin were both attached to a solid mounting base. The skin was made from a self-levelling silicone rubber 1.5mm thick with small nibs on the outside surface. This is so that when slippage occurs some of the nibs at the edge of the grasped object break contact and snap back to their original position causing local vibrations. These vibrations were then picked up by the accelerometers and PVDF strips which were attached to the underside of the skin. The signals obtained from the accelerometer have been successfully used in conjunction with a tangential normal force sensor to control a 5 linkage robotic finger, limiting the slip of an object occurring even when a sudden change in load was applied.

2.4.3 Force sensors

Dario et al [39] developed a fingertip for use on a robotic arm, using an overlapping configuration of eight rows and eight columns of piezoresistive silk-screened ink, to create an array of 64 force sensors. A piezoelectric ceramic bimorph element was also attached to the fingertip to be used as a dynamic force sensor in an attempt to detect slip. The piezoresistors had a measuring force range of 0.1N to 8N with a maximum spatial resolution of 1mm, which is the maximum resolution that a human fingertip can differentiate between two different objects [44]. The piezoresistors were successfully used to detect the grip or normal force on an object as well as any movement of the object in the grip associated with slip. The piezoelectric dynamic force sensor was not characterised for its slip sensing capabilities in this paper.

Mingrino et al, [40] investigated a method to detect the incipient slip by monitoring the normal and shear force from a grasped object. The force sensor used comprised four piezoresistive thick-film force sensors printed on a polymer film in a square configuration with each sensor being printed in a triangular shape pointing towards the centre of the square. The force applied by gripping an object is coupled to the centre of the sensor configuration via a cylinder. This then allows the normal force

and tangential force of the object to be calculated from the force ratios applied to each thick-film resistor. By monitoring the normal and tangential forces and keeping the normal: tangential force ratio above a predefined level sets the lowest coefficient of friction limit to that value. Below this value, determined by the properties of the prosthesis glove and object, slip will occur and conversely above that value no slip will occur. It is therefore advantageous to set a high safety factor, allowing a range of objects to be gripped.

Beccai et al developed a miniature silicon tri-axial force sensor [45-48]. A silicon wafer was etched to produce a cylinder supported in a larger diameter circular hole by four equally spaced beams. Piezoresistors were subsequently fabricated on the beams using an ion implantation technique. By measuring the resistance ratios of the four devices, forces in the x, y and z plane can be determined. Due to the fragile nature of silicon, once the wafer was sliced it was placed on a purpose built carrier chip, producing a sensor with dimensions of 2.3mm x 2.3mm x 1.3mm. The device has been designed to measure a maximum force of 7N. Tests on the normal and shear loads have shown a linear response with very little hysteresis.

2.4.4 Automatic slip prevention in commercially available prosthetic hands.

The OttoBock Sensor Hand™ Speed is the only commercially available prosthesis which has incorporated a sensor to automatically control grip force in order to prevent an object from slipping out of the hand. The "SUVA sensor" [49,50] as it is known, works by monitoring the tangential and normal forces of a gripped object and is similar to the device described above developed by Mingrino et al. The sensor generally works well, however, Otto Bock have allowed the user the option of turning off the automatic grip function. This is because to work effectively a minimum grip force is required to be applied to an object. This grip force is too large for some items. Therefore, when the sensor is activated and a reaction force from an object is detected the control system will close the hand until the minimum force is detected, crushing or squashing some softer objects, for example a sponge.

2.5 Review of control strategies for the Southampton Hand

2.5.1 Introduction

In order to utilise the increased functionality of the Southampton Hand a hybrid controller using the Southampton adaptive manipulation scheme (SAMS), [14] in conjunction with the UNB MyoController [51] has been proposed [52].

Myoelectric signals produced for alternative attempted movements of the arm, for example extending the elbow or flexing the elbow, exhibit different characteristics. The UNB MyoController uses these signals from a muscle pair and classifies them. Each separate classified signal can then be used to control a different function within the prosthesis, for example, wrist rotation or the opening and closing of the hand. Using this technique up to four movement types or grip postures can be realised from an extensor/tensor muscle pair.

The SAMS controller illustrated in Figure 2.6 is constructed from a number of states, which are used during object manipulation. The POSITION state allows the user to adopt the required prehensile pattern. The prosthesis is then set in a voluntary open, involuntary close mode. Therefore, in order to hold the hand open, extensor muscle activity must be detected. The hand opens proportionally to the amplitude of the signal detected. If no signal is detected then the hand will close until the force sensors detect contact with an object. At this point the hand will stop and adopt the TOUCH state with a minimum grip force applied to the object. A further flexion EMG signal will then move the controller on to the HOLD mode where the slip detectors are activated and automatically control the grip force to prevent the object from slipping out of the prosthesis. The user may then override the controller with a flex of the muscle to increase grip force in the SQUEEZE mode, or just simply release the object with an extend EMG signal.

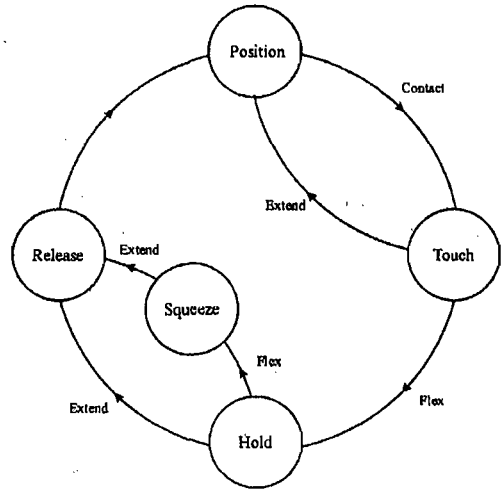

Figure 2.6: Southampton adaptive manipulation scheme (SAMS) state diagram.

Combining the UNB MyoController and the SAMS controller allows the user to initially select one of four pre-programmed prehensile grip patterns as determined by the UNB MyoController from the user's signal. From this stage onwards the SAMS hierarchical control system is activated and any change of grip pattern from the controller is ignored. At any stage during the grasping process a maintained period of extensor activity will reset the controller to the initial grip pattern select mode.

2.5.2 Direct connection to the peripheral nervous system

To connect a prosthetic hand to the peripheral nervous system is considered extremely advantageous by many researchers in the field of prosthetics [53-55]. Essentially, the original control inputs from the amputated hand are being used to control a device for the same purposes. This would provide a natural feeling control to take place with minimum cognition experienced by the user and potentially very little training would be required to use the device.

Work in the UK has investigated implanting a 4mm x 4mm, 100 element electrode array into the median nerve of an able bodied male [55]. A threshold was applied to the output signals obtained from the electrode array to control the opening and closing of a multiple degree of freedom hand operating under the SAMS control system. The hand [56] also incorporated force sensors on the fingertips, which were used to provide feedback directly to the peripheral nerves as a current in the range 80-

100 μA. Experiments were undertaken using visual feedback, force feedback and a combination of both to grip an object as lightly as possible. The results showed that using a combination of both visual and force feedback allowed the user to provide the lightest grip whereas using visual feedback or force feedback on their own showed that considerably higher grip forces were applied. The implant was successfully removed after 96 days showing no signs of infection to the subject. Post analysis of the implant indicated little evidence of rejection by the body. This suggests that this type of implant could be available for long term use in the future.

Research undertaken in the USA by Dhillon et al [54,57] has involved implanting electrodes directly into the fascicles of severed nerves in six upper limb amputees. Trials were then carried out over a period of six days using feedback to the nerves to control the grip force of a prosthetic hand. A similar test using feedback to the nerves to indicate the elbow joint position of a prosthetic arm was also carried out. Both tests used only a single input and output and no visual feedback from the user was allowed. The results are promising and demonstrate that good motor control of the prosthesis with direct feedback to the nerves can be obtained.

More research is therefore required to target specific motor functions and this technique is not likely to be available for general use in the near future. However, these initial results show that direct control inputs can be harnessed from the peripheral nerves and tactile sensor information successfully returned to the user, which looks promising for the use of returning natural hand control to a patient.

It is proposed that each motor of the Southampton hand will be controlled independently so that the user will easily be able to define the required prehensile grip pattern. The signals provided from the nerves will be proportional to the speed at which the fingers move until TOUCH is detected, at which point the signal will become proportional to the applied grip force. Once the force has remained approximately constant for a period of time the HOLD function will be activated to prevent object slip. This will replicate the automatic control of the grip force when slip has occurred in the human hand [58] and help to reduce the cognition on the user through visual monitoring of the object. The force, slip and motor encoders will also be used to send tactile feedback to the user.

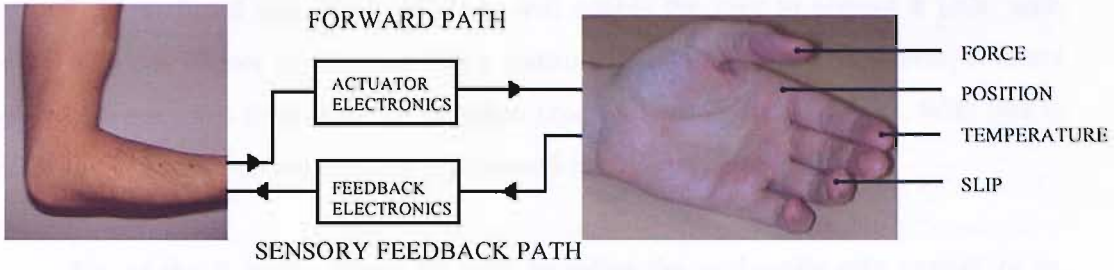

Figure 2.7: Control system using direct inputs from the peripheral nervous system.

2.5.3 Implantable myoelectric sensors (IMES)

Surface electromyography (EMG) sensors are currently the sensor of choice in controlling upper limb prosthetics. They pick up the EMG signals from a number of muscles and combine them together depending on where they are placed. Weir et al [59-63] have reported on using implantable myoelectric sensors to target specific muscles in the arm which are used to control arm function. There are a range of muscles contained in the human arm and by targeting muscles used for specific operations in the lost limb, a more natural feel to hand control will be achieved. The number of sites available for use to control the prosthesis will ultimately depend upon the level of amputation for each individual patient. An initial concept test has shown that six EMG signals can be successfully obtained from the arm. When fully developed each wireless IMES sensor will be injected into a target muscle and the signals sent to an external controller via a transcutaneous magnetic link. The sensors will be powered using an external magnetic field. Currently work is still required to reduce the size of the external reader coil to fit within a prosthesis socket. The power consumption of the reader must also be addressed to allow a suitably sized battery to be fitted within the prosthesis.

A similar project involving injecting BION™ electrical stimulators into a muscle to stimulate specific targeted muscles in stroke patients has been used to provide better upper limb control [64]. The IMES sensors will use the same packaging and implant method as used in this technique, except, instead of stimulating the muscles they will be used to detect the signals from them.

It is predicted that this technology will enable the user to control 8 DOF with more than one degree of freedom being controlled simultaneously. However, it is not clear how easy this control would be when producing some types of grip. With this in mind the following control system is proposed for a possible 8 DOF input.

Six of the 8 inputs would be used to select the prehensile grip pattern or an independent finger/thumb movement. When a pattern has been selected the same input signal will be utilised to proportionally control the grip force applied to the object. Once the user stops producing this signal the hand enters a HOLD state as defined in the SAMS controller. The user then has three options: they can override the HOLD state to apply a SQUEEZE to the object using the same input; reset the hand to return to a fully open rest position (using the PARK input) or reset the hand using one of the five other prehensile patterns using a single EMG burst. This would then set up the hand into another prehensile pattern ready for the next task.

A single input (MODE SELECT) would be used to disengage the SAMS controller and allow individual fingers or the thumb to be moved independently, or more prehensile patterns to be produced depending upon the users preferences.

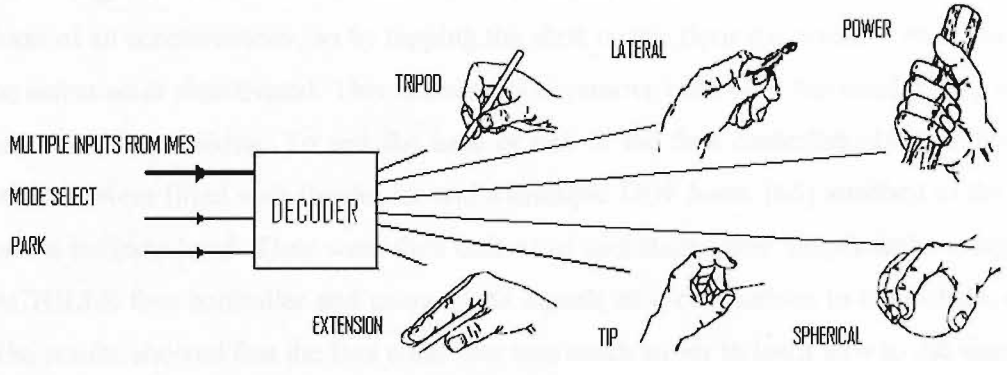

Figure 2.8: Potential control system using IMES inputs with six useful prehensile grip patterns.

2.5.4 Typical grip postures.

There are a number of different grip postures which we all use in our activities of daily living (ADL). These postures are naturally adopted before the task begins allowing the most efficient manner of undertaking a task to be achieved. For example

the lateral grip is often used for unlocking a door with a key. However, you would probably not use this type of grip when lifting a heavy object.

The six prehensile grip postures illustrated in Figure 2.8 and Figure 2.4 would allow an amputee the freedom to undertake the majority of ADL in a much more natural way than is currently allowed by a single degree of freedom tripod grip.

2.6 Alternative upper limb control inputs

2.6.1 Insole foot controller

Carrozza et al [65] have reported the development of a controller that uses selected foot movements to actuate a robotic hand. The prototype device is based around a standard shoe insole which has four purpose built pressure switches attached to it. The switches are located in four different areas, under the big toe, the heel and two at the sides of the foot. The battery and electronics are also contained within the insole under the arch of the foot. To transmit the signals to the hand Bluetooth wireless technology is used. There is also an on/off switch incorporated into the insole in the form of an accelerometer, so by tapping the shoe on the floor the pressure switches can be activated or deactivated. This is essential to remove control of the hand during other tasks such as walking. To test the ease of use of the foot controller, 10 able bodied subjects were fitted with the device and a multiple DOF hand, [66] attached to the end of the subjects hand. They were then trained to undertake some simple tasks using the ACHILLE foot controller and using EMG signals as a comparison to control the arm. The results showed that the foot controller was much easier to learn how to use than the EMG controller.

2.6.2 Targeted muscle hyper-reinnervation

Targeted muscle hyper-reinnervation is a technique developed by Kuiken et al [67] investigated in rats. It involves sewing large nerves containing many motor neurons onto a small muscle area in order to hyper-reinnervate the muscle. This then allows the muscle to be controlled using signals from the transferred nerve.

In an upper limb amputee the brachial plexus nerves, which control the muscles in the arm, become severed. There are four nerves which make up the brachial plexus nerves. These are the ulna, radial, median and musculocutaneous, and each controls different muscle groups within the arm. The number of nerve reinnervations available depends on the level of amputation in the patient's arm. For a wrist amputation the median and ulna nerve may be used to create two new EMG sites as they both control some of the muscles which actuate the hand [68]. However, to use the musculocutaneous and ulna nerves would mean loosing function from other muscles unless the patient had suffered a higher amputation. The advantage of using these new EMG sites over other sites is that the patient feels as though they are actually using their hand rather than activating a muscle which has not previously been associated with a hand or arm movement.

An operation on a bilateral shoulder disarticulation amputee [69] has proved muscle hyper-reinnervation to be successful in humans. The patient had all four brachial plexus nerves reinnervated onto a segmented pectoralis major muscle and the pectoralis minor. After surgery the patient was instructed to simulate using their arm and hand muscles everyday to stimulate the nerves and help reinnervate the muscles. It took approximately 3 months before the first signs of muscle twitching occurred and approximately 5 months before 3 out of 4 reinnervated muscles were active. Some of the sensors in the chest were also reinnervated and the patient reported feeling parts of his amputated hand and arm when certain parts of his chest were touched. The three new EMG sites were subsequently used to control a prosthetic arm. This technique is relatively new and further areas of exploration include work on increasing the number of signal outputs from the new EMG sites and using the reinnervated sensory sites for force feedback [70,71]

2.6.3 Conclusions

Future developments in harnessing natural control inputs from a subject who has suffered the loss of a hand are an essential factor in enabling the full potential of a multifunctional prosthetic hand to be realised. Developments in harnessing information from the peripheral nervous system and particularly IMES both show the potential in the future to provide these extra natural control inputs. However, even with these extra

control inputs there is still a need for some automation within the actuation of the prosthesis as found in the human hand. An example of this is the automatic increase in grip force on a held object when slip is detected.

Any new control algorithm for the control of a prosthetic hand using new input technology will have to be adaptive for different patients to take into account the level of amputation as well as personal preferences of control. Nevertheless, some of the original SAMS control states may still prove to be extremely useful in reducing the cognitive strain on the user.

Chapter 3 Piezoelectric thick-film fabrication process

3.1 The piezoelectric effect

In 1880 Jacques and Pierre Curie discovered the piezoelectric effect. Piezoelectricity is the ability of certain crystal classes or ceramics to produce an electrical charge when a mechanical force is applied. The polarity of the charge is dependent upon the type of force applied (a compressive force will cause charge to flow in the opposite direction to that of a tensile force applied to the same crystal) and the magnitude of the charge is proportional to the magnitude of the applied force. Conversely, if an electric field is applied across a piezoelectric crystal, it causes the crystal to stretch or compress, depending on the polarity of the crystal with respect to the direction of the applied electric field. This is generally referred to as the inverse piezoelectric effect [72].

The criterion for a material to exhibit piezoelectricity is a lack of a centre of symmetry within the unit cells of the materials structure. All piezoelectric materials are described as ferroelectric and some occur naturally in crystal form (crystalline structure) such as quartz or tourmaline. Besides these crystals there are also a range of piezoeceramics, which are polycrystalline materials (composed of two or more crystals). Piezoceramics are said to have a perovskite crystal structure (a cubic crystal structure), which can be described by the general formula ABO where A represents the large divalent metal ions, B is a tetravalent metal ion and O is oxygen. Figure 3.1

illustrates two unit cells of the piezoelectric material barium titanate, where the small tetravalent metal ion B is titanium surrounded by oxygen atoms and larger divalent metal atoms of barium (A).

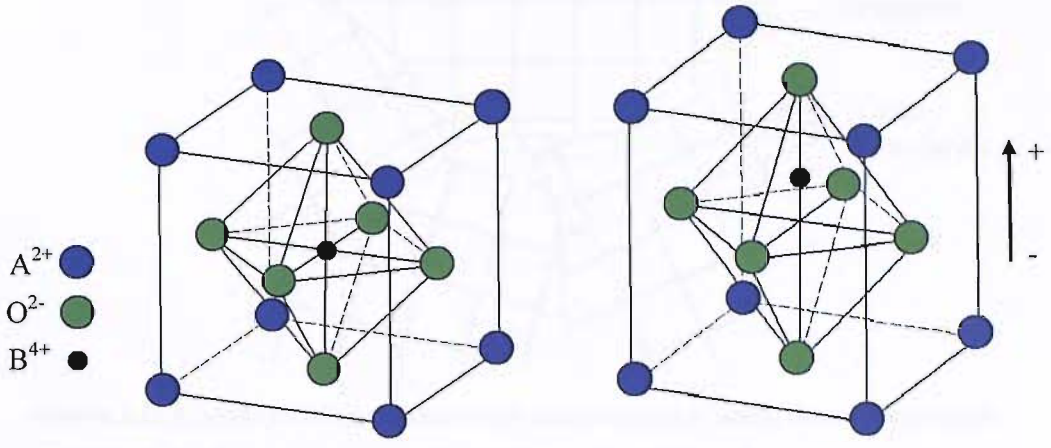

Figure 3.1: (Left) Idealised perovskite cubic lattice formed above the Curie temp. (Right) Perovskite tetragonal lattice formed below the Curie temperature.

(Illustration adapted from [72]).

The structure of a unit cell is dependant upon temperature. Above a certain temperature, known as the Curie temperature, the unit cell becomes an idealised perovskite structure Figure 3.1, left diagram) and the ionic charges within the unit are balanced (no piezoelectric properties are exhibited). Below the Curie temperature, however, the tetravalent atom is displaced from the centre of the idealised perovskite structure and the cube lengthens in the same direction causing it to become a tetragonal shape (Figure 3.1, right diagram) and producing a dipole (piezoelectric properties are exhibited).

Within a crystal structure there are a large number of unit cells stacked together. The neighbouring unit cells form locally aligned dipoles in small groups known as Weiss domains, giving a net dipole moment. The domains within a crystal structure can either be aligned, at ±90° or ±180° to each other. For polycrystalline piezoceramics, which are split up into crystallites, (cf. Figure 3.2) the Weiss domains within the crystallites are aligned in the same manner as a crystal (a crystallite is in effect a crystal with a crystalline structure). However, for the different crystallites the angles between Weiss domains can vary by Θ, $\Theta \pm 90°$ or $\Theta \pm 180°$.

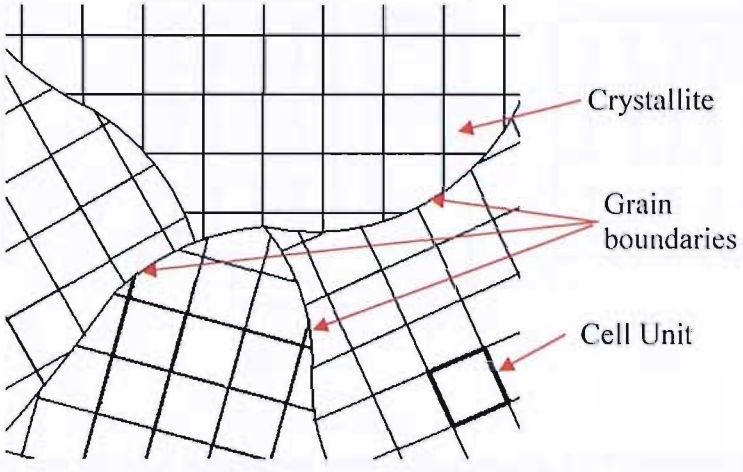

Figure 3.2: A polycrystalline structure with unit cells (not to scale) drawn within each crystallite. N.B. when observing a polycrystalline material through a microscope only the boundary lines can be seen. (Illustration adapted from [73]).

3.1.1 Poling

The resultant polarisation of each crystallite is the vector sum of all of the Weiss domains located within it. Initially within a piezoceramic the orientation of the polarisation of each individual crystallite is random and over the whole of the material tends to cancel out (Figure 3.3 (a)). The ceramic, therefore, does not have an overall polarisation and hence, does not exhibit piezoelectric properties. In order for the material to become piezoelectric the domains must be aligned by a poling process. This involves applying a large electric field to the material below the Currie temperature. The Weiss domains are forced to switch and realign towards the direction of the applied field, with the overall polarisation of each crystallite aligning with the direction of the field (Figure 3.3 (b)). The material also lengthens in the same direction. When the electric field is removed the polarities of the crystallites remain orientated in the direction of the field, although some moderate re-alignment does occur as illustrated in Figure 3.3 (c).

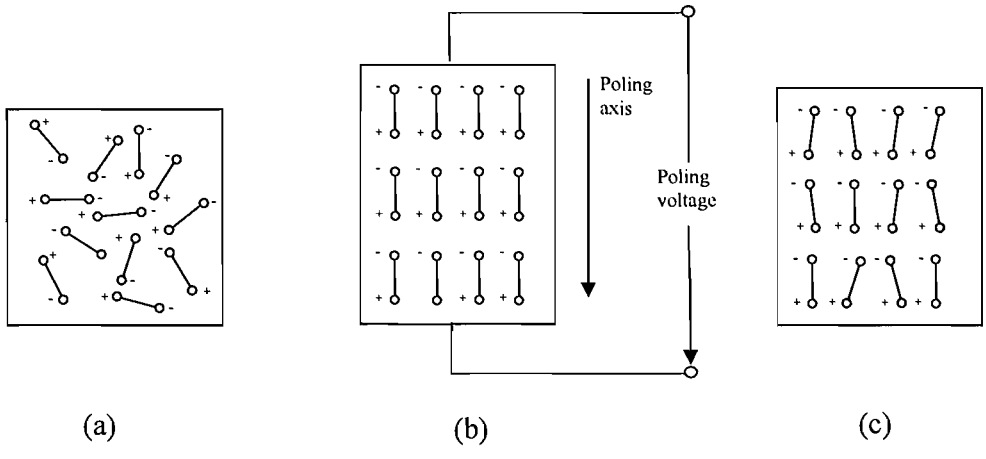

Figure 3.3: (a) Random orientation of polarisation from each crystallite. (b) Polarisation of crystallites aligned by an electric poling field. (c) Remaining polarisation of crystallites. (Illustration adapted from [72]).

Poling a ceramic in one direction does not constrain it to that original orientation and by applying a large enough electric field in the opposite direction the material can be re-poled in that direction, or any other direction. This cycle can be repeated if required. Figure 3.4 shows a typical hysteresis loop of a piezoceramic, where the saturation polarisation is the maximum polarisation achieved when an electrical field is still applied, the remnant polarisation is the remaining polarisation after the electrical field has been removed and the virginal curve represents the initial polarisation of the piezoceramic material.

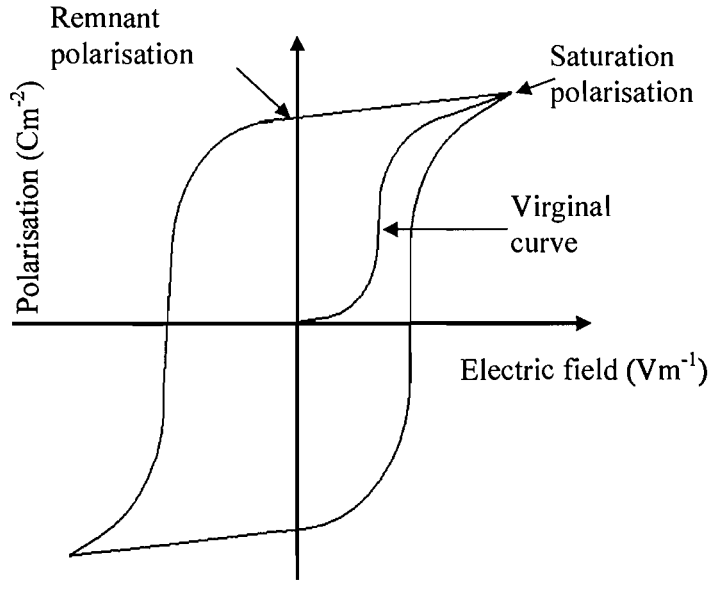

Figure 3.4: Polarisation hysteresis loop for a piezoceramic. (Illustration adapted from [72]).

3.1.2 Applications of piezoceramic materials

There is a wide range of uses for piezoceramic materials as sensors, power generators (using the piezoelectric effect) or as actuators (using the inverse piezoelectric effect). The piezoelectric effect on a ceramic cylinder is illustrated in Figure 3.5. If a polarised ceramic cylinder has no external forces applied to it, then no voltage is produced from the device in a measuring circuit (Figure 3.5 (a)). However, if a compressive force is applied to the ceramic in the plane perpendicular to polarisation then a voltage is produced (Figure 3.5 (b)). Conversely, if a tension force is applied to the same plane then a voltage in the opposite direction is produced. This conversion of mechanical energy into electrical energy is commonly used in applications such as gas lighters, accelerometers, hydrophones and microphones.

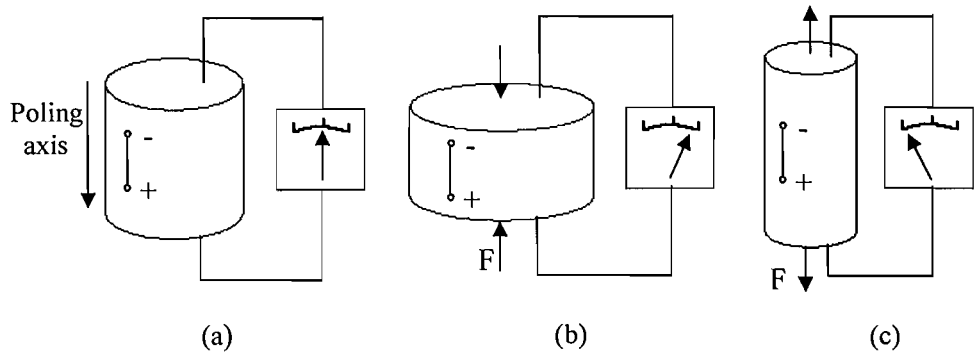

Figure 3.5: (a) A poled piezoelectric ceramic cylinder. (b) Piezoelectric ceramic cylinder in a measuring circuit undergoing an instantaneous compressive stress. (c) Piezoelectric ceramic cylinder in a measuring circuit undergoing an instantaneous tensile stress.

(Illustration adapted from [72]).

Figure 3.6 illustrates the inverse piezoelectric effect on a polarised ceramic cylinder. If a voltage of the same polarity to the ceramic is applied to the cylinder then it will shorten in length (Figure 3.6 (a)), conversly if a voltage with the opposite polarity is applied to the ceramic then it will increase in length (Figure 3.6 (b)). The ceramic cylinder may also be caused to lengthen and shorten if an alternating voltage is applied to the cylinder (Figure 3.6(c)). The frequency at which this occurs is dependant upon the frequency of the alternating voltage. This conversion of electrical energy into mechanical energy is used in a wide variety of applications including linear actuators, buzzers, high frequency loud speakers, sonar, ultrasound and ultrasonic soldering irons.

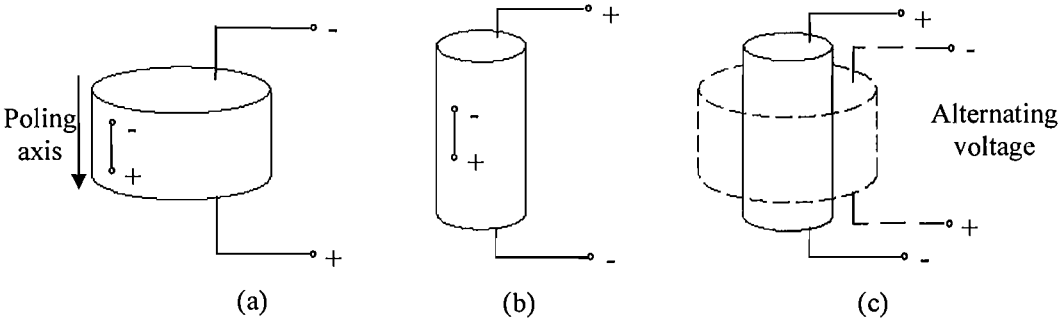

Figure 3.6: (a) Piezoceramic cylinder with electric field in the same direction as polarisation. (b) Piezoceramic cylinder with electric field opposing the direction of polarisation. (c) Alternating electric field polarity on a piezoceramic cylinder. (Illustration adapted from [72]).

3.1.3 Depolarisation

After poling the piezoelectric properties of a ceramic deteriorate with time in an exponential manner. This effect makes the ceramic become more stable as it ages. The depolarisation effect is caused by the Weiss domains moving towards their original randomly orientated state (a neutral position). This depolarisation effect can be accelerated by a number of other external parameters, such as temperature, applied electric field and mechanical stress imparted onto the ceramic. The characteristics of different piezoelectric materials are not the same and therefore some materials are more resistant to certain types of depolarisation. The characteristics of PZT ceramics for example can be altered by changing the ratios of Zirconate to Titanate [72].

Total thermal depolarisation occurs when the piezoelectric material is heated to or above its Curie temperature. It is generally recommended that to avoid any depolarisation due to thermal effects that the piezoelectric material is not subjected to a temperature more than half of its Curie temperature.

Mechanical depolarisation occurs when the stress applied to the material is large enough to disturb the orientation of the dipoles. The stress required to disturb the orientation of the dipoles also varies with different materials.

Electrical depolarisation occurs when the piezoelectric material is exposed to an electric field with the opposite polarity. If the electric field is large enough it may cause the material to become polarised in the opposite direction The field strength required for depolarisation is also dependent upon the composite type and temperature.

3.1.4 Notation and characteristic properties of piezoceramics

Piezoceramics are anisotropic and therefore the material properties are dependent upon the direction a measurement is taken with respect to that of the polarisation. To describe the orientation of the ceramic with respect to the measurement, a standard system of notation has been devised and is illustrated in Figure 3.7. The numbers 4-6 are used to describe shears within the ceramic.

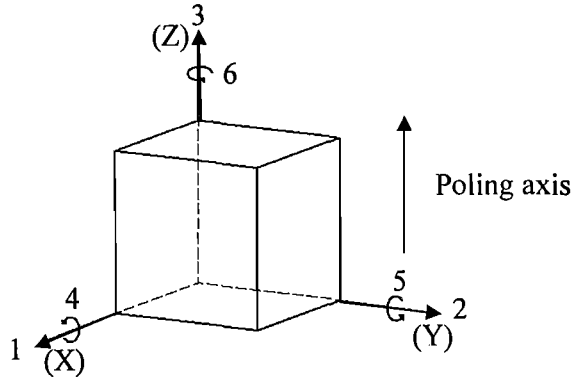

Figure 3.7: Directions of subscripts. (Illustration adapted from [72]).

When describing a property constant it is common practice to use two numbered subscripts, which represent different characteristics depending upon the measurement being taken. For example the commonly used piezoelectric charge constant, d, can be defined as either the short circuit charge density for an applied stress or alternatively a strain produced for an applied electric field (Equations 3.1.and 3.2).

d = Short circuit charge density/ applied stress (C/N) Eqn 3.1

d = Strain produced/ applied electric field (m/V) Eqn 3.2

Throughout this thesis the d_{33} characteristics of devices are measured using a Take Control PiezoMeter described section 3.9. The description of the d_{33} notation is therefore defined from equation 3.1 as the direction of polarisation and the direction of the applied force respectively. It is interesting to note however, that the measured d_{33} (or any other direction for a given material) is numerically the same for both equations 3.2 and 3.1, and the units are dimensionally the same. The d_{33} of a device provides information on the level of polarisation from the device and therefore gives an indication of its sensor and actuator capabilities.

The characteristics of piezoceramics can be described in more detail using the following set of equations.

$$D = dT + \varepsilon^T E \qquad \text{Eqn 3.3}$$

$$S = s^{E}T + dE \qquad \text{Eqn 3.4}$$

$$E = -gT + (\varepsilon^{T})^{-1}D \qquad \text{Eqn 3.5}$$

$$S = s^{D}T + gD \qquad \text{Eqn 3.6}$$

Where ε is the permittivity (F/m) (or dielectric constant), s is the material compliance (m^2/N), S is the strain induced in the material, T is the stress on the material (N/m^2), d is the piezoelectric charge constant (C/N or m/V), D is electric displacement (C/m^2), g is the voltage constant and E is the electric field (V/m).

The superscripts in the equations are used to indicate a constant condition. For example s^E is the compliance of a material under a constant electric field.

Equations 3.3-3.6 provide the electromechanical relationships of piezoelectric materials. They can also be used to calculate certain constants of piezoelectric materials, when other material properties are known.

3.1.5 Differences between thick-film piezoelectric materials and bulk piezoceramics

Conventional piezoelectric thick-films processed at a temperature below 1000°C have a different structure to their bulk ceramic counterparts. Instead of being a single polycrystalline material, once fully formed, a piezoelectric thick-film layer is constructed from small piezoceramic grains suspended in either a glass or polymer matrix. Figure 3.8 shows a scanning electron microscope (SEM) micrograph of the cross section of a thick-film piezoceramic device with a gold bottom electrode and a silver polymer top electrode. The micrograph clearly shows the piezoceramic grains within the glass matrix as well as a large number of voids throughout the film. Intuitively the addition of a binder material and number of voids within the film will affect the overall characteristics. As the piezoelectric grains are not all sintered together in a single polycrystalline structure and there are extra barriers for the charge to overcome to reach the surface electrodes (in the form of dielectric binder and voids) then d_{33} is reduced when compared to that of a bulk piezoceramic made from the same active material. The magnitude of the electric field at which dielectric breakdown occurs is reduced and therefore the potential displacement produced from a thick-film as an actuator is reduced. The mixture between binder material and active powder must,

therefore, be optimised to achieve the best results. Work on the optimisation of d_{33} of piezoelectric thick-film devices is described in more detail in Chapter 5.

Baomin et al [74,75] have reported fabricating piezoelectric thick-films without the use of a binder material within the paste. The thick-films were fabricated on sapphire substrates at a peak processing temperature of 1150 -1250°C and have been successfully transferred onto other substrate materials, such as plastics or metals using a laser transfer process.

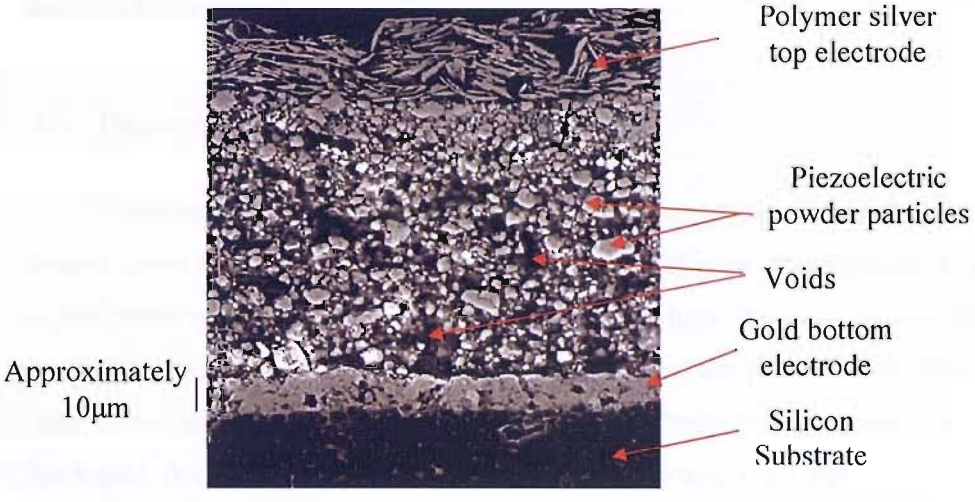

Figure 3.8: SEM micrograph of a typical cross section of a piezoelectric thick-film.

3.2 Fabricating piezoelectric thick-films

Screen printing of thick film piezoelectric devices was first reported by Baudry in 1987 [76,77]. Piezoelectric thick films offer alternative methods for fabricating piezoelectric structures as thin as 10μm compared to bulk ceramics of which it is necessary to use expensive cutting or lapping procedures in order to realise a device 50-200μm thick [78].

There are several different methods that can be used to fabricate piezoelectric thick films, including: spray painting [79], tape casting [80,81], sol gel [82] or screen printing [83]. The fabrication method used throughout this thesis is a screen printing technique. Screen printing thick-films is a low-cost and accurate method of depositing materials onto a substrate in the desired pattern with no further trimming processes required.

Throughout this research program a number of piezoelectric thick-film devices were fabricated using different processing parameters and paste mixtures. This was undertaken in order to investigate the effects these changes would have on the piezoelectric properties of devices. As well as test samples, devices were also fabricated for use as slip sensors on the Southampton Hand. The following sections are intended to provide a general introduction to the different types of thick-film piezoelectric device and to describe the processes and procedures used throughout this thesis to fabricate and test them.

3.3 Piezoelectric thick-film structures

There are two main piezoelectric thick film design types. Figure 3.9 illustrates the printed layers of these two different structure types: a) is an interdigitated design and b) is the more commonly used capacitive design, where the piezoelectric material is sandwiched between two electrodes. In both designs, the piezoelectric film forms the only direct path between the two electrodes. These two structure types can be fabricated from both low temperature curing polymer (~25-200°C) [84] and high temperature firing (~750-950°C) [85] ceramic pastes.

The majority of the devices discussed in this thesis were fabricated on 96% alumina substrates, and for PZT thick-film characterisation purposes, are of a capacitive design. To allow d_{33} measurements to be taken with a Take Control PiezoMeter, an extra electrode is printed on the underside of the alumina, as shown in Figure 3.9 (b). The operation of the Take Control PiezoMeter is described in more detail in section 3.9. This extra electrode is therefore not required to fabricate a capacitive piezoelectric thick-film device.

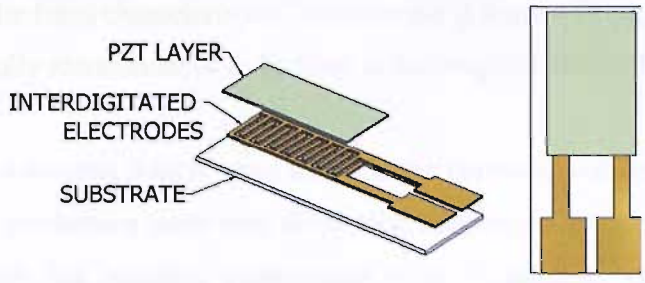

a)

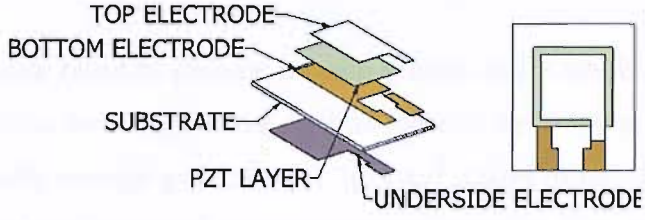

b)

Figure 3.9: a) Interdigitated piezoelectric structure. b) Capacitive piezoelectric structure.

3.4 Paste formulation

Piezoelectric thick-film pastes are generally made using three components: an active material, a binder material and a vehicle or solvent. The active material largely provides the characteristics of the film. The binder material is used to create a solid matrix within the film, which holds the active material together and fixes the film to the substrate. There are two main types of binder that are used to create thick-films: polymer and glass. Polymer binders are generally used to create thick-films that can be printed on a range of substrates. This can be achieved because the film polymerises (forms a solid matrix) at relatively low temperatures. Depending on the polymer type, this will usually occur at room temperature over a period of 24 hours. The process can, however, be accelerated up to a time of 1-2 hours by heating the film to a temperature of 150 - 200°C. This process is often referred to as curing.

There are a number of different types of thick-film glass binder [86]. They are generally available in powder form and can withstand much higher temperatures than polymers. They are used in thick-films that require high temperature processes (800-

950°C) to improve the films characteristics. This process is termed firing. The different glass types are typically recommended to be fired in the range of 380-900°C.

The vehicle is a solvent, which when added in the correct quantities to the active material and binder, produces a paste with the correct rheological properties for screen printing. In particular, the resulting paste needs to be thixotropic, exhibiting flow properties when put under pressure by a squeegee during the printing process, yet remaining solid and retaining its shape once printed.

The paste mixture (used to produce the slip sensors and a number of other test devices) was based on a powder blending method reported by Torah et al [85,87,88], using PZT powder with average grain sizes of 2μm and 0.8μm mixed in a 4:1 weight ratio, with 10% of the total weight of the mixture being made up from the glass binder material CF7575. To create the paste the PZT and glass binder powders were initially mixed with a pestle and mortar in order to evenly distribute the powder and break down any large lumps that had formed during storage. It was subsequently mixed, using a spatula, with an organic vehicle (ESL 400, Electroscience Laboratories). The mixture was then put through an Exact 35/50 triple roll mill to remove any remaining lumps within the paste, improve the dispersion of the particles and render the paste screen printable. Two different suppliers of PZT powder were used throughout this project, Morgan Electroceramics [72], who supplied PZT-5H and Ferroperm [89] who supplied PZT-Pz29.

3.5 Screen printing piezoelectric devices

3.5.1 Selecting screen fabrication parameters

The thick-film screen printing technique is used to deposit films with different characteristics in a layer-by-layer process, in order to fabricate a specific type of device. In the case of the capacitive piezoelectric device shown in Figure 3.9 (b), four separate screens are required, one for each layer. Each screen is constructed from a woven mesh of stainless steel (or sometimes nylon) wires, with individual filaments of warp and weft orientated at 90° to each other, covered in an ultra-violet sensitive emulsion and mounted in a frame under tension. The required pattern for each layer is

subsequently formed photolithographicaly on the layer of ultra-violet sensitive emulsion, leaving only the required pattern area with open mesh holes. The four patterns for the screen designs used to print an array of 30 thick-film piezoelectric devices (illustrated in Figure 3.9 (b)) onto a 4"x4" 96% alumina substrate can be seen in appendix D along with drawings of the other screen artwork used in this thesis.

Artwork for all of the screens used throughout this project were designed in-house and sent off to either DEK [90] or MCI [91] to be turned into printing screens. When ordering a new screen, there are a number of variables in screen type which must be considered. These include the mesh concentration (the number of wires per cm, ranging from 31-200), the diameter of the wire mesh (18-100μm), the angle at which the mesh crosses the screen (with respect to the top of the screen) and the emulsion thickness. A good overview of how to optimise these parameters can be found in [92]. The mesh concentration and emulsion thickness both help to control the thickness of the printed thick-film. A higher mesh density and thinner emulsion layer produces a thinner film thickness when compared to a lower mesh density and thick emulsion layer. However, when altering the mesh density the size of powder particles within the paste intended to be printed must also be considered to ensure that they can pass through the patterned areas of the mesh, as well as the minimum feature sizes of the patterns being printed.

The choice of mesh angle is intended to allow the designer to maintain a high resolution of printed films by removing the chance of a wire from the mesh lying across the straight edge of the shape intended to be printed. For example if a square shape was etched onto a screen with two of its edges lying at 90° to the top edge of the screen and a mesh angle of 90° (to the top edge) was chosen, then it would be possible that all of the edges of the square could lie a on a wire and therefore the square could be reduced in size by the wire's diameter on each side. To avoid this, the designer should ensure that all mesh wires, where possible, are at an angle to the straight line features of the pattern design. In this thesis all screens have a mesh of wires running at 45° to the top of the screen frame as illustrated in Figure 3.10.

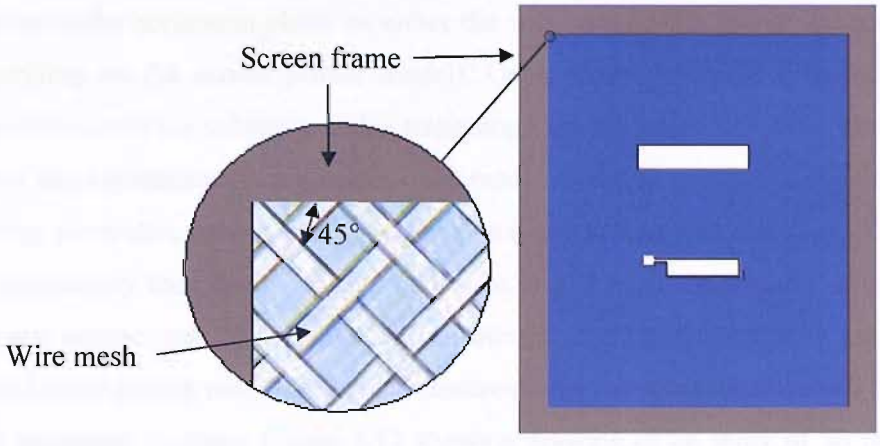

Figure 3.10: Illustration of wire mesh laid out at 45° to the top of the screen frame.

3.5.2 Alignment and print accuracy

To increase accuracy when printing, the screen is bolted to the printer and the substrate placed on a holder and held in position with a vacuum. To prevent any movement of the substrate holder during printing it is also bolted to the bed of the printer. Generic, plate substrate holders, can be used to hold an array of different substrates. However, for more accurate results when printing a batch of devices, purpose built substrate holders are generally used, where each substrate can be guided into the exact same position with either a slot cut into the holder, or a raised profile, such as small pegs. Figure 3.11 illustrates a finger linkage holder used when printing thick-film piezoelectric sensors onto the finger linkages of the Southampton Hand.

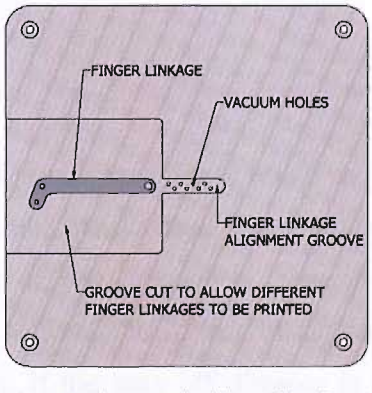

Figure 3.11: Finger linkage substrate holder. The finger linkage is slid into the area where the vacuum holes are located.

Once the substrate and screen have been secured, they need to be aligned. This is achieved visually, using three micrometers to control the x and y directions and the

rotation in the horizontal plane on either the substrate holder bed or the screen holder (depending on the screen printer model). Once visually aligned it is then common practice to cover the substrate with a transparent low tack tape and run a test print. This allows any adjustments in alignment to be made as well as printing parameters, without wasting substrates, (which can sometimes be expensive to manufacture). If the print is not satisfactory then the paste can simply be wiped from the surface of the low tack tape and another test layer printed. To ensure the alignment is accurate for thick-films printed away from a natural reference feature on the substrate, screens can be designed with alignment markers. Figure 3.12 shows a drawing of an array of 30 piezoelectric thick-film devices, with alignment markers for each layer.

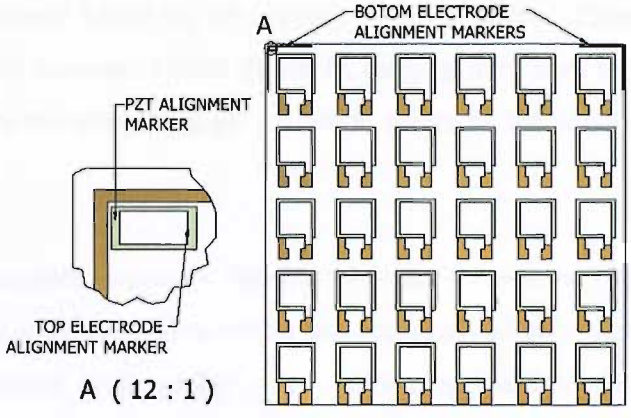

Figure 3.12: Drawing of an array of capacitive type thick-film piezoelectric devices on a 96% alumina substrate, with alignment markers for each layer.

3.5.3 Printer parameters

There are a number of printer parameters which can be adjusted to increase print quality or change printed film thickness depending on the viscosity of the paste. These parameters include: the snap off distance, squeegee pressure and print speed. The snap off distance is the distance between the surface of the screen and the substrate and is generally set to about 1mm. If the snap off distance is increased then the squeegee pressure must also be increased in order to sufficiently deflect the screen onto the underlying substrate. This has the effect of producing a thicker printed film as the surface tension on the paste (when in contact with the substrate) is increased due to the screen snapping back to its original position at an increased velocity. This acts to pull

more of the paste through the wire mesh and onto the substrate. Conversely, if the snap off distance is reduced then the film thickness is reduced. If it is too small though, the print quality maybe affected. In general the squeegee pressure should be kept as low as possible to increase the life of the screen and reduce the risk of tearing [93].

The print speed also affects the printed film's thickness, with a faster speed producing a thicker film than a slower speed. This occurs for the same reasons as stated above, for increasing or decreasing the snap off distance.

3.5.4 Squeegee hardness selection

To obtain an even thickness of print over a large area the substrate must be very flat and the squeegee blade set up parallel to the substrate. There are a number of different grades of squeegee blades available, ranging from very hard to soft. The hard rubber squeegees are used for high definition prints as the squeegee blade does not deflect.

Softer squeegees are more flexible and can be used to produce a more even thickness of print over large areas with a less accurately aligned blade. Their flexibility also acts to improve print quality when fabricating the later layers of multi-layer structures. In particular, layers that are printed onto a surface (or surfaces) which changes in height and requires the squeegee to step up over features. Figure 3.13 illustrates the step up produced for the printing of a typical capacitive design piezoelectric thick-film structure.

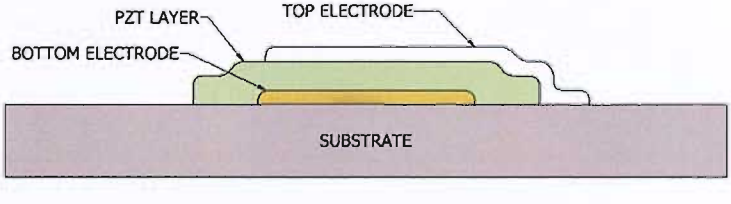

Figure 3.13: Step up in printing layers for a capacitive design piezoelectric thick-film.

3.5.5 Printing process

Once the substrate and screen are suitably aligned, the correct squeegee has been chosen and the print parameters selected, the paste is placed onto the screen in front of the squeegee printing blade. The paste is dispersed across the screen by the squeegee during the print stroke and pulled through to the underlying substrate by surface tension, thereby forming a thick-film. Figure 3.14 illustrates the printing process. The paste is then returned to its original position in a second stroke, which can either be a print stroke or a flood plane stroke. During a flood plane stroke, the squeegee does not contact the screen. Instead, a floating blade moves lightly across the un-deflected screen to leave a layer of paste over the surface of the screen.

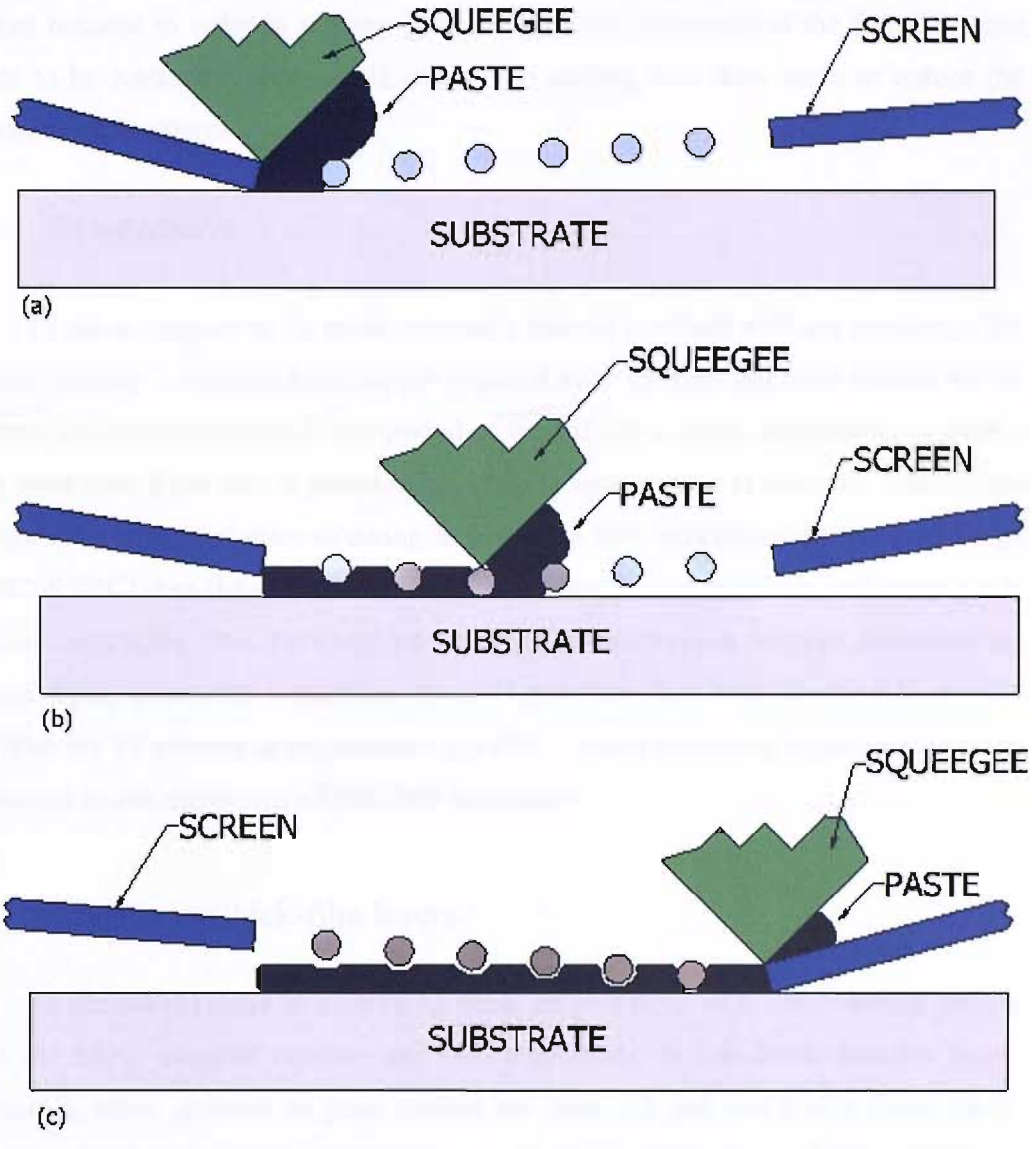

Figure 3.14: Diagram of the screen printing process (illustration adapted from [83]).

3.5.6 Film settling time

After a thick-film layer has been printed onto a substrate its surface is uneven and has a number of peaks and troughs across it. This remnant pattern is an artefact of the meshed screens used to define the thick-films geometry, since the paste is pulled through the pattern in the screen it flows around the mesh and onto the substrate. Hence, when the screen snaps back a pattern of the mesh is left on the surface of the film. The paste naturally seeps into these gaps with the flow rate dependant upon the viscosity of the film. In order to allow this to take place a settling time of around 10

minutes is generally allowed. The settling time does not completely remove the mesh pattern because in order to achieve good dimensional tolerances of the film the paste needs to be reasonably viscous. However, the settling time does serve to reduce the imposed mesh pattern.

3.5.7 Drying samples

To allow samples to be screen printed a vehicle is mixed with the powders. This vehicle (usually a solvent) is no longer required after the film has been printed and in general will evaporate over a long period of time if left at room temperature or after a very short time if the film is processed at a higher temperature. If however, some of the solvent is not removed prior to curing or firing the film (processing temperature range 150°C -950°C) then the solvent can be forced to evaporate too quickly and cause voids to form within the film. To speed up the evaporation process, without damaging the film, a drying procedure is therefore used, whereby the film is gently dried in an infra red drier for 10 minutes at approximately 140°C. Unless otherwise stated, the infra red drier used in this thesis was a DEK1209 mini drier.

3.6 Firing/curing thick-film layers

As described earlier in section 3.4 there are two types of binder material used to stick the active material together and onto a substrate. In this thesis different pastes containing either polymer or glass binders are used. All polymer binder based pastes were cured in a DEK 1209 mini drier at an approximate temperature of either 150°C for 120 minutes or 200°C for 60 minutes.

To produce a thick-film with good adhesion to the substrate with a glass binder material, the film was sintered after the drying process. This involves heating the substrate and thick-film up to a temperature between 720-950°C. To achieve this, a BTU Engineering Corporation six zone (six heating elements) belt furnace was used. The substrates were placed on a conveyor belt and left to run through the furnace, where six separate heating zones are used to control the temperature through the furnace. Figure 3.15 shows a typical 60 minute firing profile (Dupont60, Table 3.1), where a peak temperature of 850°C is reached and maintained for approximately 10 minutes.

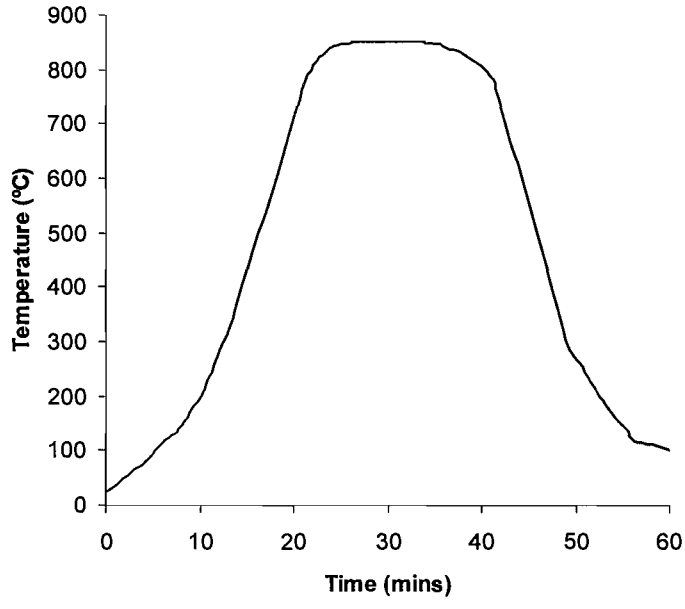

Figure 3.15: Typical furnace temperature profile, with 850°C peak temperature held for approximately 10 minutes.

Table 3.1 shows the temperatures at which each zone within the furnace are set to during the three different firing profiles used within this thesis. Generally for each firing profile a cycle time though the furnace of 60 minutes was used. This means that the heating and cooling rates of devices also changes, along with the selected peak temperature. The temperature set for each of the zones and the actual temperature of the substrate vary slightly and the substrate temperature is often lower than the set temperature.

	Zone temperature (°C)						Max approximate substrate temperature (°C)
Zone No	**1**	**2**	**3**	**4**	**5**	**6**	
RNT750 [85]	295	506	746	744	750	733	720
DC850	335	573	845	843	850	831	820
Dupont60	350	600	885	883	890	870	850
RNT1000 [85]	393	674	994	992	1000	978	950

Table 3.1: Furnace firing profiles for RNT750, DC850, Dupont60 and RNT1000.

3.7 Film thickness measurement techniques

Measuring the thickness of the PZT layer in a capacitive piezoelectric device is very important as it allows the correct voltage to be calculated in order to apply a given electrical poling field. The thickness of samples can vary between devices printed on different substrates in the same batch and even devices printed on the same substrate.

The two methods used to measure the thickness of individual devices throughout this project were a digital micrometer accurate to ±1μm and a Carl Zeiss light meter accurate to ±3μm. When using the digital micrometer the thickness of the alumina substrate was initially measured and the micrometer zeroed. Thickness readings were then taken on either one or two sides of the centre of the thick-film (as illustrated in Figure 3.16) ensuring that the micrometer did not overlap either the bottom electrode or underside electrode on the device.

The Carl Zeiss light meter was used as an alternative to the micrometer to measure the thickness of some films where a non contact method was preferable. The measurements were made on approximately the same points on the thick-film PZT layer as the micrometer was used. The light meter projects a straight beam of light on a flat surface. To measure a film thickness the beam lined up across the edge of the film and the surface of the substrate (or an underlying film). When viewed through the eyepiece, the light beam is deflected horizontally in the field of view. The degree of deflection is directly proportional to the thickness of the film and can be measured by moving a cross hair from the lower part of the beam to the top of the deflected beam with a micrometer. This film thickness measuring device has the advantage over a micrometer that the thickness of the substrate does not have to be taken into account and because it is a non-contacting method, measurements can be made while the paste is still wet.

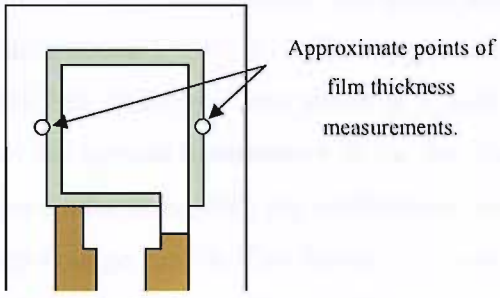

Figure 3.16: Illustration of approximate points used to measure film thickness of the PZT layer.

3.8 Poling piezoelectric thick-film devices

Piezoelectric thick-films are generally produced from a powder form of a bulk piezoceramic. They therefore have the same initial piezoelectric properties of a bulk ceramic after the firing or curing stage i.e. no net polarisation (a charge is not produced across the electrodes when the film is mechanically stressed) (refer to section 3.1.1 for a full explanation). The piezoelectric properties of the thick-film therefore have to be activated in the same manner as a bulk piezoceramic device, by applying an electrical poling field across the electrodes. Previous investigations into the poling process have shown that the d_{33} of a piezoelectric ceramic can be increased by applying the electric field at higher temperatures as well as increasing the electric field and poling times [94].

To calculate the required poling voltage for a capacitive thick-film structure, Equation 3.7 is used.

$$V = E\,d \qquad \text{Eqn 3.7}$$

Where V is the poling voltage (V), E is the poling field (MVm^{-1}) and d is the film thickness (μm). For an interdigitated design the film thickness is simply replaced by the distance between the opposing electrode digits.

To apply this equation, the PZT film thickness (capacitive design) or distance between opposing electrode digits (interdigitated design) must be known. The methods used to determine this are described in the previous section.

All of the thick-film piezoelectric devices in this thesis were poled using purpose built poling apparatus illustrated in Figure 3.17. The apparatus consists of a hot plate contained in a large metal box, with two fans inside it, a high voltage supply and a thermocouple to measure the surface temperature of the hot plate. To pole a device, wires are soldered onto the solder pads of the top and bottom electrodes (cf. Figure 3.9) and connected to the high voltage supply. The device is placed onto the hotplate and heated to the required temperature. An electric field is then applied across the piezoelectric thick-film for a period of 5 - 10 minutes. The device is cooled, with the aid of the fans, to well below the Curie temperature before the electrical poling field is removed. The majority of devices reported in this thesis were poled between 150-200°C and allowed to cool to approximately 60°C, before the poling field was removed. The elevated temperature is used during poling as it has been shown to increase the d_{33} properties of devices [94].

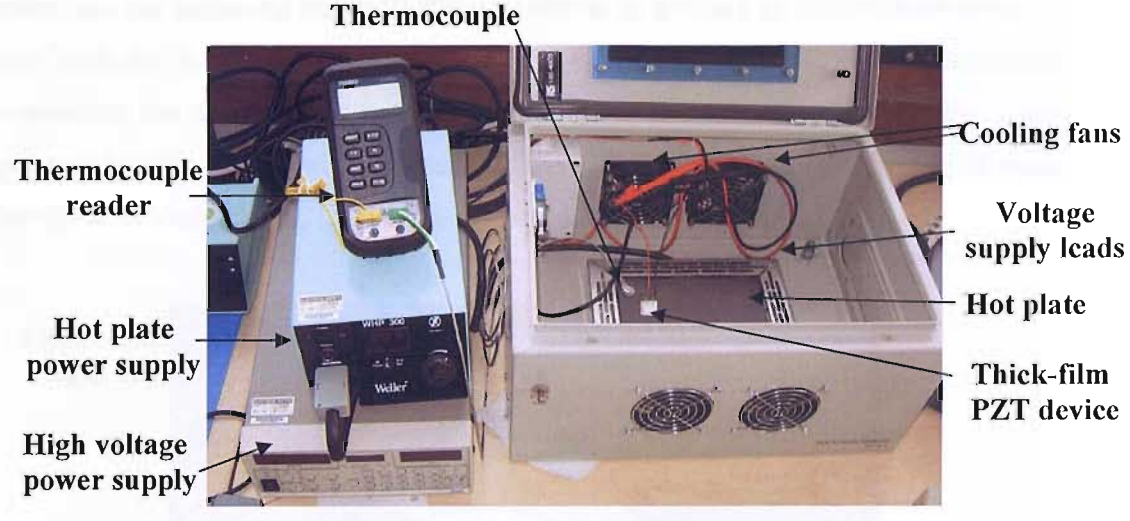

Figure 3.17: Picture of poling rig with a sample device being poled.

3.9 Measuring the d_{33} coefficient of piezoelectric thick-films

There are a number of alternative methods which have been used to test the d_{33} and d_{31} of thick film piezoelectric devices [74,79,95,96]. Throughout this project, all capacitive design piezoelectric thick-film samples were tested on a commercially available PM35 Take Control PiezoMeter with an accuracy of ±2% of the output reading [97]. This was done to provide consistency between sample readings and also

to allow the results to be accurately compared with previous work on piezoelectric thick-film devices at the university [85].

Figure 3.18 shows a thick-film piezoelectric device being tested on a Take Control PiezoMeter. The sample is held in position by the two electrodes of the PiezoMeter. To clamp the device in position the height of the upper electrode is adjusted with the "upper electrode height adjuster". The PiezoMeter works by applying a known dynamic force through the two electrodes to the piezoelectric device. The frequency of this force can be altered. However, for consistency between samples and to avoid any interference from mains noise it was set to 110Hz for measuring all devices in this project. To record the charge produced by the film, both of the electrodes from the PiezoMeter must be electrically connected to the top and bottom electrodes of the piezoelectric device. When the device is printed upon 96% alumina substrates (an insulating material) this is achieved by printing an underside electrode in line with the bottom electrode on the device (cf. Figure 3.9 (b)), and electrically connecting the pair together with an Electrolube silver conductive paint. The charge generated by the thick-film is compared to the PiezoMeters' built in reference allowing the d_{33} to be evaluated [97]. It is then displayed on a digital display.

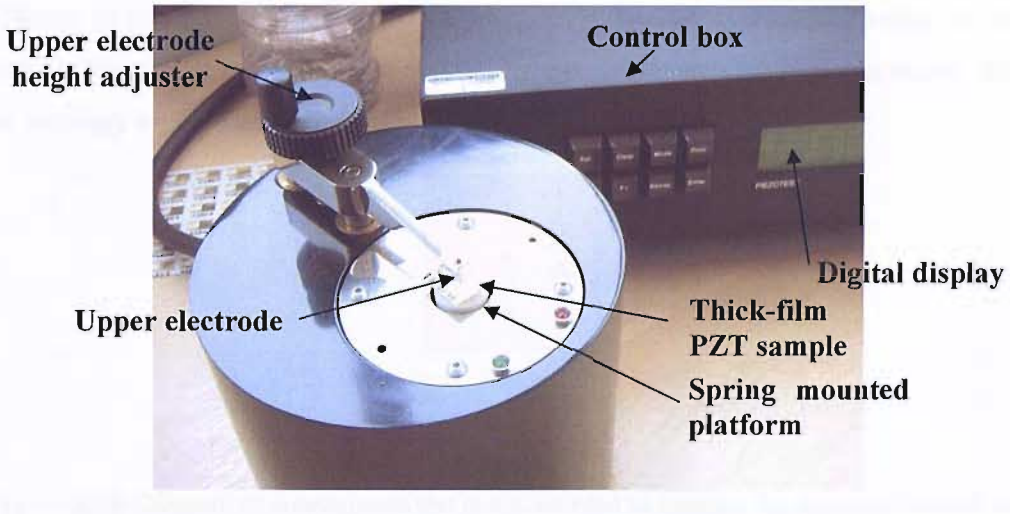

Figure 3.18: Picture of a Take Control PiezoMeter, with a thick-film sample printed on a 96% alumina substrate being tested.

3.9.1 *Calibrating the PiezoMeter*

As piezoelectric materials are also pyroelectric a method for standardising the d_{33} readings independently of temperature was used. This allowed devices to be directly compared without errors from temperature change in the lab. To achieve this, d_{33} measurements from a calibration sample with a known d_{33} at 25°C were taken before the d_{33} readings of the thick-film devices. The ratio of the calibration samples d_{33} at 25°C to the measured d_{33} was then used to provide a thick-film d_{33} measurement calibrated to 25°C (cf. Equation 3.8). All of the devices reported in this thesis have been calibrated using this technique.

$$d_{33} = (d_{33}\ \text{cal} / d_{33}\ \text{measured}) \times fd_{33} \qquad \text{Eqn 3.8}$$

Where d_{33} is the effective d_{33} of the thick-film (pC/N), d_{33} cal is the actual value of the calibration ceramic (pC/N), d_{33} measured is the measured d_{33} of the calibration ceramic (pC/N) and fd_{33} is the measured value of the thick-film device (pC/N).

As the thick-film piezoelectric devices generally give non-uniform d_{33} readings, (when taken from different positions) the average of six readings taken from three different points on each device was used to calculate an average d_{33} value for each sample. Figure 3.19 illustrates the approximate position each reading was taken. All of the readings were taken in the order 1,2,3,1,2,3.

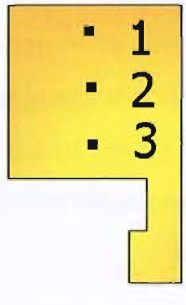

Figure 3.19: Diagram of approximate test positions used to measure the d_{33} sensitivity of each sample.

3.10 Thick-film piezoelectric device fabrication

Throughout the course of this research program a number of thick-film PZT devices were fabricated on 96% alumina substrates and type 430 stainless steel. The

methods used in each case were very similar with only the material type and firing/curing profiles altered. The firing profiles used are described in terms of their peak temperature with the full details of the furnace settings listed in Table 3.1. The following two sections describe the fabrication methods of a thick-film piezoelectric device with a gold bottom electrode and a polymer silver top electrode, printed on 96% alumina substrates and stainless steel substrates.

3.10.1 Method for printing on 96% alumina substrates.

A gold bottom electrode (ESL 8836) is initially printed onto the 96% alumina substrates and left to settle for 10 minutes before being dried in an IR heater for 10 minutes at approximately 140°C. A silver/palladium layer (ESL 9633) is then printed on the reverse side of the 96% alumina substrate to allow d_{33} readings to be taken (cf. section 3.9). The silver/palladium layer is left to settle for 10 minutes before being dried in the IR heater for a further 10 minutes at approximately 140°C. The two layers are then co-fired in a six zone belt furnace for approximately 60 minutes, reaching a peak temperature of 850°C. A piezoelectric layer (made from a paste incorporating either PZT-5H or PZT-Pz29 powder) is subsequently printed on top of the gold bottom electrode. The PZT layer is then left to settle for 10 minutes before being dried for 10 minutes at approximately 140°C, followed by a second printed PZT layer, which is also left to settle for 10 minutes before being dried at 140°C for a further 10 minutes. The PZT layers are then fired using a profile from Table 3.1. Two alternative materials were used to form a top electrode, silver polymer (ESL 1110-S) or gold (ESL 8836). Gold top electrodes were printed on top of the PZT layer, left to settle for 10 minutes before being dried at 140°C for 10 minutes and finally fired at 850°C. Silver polymer top electrodes were also printed on top of the PZT layer, left to settle for 10 minutes before being dried at 140°C for a further 10 minutes and finally cured at either 150°C for 2 hours or 200°C for 1 hour.

3.10.2 Method for printing on stainless steel types 430 and 304

Before printing can be undertaken on a stainless steel substrate it must be cleaned to remove any grease or dirt, which might affect print quality. This is achieved by wiping the substrates with clean room wipes soaked in acetone and subsequently rinsing them in de-ionised water. As steel is a conductor the PZT device can either be

insulated from the steel or alternatively the steel can be used as a bottom electrode. To avoid any issues with soldering wires onto a part of the top electrode forming the capacitive structure of the device, all samples reported in this thesis were fabricated on top of an insulated layer. This layer was created by printing a thermally matched dielectric paste, ESL4986 and ESL4916 for steel types 430 and 304 respectively. Three layers of the paste were successively, printed, left to settle for 10 minutes before being dried in an IR heater at 140°C for 10 minutes and fired at a peak temperature of 850°C. The piezoelectric thick-film devices were then fabricated on top of the dielectric layer in the same manner as described in the previous section, with the exception of the underside electrode, which was not required. In order to test d_{33} of the devices the bottom electrode was electrically connected to the steel substrate using an Electrolube silver conductive paint.

3.11 Consequences of a fire at the University

3.11.1 Introduction

In October 2005 a major fire occurred in the School of Electronics and Computer Science at the University. This fire destroyed the thick-film fabrication facilities within the department and offices containing all of the thick-film devices and other equipment used at the beginning of this project. This section details the changes in equipment and piezoelectric paste used after the fire.

3.11.2 Effects of using an alternative grade of piezoelectric powder

After the fire a new supplier for the PZT powder was established (Ferroperm) [89]. This was because Morgan ElectroCeramics no longer supply PZT-5H powder. The new powder (PZT-Pz29) was produced with specified grain sizes of 2μm and 0.8μm (the same sizes reported in R.N. Torah's thesis)[87]. The material properties were slightly different to those used in some of the earlier work in this project. In order to compare the new and old powders a control experiment was set up to fabricate comparative samples using the same paste mixture and processing parameters as reported by Torah et al. The paste was mixed from a 10%wt CF7575 glass binder with a 4:1 wt ratio between the powders of 2μm and 0.8μm respectively. The results

revealed an average d_{33} of approximately 107pCN^{-1} for samples with a silver polymer top electrode poled at 3MVm^{-1} and 200°C for 10 minutes (the poling voltage was only removed after the samples had been cooled to approximately 60°C). The d_{33} was slightly lower than the samples produced by Torah et al, using Morgan ElectroCeramics' PZT-5H powders, which were measured at 121 pCN^{-1} for samples poled at 200°C and 3MVm^{-1} for 5 minutes and 131pCN^{-1} for samples poled at 200°C and 3MVm^{-1} for 30 minutes.

3.11.3 Differences in fabrication facilities and device layout

The alternative fabrication facilities were based in a lab without class 1000 clean room grade air. This environment therefore increases the risk of contamination of devices due to dust particles. However, early work on thick-film devices was successfully carried out using the same facilities [98,99]. The other two main differences were: a different type of screen printer and a new screen design layout of devices printed onto 96% alumina substrates. The screen printer model is not believed to have any significant effect on print quality. Figure 3.20 illustrates the differences between the old sample layout (on the left) and the new sample layout (on the right). This re-design of the layout was undertaken to increase the number of devices which would fit onto a single four inch squared substrate from 18 devices to 30. The size of the PZT layer and both top and bottom electrodes are approximately the same size as the original design, the only major difference is the length of the tracks connected to the solder pads. The new layout is not expected to produce any changes in the quality of devices. The belt furnace in all cases had six heating zones and the heating zone was approximately the same length. The infra red driers were the same model used during all device fabrications.

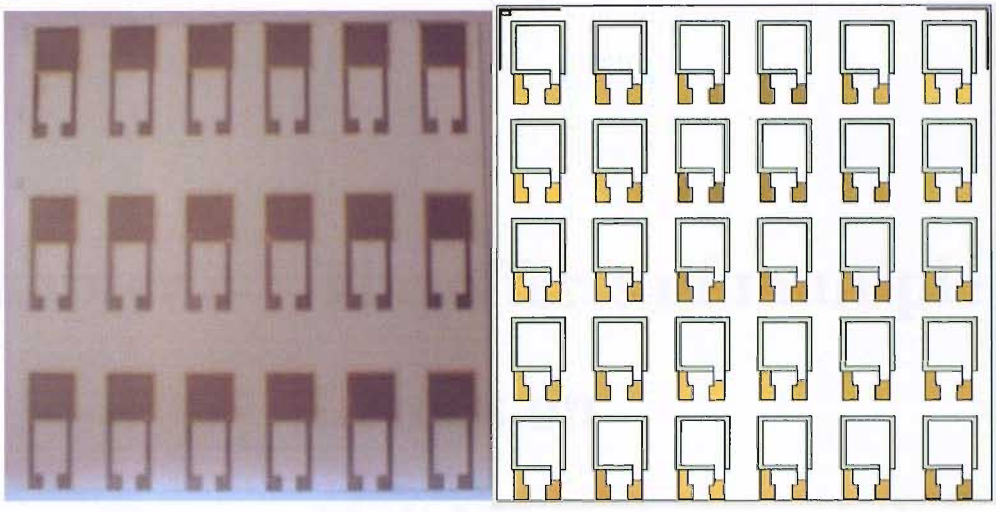

Figure 3.20: Device layouts on 4"x4" 96% alumina tiles: on the left hand side is a picture of the old design layout with 18 sample piezoelectric devices, on the right hand side is an Autodesk Inventor 10 ™ drawing of the new layout design incorporating 30 piezoelectric devices.

Chapter 4 The effects of multiple firings on stoichiometry and d_{33}

4.1 Introduction

In commercial production of bulk PZT the elements are fired in a lead atmosphere at high temperatures (> 1500°C) to minimise lead evaporation and therby any change in the stoichiometry of the final composite. It has not been reported in the literature whether this effect will occur at the lower temperatures used in thick-film fabrication (<1000°C). This chapter therefore reports on some initial investigations undertaken to answer this question.

R.N. Torah [85] proposed that the quantity of lead in PZT thick-films is reduced during each firing cycle, with the optimal ratio of lead to zirconate to titanate resulting in the highest sensor d_{33}. This has a corresponding effect on the sensitivity of thick-film PZT sensors and transducers since the greatest d_{33} values result from the optimal ratio of lead to zirconate to titanate. Experimental results on thick-film piezoceramics using a silver polymer top electrode processed at 200°C instead of using a cermet gold electrode processed at 850°C, have revealed an increase in d_{33}. However, it is unclear whether this was due to the avoidance of an extra high temperature processing stage or was due to a better electrical connection between the PZT layer and the silver polymer electrode. This issue is further confused by the results obtained from other experimental investigations into co-firing gold and PZT layers and printing PZT thick-film stacks, with multiple layers of PZT sandwiched between multiple electrodes. Co-fired gold and PZT layers were shown to produce a similar d_{33} output as those recorded when firing

each layer separately. The co-fired stacks of PZT thick-films fabricated with three layers of PZT fired once, were shown to have the same d_{33} as stacks produced with individually fired layers, where the PZT layers were fired 2-6 times, hence no additional degradation of the films properties was reported.

The melting temperature of lead is 327.5°C and the boiling point is 1749°C (Table 4.1) [100] so it is unclear exactly how much lead evaporation would occur at 850°C or 950°C in a lead-free atmosphere. Table 4.1 lists the elements contained within the piezoelectric thick-film along with their melting and boiling temperatures. It is therefore considered advantageous to investigate the effects of a possible reduction in lead and change in d_{33} sensitivity due to an increased number of firing cycles. The substrate materials used in this investigation were stainless steel type 430 (the substrate material used to fabricate the prototype fingertips 2 and 3 in Chapter 6) and 96% alumina, with a combination of gold (ESL 8836), silver/palladium (ESL9633-G) and silver polymer (ESL 1110-S) pastes to form the electrodes.

To determine the lead content in the samples, an X-ray spectrometry technique was used. To perform this analysis some of the samples were printed without a top electrode, which was intended to be printed after the analysis with the silver polymer, ESL 1110-S. This paste was chosen to limit any further changes in the PZT material composition as the polymer is typically cured between 150-200°C i.e. well below the melting point of lead. Unfortunately, all of the samples analysed using the X-ray spectrometry technique, were lost in a fire at the University (cf. Section 3.11), before any of the d_{33} readings could be taken. However, the devices fabricated with gold and silver/palladium electrodes were tested for their d_{33} characteristics. In order to complete the work, all of the samples with gold bottom electrodes (including samples intended to be printed with silver polymer top electrodes) produced on 96% alumina substrates were re-fabricated and tested. Although the samples with gold top electrodes had been tested in the original batch, it was decided that a new batch would be fabricated to use as a control. There were a number of differences in the equipment used during the fabrication of these new samples, as well as some difference in sensor design (details of the differences are described in section 3.11). Furthermore, the original manufacturer of PZT powders that had been previously used no longer commercially supply powders and so a different manufacturer of the PZT powder had to be used to fabricate the new

sensors. The results from testing some of the original devices, were therefore considered essential in validating the new experiments, without repeating the X-ray analysis.

Element	Melting Point (°C)	Boiling point (°C)
Lead (Pb)	327.5	1749
Gallium (Ga)	302.9	2204
Strontium (Sr)	777	1382
Zirconium (Zr)	1855	4409
Titanium (Ti)	1668	3287
Gold (Au)	1064	2856

Table 4.1: Melting and boiling point temperatures of elements contained within piezoelectric thick-films [100].

4.2 The theory of X-ray spectrometry

The analysis of a compound or mono-element material using X-ray spectrometry is based on the fact that chemical elements emit a characteristic radiation when subjected to an appropriate excitation. This characteristic radiation can be induced in two different manners: from either bombarding the sample with high energy radiations from an X-ray tube (or radioactive source), or alternatively by bombarding the sample with accelerated particles, such as electrons or protons [101].

The atoms of each element in the periodic table are made up of a number of shells containing electrons orbiting around the nucleus of the atom. The number of shells in which the electrons orbit is related to the atomic mass of that particular element, with the elements of higher atomic mass containing more electrons and shells than those with a lower atomic mass. Each element has a different atomic mass and when the atom is bombarded with a high energy source (X-ray source, radioactive source, accelerated electrons or protons) a number of energy exchanges occur. For example if an X-ray photon ionizes (displaces) a K shell electron (as illustrated in Figure 4.1) from the atom it creates an imbalance within the structure. The atom quickly returns to its equilibrium state by the transition of an electron from one of the outer shells, for example the L shell to the K shell. Because the energy of an electron in orbit in an outer shell is greater than that required in an inner shell, the excess energy released in moving an electron from an L shell to a K shell is liberated as a photon. In completing such a

change the potential energy of the atom is reduced. In this particular example a K_α photon is produced. The photon can then either be emitted from the atom producing a characteristic radiation, which can be used to identify a specific element, or it can ionise another electron from one of the outer shells of the atom or even a different electron in another atom in the same manner. This event is known as the Auger effect [102].

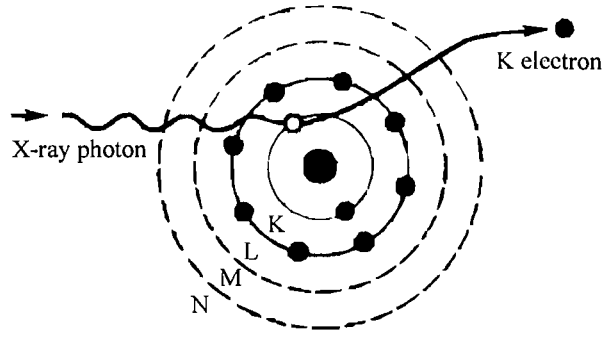

Figure 4.1: Ionisation of K shell electron by an X-ray photon.

(Illustration adapted from [102]).

In general the characteristics of an element are analysed using the K_α, K_β or the L_α, L_β photons. The emitted photons get their symbols from the shell of the replaced electron, so for example a K_α photon is released from the transition of an electron from an L to a K shell and a K_β Photon is produced from the transition of an electron from the M shell to the K shell. The L_α and L_β photons are also labelled in the same manner and illustrated in Figure 4.2.

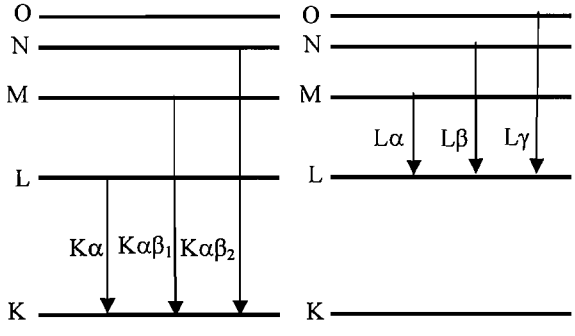

Figure 4.2: Photons produced through de-excitation of outer shell electrons

(Illustration adapted from [101]).

The characteristic photon energies are commonly known for each element in the periodic table and can therefore be compared to the value obtained by an X-ray spectrometry analysis.

4.3 Evaluation of X-ray spectrometry techniques

There are a number of different X-ray spectrometry techniques that could be used to determine material characteristics. Table 4.2 gives a brief overview of three of these techniques and their advantages and disadvantages for this particular analysis. The methods evaluated are X-ray florescence (XRF)[103], X-ray diffraction (XRD) and an energy dispersive X-ray (EDX) technique.

Technique	XRF	XRD	EDX
Information available using this technique	A qualitative analysis is possible	The material phase can be analysed however, no quantitative data can be found.	Qualitative data can be found.
Estimated time for analysing a single sample	20 minutes	An overnight analysis is required.	30 minutes
Project cost per sample.	£22	£200	£50
Advantages over other techniques	A number of samples can be analysed in a single run. Cheaper than EDX and XRD.	The material phase can be found.	SEM photos can be taken at the same time as analysis.

Technique	XRF	XRD	EDX
Disadvantages compared to other techniques	Extra analysis is required to produce quantitative information.	Very expensive and time consuming for initial analysis, modelling of the material phase is also required after analysis.	More expensive and time consuming than XRF.

Table 4.2: Comparison of X-ray spectrometry techniques.

The XRF technique was used to analyse the PZT thick-film stoichiometry due to its lower cost and faster analysis time of samples. The XRF machine also allows a number of samples to be analysed in a single run, without being monitored by an operator.

The XRF technique uses an X-ray tube source to excite elements in a specific compound. For a particular element, its X-ray spectrum must be within the range of the tube. Figure 4.3 shows an example of the intensity distribution of a tungsten anode X-ray tube at 100keV.

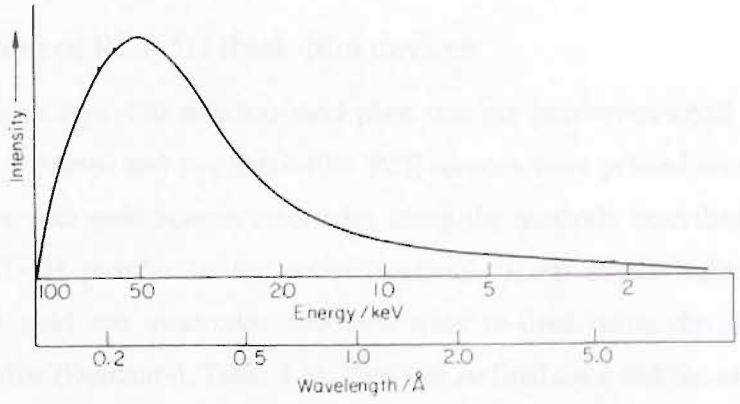

Figure 4.3: Intensity distribution of a tungsten anode X-ray tube at 100keV (illustration adapted from [101]).

The excitation voltage is inversely related to the minimum wavelength of an element that can be detected (Equation 4.1), which means for a maximum voltage there will be a minimum wavelength.

$$\lambda = \frac{hc}{V_0} \quad (1) \qquad \text{Eqn 4.1}$$

Where λ is the minimum wavelength in Å, h is Planck's constant, c is the velocity of light (ms^{-1}) and V_0 is the tube excitation voltage (V).

In general the maximum intensity of an excitation is produced at half the voltage applied to the X-ray tube as shown in Figure 4.3 (note the non linear scale). The intensity can be increased by applying a higher current to the X-ray tube. This serves to increase the number of detected emissions from the sample, or the count rate, over a set time period. Alternatively this can be achieved by increasing the amount of time the beam is focused on one specific area (count time). The range in intensity produced by the tube means that elements with excitation energy lying close to half of the voltage used to power the tube will produce more counts than an element which has an excitation energy of for example $1/10^{th}$ of the excitation voltage. Therefore the count of one element is not directly comparable to the count of a different element. In order to accurately investigate different elements, a number of alternative X-ray tubes can be selected to target the elements excitation energy. A number of standards do also exist for calculating precise element quantities in specific materials.

4.4 Fabrication of PZT-5H thick-film devices

A 2mm thick type 430 stainless steel plate was cut into seven small rectangular sections 25mm x 30mm and two thick-film PZT sensors were printed on each of the seven substrates with gold bottom electrodes using the methods described in section 3.10.2 and PZT-5H powder as the active material. Three of the substrates were fabricated with gold top electrodes and two were re-fired using the 850°C peak temperature profile (Dupont60, Table 3.1). One was re-fired once and the other re-fired twice. Three of the remaining four substrates (without top electrodes) were also re-fired at 850°C, to produce samples where the PZT layer had been fired, two, three or four times.

A further 8 substrates of devices (18 devices on each substrate) were fabricated on 96% alumina substrates using the same method described in section 3.10.1. Four substrates were fabricated with gold electrodes (ESL 8836) and four with

silver/palladium electrodes (ESL 9633-G). The silver/palladium electrodes were fabricated using the same processing parameters as the gold electrodes.

A number of devices from each substrate were again left without a top electrode for the XRF analysis, with the intention that a silver polymer top electrode would be printed after the analysis. The number of firing cycles, electrode and substrate materials for all of the samples are listed in Table 4.3, where Au indicates that gold paste (ESL 8836) was used to form the electrode and Ag/Pd indicates that silver/palladium paste (ESL 9633-G) was used to form the electrode.

Sample Type	**Substrate type**	**Bottom electrode type**	**Top electrode type**	**Number of firings of PZT layer**
SSGG-2	Steel	Au	Au	2
SSGG-3	Steel	Au	Au	3
SSGG-4	Steel	Au	Au	4
SSG-1	Steel	Au	N/A	1
SSG-2	Steel	Au	N/A	2
SSG-3	Steel	Au	N/A	3
SSG-4	Steel	Au	N/A	4
AGG-2	Alumina	Au	Au	2
AGG-3	Alumina	Au	Au	3
AGG-4	Alumina	Au	Au	4
AG-0	Alumina	Au	N/A	0
AG-1	Alumina	Au	N/A	1
AG-2	Alumina	Au	N/A	2
AG-3	Alumina	Au	N/A	3
AG-4	Alumina	Au	N/A	4
ASS-2	Alumina	Ag/Pd	Ag/Pd	2
ASS-3	Alumina	Ag/Pd	Ag/Pd	3
ASS-4	Alumina	Ag/Pd	Ag/Pd	4

Sample Type	Substrate type	Bottom electrode type	Top electrode type	Number of firings of PZT layer
AS-1	Alumina	Ag/Pd	N/A	1
AS-2	Alumina	Ag/Pd	N/A	2
AS-3	Alumina	Ag/Pd	N/A	3
AS-4	Alumina	Ag/Pd	N/A	4

Table 4.3: Overview of devices fabricated.

4.5 XRF processing method

An ITRAX XRF machine was used to analyse the stoichiometry of the thick-film piezoelectric devices fabricated without top electrodes. Initially all of the component materials' elements required to be analysed have to be selected. This was accomplished by analysing a single device from each batch under the XRF beam. From this analysis a spectrograph of the piezoelectric thick-film compound was produced, which gave a graphical indication of the excitation energies of elements which are present. The required elements were then manually selected from the spectrograph. Figure 4.4 shows a spectrograph of a thick-film PZT sample with a gold bottom electrode printed on a 96% alumina substrate.

The number of counts from each peak shown in the spectrograph indicates the level of excitation activity of each element. The elements present in the thick-film can be identified from the element energy characteristics shown in Table 4.4. For example it can be seen that the L_{α} and L_{β} energies of lead are 10.550 keV and 12.612 keV respectively, and are both present on the spectrograph.

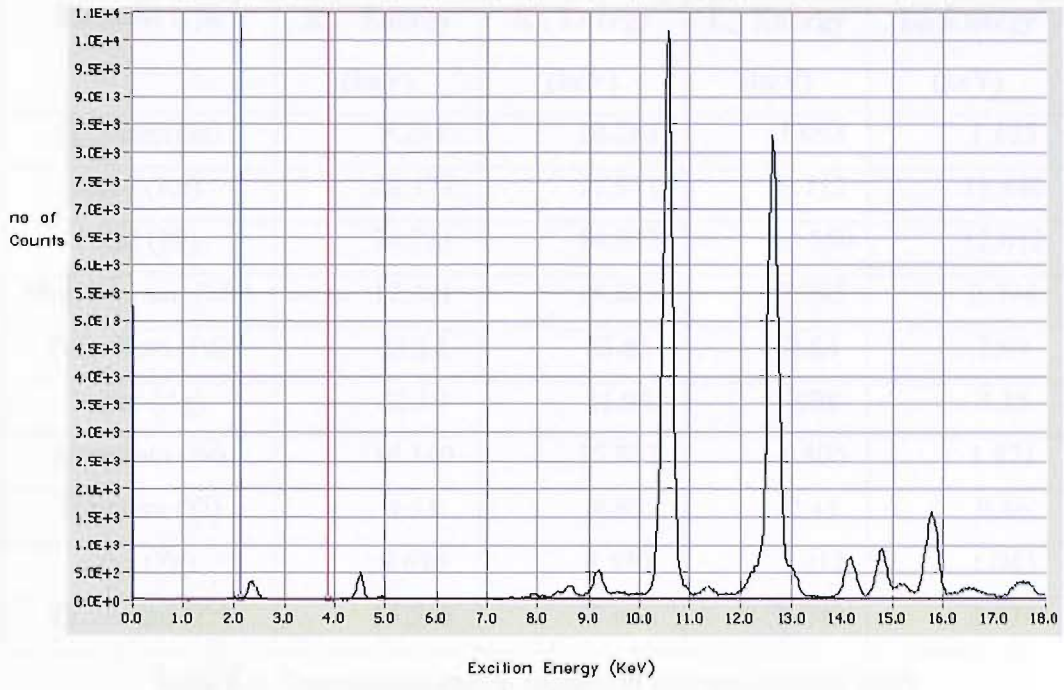

Figure 4.4: Spectrograph of PZT sample with a gold bottom electrode on a 96% alumina substrate.

After all of the relevant elements had been selected, the samples were analysed on the ITRAX XRF machine. The count activity was then recorded on the graphs shown in Figure 4.5 – 4.7. On the graphs, each element is labelled across the top of the abscissa, with a scale indicating the level of activity beneath the label. The two columns labelled inc and coh in Figure 4.5 are background activities from the X-ray tube and can be ignored. The superimposed drawings of the PZT devices on the left hand side of the graph indicate the approximate position of the devices, relative to the excitation beam, when analysed. Each of the drawings is labelled to allow easy identification of the processing parameters used to fabricate it (refer to Table 4.3). The activity of each element from the samples can be tracked horizontally across the graph with respect to the drawings. Each separate sample can be seen as a block of activity moving vertically down the page from the plot of each element (with the exception of columns labelled Zn, inc and coh in Figure 4.5 and Figure 4.7). The recorded lead activity for each sample shows a clear example of this.

Element type	K_α Energy (keV)	K_β Energy (keV)	L_α Energy (keV)	L_β Energy (keV)
Gallium (Ga)	9.241	10.263	1.098	1.125
Gold (Au)	68.177	77.971	9.712	11.440
Lead (Pb)	74.221	84.922	10.550	12.612
Molybdenum (Mo)	17.441	19.605	2.293	2.394
Palladium (Pd)	21.12	23.82	2.84	2.99
Silver (Ag)	22.10	24.94	2.98	3.15
Strontium (Sr)	14.140	15.833	1.806	1.871
Titanium (Ti)	4.51	4.93	0.45	0.46
Zinc (Zn)	8.630	9.570	1.012	1.043
Zirconium (Zr)	15.748	17.665	2.042	2.124

Table 4.4: Characteristic photon energies of relevant elements [104].

4.6 Results

4.6.1 Results from XRF analysis

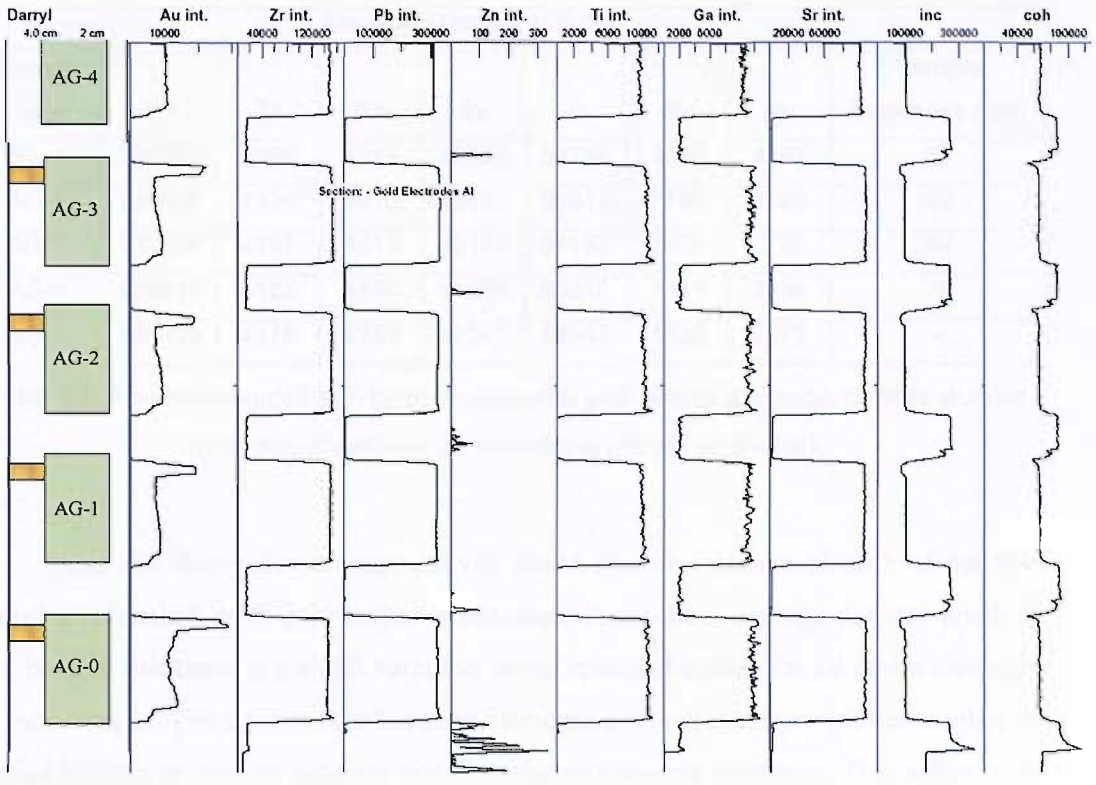

Figure 4.5: XRF activity count of thick-film PZT samples with a gold bottom electrode printed on a 96% alumina substrate. The activity across the thick-film was recorded in 200μm increments and the count time used was 25s per increment.

Figure 4.5 shows the activity of the elements recorded from five separate devices. The five samples were all fabricated on 96% alumina substrates with gold bottom electrodes. The only differences being that each sample has undergone a different number of firing cycles at a peak temperature of 850°C. The sample at the top of the graph was fired four times, whilst the samples below it were fired, three, two, one and zero times respectively (from top to bottom). Only half of the first sample was analysed, as it was initially used to define the elements present on the alumina substrate.

The results show a relatively uniform distribution of activity for all of the elements on the 96% alumina substrates, within single samples and also between samples with different numbers of firings, the only exception being a large spike in activity at the beginning of each of the gold samples. This initial increase in gold activity can be attributed to the XRF beam exciting the gold connector track of the bottom electrode.

	Average element activity							
Sample Type	Pb	Ti	Ga	Sr	Zr	Mo	Au	Sample thickness (μm)
AG-4	125330	3989	4215	40063	59798	1655	4163	61
AG-3	133052	4330	4610	42451	61613	1795	3599	92
AG-2	130839	4197	4511	42118	61153	1750	3755	84
AG-1	129417	4122	4469	41863	60316	1719	3656	76
AG-0	130459	4375	4753	42347	58948	1829	5275	-

Table 4.5: Average recorded activity of devices with gold bottom electrodes on 96% alumina substrates (count over 25 seconds per 200μm increment).

Table 4.5 shows the average activity count over the surface of each of the five samples fabricated with gold bottom electrodes. From these average activity levels it can be seen that there is a slight variation in the recorded counts for all of the elements in each sample. The relationship between elements does not change with the number of firings but can be seen to increase non-linearly with sample thickness. This effect is an artefact of XRF on thin samples and is due to the excitation beam being able to penetrate the entire depth of the sample. The non-linear increase in activity is simply due to the Auger effect, which is described in more detail in section 4.2. Where possible, the penetration of the beam is set to a common depth, which is the same for each sample. This allows a direct comparison of the quantity of an element to be made between samples by comparing the count rate of each sample.

Sample Type	Avg Pb activity/ avg Ti activity	Avg Pb activity/ avg Zr activity	Avg Pb activity/ avg Sr activity	Avg Pb activity/ avg Ga activity
AG-4	31.4	2.1	3.1	29.7
AG-3	30.7	2.2	3.1	28.9
AG-2	31.2	2.1	3.1	29.0
AG-1	31.4	2.1	3.1	29.0
AG-0	29.8	2.2	3.1	27.4

Table 4.6: An indication of piezoelectric thick-film stoichiometry for samples printed on 96% alumina with gold bottom electrodes.

Table 4.6 shows the ratio of average lead activity over each sample to the average activity of the other four elements analysed within the PZT layers. The activity count ratios for each of the samples are similar despite having undergone a different number

of firing cycles. In spite of the limitations previously described when directly comparing element activity counts, these result suggest that the stoichiometry of the film remains approximately the same for samples fired up to four times at a peak temperature of 850°C.

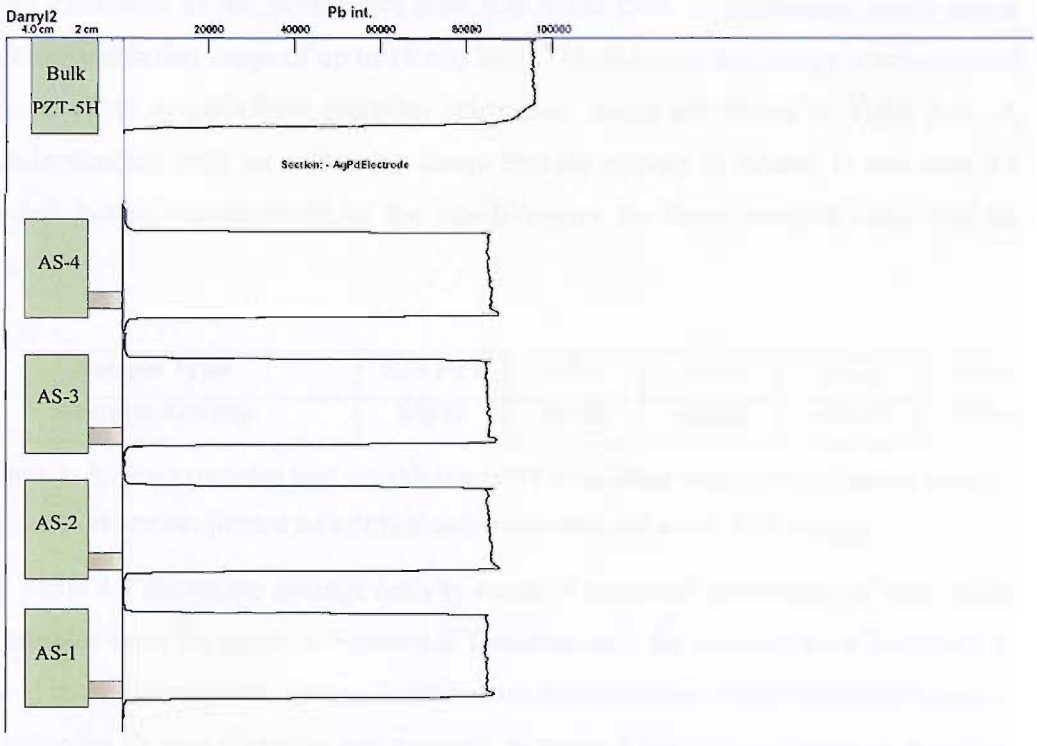

Figure 4.6: XRF activity count of thick-film PZT samples, with a silver/palladium bottom electrode, printed on a 96% alumina substrate. The activity on the surface of the thick-film was analysed in 200μm increments and the count time was 20s per increment.

Figure 4.6 shows the activity count of lead in five different samples on 96% alumina substrates. The top sample is a bulk PZT-5H ceramic cut to a thickness of approximately 250μm and placed on top of the same type of 96% alumina substrate as the other samples were printed on. The four remaining samples are thick-film PZT devices with silver/palladium bottom electrodes, all of which have been processed at 850°C with the number of firing cycles indicated by their respective legends in the figure (refer to Table 4.3).

The graph indicates a relatively uniform activity of lead over the thick-film samples with the bulk PZT sample at the top showing approximately 20% higher activity than the thick-film samples. This can be attributed to the bulk sample having a

much denser structure and also not containing a glass binder material. The bulk sample was also 250μm thick, compared to the thick-film samples, which were all less than 100μm thick.

Unfortunately it was not possible to compare the activity of the silver/palladium bottom electrodes as the florescence tube was made from molybdenum, which had a maximum excitation range of up to 19.605 keV. This is below the energy level required to excite silver or palladium electrons (excitation levels are shown in Table 4.4). A misunderstanding with the technician meant that the activity of Zr and Ti was also not recorded; hence a comparison of the stoichiometry for these samples could not be made.

Sample Type	Bulk PZT	AS-4	AS-3	AS-2	AS-1
Average Activity	53997	48435	48248	48440	48016

Table 4.7: Average recorded lead activity from PZT thick-films with silver/palladium bottom electrodes printed on a 96% alumina substrate and a bulk PZT sample.

Table 4.7 shows the average activity count of lead over the surface of each of the five samples from the graph in Figure 4.6. Unfortunately the samples were destroyed in a fire at the University (cf. section 3.11) before the thickness of the individual samples was recorded. It was therefore not possible to make a comparison between recorded activity and sample thickness.

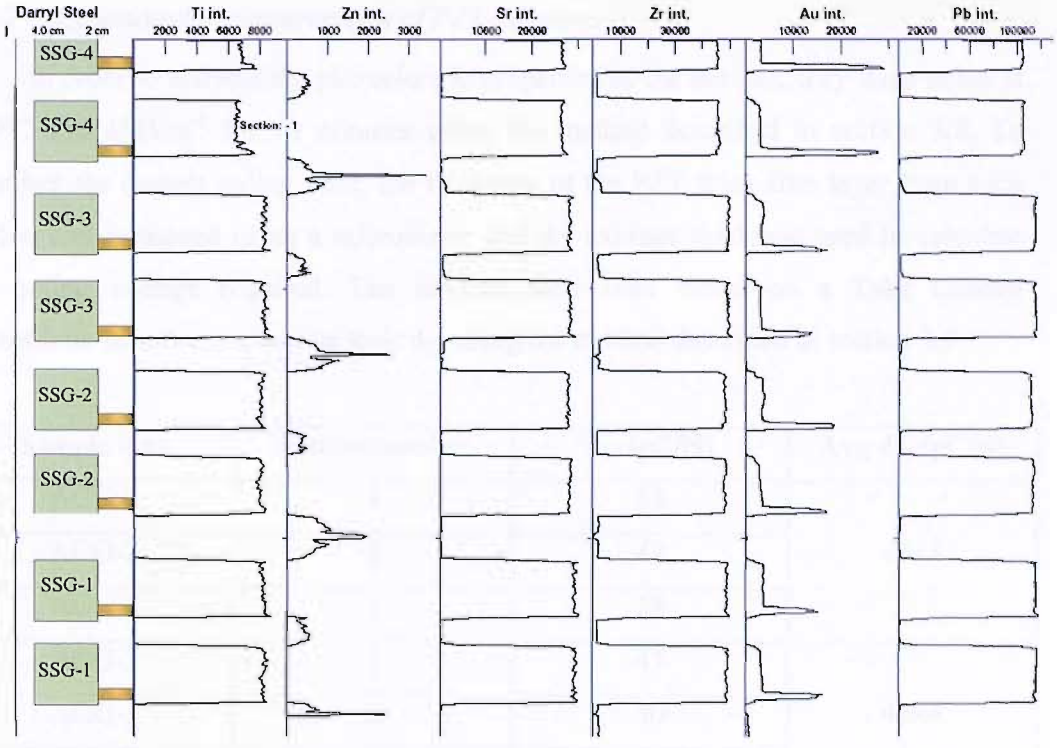

Figure 4.7: XRF activity count of thick-film PZT samples, with a gold bottom electrode, printed on a stainless steel (type 430) substrate. The activity on the surface of the film was analysed in 400μm increments and the count time was 25s per increment.

Figure 4.7 shows the activity of the elements recorded from eight separate thick-film devices, printed on stainless steel (type 430). The eight devices are split up into pairs, which were fabricated at the same time (two devices were printed onto each substrate). The four pairs of samples were all processed at 850°C, with the number of firing cycles indicated by their respective legends in the figure. These samples also showed a relatively uniform activity of all element types with the exception of the devices fired 4 times, which have lower Ti, Sr, Zr and Pb activity counts. The lower count for this sample is believed to simply be due to the thickness of the sample. However, this can not be confirmed, as the sample thickness was not measured before the samples were lost in a fire at the University (cf. section 3.11). By visually inspection the graphs appear to show that the stoichiometry of the devices is preserved. Ideally the ratios would have been calculated from the mean count values, unfortunately this data was lost in a fire and is no longer available.

4.6.2 d_{33} sensitivity measurements of PZT-5H devices

In order to activate the piezoelectric properties of the devices, they were poled at 150°C and 4MVm^{-1} for 10 minutes using the method described in section 3.8. To calculate the correct poling field, the thickness of the PZT thick-film layer from each device was measured using a micrometer and the average thickness used to calculate the poling voltage required. The devices were then tested on a Take Control PiezoMeter in order to evaluate their d_{33}, using the method described in section 3.9.

Sample type	Sample number	d_{33} (pC/N)	Avg d_{33} (pC/N)
AGG-2	1	53	46±8
AGG-2	2	48	
AGG-2	3	38	
AGG-3	1	45	49±4
AGG-3	2	50	
AGG-3	3	53	
AGG-4	1	46	48±2
AGG-4	2	50	
AGG-4	3	49	

Table 4.8: Effective d_{33} of samples with gold electrodes printed on 96% alumina.

The results from Table 4.8 show that there is not a significant difference in the measured d_{33} within a group of sensors fired the same number of times or between groups of sensors fired a different number of times. This is in agreement with the XRF results obtained from the samples without top electrodes.

Sample type	Avg d_{33} (pC/N)	Number of samples	Standard deviation
ASS-2	48.5	6	4.1
ASS-3	46.1	6	3.3
ASS-4	53.5	3	10.1

Table 4.9: Average d_{33} of devices with silver/palladium electrodes, printed on 96% alumina substrates.

The results from the devices with silver/palladium electrodes (Table 4.9) have a similar d_{33} sensitivity when the PZT layer is fired up to 4 times at a peak processing temperature of 850°C.

4.6.3 d_{33} sensitivity measurements of PZT-Pz29 devices

Piezoelectric thick-film devices made with the new powder were fabricated on ten 4" 96% alumina substrates using the same method described in section 3.10.1. The paste for the piezoelectric layer was made from a PZT-Pz29 powder and all bottom electrodes were fabricated using the gold paste ESL 8836 (cf. section 3.11.2). On seven of the substrates the piezoelectric layer was fired at a peak temperature of 850°C and the remaining three substrates at a peak temperature of 950°C. Of the seven substrates fired at a peak temperature of 850°C, three of them had a gold top electrode (ESL 8836) printed on top of the PZT layer, along with one and a half of the substrates (45 devices) previously fired at a peak temperature of 950°C. The gold top electrode was processed using the same parameters used to define the bottom electrodes.

In order to evaluate the effects of a different number of firing cycles on the sensitivity of the piezoelectric thick-films, each substrate was fired a different number of times, and some with different firing profiles. Table 4.10 lists the number of firing cycles, peak processing temperature and top electrode material used to fabricate each batch of devices. For each substrate where a peak firing temperature of 950°C was used, any firings at 850°C were always undertaken afterwards. The silver polymer top electrode layer was printed after all firing cycles had taken place and in each case was cured at approximately 200°C for 60 minutes. The initial firing of the film was always without any form of top electrode and the second firing (in the case of samples with gold top electrodes) was after the deposition of the gold top electrode. The second firing was therefore used to fire the gold layer as well as the PZT layer.

Sample type	**Top Electrode type**	**No of times PZT layer was fired at 950°C**	**No of times PZT layer was fired at 850°C**	**Total No of times PZT layer was fired**
G9-4	Au	1	3	4
G9-2	Au	1	1	2

Sample type	Top Electrode type	No of times PZT layer was fired at 950°C	No of times PZT layer was fired at 850°C	Total No of times PZT layer was fired
G8-4	Au	0	4	4
G8-3	Au	0	3	3
G8-2	Au	0	2	2
P9-4	Ag Polymer	1	3	4
P9-1	Ag Polymer	1	0	1
P8-4	Ag Polymer	0	4	4
P8-3	Ag Polymer	0	3	3
P8-2	Ag Polymer	0	2	2
P8-1	Ag Polymer	0	1	1

Table 4.10: Sample types fabricated using PZT-Pz29. Where Au represents a gold top electrode formed from the paste ESL 8836 and Ag represents the silver polymer paste ESL 1110-S.

A number of samples from each substrate were subsequently poled using the same method described in section 4.6.2. To calculate the required electrical field strength the thickness of all of the samples were measured using a Carl Zeiss light meter and the average thickness from each substrate used to calculate the voltage required (cf. section 3.8).

Sample type	Avg d_{33} (pC/N)	Number of samples tested	Standard deviation
P9-1	98	5	5
P9-4	76	4	0.6
P8-4	73	16	5.3
P8-3	83	11	3.5
P8-2	82	10	3.0
P8-1	76	17	8.6
G9-4	59	12	6.2
G9-2	60	14	5.1
G8-4	58	16	3.6

Sample type	Avg d_{33} (pC/N)	Number of samples tested	Standard deviation
G8-3	63	18	3.2
G8-2	62	16	4.7
G8-3/9-1F	51	5	4
G8-3/9-1	52	6	2.6

Table 4.11: Average d_{33} produced for samples with multiple firings.

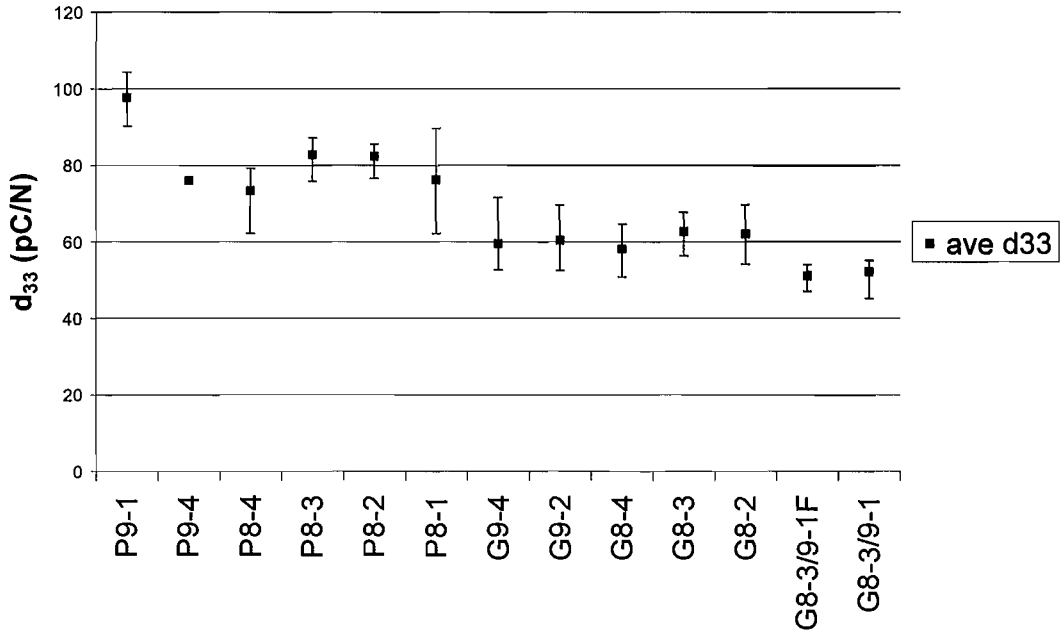

Figure 4.8: Average d_{33} values of devices fired at different temperatures and a number of times, with the maximum and minimum values indicated with error bars. The details of processing for each device type is listed in Table 4.10.

From Figure 4.8 it can be seen that the four samples which were fired without a top electrode at 850°C but instead were printed with a silver polymer top electrode at a temperature of 200°C showed little variation in their d_{33} readings, even though they had been fired between 1-4 times (P8-1 – P8-4). However, the standard deviation of the d_{33} sensitivity of samples only fired once was considerably higher than devices fired two, three or four times (8.6 compared to 3, 3.5, and 5.3 respectively). The devices fabricated with gold top electrodes at 850°C also retained their d_{33} sensitivity when fired up to 4 times (G8-2 – G8-4).

Devices where the PZT layer was fired at a peak temperature of 950°C and subsequently had a polymer top electrode printed (P9-1) produced a d_{33} approximately 20% higher than the devices fired between 1-4 times at 850°C (P8-1 – P8-4) with polymer top electrodes, and 60% higher than devices fabricated with gold top electrodes fired between 2-4 times (G8-2 – G8-4). These results are consistent with the results obtained from devices fabricated with PZT-5H (Table 4.8 and Table 4.9) and previous work reported by other researchers using the same electrode materials[85] and shows that it is the top electrode material which has the greater effect on the sensitivity of the devices fired at a peak temperature of 850°C rather than the number of firings. It is not fully understood why this is the case, but could be due to the polymer silver contacting a larger area of the PZT films surface, therefore, allowing more charge from the device to be measured with the same applied force from the PiezoMeter. However, the quoted resistance values for the gold conductor is lower than that of the silver polymer paste 6mΩ/□ compared to 50mΩ/□.

All of the devices initially fired at 950°C and then re-fired at 850°C to form the gold top electrode (G9-2, G9-4) had d_{33} values in the same range as the samples fired at 850°C. This was not expected as it was believed that the increased sintering of the PZT layer at the higher temperature would determine the characteristics of the film and remain unchanged even when re-fired at a lower temperature. To investigate this further the samples processed with gold top electrodes and with the PZT layer fired 3 times at 850°C (G8-3) were re-fired at 950°C. Five samples were fired using the standard 60 minute RNT1000 firing cycle (G8-3/9-1) and a further 5 samples using a faster version of the RNT1000 firing profile, where all zones were set to the same temperatures, but the firing cycle time reduced to 30 minutes (G8-3/9-1F). All of the devices were re-poled and tested using the same parameters defined in section 3.8 and 3.9. The results showed a decrease in the d_{33} for both sample types of approximately 15%.

Devices with a gold top electrode fired at 950°C and then subsequently re-fired at 850°C (G9-4, G9-2) exhibited the same d_{33} sensitivity as devices which were only fired at 850°C (G8-2 – G8-4). Further processing of devices fired at 850°C 3 times by re-firing them at 950°C (G8-3/9-1) showed a degrading in average sensitivity by

approximately 15%. This suggests that the sensitivity characteristics depend not only on the initial firing, but also subsequent firing cycles as well, when devices are fired at 850°C. Therefore, when printing and firing a number of different thick-film sensors on a single substrate the advantage of sintering the PZT layer at 950°C is lost if the device is re-fired at 850°C.

The PZT layer of the devices initially fired at 950°C and then fired a further three times at 850°C (P9-4) had degraded and poling at $4MVm^{-1}$ could not be achieved. The samples were therefore poled at approximately $3MVm^{-1}$. However, out of 20 samples, on which poling was attempted, only 4 devices did not suffer electrical break down.

4.6.4 Conclusions

The XRF results suggest that there is no change in stoichiometry of a PZT-5H thick-film when it is fired 1 – 4 times at a peak temperature of 850°C.

Thick-film piezoelectric devices fabricated from PZT-5H with gold or silver/palladium electrodes as well as devices fabricated from PZT-Pz29 with gold and silver polymer electrodes, have been shown to retain their d_{33} sensitivity when fired 4 times at a peak temperature of 850°C. It is therefore possible to print the piezoelectric device as the first sensor on a substrate when a number of different thick-film devices are required to be fabricated on the same substrate. The similar results obtained from devices fabricated with gold electrodes, using both powder types, suggests that the devices fired multiple times at 850°C without a top electrode would produce the same results for each powder type.

Using silver polymer as the top electrode material of a piezoelectric thick-film device produces a d_{33} approximately 20% higher than devices fabricated with a gold top electrode at the same peak temperature of 850°C. This may be due to a larger contacting area between the surface of the electrode and the PZT film, however further investigation is required to confirm this theory.

Firing PZT-Pz29 thick-film devices at a peak temperature of 950°C and subsequently re-firing them at 850°C with gold top electrodes produces devices with the same sensitivity as devices fired twice at 850°C with gold top electrodes. Therefore,

there is no advantage in processing devices at 950°C if they are going to be subjected to subsequent firings at 850°C.

Re-firing devices at 950°C with gold top electrodes, which have previously been fired 3 times at 850°C reduces their sensitivity by approximately 20%. This may be due to an increase in the lead loss at the higher firing temperature or a change in physical structure and therefore merits further investigation.

Chapter 5 A binderless thick-film piezoelectric paste

5.1 Introduction

Conventional piezoelectric thick-film pastes fired at a temperature below 1000°C are mixed with a binder material in order to stick the film to a substrate (cf. section 3.4). Binder materials are commonly used in the majority of all commercially available thick-film pastes [105]. However, all conventional binder materials are dielectrics. This means that when they are mixed with the active piezoelectric powders the conductivity between powder grains can be reduced and therefore the piezoelectric properties of the thick-film may be reduced. The peak processing temperature used to fire or cure a piezoelectric thick-film with a binder material has been shown to affect the sensitivity of the film as well as limiting the types of material the device can be fabricated on [85].

In order to investigate the effects of removing the binder material from the paste formulation and the peak processing temperature on film adhesion and d_{33}, a number of devices were fabricated with peak processing temperatures of approximately 150°C, 720°C, 850°C and 950°C.

5.2 Design and characterisation of a test structure

5.2.1 Paste Mixture

The paste mixture was based on the powder blending method reported by Torah et al [85,87,87,88]. The new formulation used the same 4:1 weight ratio of the two different PZT powder grain sizes (2μm and 0.8μm respectively) as used to create all of the other devices in this thesis (refer to section 3.4). The only difference is that the glass binder (CF7575) was not added to the paste mixture. The PZT powder used to fabricate the paste was PZT-Pz29 supplied by Ferroperm [89].

The method used to fabricate the paste was essentially the same as described in section 3.4. A pestle and mortar was used to mix up the two powders and remove any lumps before adding the solvent (ESL 400) and finally running the mixture through a triple roll mill to evenly disperse the powder and make the paste screen printable.

5.2.2 Test structure for binderless paste.

In order to allow the new paste to be successfully printed without delaminating (due to a lack of binder material), a new test structure was designed to hold the PZT layer in place. Figure 5.1 illustrates the thick-film layers required to fabricate the new capacitive design test structure. It differs from the conventional capacitive structure shown in Figure 3.9 (b) since the PZT layer does not overlap the bottom electrode. Therefore, in order to separate the top and bottom electrodes and secure the edges of the PZT film, an extra dielectric windowing layer was printed on top of the bottom electrode and overlapping the edges of the PZT film. The top electrode was subsequently printed over both the PZT film and the dielectric layer. The silver/palladium underside electrode shown in Figure 5.1 does not make up part of the capacitive structure. It is simply included to allow measurement of the d_{33} coefficient (on a Take Control PiezoMeter) by electrically connecting it to the bottom electrode after poling. This process is described more fully in section 3.9.

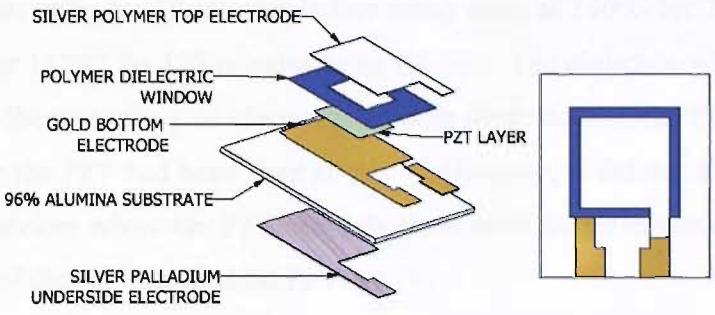

Figure 5.1: Capacitive type test structure for binderless piezoelectric paste.

The devices were printed on 4"x 4" 96% alumina tiles using the same screens as used to print the 30 devices per substrate (illustrated in Figure 3.20) with the exception of the PZT layer screen which was replaced with two different screens; one to allow smaller PZT squares to be printed in the centre of the bottom electrode and a second screen for the dielectric window layer. Drawings of the screen templates used to fabricate each layer of the devices can be found in appendices D.

5.2.3 Fabrication method

Four substrates were initially printed with gold bottom electrodes (ESL 8836) and a silver/palladium underside electrodes (ESL 9633) using the same processing parameters described in section 3.10.1.

Two layers of the binderless piezoelectric paste were printed on top of the gold electrodes. After each layer was printed it was left to settle for 10 minutes before being dried in an IR drier for 10 minutes at 140°C. One of the substrates (30 sample devices) was fired at a peak temperature of 820°C (DC850 furnace profile, Table 3.1) in order to sinter the PZT. The PZT layer on the remaining three substrates were simply left without any further processing. The thickness of the PZT layer of 4 devices from each substrate was then measured using a Carl Zeiss light meter and the technique described in section 3.6. The devices were found to be of a uniform thickness approximately 80μm thick (± 5μm).

A dielectric windowing layer (ESL-240SB) was subsequently printed around the edges of the PZT layer on two substrates, one where the PZT film had been fired at 820°C and one where the PZT film had only been dried at 140°C. The dielectric layer

was then left to settle for 10 minutes before being dried at 140°C for 10 minutes and finally cured at 150°C for 120 minutes in an IR drier. The dielectric windowing layer successfully adhered to the gold electrodes on both substrates and the PZT layer on the devices where the PZT had been fired at 820°C. However, it did not stick to the PZT layer on the devices where the PZT had only been dried for 10 minutes and formed a raised square of dielectric around the PZT.

A silver polymer top electrode layer (ESL 1110-S) was then printed on top of the PZT/polymer dielectric layers of both substrates, left to settle for 10 minutes before being dried at 140°C for 10 minutes and finally cured at 150°C for two hours. Unfortunately the edges of the dielectric layer on the samples where the PZT paste was only dried were brittle and the silver polymer top electrode could not be successfully printed on top of the windowing layer as the force from the squeegee during the print stroke snapped off parts of the windowing layers around the PZT, exposing the bottom electrode. Figure 5.2 shows the polymer windowing layer and top electrode delaminated from around the edges of the PZT layer.

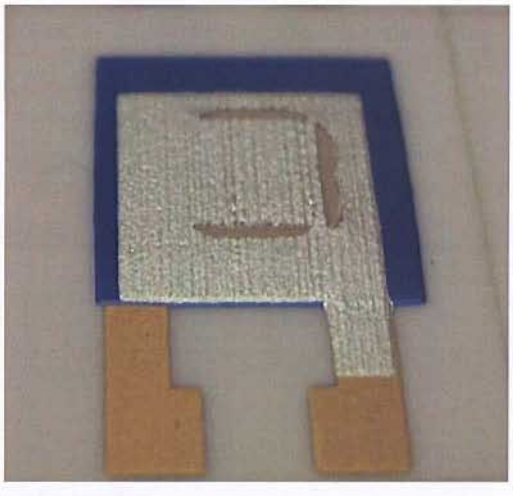

Figure 5.2: Picture of a device with the PZT layer dried at 140°C and the polymer windowing layer cured before the top electrode was printed.

It is believed that the polymer dielectric window did not adhere to the PZT layer because not all of the solvent had been evaporated during the 10 minute drying time, whereas the other substrate had been processed at a peak temperature of 820°C during firing, which would have evaporated all of the solvent.

To investigate this further, one of the two remaining substrates where the PZT layer had been dried for 10 minutes at 140°C was put back into the IR drier for a further 60 minutes at 140°C to remove more of the solvent from the PZT layer. After this process the PZT film was noticeably more powdery than the films on the previous two substrates. A dielectric windowing layer was subsequently printed and cured using the same parameters used on the initial two substrates. Unfortunately the windowing layer also delaminated around the edges of the PZT and the devices were therefore discarded.

In a further attempt to produce devices at a low processing temperature, (a maximum temperature of 150°C) the final substrate where the PZT layer had only been dried (at 140°C for 10 minutes) was printed with a layer of the polymer windowing dielectric. This layer was left to level for 10 minutes and dried at 140°C for 30 minutes in 10 minute intervals, before having a silver polymer top electrode printed on top of both the PZT and polymer windowing layer. The 30 minute drying time was considered necessary as after inspecting the windowing layer after 10 and 20 minutes it was believed to be too tacky to print on without affecting the print quality of the silver polymer layer or damaging the windowing layer.

The silver polymer top electrode was left to level for 10 minutes before being dried in the IR heater at 140°C for 10 minutes and finally co-cured with the windowing layer at 150°C for 120 minutes. This method proved to be successful and both the windowing layer and the top electrode exhibited good adhesion to the surface of all of the devices.

5.2.4 Breakdown voltage of samples

The electrical breakdown strength of each of the two sample types was investigated by applying an electric field across the top and bottom electrodes of the sample using an SRS PS310/1250V-25W high voltage source, with a maximum voltage supply of 1250V (the same high voltage supply used for poling samples as detailed in section 3.8). Five individual specimens were tested from each of the three sample types at room temperature (≈25°C) and all were found to withstand an electric field strength

of approximately $5MVm^{-1}$ before the dielectric layer sandwiched in between the two electrodes failed. In all of the samples the PZT layer did not breakdown under the electric field. The electrical break down strength of the dielectric paste ESL-240SB is quoted at $10MVm^{-1}$ [105]. The measured thickness of the polymer dielectric layer (using a micrometer) was approximately 45μm ±3μm and so the dielectric layer failed at a lower electric field strength of approximately $7MVm^{-1}$.

5.2.5 Poling samples

In order to make comparisons between the binderless piezoelectric thick-films with conventional piezoelectric thick-films containing binder materials, eight samples from each of the two substrates were poled at 200°C for 10 minutes before being allowed to cool to 60°C, at which point the poling voltage was removed. A voltage of 320V (giving an electric field of approximately $4MVm^{-1}$) was used to pole each of the devices.

After poling, the bottom electrode and the underside electrode were electrically connected with Electrolube silver conductive paint and the samples were tested on a Take Control PM35 PiezoMeter to determine their d_{33} characteristics (cf. section 3.9). Average d_{33} values are shown in Table 5.1 along with the maximum and minimum recorded d_{33} values and standard deviation.

Dielectric and top electrode processing	Peak PZT processing temperature (°C)	Avg d_{33} (pCN^{-1})	Max d_{33} (pCN^{-1})	Min d_{33} (pCN^{-1})	Standard deviation
Cured separately	820	75	81	70	5.8
Co-cured	150	20	21	18	1.2

Table 5.1: Sensitivity values for each processing type.

5.2.6 Discussion

Table 5.1 and Table 5.4 shows that the devices fabricated with the binderless paste and processed at a peak temperature of 150°C have an average d_{33} approximately

33% higher than piezoelectric thick-films with a polymer binder material (type 5) (20pC/N compared to 15pCN^{-1}). The devices fired at 820°C have a d_{33} approximately comparable to devices processed at a higher peak temperature of 850°C, with a glass binder [85]. The electric field strength required to breakdown the PZT thick-film could not be evaluated due to the printed dielectric windowing layer not being able to withstand an electric field strength equivalent to 5MVm^{-1} for the PZT layer. These results have shown that fabrication of thick-film piezoelectric devices with a binderless paste is feasible and that processing the devices at higher temperatures increases the d_{33} of the device.

5.3 SEM micrographs of samples

In order to investigate the level of adhesion from the binderless paste at different processing temperatures a further batch of devices was fabricated.

Five 4"x4" 96% alumina substrates were printed with gold bottom electrodes (ESL 8836) and silver/palladium underside electrodes (ESL 9633), which were processed using the same method described in section 3.10.1. Two layers of the binderless piezoelectric paste were printed, left to settle for 10 minutes and then dried at 140°C for 10 minutes in an IR drier.

Three of the substrates were then fired in a six zone belt furnace (the temperature of each of the furnace zones is recorded in Table 3.1). One substrate was processed at a peak temperature of 950°C (RNT1000 firing profile), a second substrate with a peak temperature of 850°C (Dupont60 profile) and the third substrate with a peak temperature of 720°C (RNT750 profile). A further two substrates were simply left without any further processing to the PZT layer. The thickness of the PZT layer from 4 devices on each substrate was subsequently measured using a Carl Zeiss light meter and the technique described in section 3.6. The film thickness was found to be relatively uniform (maximum deviation ±7μm) and the average results are recorded in Table 5.2.

The substrates had two layers of a polymer dielectric (ESL 240-SB) printed around the edges of the PZT layer to anchor the PZT layer to the underlying gold

electrode. Each layer was formed with two print strokes (to increase the film thickness) left to level for 10 minutes and then dried at 140°C for 30 minutes. A silver polymer top electrode (ESL 1110-S) was then printed on top of the PZT and dielectric layer, left to settle for 10 minutes before being dried at 140°C for 10 minutes and finally co-cured with the dielectric layer at 150°C for 2 hours. The thickness of the dielectric layer from 5 samples was then measured at approximately 125μm ± 5μm using a micrometer.

In order to investigate the level of sintering between PZT powder particles, at the different processing temperatures, several devices from each substrate were removed from the batch prior to the silver polymer top electrode being printed. This allowed SEM micrographs to be taken of the surface of each sample type. The SEM micrographs of all of the samples are shown in Figure 5.3 – 5.7.

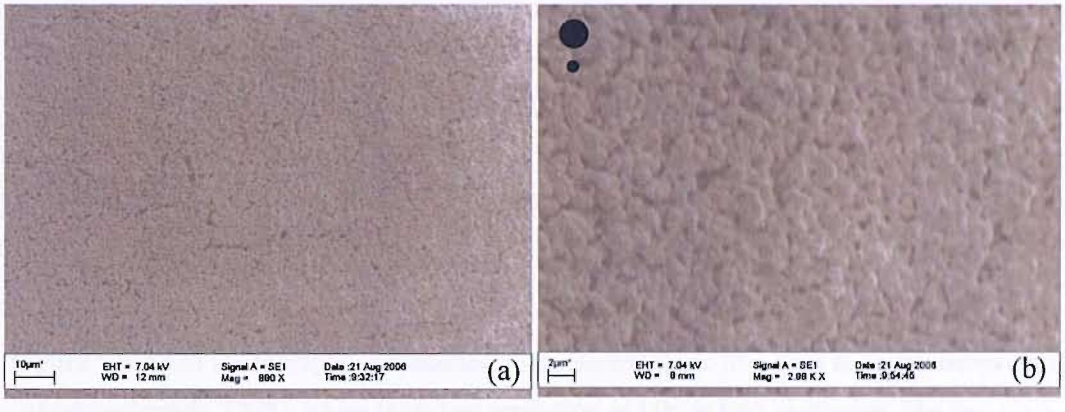

Figure 5.3: SEM micrographs of binderless piezoelectric thick-film fired at a peak temperature of approximately 950°C, where (a) is low resolution and (b) is high resolution. The two black circles shown in b) represent particle sizes of 2μm and 0.8μm diameters.

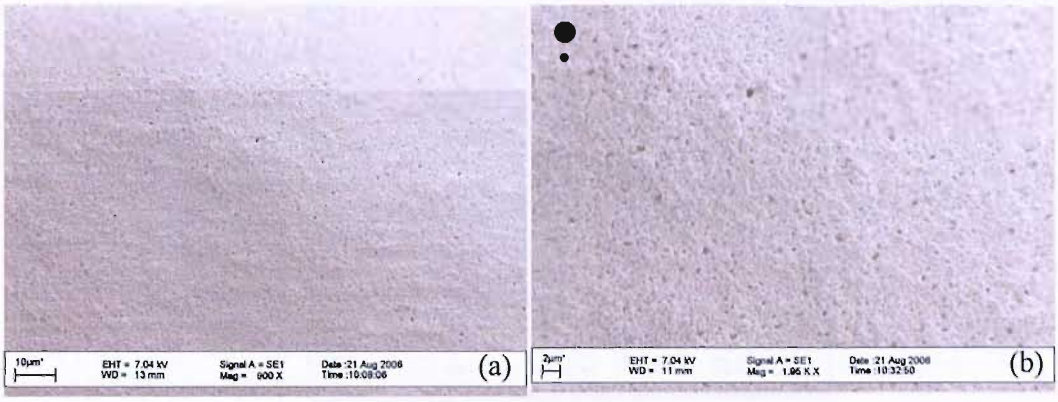

Figure 5.4: SEM micrographs of binderless piezoelectric thick-film fired at a peak temperature of approximately 850°C, where (a) is low resolution and (b) is high resolution. The two black circles shown in b) represent particle sizes of 2μm and 0.8μm diameters.

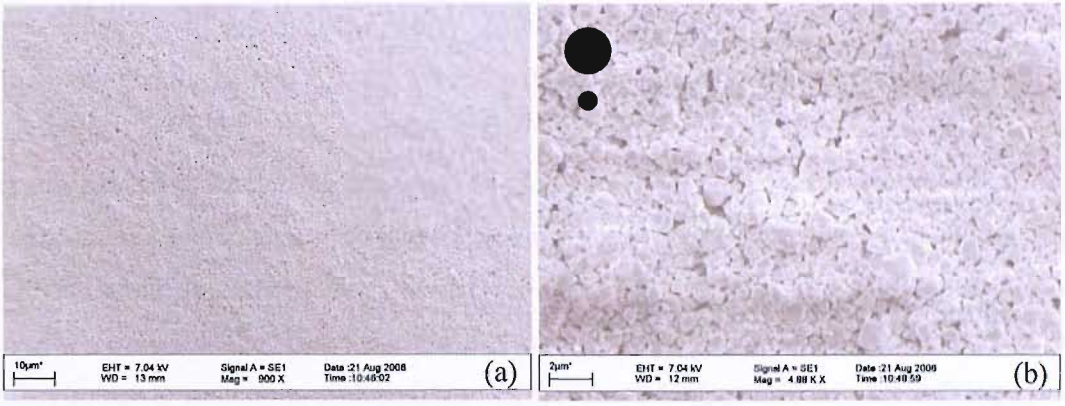

Figure 5.5: SEM micrographs of binderless piezoelectric thick-film fired at a peak temperature of approximately 720°C, where (a) is low resolution and (b) is high resolution. The two black circles shown in b) represent particle sizes of 2μm and 0.8μm diameters.

Figure 5.6: SEM micrograph of binderless piezoelectric thick-film cured at 150°C for 30 minutes in an IR drier.

Figure 5.7: SEM micrograph of a conventional piezoelectric thick-film fired at approximately 850°C with a glass binder.

Figure 5.3 to 5.6 show SEM micrographs of the surfaces of the binderless piezoelectric films produced using different processing temperatures. The SEM micrographs in Figure 5.3 to 5.5 a) and Figure 5.6 show a very densely packed structure for all of the samples when compared to an SEM micrograph of a conventional piezoelectric thick-film (with a glass binder) shown in Figure 5.7, which appears to show a greater density of surface voids. There are, however, a number of visible crack formations over the surface of the film fired at a peak temperature of 950°C. This is likely to be due to the higher cooling rate experienced by the samples, as they return to room temperature from a higher firing temperature in a fixed firing cycle time.

The increase in temperature can be seen to produce a higher level of sintering between the PZT powder grains, with the PZT grains being very apparent in the SEM of the sample dried at 150°C (Figure 5.6) and at higher temperatures becoming less visible. The grains in the structure of the sample fired at a peak temperature of 950°C (Figure 5.3) appear to be more highly sintered together and although the outline of some of the grain boundaries are still visible, they are fused together. The increase in the sintering of powder particles is evident in Figure 5.3 to 5.5 (b) when comparing the 2µm and 0.8µm diameter reference circles to visible grain boundary sizes.

5.4 Some physical characteristics of binderless paste

5.4.1 Testing the level of bonding between PZT thick-film and substrate

Scratch test

The scratch test involves using a metal blade or scribe to scratch the surface of a film in order to assess the level of adhesion between the film and the surface it is printed onto. There is no standardised scratch test method - it is generally used as a quick comparison between samples. There are two different methods of scratch test. A constant applied force method (looking at the size of scratch produced for a similar applied force) or a method where the force varied so that the minimum force required to remove the film is used. The former method was used here employing a flat head screw driver with a 1mm wide blade. The tests showed that the films of samples produced at lower temperatures were more easily removed than those fired at the highest temperature. This can be attributed to the differing degree of sintering that had taken place during the different peak processing temperatures and is evident in the SEM micrographs. Although all of the films could be removed (and by definition, failed the scratch test) they all exhibited good adhesion to the substrate and did not fall off even when the substrate was tapped on a table.

Tape test

The tape test involves sticking a strip of adhesive tape over the surface of a film and then peeling back the tape. The amount of material removed by the tape gives an indication of how well the film is stuck to the surface it is printed on. Traditionally, if any of the printed film is removed by the tape then it is considered to have failed the test. When applied to the binderless films all of the samples passed, with the exception of the samples fired at 720°C, of which a small layer of the PZT powder was removed by the tape.

By comparison, when the scratch and tape tests were applied to the piezoelectric thick-films with glass or polymer binders, all samples passed both tests.

5.4.2 Breakdown voltage of samples

The breakdown strength of each sample type was investigated using the same method described in section 5.2.4. Five individual specimens were tested from each sample type and all were found to withstand the maximum 1250V level with the exception of the samples fired at a peak temperature of 950°C, which withstood an average voltage of 1150V. From these measurements the electric field strengths could be calculated using the average film thickness for each sample type (cf. Table 5.2). The electric field strength for all samples was in excess of $17MVm^{-1}$, with the exception of the samples fired at 950°C, which had an average breakdown electric field of $14.4MVm^{-1}$. This is 3 to 4 times higher than the thick-film piezoelectric samples produced with glass or polymer binders which usually fail at 3.5 – 5 MVm^{-1} [94]. This large increase in ability to withstand electric fields is believed to be due to a decrease in the voids produced in the binderless thick-films. Typically glass has an electric breakdown voltage of around 14-26 MVm^{-1} [106] and makes up 12% volume of the paste mixture compared to PZT, which makes up 88% volume of the pastes mixture (excluding solvent which is evaporated from the film). Experiments undertaken poling glassy PZT thick-films in oil have shown that they can withstand electric fields up to $30MVm^{-1}$ [85]. It is therefore believed that the electrical breakdown strength is lowered by the presence of voids within the film and that their number is greater in the glass based paste. This is somewhat supported by the evidence from the SEM micrographs, which show that there is a reduction in voids on the surface of the binderless thick-film devices when compared to a sample with a glass binder (cf. Figure 5.3 – 5.7). The surface topology of the binderless paste samples fired at a peak temperature of 950°C also show a number of cracks within their surface and this could be the reason for the reduced maximum breakdown electric field strength when compared to the binderless paste samples with lower peak processing temperatures.

Peak processing temperature (°C)	Average Sample thickness (μm)	Average breakdown voltage (V)	Average breakdown field strength (MVm^{-1})
150	70	>1250	>17.9
720	70	>1250	>17.9
850	72	>1250	>17.4
950	65	~1150	~14.4

Table 5.2: Average breakdown voltage and field strength of 5 specimens for each processing temperature.

5.5 Measurement of d_{33} sensitivity

In order to make comparisons between the binderless piezoelectric thick-films with conventional piezoelectric thick-films containing binder materials, 15 devices from each substrate were poled at 200°C for 10 minutes (with the exception of the low curing samples, where 15 devices from one of the two substrates was poled at 150°C for 10 minutes) before being allowed to cool to 60°C, at which point the poling voltage was removed. A voltage of 450V (giving an electric field of approximately $6MVm^{-1}$) was used to pole each of the sample types. Three further devices, which had been processed at a peak temperature of 950°C, were poled at 200°C and 750V (approximately $11MVm^{-1}$) for 10 minutes before being allowed to cool to 60°C before the poling voltage was removed.

After poling, the bottom electrode and the underside electrode were electrically connected with Electrolube silver conductive paint and the samples were tested on a Take Control PM35 PiezoMeter to determine their d_{33} characteristics (cf. section 3.9). Average d_{33} values are shown in Figure 5.8 and Table 5.3 along with the maximum and minimum recorded values and standard deviation.

Peak PZT processing temperature (°C)	Poling temperature (°C)	Poling voltage (V)	Avg d_{33} (pCN^{-1})	Max d_{33} (pCN^{-1})	Min d_{33} (pCN^{-1})	Standard deviation
150	150	450	17	18	14	0.55
150	200	450	19	20	18	0.53
700	200	450	50	53	46	3.12
850	200	450	125	134	116	9.53
950	200	450	168	186	145	12.67
950	200	750	165	178	158	11.14

Table 5.3: Sensitivity values for each processing type.

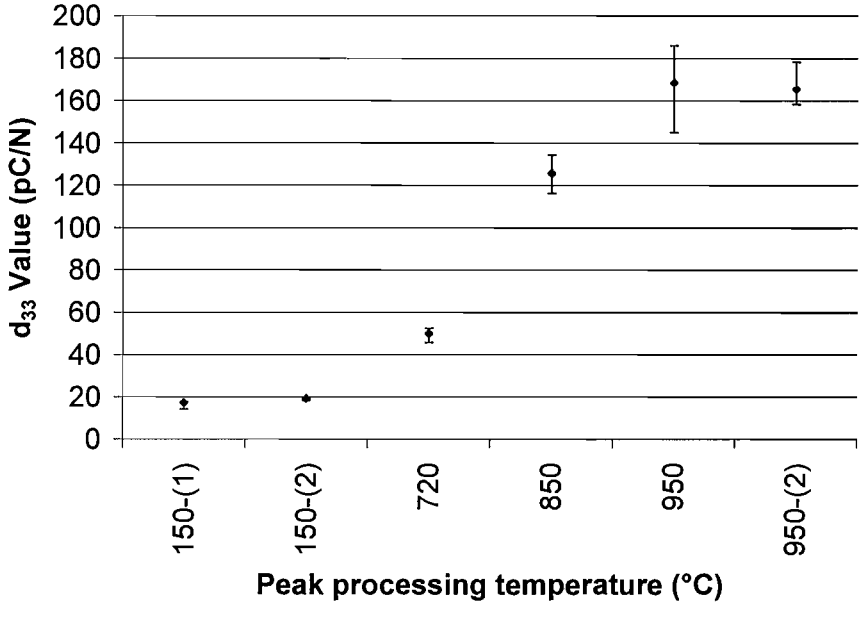

Figure 5.8: Average d_{33} readings for different processing temperatures, with the maximum and minimum d_{33} values indicated with error bars. The samples labelled 150-(1) and 150-(2) refer to the poling temperatures of 150°C and 200°C for (1) and (2) respectively, and 950-2 refers to the three samples poled with 750V.

5.6 Discussion

Table 5.4 shows a comparison of the d_{33} sensitivities for each type of piezoelectric material reported in this thesis along with some others obtained from the literature. From this table it can be seen that the piezoelectric thick-films produced with a glass binder and using the PZT-Pz29 powder from Ferroperm (Type 9) are approximately 22% less sensitive than those produced with the PZT-5H powder from Morgan Electro Ceramics (Type 4) (107pCN^{-1} compared to 131pCN^{-1} when fired at 950°C). Table 5.4 also shows that the new binderless thick-film PZT paste produces on average a 57% increase in the d_{33} when fired at the same peak temperature of 950°C with the average d_{33} output increasing from 107pCN^{-1} to 168pCN^{-1}. The binderless samples fired at a peak temperature of 850°C exhibited a 17% increase in sensitivity when compared with the conventional glassy PZT paste fired at a peak temperature of 950°C, and the samples processed at a maximum temperature of 150°C produced an increase in sensitivity of 33% over polymer piezoelectric thick-films. However, this is still 50% lower than reported for conventional polymer materials such as PVDF. The measured d_{33} values are reduced compared to the actual d_{33} values of the film, which has been shown to be reduced due to the clamping effect of the substrate by up to 74% [84,85].

Type	**Description of material**	**Maximum reported d_{33} Value (pCN^{-1})**
1	TRS610.	690 [107]
2	Bulk PZT-5H (Morgan ceramics).	620 [72]
3	Bulk PZT-Pz29 (Ferroperm).	575 [89]
4	PZT-5H (Morgan ceramics) thick-film with glass binder.	131 [87]
5	PZT-5H thick-film with polymer binder.	15 [108]
6	Piezoelectric paint.	20 [79]
7	PVDF.	30 [42]
8	PZT thick-film deposited by laser transfer method.	-124 (d_{31}) [74]
9	PZT-Pz29 (Ferroperm) thick-film with glass binder	107
10	Binderless thick-films fired at a peak temperature of 1000°C.	168
11	Binderless thick-films fired at a peak temperature of	125

Type	Description of material	Maximum reported d_{33} Value (pCN^{-1})
	850°C.	
12	Binderless thick-films fired at a peak temperature of 720°C.	50
13	Binderless thick-films cured at a peak temperature of 150°C and poled at 200 °C.	20
14	Binderless thick-films cured and poled at a peak temperature of 150°C.	18

Table 5.4: List of reported d_{33} values for different piezoelectric samples.

Increasing the poling field from $4MVm^{-1}$ to $6MVm^{-1}$ for the samples where the PZT layer was processed at 150°C, did not appear to affect the d_{33} sensitivity. Furthermore, samples processed at a peak temperature of 950°C in a $10MVm^{-1}$ electric field and a temperature of 200°C for 10 minutes did not show an increase in d_{33} of devices over samples poled in a $6MVm^{-1}$ electric field using the same temperature and time parameters. This is consistent with results from tests on piezoelectric thick-film devices with binder materials, which have shown d_{33} to increase with an increase poling field up to an optimum field (devices were poled up to $4MVm^{-1}$) [94]. To fully characterise the relationship between the peak PZT processing temperature and the effect of the applied electric field further tests are required on all four sample types so that the relationship between poling field strength and processing temperature can be more thoroughly analysed.

The substantial increase in d_{33} from devices fabricated with the binderless paste, along with the thick-films' ability to withstand a much higher electrical field, makes them an ideal candidate for improving existing sensor and actuator applications [109]. The successful fabrication of devices at a peak processing temperature of 850°C also provide a degree of compatibility with silicon MEMS structures [95]. The test structure used in the fabrication of the binderless piezoelectric thick-films would also act as a barrier layer between the silicon and PZT potentially reducing or preventing lead contamination within the silicon structure. The micrographs in Figure 5.3 – 5.5 b) indicate an increase in the level of sintering between powder particles. This is backed

up by the tape and scratch tests and an increase in measured d_{33} from samples fired at 720°C, 850°C and 950°C.

5.7 Conclusions

A piezoelectric paste without a binder material has been developed and used to successfully fabricate piezoelectric thick-film devices at peak processing temperatures of 150°C, 720°C, 820°C, 850°C and 950°C allowing the paste to be screen printed onto a variety of substrate materials. The paste material has been used to fabricate devices with significantly enhanced d_{33} coefficients, producing a 28% higher d_{33} than glassy thick-film devices processed at the same peak temperature of 950°C, (168pC/N compared to 131pC/N) and comparable d_{33} coefficients from devices when the binderless paste is processed at a lower peak temperature of 850°C (125pC/N). This is the first time a binderless piezoelectric paste has been successfully used to fabricate thick-film devices below 1000°C.

Devices processed at a peak temperature of 150°C produced an increase in sensitivity of 33% over polymer piezoelectric thick-films. However, this is still 50% lower than reported for conventional polymer materials such as PVDF.

All of the devices fabricated with the new paste were able to withstand electric fields 3-4 times higher than devices fabricated with conventional piezoelectric thick-film pastes produced with glass or polymer binder materials (14.4MVm^{-1} to over 17MVm^{-1} compared to 3.5 -5 MVm^{-1}).

The binderless paste showed good adhesion properties to 96% alumina substrates for all of the peak processing temperatures tested. This provides the opportunity to enhance a number of applications already utilising thick-film piezoelectric devices.

Chapter 6 Thick-film piezoelectric slip sensors

6.1 Prototype fingertip designs

6.1.1 Introduction

To increase the functionality of the Southampton Hand a range of thick-film sensors were integrated into the prosthesis. These sensors were designed to mimic the actions of the fast acting mechanoreceptors (slip), slow acting mechanoreceptors (force/grip pressure) and the thermosensitive afferent units (temperature) found in the glabrous skin of the human hand [110] and were integrated into the prosthesis. Previous work on integrating sensors into prosthetics and robots has commonly concentrated on the fingertips of the device, which is the perceived point of contact with an object (refer to section 2.4 for a review of the previous research undertaken in this area). It was therefore decided that an obvious starting point for the integration of the sensors with the hand would be through a fingertip design.

Figure 6.1 – 6.3 illustrate the prototype fingertips with the three types of sensor. The piezoelectric dynamic force sensor is used to detect slip in a similar manner to the fast adapting mechanoreceptive afferent units. So for example, when a step input is applied, a signal is generated which decays with time. The sensor is thus used to detect vibrations across the fingertip associated with slip.

In each of the three prototype designs a capacitive structure is used (cf. section 3.3 for details on conventional piezoelectric thick-film structures). The surface area of the electrodes of the piezoelectric thick-film along with the film thickness affects the capacitance and open circuit voltage of the device, but not the charge output, which remains constant. The charge output is also independent of all of the thick-films dimensions [72]. However, the area of the devices in all three fingertip designs is maximised with respect to remaining space, this is simply to increase the capacitance of the device and allow a larger capacitor to be used in the charge amplifier circuit (from equation 6.1), and is described in more detail in section 6.4.4.

$$C = \frac{\varepsilon A}{d} \qquad \text{Eqn 6.1}$$

Where C is the capacitance (F), ε is the permittivity of the PZT (Fm^{-1}), A is the area of overlap between the two electrodes (m^2) and d is the distance between the top and bottom electrodes (m).

The optimal position for the slip sensor would be as close to the root of the cantilever beam as possible i.e. where the force sensors are located in all three designs. This is because the closer to the root of the beam the higher the strains (change in strain for the dynamic force sensor) produced on the fingertip. However, the slip sensor was not located in this position for any of the three prototype designs as it was believed that it was more important to locate the strain gauges (force sensor) in this position instead.

The piezoresistive strain sensors act as slow adapting mechanoreceptive afferent units. In all three prototype designs the fingertips are modelled on a cantilever beam structure, with the piezoresistors located close to the root, where the maximum strain is produced [111]. When a force is applied to the end of the fingertip the structure bends and the resistance of the piezoresistors change in proportion to the applied force.

The temperature sensor (formed from a thermistor paste) represents the thermosensitive units found in the human hand and can be used for temperature compensation of the other sensors, which could range from -30°C in cold climates to over 50°C when holding hot objects. The sensor could also be used to alert the user if

the object is too hot or too cold, allowing the user to avoid unnecessary damage to the prosthesis.

The fabrication techniques used to produce the thick-film piezoresistive and piezoelectric sensors involve the use of a high temperature furnace with a processing temperature in the range of 850°C to 950°C and is described in more detail in section 3.6. As a consequence of the high processing temperatures used, the substrate choice is limited. Typically a ceramic substrate such as alumina is used. Unfortunately, due to the brittle nature of ceramics they are inappropriate for this type of fingertip, which would be expected to experience large strains in order to increase the force sensitivity from the piezoresistive strain gauges. However, previous work with stainless steel substrates has proved their compatibility with the thick-film process [112-118]. It was therefore decided that a substrate made from 3mm thick stainless steel type 304 would be used for the first prototype fingertip.

Several different methods of attaching the prototype fingertip to the finger were considered including: gluing, clamping and bolting. It was, however, decided that the most convenient method of attachment would be through the bolting method, as it allows a quick and easy method of replacing damaged or faulty fingertips without the need to replace the end section of the finger. This method also has the advantage of not producing a proud section, which may contact an object during grasping instead of the fingertip, which is intrinsic of a clamped version.

6.1.2 Prototype fingertip 1

The piezoelectric dynamic force sensor (slip sensor) covered an area from the middle of the fingertip to the distal end. However, due to complications the device was not realised. Details of these complications are described in section 6.1.5.

The static force sensor is located at the root of the cantilever beam and consists of four thick-film resistors, (R1-R4) arranged in a half Wheatstone bridge configuration. R1 and R3 are the passive components of the bridge circuit, located at the end of the beam, where ideally there should be no strain. However, ANSYS™ analysis on the fingertip structure has shown that these resistors are subjected to approximately 60% of the strain on the active resistors R2 and R4 with a simulated force of approximately

200N (cf. appendix F for details of the analysis). This means the force sensor is not as sensitive as it would have been if no strain was imparted on the dummy strain gauges. The force sensor does however still work well, and the proximity of the dummy and active gauges has the inherent advantage of temperature compensation over other designs. The characteristics and methods used to test the force sensor can be found in [119].

The dimensions of the fingertip were calculated using beam theory in order to produce a force sensor with a measuring range up to 100N, with a safe maximum strain limit of approximately 1milli strain.

The temperature sensor is located in between the force and dynamic force sensors. Retrospectively the temperature sensor may have been better located either at the distal end of the beam or proximal to the attachment point, where the lowest strains would be experienced and hence the least change in resistance from the sensor, for a given applied force. However, whilst the thermistor does exhibit a degree of strain sensitivity, it is low by comparison to its temperature sensitivity approximatly10ppm compared to 4100ppm/°C for the temperature coefficient of resistance.

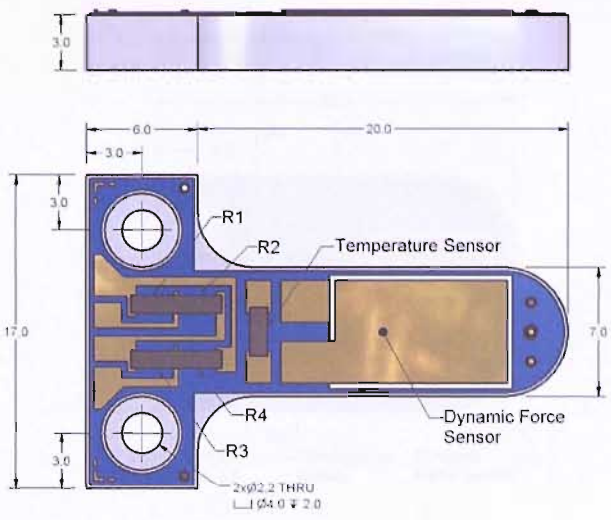

Figure 6.1: Prototype fingertip 1, fabricated using a stainless steel type 304 substrate (all dimensions in mm).

6.1.3 Prototype fingertip 2

The dynamic force sensor (slip sensor) is again located distal to the root of the beam, and is a square shape, instead of the rectangle device designed for prototype 1.

The force sensor is comprised of any of two of the three resistors labelled R1-R3. This design differs from the half Wheatstone bridge configuration as the force can be calculated independently of the position of where it is applied (as long as the force is applied distal to the resistors' location on the beam) using resistance ratios. This technique and experimental results are described in more detail in [120] and an ANSYS™ analysis of the strain across the fingertip is described in appendix F.

The temperature sensor was fabricated using the same paste as in prototype 1. However, in this design it has been located proximal to the root of the beam as the change in strain in this region is very low, (in comparison to other position distal to the root of the beam) when a force is applied to the fingertip. The test method and characteristics of the temperature sensor are described in [120].

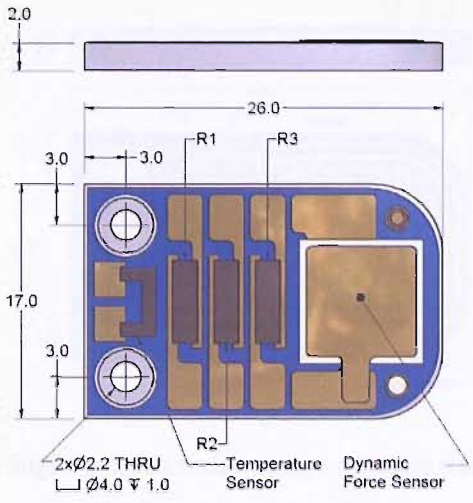

Figure 6.2: Prototype fingertip 2, fabricated using a stainless steel type 430 substrate (all dimensions in mm).

6.1.4 Prototype fingertip 3

The dynamic force sensor (slip sensor) has been located in the centre of the fingertip, where a higher change in strain will be experienced during object vibration compared to prototypes 1 and 2. The sensors shape has also been altered from the previous designs to a circular design. This is simply to maximise the surface area of the device, and not expected to affect the output from the device.

The force sensor is constructed from two resistors (R1 and R2, Figure 6.3) and operates in the same manner as described in section 6.1.3. However, to maximise the space on the fingertip only two piezoresistors were fabricated.

The temperature sensor has also been redesigned and meanders around the distal end of the fingertip. The increased length of the thermistor provides a larger resistance compared to prototype 1 and 2 for a given temperature. Therefore, as the % change of resistance remains the same per change in °C (the same paste is used on each of the prototype devices), the change in resistance (Ω) of the device is increased, making measurements of differences in resistance far simpler and less prone to error and hence improving temperature measurement resolution.

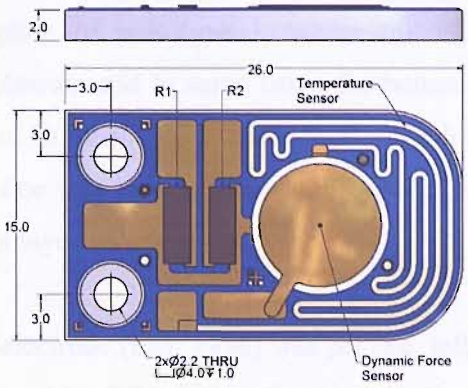

Figure 6.3: Prototype fingertip 3, fabricated using a stainless steel type 430 substrate (all dimensions in mm).

6.1.5 Sensor fabrication for prototype fingertips

Fingertip shapes were cut from a 3mm thick stainless steel plate (type 304), for prototype fingertip 1 and a 2mm thick stainless steel (type 430) plate for prototype fingertips 2 and 3. The steel was then degreased using acetone and subsequently rinsed in deionised water to remove any potential contaminants, which could affect the print quality. To isolate the sensors electrically from the stainless steel substrate three layers of a dielectric paste, (thermally matched to the steel type, (ESL 4916) for prototype 1 and (ESL 4986) for prototypes 2 and 3) were successively printed. Each layer was left for 10 minutes to level out before being dried using an IR heater for 10 minutes at approximately 150°C. The substrates were then fired in a belt furnace at a peak temperature of 850°C (Dupont60 profile Table 3.1). A single layer of gold paste (ESL 8836) was then printed on top of the dielectric, left to level, dried and fired (using the same parameters used to create the dielectric layer) to form the bottom electrodes for each of the sensors. The piezoresistors (ESL 3914) and thermistor (ESL PTC-2611) were subsequently printed and fired in a further two stages using the same parameters. The PZT paste used to fabricate the piezoelectric layers for prototype 1 and 2 was mixed using PZT-5H powder as the active material and prototype 3 used PZT-Pz29. Details of the paste formulation and preparation can be found in section 3.4. The piezoelectric layer was printed and left to level for approximately 10 minutes before being dried in an IR drier at 150°C. A second layer was then printed on top of the first, left to level for 10 minutes before again being dried at 150°C in an IR drier. The two layers were then co-fired at a peak temperature of 850°C for prototype 1 and 3 and

950°C for prototype 2, producing a film thickness in each case of approximately 100µm, with the exception of prototype 1, where the PZT layers fractured and delaminated from the substrate and in some cases the bottom electrode and dielectric layers were also removed. It is not fully understood why this occurred, though, it is believed that it may be due to a thermal mismatch between layers and is why it was only observed in the final layer.

Finally a top gold electrode (ESL 8836) was printed, left to level, dried and fired using the same parameters used to define the gold bottom electrodes. Figure 6.4 illustrates the printed layers on prototype fingertip 2.

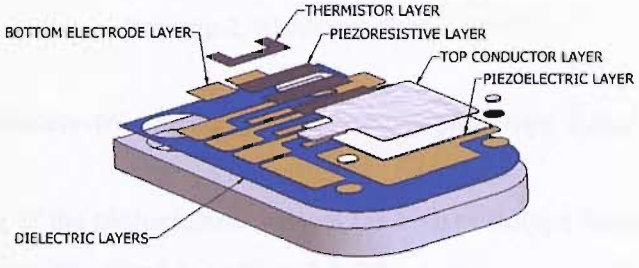

Figure 6.4: Printing layers required to create prototype fingertip 2.

Layer type	Paste type, used for prototype fingertips		
	Prototype 1	**Prototype 2**	**Prototype 3**
Dielectric	ESL 4916	ESL 4986	ESL 4986
Bottom electrode	ESL 8836	ESL 8836	ESL 8836
Piezoresistor	ESL 3914	ESL 3914	ESL 3914
Thermistor	ESL PTC-2611	ESL PTC-2611	ESL PTC-2611
Piezoelectric	PZT-5H	PZT-5H	PZT-Pz29
Top electrode	N/A	ESL 8836	ESL 8836

Table 6.1: Overview of the pastes used on each of the 3 prototype fingertips. Each layer was allowed to settle for 10 minutes after printing, before being dried at approximately 150°C in an IR drier and then fired at 850°C (with the exception of the piezoelectric layer for prototype fingertip 2, which was fired at 950°C).

6.1.6 Poling piezoelectric thick-films on prototype fingertips 2 and 3

The poling of the piezoelectric sensors for both prototype designs was undertaken using the apparatus described in section 3.8. The devices were subsequently tested for their d_{33} characteristics using a Take Control PiezoMeter and the method described in section 3.9. In order to prepare the devices for testing the bottom electrode from each device was electrically connected to the stainless steel substrate using Electrolube silver conductive paint.

To activate the piezoelectric sensor on prototype 2 devices, a poling field of $4MVm^{-1}$ (approximately 400V) was applied across the piezoelectric layer for 30 minutes at 150°C. The sample was then allowed to cool to room temperature before the electric field was removed. The measured d_{33} sensitivity value for the devices was around 46 ± 2 pC/N.

To activate the piezoelectric sensor on prototype 3 devices, a poling field of 3MVm-1 (approximately 300V) was applied across the piezoelectric layer for 10 minutes at 200°C. The sample was then allowed to cool to approximately 60°C before the electric field was removed. This yielded d_{33} sensitivity values of around 84 ± 8 pC/N, considerably higher than those obtained from prototype 2. This is believed to be due to the higher temperature used during poling.

6.2 Finger linkage slip sensor

Previous research on fabricating slip sensors for prosthetic hands has concentrated on locating the devices on a fingertip or fingertips of the prosthesis and this was the initial approach adopted in this study. This location is probably considered the obvious choice as the fingertips of the human hand have the highest concentration of fast adapting (FA) afferent units (dynamic force sensors) with around 220 units per cm^2 compared to 80 units per cm^2 across the rest of the fingers and 40 units per cm^2 in the palm of the hand [44,110]. This high resolution of sensors allows us to pick up local micro vibrations associated with object slip. The level of information provided by these sensors, however, is not required for the automatic control of a prosthetic hand where a single sensor is believed to be adequate. The sensor location can, therefore, be positioned on the finger in a place where the object is not contacted, as long as the vibrations can be detected when an object slips from the grip of the prosthesis. The linkages in the finger unit from Figure 2.5 act as a beam, with the root being located where the links intersect with the knuckle block. Therefore, if an object was held in a tip grip, with the face of the fingertip perpendicular to the floor and it began to slip then the length of finger linkages would act as an amplifier of the vibrations in the face of the linkages. The side of some of the links (particularly link ACD) are therefore a good candidate for a position to fabricate a thick-film slip sensor. Furthermore, the linkages are closer to the palm, where it is envisaged that the processing electronics and power supply will be located. By placing the sensors on the links closer to the palm the wires required to connect sensors will be shorter (depending on the link chosen) and will not have to bend as much as wire connected to a fingertip sensor, when the finger is flexed or extended. The three links ACD, BCE and DF were therefore chosen to have piezoelectric slip sensors fabricated on them so the sensitivity and slip characteristics of the devices could be compared with the devices fabricated on the fingertips.

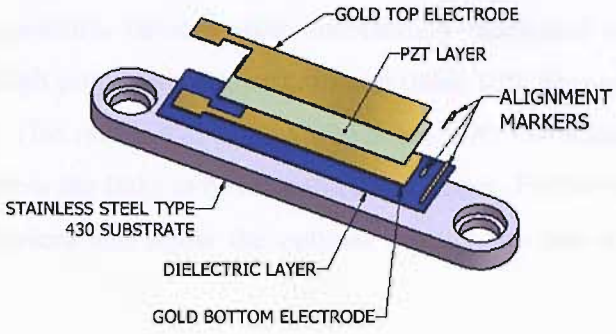

Figure 6.5: Printed layers of piezoelectric sensor on finger link DF.

6.3 Fabrication method

The finger linkages ACD, DF and BCE were cut from a 2mm thick stainless steel (type 430) plate and thick-film piezoelectric devices fabricated on each linkage using the method described in section 3.10.2 using PZT-Pz29 as the active material. Figure 2.3 illustrates the printed layers used to fabricate the piezoelectric sensors on finger links ACD, DF and BCE. Figure 6.6 shows a picture of the three linkages after all fabrication processes.

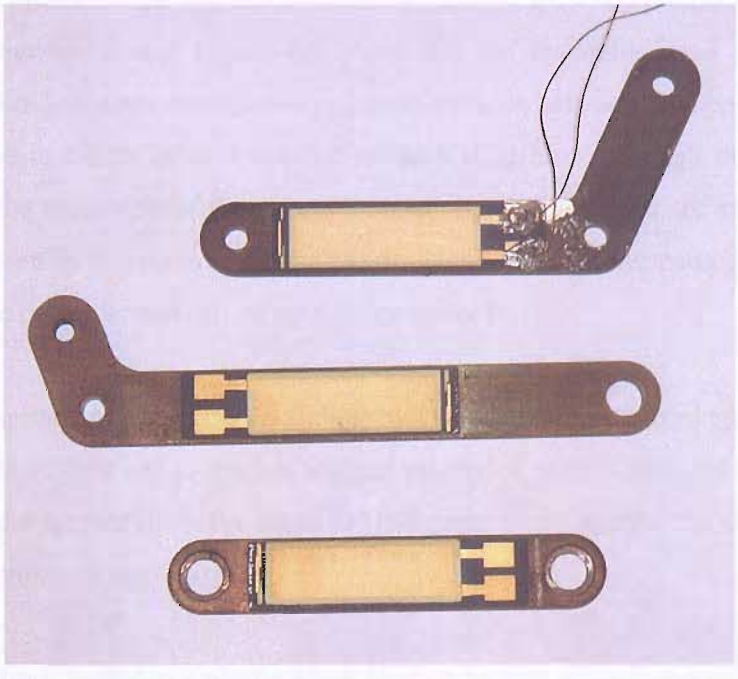

Figure 6.6: Picture of stainless steel type 430 finger linkages from the Southampton Hand, with capacitive type piezoelectric thick-film devices printed on them.

All of the piezoelectric devices were successfully fabricated on the linkages, however, due to the high processing temperatures an oxide film formed on the surface of the exposed metal. This meant that some of the holes, with low tolerances had to be re-bored in order to allow the links to be assembled in a finger. Further work is required to characterise the devices and allow the optimal position for the slip sensor to be established.

6.4 Characterising thick-film piezoelectric slip sensors

6.4.1 Experimental Setup

In order to quantify the ability of the piezoelectric sensor to detect slip it must be compared in some way to the real slip of an object. To achieve this, a slip apparatus was designed and built. It incorporated a rotary encoder to monitor object movement and acceleration, thus allowing a comprehensive comparison of the object's movement with that of the slip sensor signal. Due to a fire at the university the slip apparatus had to be rebuilt after tests on prototype fingertip 2 had been carried out.

Figure 6.7 illustrates the slip test equipment used for the experiments undertaken on prototype fingertip 2 and Figure 6.8 illustrates the apparatus used for testing prototype fingertip 3. There are only two major differences between the apparatus, one being the method in which force is applied to the sliding block through the fingertip and the second the resolution of the rotary encoder. Both differences are explained in more detail later on in this section. Technical drawings of all of the parts specifically designed to make the apparatus can be seen in appendix E.

The test equipment comprises a sliding block made from aluminium with four nylon headed screws attached to the bottom and two nylon screws attached to the side of the block. These screws allow the block to slide more freely against the side and the bottom of the aluminium angle base.

The fingertip is bolted to a plastic block held up by two studs in the same manner as it would be connected to the end of the Southampton Hand prosthetic finger (cf.

Figure 2.5). To allow different forces to be applied to the fingertip two compression springs were placed over the studs so that when the nuts are tightened the springs apply a force to the block, which is then coupled through the end of the fingertip and onto the sliding block. For the apparatus illustrated in Figure 6.8 the two springs were replaced with a spring balance attached to a retort stand and the fingertip holder. To increase the force applied through the fingertip the retort stand was simply moved away from the angle base thus stretching the spring. This feature allows a range of applied fingertip forces to be set for both sets of apparatus.

Figure 6.9 illustrates the attachment designed to allow the fingertips and side linkage slip sensors to be tested using the same apparatus setup.

To replicate slip, weights are attached to the front of the aluminium block via a metal cable and hung over a pulley attached to the base. When the weight is released it drops to the floor causing the "sliding block" to slip past the fingertip.

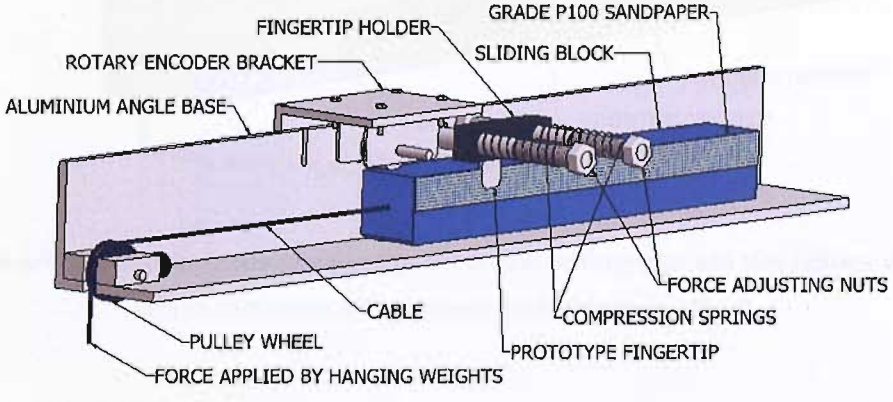

Figure 6.7: Slip test apparatus design 1 (used to test prototype fingertip 2).

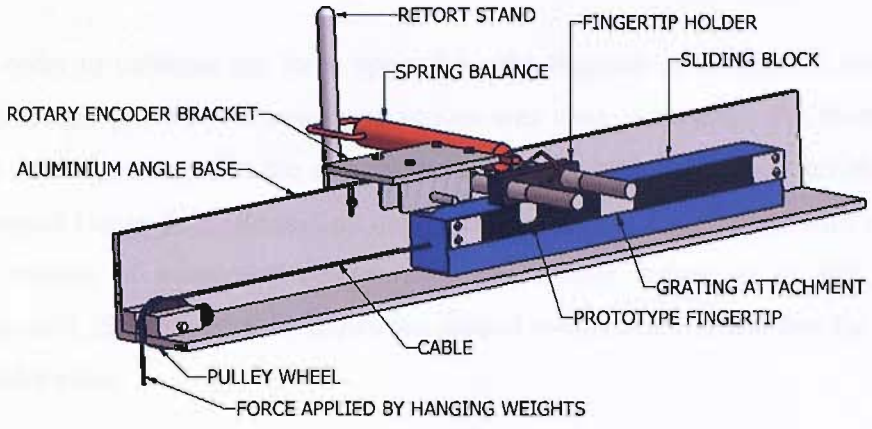

Figure 6.8: Slip test apparatus design 2 (used to test prototype fingertip 3).

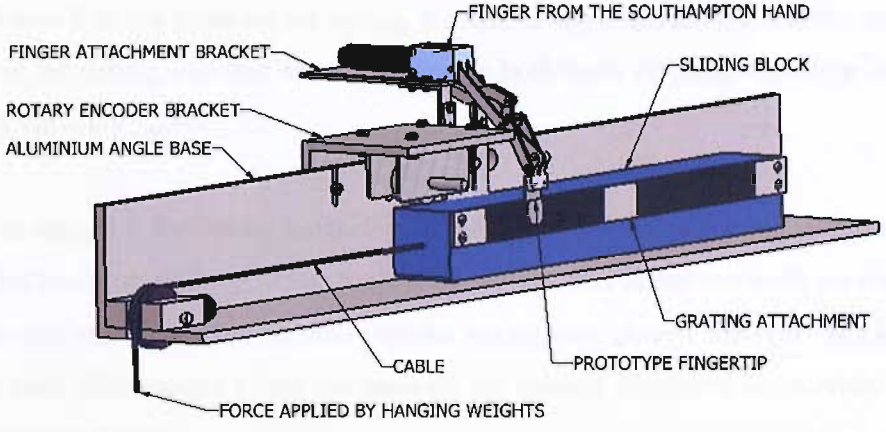

Figure 6.9: Slip test apparatus, designed to test prototype fingertips and side linkage sensors whilst attached to a finger from the Southampton Hand.

A HEDS-5540 three channel rotary encoder with a resolution of 500 pulses per revolution (ppr) was mechanically coupled to the top of the block via a wheel using the bracket shown in Figure 6.7. For design 1, the wheel has a 44mm diameter and a circumference of approximately 138mm. With 500 pulses per revolution from the encoder, a linear resolution of 0.276mm per pulse is obtained. In design 2, however, the diameter of the wheel was reduced to 23.8mm with a circumference of 75mm and therefore had an increased linear resolution of approximately 0.15mm per pulse.

6.4.2 *Calibration of applied fingertip force*

In order to calibrate the force applied by the fingertip in design 1 a Mecmesin Compact Gauge [121] force measuring device was used to measure the force at the fingertip holder block whilst the nuts were tightened together one full turn at a time. The Compact Gauge force measuring device is a hand held force gauge with a digital readout capable of measuring compression and tension forces up to 50N with a resolution of 0.25N. Figure 6.10 shows the plotted results and confirm that the springs obey Hooke's law:

$$F = kx \qquad \text{Eqn 6.2}$$

Where F is the force on the spring, k is the spring constant and x is the change in length of the spring, and that for a full turn on both bolts the fingertip force increased by approximately 1.26N.

For design 2 the spring balance was calibrated by hanging 100g weights on the end of its hook, up to 500g. After each 100g weight was added the scale on the spring balance was recorded. This showed that the spring also closely followed Hooke's law and for each 100g weight added the scale on the balance displayed an increase in force of approximately 1N.

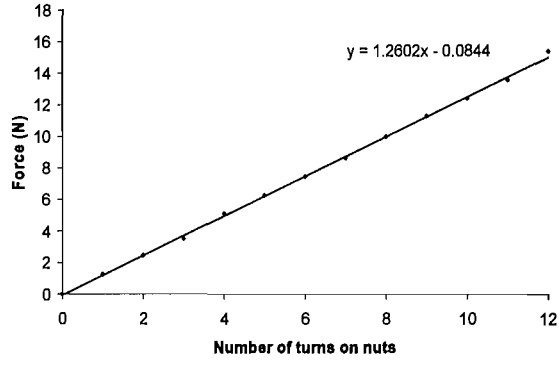

Figure 6.10: Force calibration of compression springs (slip apparatus design 1).

6.4.3 *Data collection*

In order to easily manipulate and analyse the signals, data were collected using a National Instruments 6036E data acquisition card (DAQ) and a purpose built program

written in LabVIEW™ 7.1. The 6036E is a 16-bit card with 16 analogue inputs, 2 analogue outputs and a maximum sampling rate of 200kS/s. The labview virtual instrument (VI) consists of three sub VI's to collect sample data, trim data and produce FFT's of sampled data. The program to collect data allows all DAQ card channels to be selected individually and their sampling rates to be adjusted. The VI is also setup to trigger when a PZT signal is detected, storing a sample of the data in the memory ready to be saved to a file. These data are displayed on a graph, which can be viewed at the same time as the real time data. The length of the sample to be saved can also be altered by simply entering in the time required in seconds. There is also a pre-sample feature to allow data to be recorded a set time (manually specified) before the trigger is detected, as well as a manual override button for the trigger. All of these features can be altered whilst the program is running.

This program was designed to allow small samples of data to be collected and labelled without having to save large amounts of data. Details of the program code and a description of how it operates are shown in appendix B.

6.4.4 Electrical circuit design

The charge output from all piezoelectric materials is very low and traditionally measured in pC/N. In order to easily measure the charge it is converted into a voltage, and to make use of the full potential of the data acquisition card the maximum signal must be amplified to be within a ±10V range. The circuit must also contain an anti-aliasing filter which cuts out any frequencies above half of the sampling rate and allows an accurate digital picture of the signal to be generated [122]. Figure 6.11 illustrates the process used to amplify and filter the signal before these data were recorded. The full circuit diagram can be seen in appendix C.

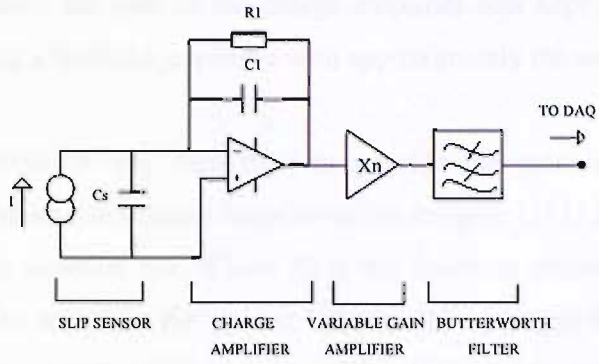

Figure 6.11: Charge amplifier with gain control and 8-pole Butterworth filter.

The charge amplifier shown in Figure 6.11 was constructed from a single operational amplifier. It is a virtual earth amplifier and works on the principal that the two inputs are closely balanced. However when a charge is produced from the piezoelectric thick-film it produces a voltage at the inverting input of the charge amplifier. (cf. Equation 6.3). To maintain the balance at the two inputs a current is fed back from the output to the inverting input through resistor R1. This current produces a measurable voltage at the output (V_{out}) given by equation 6.4.

$$i = \frac{dQ}{dt} \qquad \text{Eqn 6.3}$$

$$i = \frac{Vout}{R_1} \qquad \text{Eqn 6.4}$$

The gain from the circuit can then be deduced from Equation 6.5.

$$G = \frac{C_s}{C_1} \qquad \text{Eqn 6.5}$$

Where C_1 is a feedback capacitor in the circuit and C_s is the capacitance of the piezoelectric thick-film. This circuit is good for testing a single piezoelectric thick-film. However, the capacitances of the piezoelectric sensors differ between samples due to slight variations in sample thickness and electrode surface area, (from equation 6.1 a typical plate capacitor) and for the devices on the prototype fingertips are typically in the range of 1-3nF. Thus to maintain the same gain between devices either the capacitor C_1 must be altered to maintain the ratio, or the gain must be altered at a later stage.

Throughout this thesis the gain of the charge amplifier was kept as near to unity as possible by selecting a feedback capacitor with approximately the same value of C_s.

A second amplifier was then used to provide the gain in the circuit. This differential amplifier uses resistance ratios to define its gain, [123] and the gain for this stage is defined by equation 6.6. Where R_2 is the feedback resistor from the second differential amplifier and R_3 is the resistor between the output of the charge amplifier and the inverting input of the differential amplifier (refer to circuit diagram Appendix C).

$$G = \frac{R_2}{R_3} \qquad \text{Eqn 6.6}$$

The total gain of the circuit is simply the product of Equations 6.5 and 6.6 i.e.

$$G_{total} = \frac{C_s.R_2}{C_1.R_3} \qquad \text{Eqn 6.7}$$

The value of the feedback resistor R1 in the initial stage of the charge amplifier is important since it controls the decay time and amplitude of the output from the piezoelectric sensor. A high value resistor will produce a longer decay time with a high signal output whilst a small value resistor will produce a faster decay time with a low signal output. For this particular application a 1MΩ resistor was found to produce an optimal response.

To avoid aliasing issues an anti-aliasing filter was incorporated into the circuit to allow frequencies above half of the sampling rate to be rejected thus allowing an accurate digital picture of the signal to be generated. For this purpose a Maxim 291 switched capacitor low pass 8 pole Butterworth filter was selected, as it was available in a simple eight pin DIP package and offers a sharp cut-off at the programmed frequency. The filter requires a clock input to determine cut-off frequency and has a 100:1 clock to corner frequency ratio. This means that the clock frequency has to be set 100 times higher than the cut off frequency required.

6.4.5 Eliminating mains noise from the PZT signal

As the PZT sensor is connected to the electronics via two 5cm wires (for both apparatus setups) and the fact that the signals from the PZT sensor are inherently very small, (and have to be amplified by approximately 1000 times) there is a pickup and amplification of 50Hz mains noise. In the real application noise will be reduced by locating the charge amplifier next to the sensor, which was not possible in this case due to the size of the prototype electronics. This technique is common practice in myoelectric and EMG applications where the majority of the signals obtained from muscles are in the 10Hz – 1kHz range [124-126] The circuit will also be powered by a battery, which has also been shown experimentally to reduce noise levels. Figure 6.12 (a) shows the signal when the amplifier circuit is powered by a mains source whilst Figure 6.12 (b) shows the output of the signal when the circuit is powered by a battery source. This reduced the peak noise level from 60mV to approximately 30mV for the experimental setup used to test prototype fingertip 2. Both signals show a high initial output when tapped, which decays quickly with time and is notably different to that of the slip signal shown in Figure 7.2 This characteristic could be utilised within a control system in the hand to avoid erroneous closure, for example if the user accidentally bumps into an object or taps the table. The signal can also be used to indicate the first contact with an object when the hand is closing.

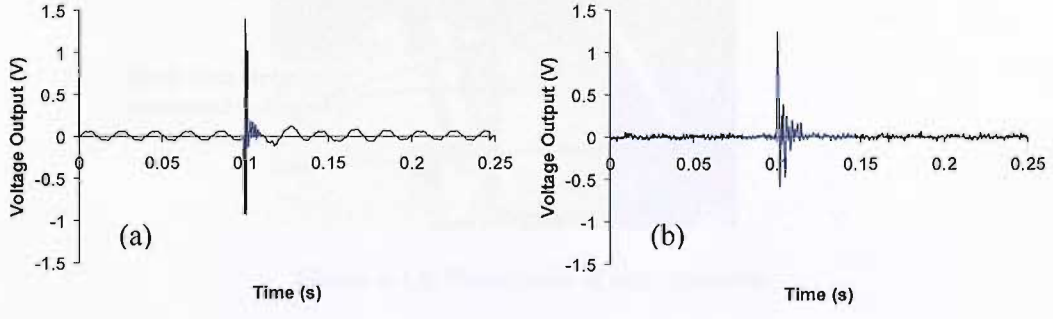

Figure 6.12: Output signal of the PZT sensor when it is lightly tapped and the circuit is (a) powered by a mains source and (b) powered by a battery source.

A small number of modifications were made to the measurement circuit to improve mains noise rejection prior to testing prototype fingertip 3. These measures included, twisting all power supply and earth wires together, connecting an earth wire to the aluminium angle base and the fingertip substrate, wrapping an earth wire around

the signal wires from the PZT sensor to the amplifier electronics and using aluminium foil (connected to the power supply earth) as a shield for the electronics. Examples of these measures are illustrated in Figure 6.13and Figure 6.14. The combination of these measures effectively eliminated the mains noise for a PZT signal amplification of 1000.

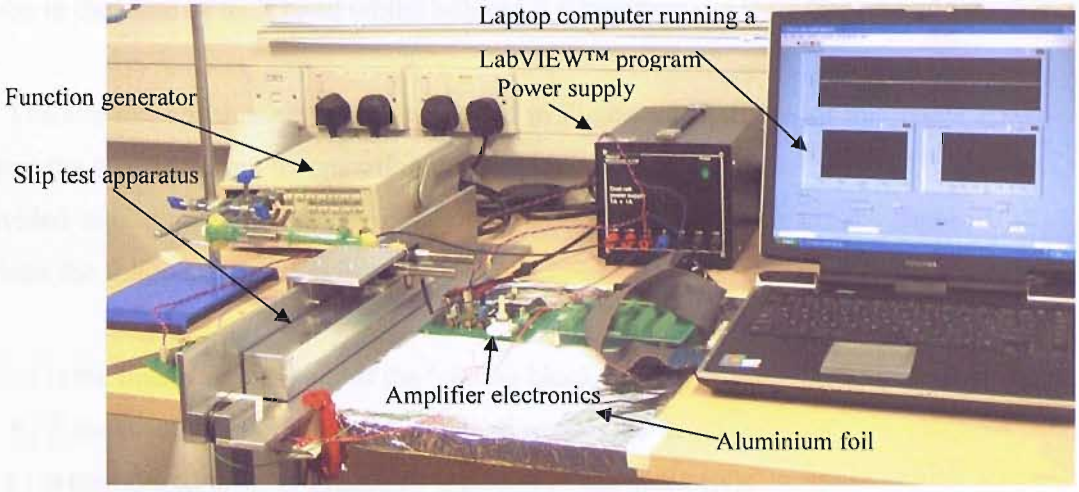

Figure 6.13: Photograph of equipment setup, incorporating slip apparatus design 2.

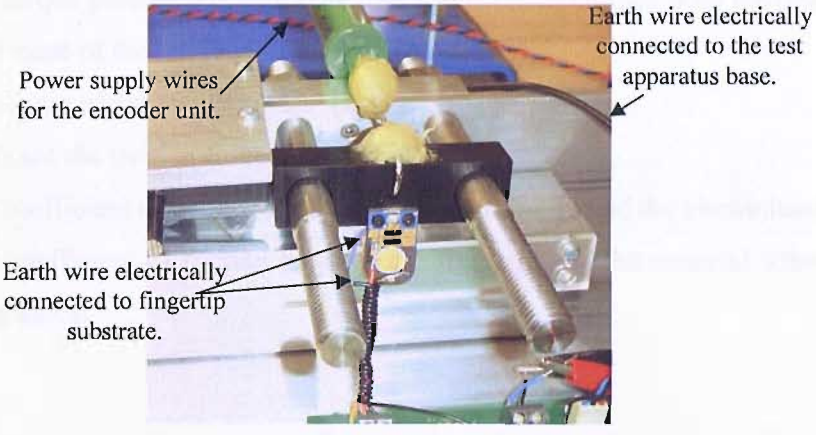

Figure 6.14: Photograph of test apparatus.

6.4.6 Analysis of the forces acting on the slip test apparatus

Analysing the forces acting upon the test rig components and performing some simple experiments allowed the coefficient of friction between the fingertip and the sandpaper adhered to the sliding block to be calculated. Using similar methods the coefficient of friction between the test rig base and the nylon screws was also obtained. The coefficient of friction between the fingertip and contacting surface is important to

enable a comprehensive evaluation of the sensor's capabilities when detecting slip on everyday objects as there is expected to be a limit at which the coefficient of friction is too low to produce a signal. This limit is not expected to affect the use of the sensor as the user may be able to visually assess an object before deciding upon the grasp pattern they will use to pick up or hold that object. For example, most people would cup an ice cube in the palm of their hand whilst holding it rather than use their fingers and thumb.

The slip test apparatus has been modelled in Figure 6.15 with all of the forces acting upon the test rig during its operation denoted. For ease of analysis Figure 6.15 has been divided into smaller free body diagrams (FBD) shown in Figure 6.16 - Figure 6.18, where the following notation is used:

A_1 is the linear acceleration of the 'sliding block' (ms^{-2});
A_2 is the linear acceleration of the 'falling mass' (ms^{-2});
F_1 is the normal force produced by the mass of the block (N);
F_2 is the force applied by the fingertip (N);
F_3 is the inertial and frictional forces from the encoder (N);
F_4 is the torque produced from the inertial and frictional forces from the pulley (Nm);
M_1 is the mass of the 'sliding block' (kg);
M_2 is the mass of the 'falling mass' (kg);
T_1 and T_2 are the tension forces in the cable (N);
μ_1 is the coefficient of friction between the nylon screws and the aluminium base;
μ_2 is the coefficient of friction between the fingertip and the material adhered to the sliding block.

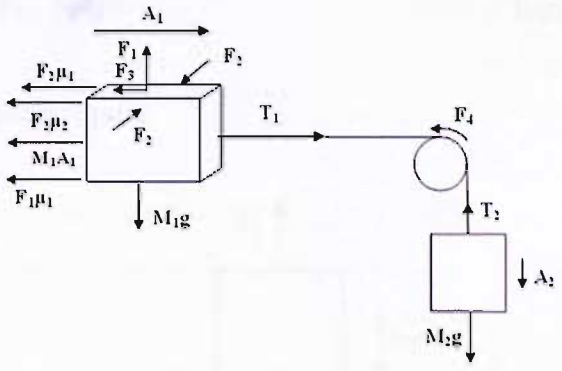

Figure 6.15: Test apparatus system, with forces and accelerations labelled during normal operation.

1) Analysis of the sliding block:

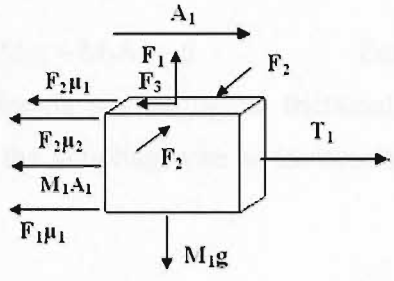

Figure 6.16: Free body diagram of sliding block.

Resolving forces horizontally:

$$T_1 - M_1A_1 - F_3 - F_1\mu_1 - F_2\mu_2 - F_2\mu_1 = 0 \quad \text{Eqn 6.8}$$

The tension force in the metal cable T_1 is opposed by the friction forces created between the nylon screws on the sliding block and the bottom ($F_1\mu_1$) and side ($F_2\mu_1$) of the aluminium base. Friction forces created between the fingertip and material adhered to the sliding block ($F_2\mu_2$) as well as inertia forces from the sliding block itself (M_1A_1) and the inertia and fictional forces from driving the motor encoder (F_3) also oppose the tension force in the metal cable.

Resolving forces vertically:

$$F_1 - M_1 g = 0 \qquad \text{Eqn 6.9}$$

2) Analysis of the falling mass:

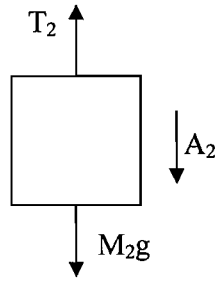

Figure 6.17: Free body diagram of falling mass.

There are no forces acting in the horizontal plane, therefore resolving forces vertically:

$$T_2 - M_2 g - M_2 A_2 = 0 \qquad \text{Eqn 6.10}$$

Assuming negligible inertia and negligible frictional losses of the pulley and encoder assembly and that the coupling wire is inextensible provides the following linking equations.

$$F_3 = 0 \qquad \text{Eqn 6.11}$$

$$F_4 = 0 \qquad \text{Eqn 6.12}$$

$$T_1 = T_2 \qquad \text{Eqn 6.13}$$

$$A_1 = A_2 \qquad \text{Eqn 6.14}$$

Substituting equations 6.9 to 6.14 into equation 6.8 yields the expression:

$$A_1[M_1 - M_2] + \mu_1[F_2 + F_1] + \mu_2 F_2 - M_2 g = 0 \qquad \text{Eqn 6.15}$$

This expression leaves three unknowns μ_1, μ_2 and A_1, which can all be found experimentally.

3) Experimentally determining μ_1 for test apparatus design 1:

To determine the sliding coefficient of friction μ_1 the sliding block was pulled along the base of the test rig at an approximate constant velocity by hanging weights on

the metal cable, suspended over the pulley, and without the fingertip in contact with the block. To obtain an approximate constant velocity the sliding block was set in motion by slowly pulling the metal cable, it was then visually assessed to see if it continued at a similar velocity up to the aluminium angle base (c.f. Figure 6.8). The force T_1 was then calculated from the weight required to make the block slide (illustrated in Figure 6.18). This could also have been achieved by monitoring the encoder signal, however, the former method was chosen for its simplicity.

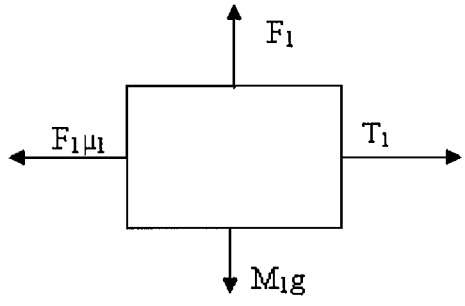

Figure 6.18: Free body diagram of sliding block being pulled along at a constant velocity.

Resolving forces horizontally:

$$T_1 - F_1\mu_1 = 0 \qquad \text{Eqn 6.16}$$

The experiment was conducted six times and an average T_1 value of approximately 2.7N was recorded in Table 6.2. The mass of the sliding block M_1 was 1.34kg and taking the acceleration due to gravity to be 9.81 ms^{-2} allows the coefficient of friction between the nylon screws and aluminium test rig base to be calculated by substituting equation 6.9 into equation 6.16.

$$\mu_1 = \frac{T_1}{M_1 g} \approx 0.2 \qquad \text{Eqn 6.17}$$

The value determined for μ_1 of 0.2 is comparable with that found in the literature, giving confidence in this experimental method. For example, Carvill quotes the coefficient of friction for Nylon on steel under low pressure and with no lubrication as lying within the range 0.3 to 0.5 [111].

4) Experimentally determining μ_2 for setup with prototype fingertip 2:

The same procedure was then applied to the test rig to calculate the sliding coefficient of friction between the fingertip and the grade P100 sandpaper adhered to the sliding block (μ_2), with a known force (F_2) applied to the sliding block by the fingertip (cf. Figure 6.16).

Resolving forces horizontally:

$$T_1 - F_2\mu_1 - F_2\mu_2 - F_1\mu_1 = 0 \qquad \text{Eqn 6.18}$$

Rearranging 6.18 allows μ_2 to be calculated.

$$\mu_2 = \frac{T_1 - F_1\mu_1}{F_2} - \mu_1 \qquad \text{Eqn 6.19}$$

F2 Value (N)	Average T1 Value (N)	Average μ2 Value
0	2.70 ± 0.00	N/A
1	3.15 ± 0.05	0.27 ± 0.05
2	3.65 ± 0.05	0.29 ± 0.03
3	4.20 ± 0.00	0.31 ± 0.00
4	4.75 ± 0.05	0.32 ± 0.01

Table 6.2: Average coefficient of friction values recorded at different applied forces for slip test apparatus design 1 and prototype fingertip 2 on a grade p100 sandpaper.

In order to determine the coefficient of friction value the force applied by the finger tip was increased from 0 to 4 N in 1N increments. At each force increment three T_1 force values were taken using the hanging weight method described earlier. The fingertip force was then reset and the experiment was repeated. The average of six runs was used to calculate an average μ_2 value at each force. These average values were then used to calculate an overall average μ_2 value of approximately 0.3. This compares favourably with published values of friction coefficients between similar types of

materials (e.g. 0.2 for metal on metal, 0.4 for leather on metal and 0.5 for Acrylic on metal)[111].

Chapter 7 Experimental testing of prototype fingertip 2

7.1 Introduction

The ability of the human hand to detect and act on slip signals has its limitations for certain objects with low coefficients of friction, say, for example: an ice cube or a bar of soap. It is therefore not unreasonable to expect similar limitations from the PZT sensor, since it also monitors vibrations. The PZT sensor is a dynamic force sensor and as such when a step input is applied to the device a signal is produced, which decays with time, depending on the connected electronics. The velocity of the sliding object will therefore affect the output signal. This section investigates the slip signal produced in terms of distance travelled, velocity and acceleration of the sliding block, from a sliding interface between prototype fingertip 2 and grade p100 sandpaper, with a coefficient of friction of approximately 0.3 and a force of approximately 1.25N being applied by the fingertip.

7.2 Experimental method

The compression springs on the slip test apparatus (design 1, Figure 6.7) were adjusted so that the fingertip applied approximately 1.25N of force to a sheet of grade P100 sandpaper (with a similar surface roughness to that found on the striking surface of a match box), adhered to the side of the "sliding block" with double sided tape. A small stainless steel washer was glued to the back of the fingertip to prevent it being damaged by the sandpaper; but still allowing vibration forces to be coupled to the sensor. Supported weights were attached to the cable connected to the "sliding block"

(cf. Figure 6.7). When released, this caused the block to accelerate past the fingertip, simulating slip. This experiment was subsequently repeated a number of times and the results analysed in terms of the acceleration and velocity at which an initial slip signal was detected.

7.3 Setting a threshold level to detect a slip signal for prototype 2

With the electronics connected to prototype 2 a background noise reading was measured and rectified while the block was stationary. This revealed a peak noise level of 60 mV, allowing a suitable threshold of 100 mV to be selected for validating when the PZT signal was considered to be active. For each trial the PZT and encoder signals were recorded simultaneously. The recorded PZT sensor signals were post-processed in software. This involved firstly converting the digitised bi-polar signals into their uni-polar equivalents, in effect performing simple rectification. The resultant data set was then scanned in chronological order with each component of the data set being compared to the preset threshold level. Whenever the former exceed the latter, a threshold crossing event was recorded.

Setting Type	Value
Differential amplifier gain	1,000
Approximate charge amplifier gain	10
Total PZT signal gain	1,000
High pass filter cut off frequency (Hz)	10,000
DAQ card sampling rate for each channel (Hz)	20,000
DAQ card channels used to sample slip sensor	0
DAQ card channels used to sample encoder signals (2 channels)	4,5
Data points recorded for each trial (ms) (200ms pre-trigger)	20,000
Approximate fingertip force (N)	1.25

Table 7.1: Setup values of all adjustable equipment and software parameters used in trials on prototype fingertip 2.

7.4 Calculating "sliding block" acceleration

Calculating the acceleration and velocity of the "sliding block" allowed a direct comparison to be made between trials when the conditions of slip were the same and when they were not, and if this had any effect on the output signal. To obtain the acceleration of the block the cumulative encoder count was plotted with respect to the square of the time, as shown in Figure 7.1. The value of the acceleration can then be determined by multiplying the gradient of the graph by twice the encoder resolution (from $s = ut + \frac{1}{2}at^2$). Figure 7.1 shows the encoder response to be linear indicating that the block is accelerating at a constant rate as expected. Similar responses were obtained for each of the trials, showing constant acceleration of the block in each case.

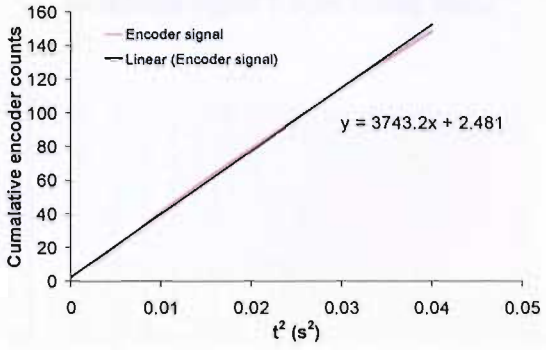

Figure 7.1: Integrated encoder signal.

7.5 Trimming data

One second of data (20,000 data points) was collected for each trial. These data were then imported into a MicroSoft Excel™ spreadsheet where each file was individually trimmed down to 3000 data points (150ms) for each of the two encoder signals and the PZT signal (9000 data points in total). Because the capture of data from each trial was triggered by the Labview™ program (described in appendix B), each trial started at a different time, with respect to when the sliding block started to move (first encoder signal). Therefore, in order to standardise the starting point of each trial the sample data was normalised to include 200 data points (10ms of data) before the sliding block began to move. This was achieved by locating the first encoder signal and taking the data 200 points before it occurred and 2800 after.

7.6 Results

Figure 7.2 shows a typical signal obtained from the encoder and piezoelectric sensor when the block slides across the aluminium base with approximately 1.25N of force being applied to the block by the fingertip. The encoder signals shown in plots (a) and (b) are 90° out of phase and both show a narrowing in pulse width with time. This indicates that the block is accelerating. Section (c) illustrates the output from the piezoelectric sensor. It is interesting to note that the amplitude of the sensor signal tends to increase as the block accelerates. Finally (d) shows the rectified piezoelectric sensors output with a superimposed threshold level of 100 mV.

a) Encoder signal 1 from sliding block.

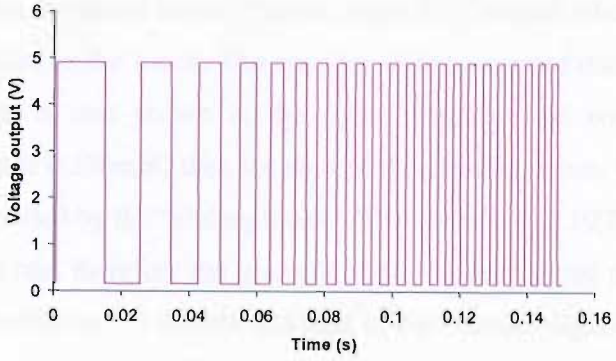

b) Encoder signal 2 from sliding block.

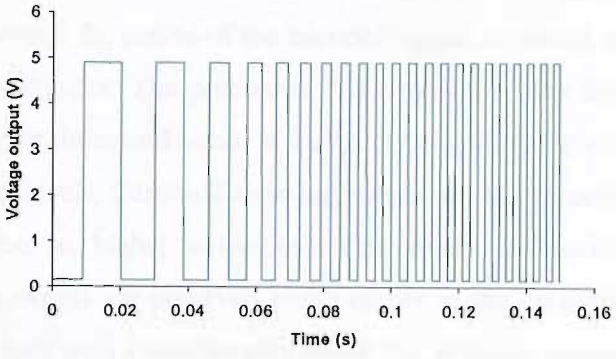

c) Slip signal from PZT sensor.

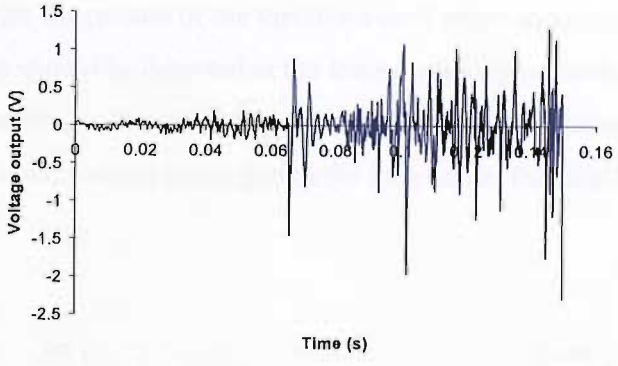

d) Rectified slip signal from PZT sensor with superimposed 0.1V threshold.

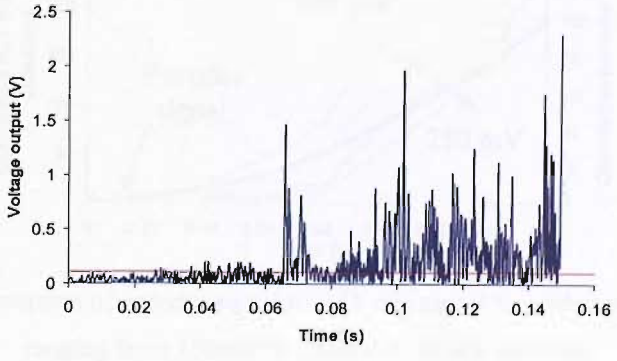

Figure 7.2: Encoder and PZT signals before and after rectification.

Figure 7.3 shows the cumulative number of post-processed threshold crossing events, for different threshold levels, from a single PZT sensor when a fingertip force of 1.25N was applied to the block. The encoder signal recorded during the acquisition of the sensor data is also shown in the figure. Because the encoder has a fixed resolution (1 count is 0.276mm) then the sum of the encoder counts is a direct measure of the distance travelled by the "sliding block". The encoder and PZT sensor signals are sampled at a fixed rate, therefore the gradient of the encoder signal represents velocity. It can be seen from Figure 7.3 that the gradient of the encoder signal increases over the duration of the experiment, which implies that the velocity increases with time (left to right across the graph) i.e. the block is accelerating. This is confirmed in plots (a) and (b) of Figure 7.2 where the period of the encoder signals is shown to decrease over the duration of the experiment. The processed PZT signal for each threshold level meets the x-axis at different times and hence at different velocities. Figure 7.2 (d) shows that at higher threshold levels, threshold crossing events are not recorded until later on in the experiment (i.e. at higher velocities). Conversely, at lower threshold values, threshold crossing events are observed much earlier in the experiment when the PZT sensor exhibits signals with a smaller magnitude (i.e. at lower velocities). Thus there is a limiting velocity before which slip cannot be detected, and the value of this velocity is proportional to the magnitude of the threshold used when counting threshold crossing events. Ideally slip should be detected at the lowest velocity possible but this is where a trade off exists: setting a threshold level too low means that extraneous noise could register as a threshold crossing event giving the impression that slip had occurred when it hadn't.

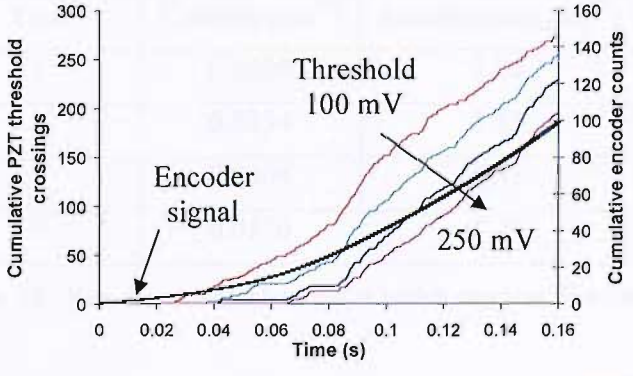

Figure 7.3: Comparison of encoder signal to PZT slip signal for different threshold values ranging from 100mV to 250mV in 50 mV intervals.

Figure 7.4 shows the cumulative PZT sensor threshold crossing events recorded over the distance travelled by the sliding block (determined from the encoder count and encoder resolution) for four trials with a fingertip force of approximately 1.25N on grade P100 sandpaper and with a sensor signal threshold value of 100 mV. Each of the trials are therefore repeats of the same surface interface, however the acceleration for each trial can be seen to vary (Table 7.2), this is simply due to the different weights required to overcome stiction. The values of the linear regression coefficients (displayed in the legend) show the highly linear fit for each trial. At a threshold of 100 mV, slip was detected after the block had moved a distance between 1.10mm – 1.66mm. Table 7.2 shows that the velocity (determined from the encoder signals recorded simultaneously for each trial and from the sampling rate) at which the initial slip was detected was similar for the first three trials with an average value across all four trials of approximately 0.025 ± 0.008 ms^{-1}

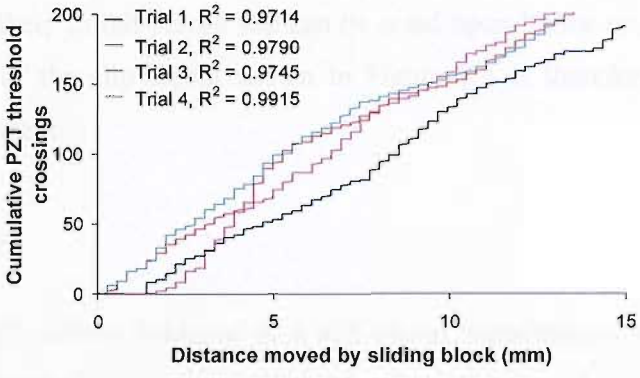

Figure 7.4: Indication of sensor repeatability.

Trial	Velocity (ms^{-1})	Acceleration (ms^{-2})
1	0.0280	2.06
2	0.0334	1.55
3	0.0304	1.85
4	0.0176	1.44

Table 7.2: Velocity and acceleration at which slip was first detected.

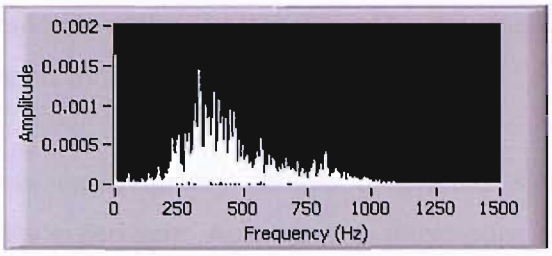

Figure 7.5: Linear power spectrum FFT of trial 1.

Figure 7.5 shows a linear power spectrum FFT for a typical trial and reveals that the frequency content of the slip signal for this particular material combination is contained in the approximate range of 200-1000 Hz. This frequency range is likely to be dependant upon the type of material in contact with the fingertip. The frequency content of the signals in this application is important, because although higher frequencies would allow object slip to be detected faster, they also require a faster sampling rate to accurately detect the signal. However, if the frequency content is to low an object is likely to fall before slip can be acted upon by the prosthesis user. The frequency range of the slip signal shown in Figure 7.5 is therefore believed to be desirable by the author.

7.7 Discussion

Figure 7.2 (c) shows evidence of a slip signal superimposed over background noise level (in this case 50Hz mains noise). However, the piezoelectric sensor's signal is smaller than the noise signal and so a threshold cannot be accurately applied to it at an object velocity below 0.034 ms^{-1}. This suggests that if the 50Hz noise is reduced by placing the electronics closer to the sensor and powering the electronics with a battery source then the slip signal may be detectable at a lower velocity, and possibly before the object has moved 1mm. The rejection of the 50Hz noise would also allow a much higher amplifier gain to be applied, allowing the slip signals to be investigated in greater detail.

Figure 7.4 shows a linear relationship between the cumulative encoder counts and cumulative piezoelectric sensor's threshold crossing events. Since the encoder signal is a direct representation of the distance the object has moved, then the processed PZT

signal represents an estimate of the distance moved by the object. The processed PZT signal therefore represents movement of the block, hence slip.

Figure 7.5 shows the frequency content of the slip signal for the material combination used in the experiment. Although this information may not be useful for quickly detecting slip, it could potentially be used in the future to send surface texture information back to user via direct connection to the peripheral nervous system. The frequency content of signals is therefore considered an interesting area of future research.

During everyday use there are a number of sources potentially producing erroneous signals from the slip sensor. These include bumping into an object or simply scratching your leg. For this reason the sensor is intended to be used in conjunction with force sensors, motor encoders for finger tip position and an intelligent control system. It is clear from comparing the piezoelectric sensor's response when lightly tapped to that of an object sliding that they are different and hence the tapping signals could be ignored. However, actions such as scratching your leg are likely to produce a similar response to a slip signal, so to avoid erroneous hand closure the position of the fingers and force applied to them can be taken into account, only allowing the signals from the slip sensor to be acted upon when the hand is in a grip mode.

It is likely that the surface properties (e.g. surface roughness, geometry, coefficient of friction between object and prosthesis) of a held object are related to the frequency and amplitude output of the piezoelectric sensor with respect to the velocity the object is travelling. If correct, then an FFT analysis maybe useful alongside other tactile information such as grip force in determining these characteristics. However this type of analysis would have limitations if used to control the force applied to an object within a prosthetics application. This is because a number of samples would have to be recorded before the surface properties could be determined. In real terms this would mean the user of the prosthesis might have dropped the object they were holding before the surface properties and hence the force required to be applied to the object were determined. It is also a useful analysis in determining the frequencies which may be filtered out of the signal and also the minimum sampling rate which would be required

in a prosthetics application to cover a range of surface geometries, coefficients of friction and velocities.

The analysis of the signal frequency content for different materials and surface geometries is important to enable an optimal frequency range to be selected for use in a prosthesis. This particular material combination shows very usable frequency content with few low frequency components (below 100Hz), thus enabling mains noise to be removed and allowing enough characteristic data to be collected in a short period of time so that object slip can be detected quickly. The higher end of the frequency range is also not too high as to require a fast sampling device.

Other limitations may include low coefficients of friction not producing a large enough signal to define an object's slip, the damping effects of different glove types worn and the position of the slip sensor in the prosthetic hand.

7.8 Conclusions

With a coefficient of friction of approximately 0.3 between the fingertip and sandpaper, it was determined that a velocity of 0.025 ± 0.008 ms^{-1} must be exceeded before a slip signal above the background noise was able to be used to detect slip. By reducing the threshold value used in the detection of threshold crossing events from 250mV to 100mV it has been shown that the velocity at which the initial slip detection occurs is decreased. It is also evident that the slip signal from the PZT sensor began before it was detected at the threshold of 100mV. There is therefore scope to reduce the background noise signal and use a much lower threshold value or increase the output gain, which would then allow the accurate detection of slip at lower velocities. This is the first experimental evidence that this type of thick-film piezoelectric sensor can be used to detect slip. The slip signal is a measure of relative velocity between the object and finger surface. It can be processed to obtain an estimate of the relative distance that an object has slipped. Further work is therefore required to investigate the lowest possible coefficient of friction required to trigger the signal at an acceptable object velocity with an optimal fingertip design.

This investigation has also demonstrated the suitability of the apparatus to simulate slip under a range of conditions e.g. acceleration, coefficient of friction and fingertip force.

Chapter 8 Effect of a cosmesis covering on PZT slip signal for two different gratings

8.1 Introduction

Given that an anthropomorphic prosthesis is covered by a cosmetic glove it is essential that any sensors located on the skeletal structure of the prosthesis will work with a covering. In order to test the piezoelectric slip sensor under these conditions a section of Otto Bock cosmesis glove was adhered to the prototype 3 fingertip. The previous section describes the effects of grade P100 sandpaper on the thresholded slip signal of the prototype 2 fingertip. The sand paper had a regular surface texture and the signal produced from the sensor was equivalent to the velocity of the sliding block. It was therefore considered advantageous to investigate the effects of regular surface features on the output signal of the slip sensor. This was achieved by fabricating a sliding block attachment with two different grating sizes. The method used to achieve this and the results obtained are described in this section.

8.2 Fingertip preparation

The top section of an Otto Bock Sensor Hand™ speed cosmetic glove was cut out in the shape of the prototype 3 fingertip (refer to section 6.1.4 and 6.1.5 for dimensions and fabrication details of prototype fingertip 3). This section of glove was selected as it

is approximately 1mm thick with a uniform surface texture. The newly tailored rubber was adhered to the back of the fingertip (the side without the sensors printed on) with an epoxy resin. Figure 8.1 illustrates the section of rubber cosmesis adhered to the fingertip.

Figure 8.1: Prototype Fingertip with a tailored section of Otto Bock cosmetic glove adhered to the back.

8.3 Experimental method

In order to characterise the thick-film piezoelectric slip sensor on the prototype 3 fingertip, test apparatus and electrical amplifiers were designed and built. A description of the apparatus used in the following experiment is described in more detail in section 6.4.1 with a picture of the test apparatus in Figure 6.8 and the amplifier layout in Figure 6.11.

A 310mm long Perspex block attachment with two sets of grooves cut 0.1mm wide and 0.19mm deep was bolted onto the sliding block. One set of grooves, covering 109mm of the block, were spaced a distance of 1mm apart. The second set of grooves, covering the last 109mm of the block, were spaced at 0.5mm apart. Figure 8.2 illustrates the dimensions of the grooves for each of the attachments. At the beginning of each trial the sliding block was placed approximately 70mm away from the foam stopper (on the test apparatus illustrated in Figure 6.8). To replicate slip, weights were added to the end of the wire cable in 50g increments until stiction was overcome and the block began to slide. Eight slip signals from each grating were recorded using a DAQ card and a purpose written Labview™ program detailed in section 6.4.3. The data was subsequently analysed to show the distance the sliding block had travelled in the first 200ms, the average acceleration of the block, (using MicroSoft Excel) and the

frequency content of the slip signal using the power spectrum FFT function in Labview™. Table 8.1 lists the values of all the adjustable equipment and software parameters used in the trials.

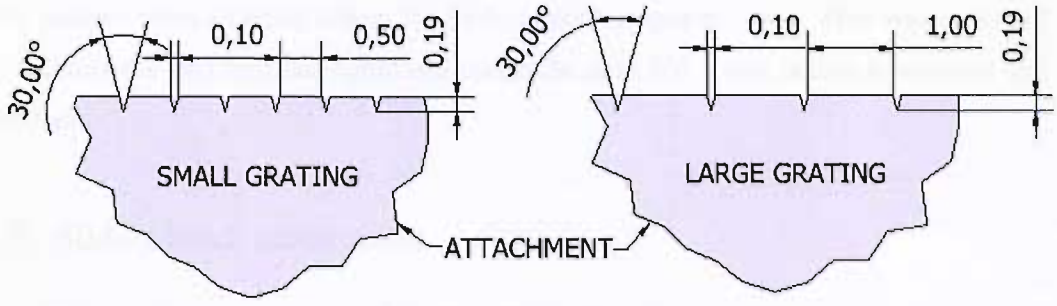

Figure 8.2: Diagrams of small and large gratings on the sliding block attachment (all dimensions in mm).

Setting Type	Value
Differential amplifier gain	1,000
Approximate charge amplifier gain	1
Total PZT signal gain	1,000
high pass filter cut off frequency	10,000
DAQ card sampling rate for each channel (Hz)	50,000
DAQ card channels used to sample slip sensor signal	0
DAQ card channels used to sample encoder signals (2 channels)	4,5
Data recorded for each trial (ms) (80ms pre-trigger)	380
Approximate fingertip force (N)	1

Table 8.1: Setup values of all adjustable equipment and software parameters used in the trials on prototype fingertip 3.

8.4 Processing and analysing data

8.4.1 Trimming data

The PZT and encoder signal data was then imported into a MicroSoft Excel™ spreadsheet where each file was individually trimmed down to 10,000 data points (200ms) for each of the encoder signals and the PZT signal (30,000 data points in total).

Because the capture of data from each trial was triggered by the Labview™ programme, the 380ms of data for each trial started at a different time, with respect to when the sliding block started to move (first encoder signal). Therefore, in order to standardise the starting point of each trial the sample data was trimmed to include 500 data points (10ms of data) before the sliding block began to move. This was achieved by locating the first encoder signal and taking the data 500 points before it occurred and 9500 after.

8.5 Sliding block acceleration

Due to the manner in which the sliding block was forced to accelerate (by applying weights in 50g increments) the acceleration between trials was expected to vary. Therefore, calculating the acceleration of the sliding block allowed a comparison to be made between trials, with respect to how the differences may have affected the PZT sensors output signal. To obtain the acceleration the same method described in section 7.4 was used.

8.6 Setting a threshold level to detect slip

The trimmed PZT and Encoder signals were placed in a MicroSoft Excel spreadsheet, where the PZT signal was rectified and a threshold of 400mV was used to bisect the signal. Each time the threshold was crossed by the PZT signal a threshold crossing event was recorded. This was then used as a comparison against the encoder signal (distance the sliding block had moved). The threshold level could have been set considerably lower as there was very little noise superimposed on the signal, however, as the PZT signal for all the samples was over 500mV an arbitrary value of 400mV was chosen.

8.7 Calculating the coefficient of friction

The coefficient of friction between the two different Perspex gratings and cosmesis was found experimentally using the same technique described in section 6.4.6. Table 8.2 and Table 8.3 show the approximate coefficient of friction values obtained from fingertip forces of 1 - 3N, with an average of 2.55 and 2.38 for the large

and small gratings respectively. This is within the limits of published values of friction coefficients for a rubber on a solid of 1-4 [127].

F_2 Value (N)	Average T_1 Value (N)	Average μ_2 Value
0	2.90 ± 0.00	N/A
1	6.05 ± 0.15	2.93 ± 0.15
2	8.45 ± 0.15	2.56 ± 0.08
3	10.00 ± 0.00	2.15 ± 0.00

Table 8.2: Coefficient of friction from an interface between Perspex (large grating) and an Otto Bock glove.

F_2 Value (N)	Average T_1 Value (N)	Average μ_2 Value
0	2.9 ± 0.00	N/A
1	5.9 ± 0.10	2.78 ± 0.10
2	8.10 ± 0.10	2.38 ± 0.05
3	9.50 ± 0.00	1.98 ± 0.00

Table 8.3: Coefficient of friction from an interface between Perspex (small grating) and an Otto Bock glove.

8.8 Results

Figure 8.3 (a) and (c) show the typical signals obtained from the PZT sensor when the block slides past the fingertip, for the two different gratings and a fingertip force of approximately 1N being applied.

(a) Slip signal produced from PZT sensor (trial 1, small grating).

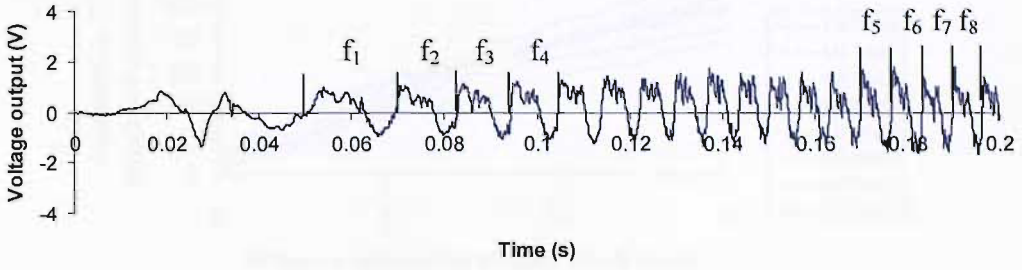

(b) Rectified slip signal from PZT sensor, with a superimposed 0.4V threshold (trial 1, small grating).

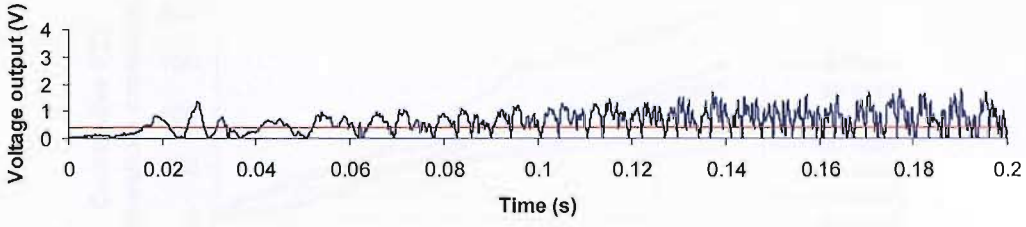

(c) Slip signal produced from PZT sensor (trial 1, large grating).

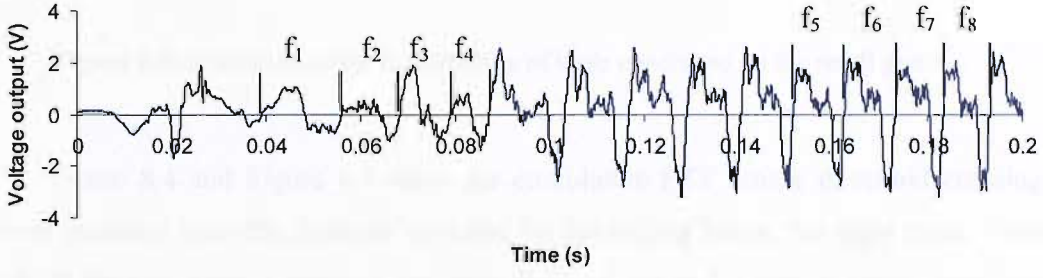

(d) Rectified slip signal from PZT sensor, with a superimposed 0.4V threshold (trial 1, large grating).

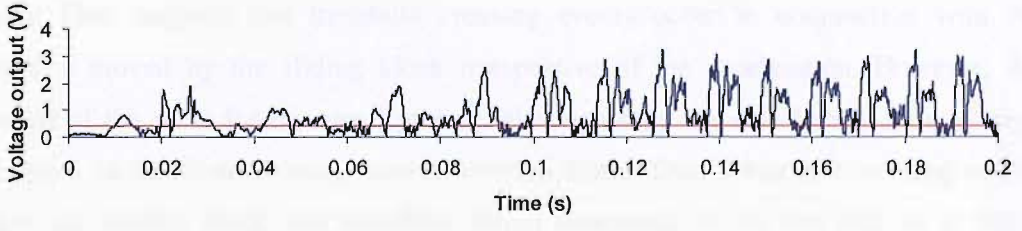

Figure 8.3: Slip signals produced from PZT sensor before and after rectification.

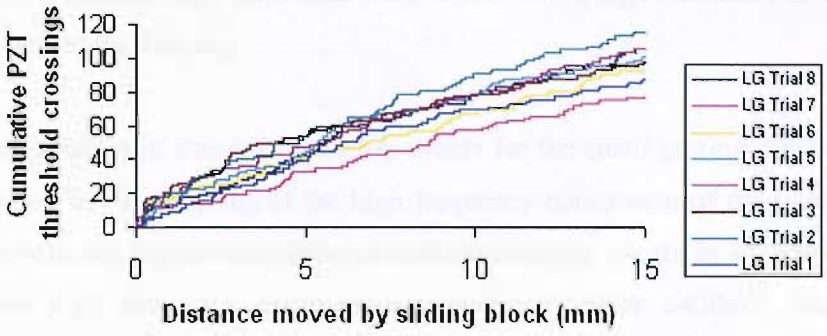

Figure 8.4: Indication of the repeatability of trials conducted on the large grating.

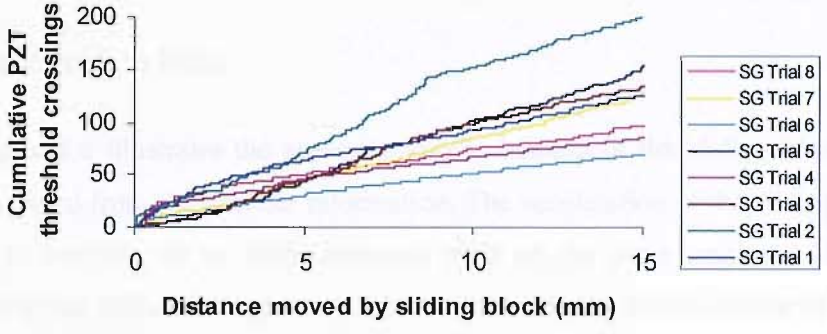

Figure 8.5: Indication of the repeatability of trials conducted on the small grating.

Figure 8.4 and Figure 8.5 show the cumulative PZT sensor threshold crossing events recorded over the distance travelled by the sliding block, for eight trials, from each of the two grating types, a fingertip force of 1N and a sensor signal threshold value of 400mV. The spread of the plots for the large grating show good repeatability between trials. The plots are linear, moving up in steps from the left of the graph to the right. This suggests that threshold crossing events occur in conjunction with the distance moved by the sliding block irrespective of the acceleration. However, the spread of the plots for the small grating, although they are also linear, show a large variation in threshold crossing events between trials. Trial 2 has 200 crossing events after the sliding block has travelled 15mm compared to 69 for trial 6, a 290% difference.

From visually inspecting the signals produced from trial 1 of the small and large gratings (Figure 8.3 (a) and (c)) it can be seen that all of the signals are constructed

from a low frequency high amplitude component, with a high frequency low amplitude signal Superimposed on top.

The variation in threshold crossing events for the small grating can be attributed to a variation in the sampling of the high frequency component of the signals. Where, the trials with the higher cumulative threshold crossing events in Figure 8.5, simply have more high frequency components crossing at either ±400mV (the sampling threshold). However, this is not the case with the large grating trials, where the high frequency component of the signals is regularly sampled in each of the trials.

8.9 Acceleration Data

Figure 8.6 illustrates the approximate acceleration of the sliding block for each trial, calculated from the encoder information. The acceleration of the sliding block can be seen to vary by up to 100% between trials on the same gratings. This can be attributed to the different weights required to overcome the initial stiction of the sliding block on the aluminium angle and the contact with the fingertip between trials.

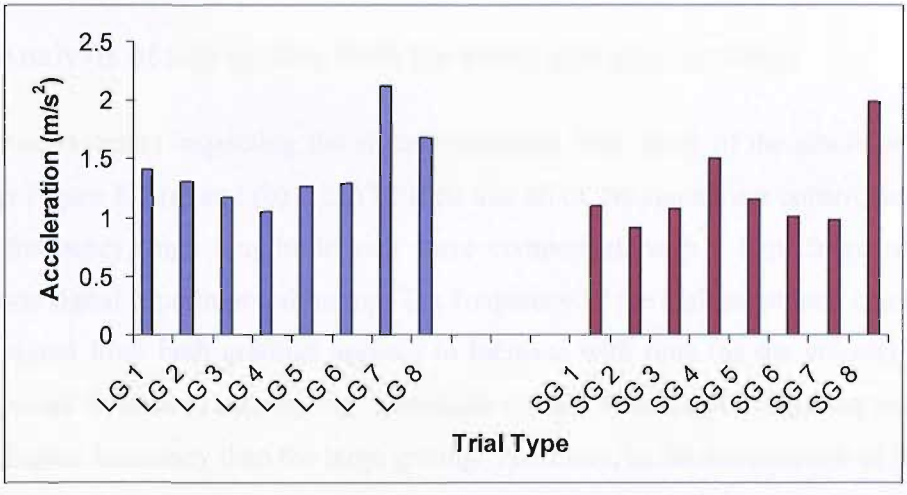

Figure 8.6: Average sliding block acceleration for each trial over the initial 190ms of slip.

8.9.1 Calculating the velocity at which slip is first detected

The velocity at which slip was initially detected was calculated by using the time taken to travel one full encoder count. The encoder count selected in each case corresponded to the time of the initial thresholded slip signal. At a threshold of 400mV,

slip was first detected after the sliding block had moved a distance of approximately 0.15mm (one encoder count) for the trials with the large grating and up to 0.45mm for the trials with the small grating. The velocity at which slip was detected varied between trials with a maximum velocity of $0.027ms^{-1}$ for both trials with a standard deviation of $0.009ms^{-1}$ and $0.01ms^{-1}$ for the large and small grating trials respectively. The variation in initial velocity can be attributed to the block overcoming stiction.

Trial	Velocity (ms^{-1})		Trial	(Velocity ms^{-1})
LG 1	0.024		SG 1	0.008
LG 2	0.013		SG 2	0.008
LG 3	0.006		SG 3	0.021
LG 4	0.023		SG 4	0.027
LG 5	0.008		SG 5	0.000
LG 6	0.023		SG 6	0.009
LG 7	0.027		SG 7	0.010
LG 8	0.007		SG 8	0.026

Table 8.4: Velocity at which slip was first detected.

8.10 Analysis of slip signals from the small and large gratings

From visually inspecting the signals produced from trial1 of the small and large gratings Figure 8.3 (a) and (b) it can be seen that all of the signals are constructed from a low frequency, high amplitude sine wave component, with a high frequency low amplitude signal superimposed on top. The frequency of the high amplitude component of the signal from both gratings appears to increase with time (as the velocity of the sliding block increases) and the high amplitude signals from the small grating appear to have a higher frequency than the large grating. Therefore, as the acceleration of the trial from the small grating is lower than the large grating ($1.1ms^{-1}$ compared to $1.4ms^{-1}$) then it appears as though the high amplitude signals are related to the resolution of the gratings. The pattern from the PZT signals is repeated in all 16 trials. This section uses several different analytical techniques to investigate the cause of the low frequency high amplitude, and high frequency low amplitude components of the signals.

8.10.1 Investigating the frequency content of the high amplitude signals

In order to asses the change in frequency of the high amplitude sine wave component of the slip signal from trial 1 of the two different gratings, the wavelength of eight sections from each of the trials were selected. The frequency was subsequently calculated using the time data from when the signal bisected the abscissa (i.e. f=1/t). The selected wavelengths are highlighted in Figure 8.3 (a) and (c) with the corresponding frequencies recorded in Table 8.5.

	Frequency (Hz)							
	f1	**f2**	**f3**	**f4**	**f5**	**f6**	**f7**	**f8**
Small grating trial 1	54	75	87	97	149	151	159	149
Large grating trial 1	53	81	95	120	93	91	99	102

Table 8.5: Frequencies calculated from individual wavelengths of selected high amplitude signals from trial 1 of the small and large grating.

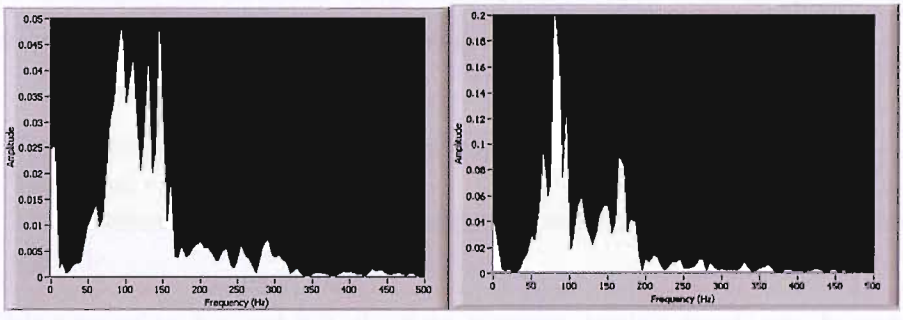

(a) (b)

Figure 8.7: Linear power spectrum FFT graphs of two separate trials. (a) Trial 1, small grating with a sliding block acceleration of 1.1 m/s^2 (b) Trial 1, large gratings with a sliding block acceleration of 1.4m/s^2.

Figure 8.7 shows linear power spectrum FFT graphs produced from trial 1 of the unprocessed PZT signals for the two different grating spacing's. The two graphs confirm the presence of the frequencies in the range of 50 – 120Hz and 50 – 160Hz for the small and large grating respectively. Extending the abscissa scale on each graph also revealed a lower amplitude high frequency component up to 1500Hz for each trial (although the graphs shown here have been truncated to 500Hz in order to display the low frequency components of the signal more clearly).

Power spectrum FFT graphs were also obtained from the seven remaining trials of each grating type. They all show a range of different peak frequencies, which have no obvious correlation to the grating type or the acceleration of the sliding block. It is also interesting to note that the amplitude of the frequency for the small gratings tail off around 300-350Hz compared to the large gratings, which tend to tail off around 200-250Hz depending on the trial. Higher frequency signals were also present in all trials up to approximately 1500Hz.

8.10.2 Theoretical frequencies induced by gratings from a single point contact

The lowest possible vibration frequency induced from an interaction between the fingertip and the grating would be from a single point contact. Therefore, if each grating were detected as the sliding block accelerated, producing a continuous waveform with decreasing wavelength (increase in frequency) then the theoretical frequencies from a given acceleration and grating spacing can be calculated.

To investigate the theoretical frequencies produced from a single point contact, if the wavelength was continuous, the following assumptions were made:

- The single point contact starts at the edge of the grating.
- The initial velocity is 0.
- The acceleration throughout the trial is constant (calculated from the encoder signal).

Using equation 8.1 and 8.2, the time between grating events can be calculated from the acceleration of the sliding block and the distance travelled. The frequency can then be calculated using equation 8.3.

$$t_n = \sqrt{\frac{2s_n}{a}} \qquad \text{Eqn 8.1}$$

$$s_n = n \times r \qquad \text{Eqn 8.2}$$

Where n is the number of grating events; r is the resolution of the grating (m); a is the sliding block acceleration (ms^{-2}) and t_n is the time taken to reach each grating (s) (as illustrated in Figure 8.8).

$$f_n = \frac{1}{dt_n} \qquad \text{Eqn 8.3}$$

$$dt_n = t_n - t_{n-1} \qquad \text{Eqn 8.4}$$

Where: $dt_n = t_n - t_{n-1}$

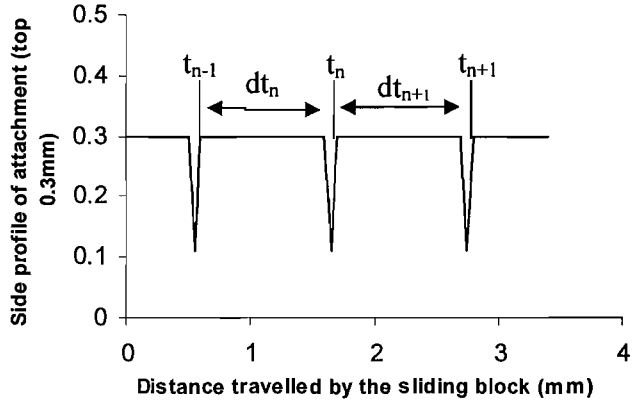

Figure 8.8: Model for calculating frequency from a single point contact (large grating).

Grating number	SG Trial 1 frequency (Hz)	LG trial 1 frequency (Hz)		Grating number	SG Trial 1 frequency (Hz)	LG trial 1 frequency (Hz)
1	30	25		18	253	212
2	73	61		19	260	218
3	95	80		20	267	224
4	113	94		21	274	229
5	128	107		22	281	235
6	142	119		23	287	240
7	154	129		24	294	
8	166	139		25	300	
9	176	148		26	306	
10	187	156		27	312	
11	196	164		28	318	

Grating number	SG Trial 1 frequency (Hz)	LG trial 1 frequency (Hz)		Grating number	SG Trial 1 frequency (Hz)	LG trial 1 frequency (Hz)
12	205	172		29	323	
13	214	179		30	329	
14	222	186		31	334	
15	231	193		32	340	
16	238	199		33	345	
17	246	206				

Table 8.6: Theoretical frequencies produced from a single point contact from trial 1 of the large and small gratings.

From Table 8.6 it can be seen that a single point contact would induce frequencies in the range of approximately 25Hz to 240Hz and 30Hz to 350Hz from trial 1 of the large and small gratings respectively. These frequencies are present in the FFT graphs shown in Figure 8.7, however, they are not the high amplitude sine wave component of the signals. Table 8.5 shows the small grating has large amplitude signals up to 160Hz whereas the large grating has large amplitude signals up to 120Hz. The high amplitude sine wave component of the signals is therefore not directly related to the grating gaps. It is believed that the component of the signal is caused by slip stick between the contacting surfaces caused by the deformation of the rubber cosmesis due to high shear forces, and can be attributed to the high coefficient of friction between the rubber and Perspex of 2.38 from the small grating and 2.55 from the large grating.

8.11 Investigation into the fundamental frequencies of vibration

8.11.1 ANSYS model of the fundamental frequencies of prototype fingertip 3.

The fundamental frequencies and modes of vibration of the prototype fingertip 3 were modelled in Autodesk Inventor 10™. This allowed the output frequency of the slip signals from a large and small grating surface to be compared to the modelled fundamental frequencies of the fingertip. There are several different ways which the constraints applied to the model could be interpreted, therefore, four models all with different potential constraints were analysed.

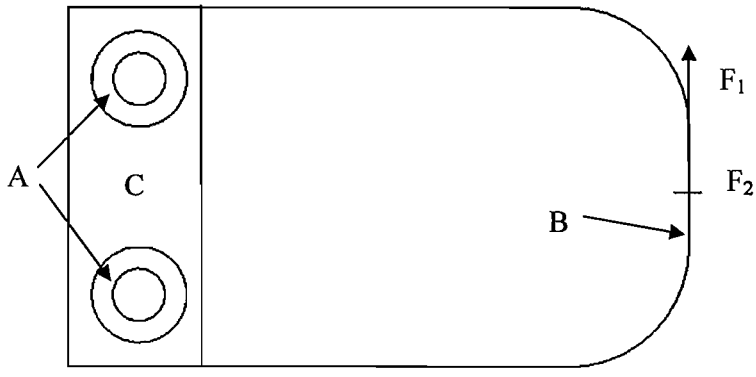

Figure 8.9: Model of prototype fingertip 3 showing the location of all constraints.

With reference to Figure 8.9 the following constraints and assumptions were made in this model for each of the models:

1. The thick-film sensors do not contribute to the substrate stiffness.

Model 1

2. The top bolt hole lines "A" are constrained in the X,Y and Z planes.
3. Force F_1 is 2.4N and is applied tangential to the end face of the fingertip (to replicate the force from the sliding block during slip F=μN).
4. Force F_2 has a magnitude of 1N and is applied to line "B" directed out of the paper.

Model 2

2. The top bolt hole lines "A" are constrained in the X,Y and Z planes.
3. Force F_2 has a magnitude of 1N and is applied to line "B" directed out of the paper.

Model 3

2. The top and bottom bolt hole lines "A" are constrained in the X,Y and Z planes.
3. Force F_1 is 2.4N and is applied tangential to the end face of the fingertip (to replicate the force from the sliding block during slip F=μN).
4. Force F_2 has a magnitude of 1N and is applied to line "B" directed out of the paper.

Model 4

2. Area "C" is constrained in the X,Y and Z planes.
3. Force F_1 is 2.4N and is applied tangential to the end face of the fingertip (to replicate the force from the sliding block during slip F=μN).
4. Force F_2 has a magnitude of 1N and is applied to line "B" directed out of the paper.

5. The area "C" on the underside of the fingertip is constrained in the X, Y and Z planes.

Material Properties

Young's Modulus = 1.903×10^5Mpa

Poisson's ratio = 0.305

	Frequency (Hz)		
Model number	**Mode 1**	**Mode 2**	**Mode 3**
1	2017	9416	12830
2	2017	9416	12830
3	2696	10085	15131
4	4009	12412	20790

Table 8.7: Predicted fundamental frequencies of prototype fingertip 3 from 4 models with different constraints.

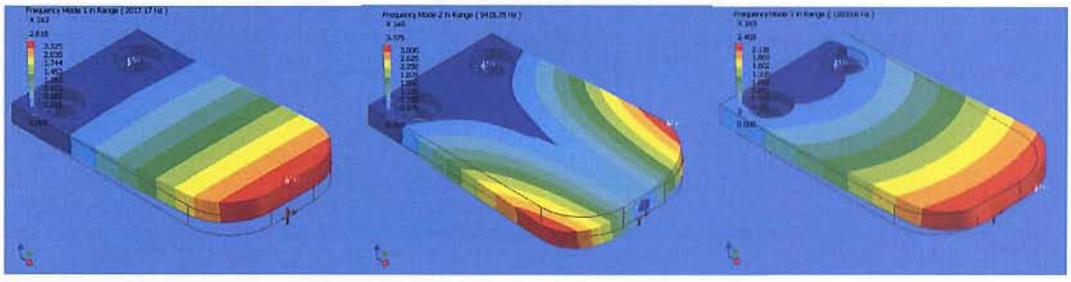

(a) Mode 1 (b) Mode 2 (c) Mode 3

Figure 8.10: Fundamental frequency modes for prototype fingertip 3

Figure 8.10 illustrates the 3 modes of vibration for the prototype fingertip 3. The scale of colours simply give an indication of the stress distribution caused by the fingertips vibration, however, this does not take into account the stress caused by the deformation of the fingertip. The results from the simulations show that the lowest fundamental frequency would come from Mode 1, with both models 1 and 2 predicting a frequency of 2kHz. This frequency is higher than the frequencies shown in the FFT signals produced from all of the trials from both gratings. This result would suggest that the fingertip is not being excited into a fundamental mode of vibration by the grating.

8.11.2 Tapped response of PZT sensor

In order to investigate the frequency response caused by an impulse force, from the PZT sensor, the fingertip was setup to apply a 1N force to the sliding block (replicating the conditions during the sliding trials). The top of the fingertip holder (Figure 6.8) was then lightly tapped and the output signal from the PZT sensor was recorded, using the same setup parameters listed in Table 8.1. This process was repeated and both signals were subsequently analysed using the FFT function in Labview™. Figure 8.11 shows a typical output signal and Figure 8.12 shows the frequency response. The FFT's from both trials showed a dominating frequency of approximately 2kHz. This is in agreement with the ANSYS models 1 and 2, which suggest the fingertip is vibrating in model of Figure 8.10. From this analysis and the FFT's it can be seen that during sliding the fingertip does not vibrate at any of its fundamental frequencies during the trial with two different gratings.

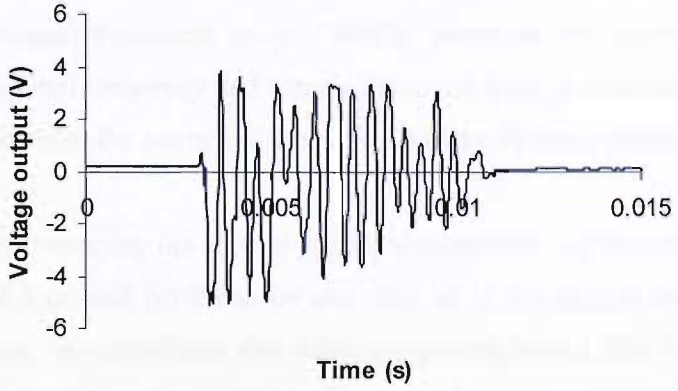

Figure 8.11: Tapped response from PZT sensor.

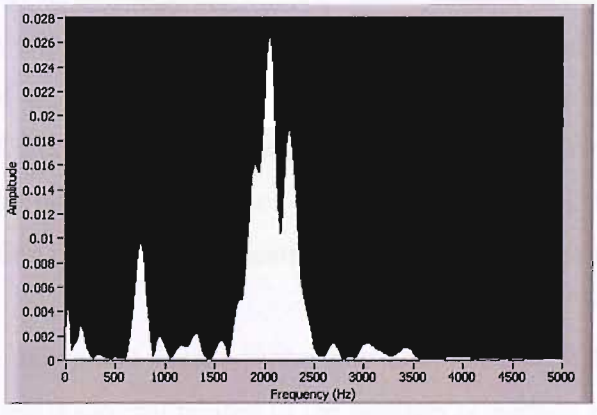

Figure 8.12: Power spectrum FFT of tapped response from the PZT sensor.

8.11.3 Discussion

An Otto Bock cosmetic glove designed for the Sensor Hand™ speed model has been successfully adhered to the prototype fingertip and used as the contacting surface to transmit slip signals to the PZT sensor. A search of the literature has revealed no reported work on the use of commercially available cosmesis covers, on slip sensors, for prosthetic hands. With a coefficient of friction between Perspex and rubber of approximately 2.38 from the small grating and 2.55 from the large grating slip was detected before the sliding block had slipped 0.6mm reaching a maximum velocity of $0.027ms^{-1}$.

An ANSYS analysis of prototype fingertip 3 showed that the lowest fundamental frequency of the fingertip was approximately 2kHz. The analysis was subsequently verified by using a force impulse test on the fingertip and analysing the frequency using the FFT function in Labview™. The FFT's taken from each of the trials on the two gratings show a frequency content up to 1500Hz, therefore the fingertip does not vibrate at its fundamental frequency and signals produced from the slip sensor are from a forced vibration between the contact of the rubber and the Perspex grating.

From visually inspecting the signals produced from trial 1 of the small and large gratings in Figure 8.3 (a) and (c) it can be seen that all of the signals are constructed from a low frequency, high amplitude sine wave component, with a high frequency low amplitude signal propagating on top. The high amplitude component of the frequency has been shown to be too low in frequency to be induced directly by the gratings or by a fundamental frequency of the fingertip. It is therefore believed that this component of the signal is caused by slip stick between the contacting surfaces and can be attributed to the high coefficient of friction between the rubber and Perspex of 2.38 from the small grating and 2.55 from the large grating. This is further supported by the lack of correlation between the peak frequencies of the trials for both grating types and the acceleration of the sliding block and is indicative of the random nature of slip stick.

The results have shown that using a rubber cosmesis to transmit the slip signals to the PZT sensor that signals directly related to the gratings or surface texture could not easily be identified and further analysis is required to determine if textures can be differentiated. However, it is clear that to automatically control a prosthesis using slip

detection the surface texture of the grasped object is not necessarily important so long as slip can be detected and differentiated from other erroneous inputs such as accidentally knocking into a table.

Figure 8.4 and Figure 8.5 show a linear relationship between the cumulative encoder count and cumulative piezoelectric sensor's threshold crossing events. The slip signal is, therefore, a measure of relative velocity between the object and finger surface. It can be processed to obtain an estimate of the relative distance that an object has slipped.

In order to accurately detect and compare the difference in texture of two surfaces (in this case the two grating sizes) the contact point or points on the fingertip should be the same for each material surface. Previous research has suggested using ridges to maximise the vibrations produced from a sliding object, however, the simplest and arguably most effective contact would be a cone shape protrusion. This would provide a single vibrating input similar to a stylaphone needle.

8.11.4 Conclusions

Given that an anthropomorphic prosthesis is covered by a cosmetic glove it is essential that any sensors will need to work with this covering. This sensor can detect slip repeatably, at a sliding object velocity of $0.027ms^{-1}$ with a fingertip force of 1N on two different Perspex gratings, and it can do this with a cosmesis material between the sensor and object surface. This research demonstrates for the first time that a thick-film piezoelectric slip sensor can operate with a cosmesis cover. The PZT sensor can therefore, potentially be used in conjunction with a cosmetic glove. The design of the glove, i.e. the texture, material properties and any predominant features are likely to impact on not only the PZT sensors ability to detect slip but also the possibility to detect an objects surface texture.

The slip signal is a measure of relative velocity between the object and finger surface and can be processed to obtain an estimate of the relative distance that an object has slipped.

Force impulse tests showed experimentally and theoretically that the lowest of the fingertips fundamental vibration modes has a frequency of approximately 2kHz. This frequency could therefore potentially be used to eliminate erroneous signals, for example bumping into a table, as the frequency content of all of the signals caused by slip from the rubber and Perspex interface was found to be limited up to 1500Hz.

Piezoelectric thick-film devices offer a cheap robust solution for a slip sensor for a prosthetic hand. Thick-film devices can be easily and cheaply mass produced and the module design approach of using a detachable fingertip means that faulty or damaged devices can easily be replaced.

Chapter 9 Conclusions and future work

9.1 Conclusions

9.1.1 Piezoelectric slip sensors

Thick-film piezoelectric slip sensors have been fabricated and tested on two different prototype fingertip designs. The results from prototype fingertip 2 have shown that with a coefficient of friction of 0.3 between the fingertip and grade p100 sandpaper that slip can be detected repeatably after a velocity of 0.025± 0.008ms^{-1} has been reached. Results from testing prototype fingertip 3 showed that slip could be successfully detected with a cosmesis material present between the sensor and two different Perspex gratings. With a coefficient of friction of approximately 2.4 a maximum velocity of 0.027ms^{-1} was reached before slip was detected. This research demonstrates for the first time that a thick-film piezoelectric sensor can be used to detect slip, and that it can continue to do this even when a cosmesis material is placed between the sensor and object surface. The PZT sensor can therefore, potentially be used in conjunction with a cosmetic glove.

This research has shown that for this type of slip sensor the slip signal produced from these experiments is a measure of the relative velocity between the object and finger surface and can be processed to obtain an estimate of the relative distance that an object has slipped.

This work demonstrates that piezoelectric thick-film devices are a viable solution for a slip sensor for a prosthetic hand. The thick-film fabrication method is an accurate and cheap method of mass producing these slip sensors and would be compatible with most of the current commercially available myoelectric prosthetics, with minimum redesign of the prosthesis. For example, the Touch Bionics iLimb Hand™ has a replaceable fingertip module, which could be replaced with a new module that incorporates a thick-film slip sensor, whilst the Otto Bock SensorHand Speed has a flat surface on the end of each of its three digits, which could accommodate a thick-film piezoelectric device.

9.1.2 The effects of multiple firings on stoichiometry and d_{33}

Thick-film piezoelectric devices fabricated from PZT-5H powder (Morgan Ceramics) with gold or silver/palladium electrodes as well as devices fabricated from PZT-Pz29 powder (Ferroperm) with gold and silver polymer electrodes, have been shown to retain their d_{33} sensitivity when fired up to 4 times at a peak temperature of 850°C. These results are consistent with XRF results, which show that there is no change in stoichiometry of a PZT-5H thick-film when it is fired 1 – 4 times at a peak temperature of 850°C. This demonstrates that it is possible to print piezoelectric thick-films at an earlier stage in the fabrication process (if a number of different devices are required to be fabricated on the same substrate), when conventionally it has been suggested that in order to retain their levels of sensitivity, piezoelectric thick-films should be processed at the latest possible stage.

The study also showed that firing PZT-Pz29 thick-film devices at a peak temperature of 950°C and then subsequently re-firing them at a lower temperature of 850°C produces devices with the same sensitivity as devices fired twice at 850°C. Hence, there is no advantage in processing devices at 950°C if they are going to be subjected to subsequent firings at 850°C. Therefore, if a number of different thick-film materials are required to be fabricated on a single substrate and need to be fired at 850°C, then there is no advantage of increased sensitivity whether the piezoelectric thick-film is printed first or last on the substrate. An example of the application of this is the prototype fingertips.

Re-firing devices at 950°C with gold top electrodes, which have previously been fired 3 times at 850°C reduces their sensitivity by approximately 20%. It is therefore recommended that devices fired at 850°C at least three times should not be subjected to a further firing cycle at 950°C, unless a reduction in sensitivity is acceptable. This discovery can help to make significant savings for the hybrids industry through the use of an optimal processing temperature.

It has also been shown that using silver polymer as the top electrode material of a piezoelectric thick-film device produces a d_{33} approximately 20% higher than similar devices fabricated with a glassy gold top electrode at the same peak temperature of 850°C.

9.1.3 Binderless piezoelectric paste

A piezoelectric paste without a binder material has been developed and used to successfully fabricate piezoelectric thick-film devices at peak processing temperatures of 150°C, 720°C, 820°C, 850°C and 950°C allowing the paste to be screen printed onto a variety of substrate materials. The paste material has been used to fabricate devices with significantly enhanced d_{33} coefficients, producing a 28% higher d_{33} than glassy thick-film devices processed at the same peak temperature of 950°C, (168pC/N compared to 131pC/N) and comparable d_{33} coefficients from devices when the binderless paste is processed at a lower peak temperature of 850°C (125pC/N). This is the first time a binderless piezoelectric paste has been successfully used to fabricate thick-film devices below 1000°C.

Devices processed at a peak temperature of 150°C produced an increase in sensitivity of 33% over polymer piezoelectric thick-films. However, this is still 50% lower than the values reported for conventional polymer materials such as PVDF.

All of the devices fabricated with the new paste were able to withstand electric fields 3-4 times higher than devices fabricated with conventional piezoelectric thick-film pastes produced with glass or polymer binder materials (14.4MVm^{-1} to over 17MVm^{-1} compared to 3.5 - 5 MVm^{-1}). The binderless paste showed good adhesion properties to 96% alumina substrates for all of the peak processing temperatures tested.

The increase in d_{33} sensitivity and the ability to withstand higher electrical field strengths means that the binderless paste can be used to enhance a number of existing devices fabricated with glass or polymer based binder materials, including: micro pumps, accelerometers, ultrasonic motors, and the slip sensor used in the prosthetic hand [109].

9.2 Future work

9.2.1 Piezoelectric slip sensors

Testing of prototype fingertips

There are a range of contact parameters which may vary during everyday object manipulation with a prosthesis. These parameters include: surface texture, coefficient of friction, object velocity before slip is detected and the effects of grip force. These parameters are likely to affect the output signal of the slip sensor. It is therefore recommended that these parameters are investigated.

If it proves possible to detect surface texture then the signals could potentially be used to feedback tactile information to the user, either through the peripheral nerves or through a vibrating actuator placed on the skin of the user. The surface texture is also likely to act with the coefficient of friction to produce a minimum required velocity for slip detection.

Knowing the effects of applied force on the slip signal would be beneficial, if signal damping or amplifying was to occur, in which case force information could be used to alter the gain of the electronic amplifier.

Sensor location

The work presented in this thesis concentrated on a slip sensor located in the fingertip of the prosthesis, However, there are a number of other viable locations for a slip sensor including the finger linkages of the Southampton Hand, where the vibrations will be amplified by an object gripped within the prosthesis. It is therefore recommended that these potential locations are investigated and compared to a fingertip slip sensor.

Processing the signal

The thresholding method used to analyse the data only uses a small amount of the information provided by the slip signal. It would therefore be interesting to look at other methods of obtaining more information from the data, for example using two or three simultaneous thresholds levels to allow the slip signals amplitude to be taken into consideration. Alternatively the FFT data could be analysed and used to indicate a change in frequency content of the signal and hence slip.

9.2.2 Piezoelectric thick-film processing

There is still a huge potential in the development of piezoelectric thick-films, with and without binder materials, to optimise certain characteristics for specific applications and manufacturing procedures. Suggested areas of future work include: investigating the effects of firing cycle times, cooling/heating rates and the stoichiometry of the PZT layer when fired a number of times at a peak temperature of 950°C. It is suggested that the investigation of the stoichiometry be carried out using an EDX technique instead of the XRF technique described in Chapter 4. This alternative technique can be used to penetrate a common depth within the film of around 5μm, which would allow a direct comparison of element activities to be made between samples of different thicknesses. EDX machines are also commonly attached to SEM's, and hence the surface of the samples can usually be closely examined with the same machine.

9.2.3 Binderless thick-film piezoelectric paste

As the piezoelectric thick-film could be removed more easily than conventional glassy or polymer based devices using the scratch test, it is recommended that further characterisation of the film is carried out. Particularly on devices processed at 720°C and below this temperature. The effects on the d_{33} coefficient of repeated vibration and cycling the devices with an electric voltage would be of particular interest for sensor and actuator applications to ensure the devices retain their characteristics, and the film does not delaminate.

High temperature applications

Thick-film devices with Curie temperatures higher than PZT-5H (>195°C) are desirable for a number of applications including downhole oil pipe pressure sensing. Glassy thick-film devices have been reported using several different materials including PZT-5A and bismuth titanate, with Curie temperatures of 350°C and 750°C respectively. However, one of the trade offs with using these active materials is the lower d_{33} than can be obtained from PZT-5H thick-films, which has been reported at 64pC/N for PZT-5A and 2.9pC/N for bismuth titanate [128]. Fabricating these devices with a binderless paste may significantly increase the obtainable d_{33} based on the results reported here with the binderless PZT-Pz29 paste. To achieve this would involve using a dielectric window material resistant to temperatures up to 750°C and testing its compatibility with the piezoelectric materials. Suggested windowing and top electrode materials are the commercially available dielectric (ESL 4986) and the gold electrode material (ESL 8836).

Low temperature devices

The results in Chapter 4 showed that replacing the gold top electrode (ESL 8836) with a silver polymer electrode (ESL 1110-S) increased the d_{33} of devices by approximately 20%. Therefore, it is considered advantageous to investigate the effects of using the same silver polymer electrode material to form the top and bottom electrodes of the binderless paste device processed at a peak temperature of 150°C. In order to maximise the d_{33} obtained from such devices. Investigating the elastic properties of devices would also be beneficial to determine the maximum strain the devices can withstand. This could be achieved by printing devices with polymer top and bottom electrodes onto flexible substrates[108,129,130].

Capacitive structure for binderless pastes

A re-design of the test pattern used for the testing of the binderless paste is required to maximise the space available for printing the active layer of a device on a substrate of a fixed area. The minimum number of layers that can be used to form an encapsulated PZT layer in a capacitive type structure is four, (bottom electrode,

Piezoelectric, dielectric window, and a top electrode). This can be achieved if the area of the bottom electrode was smaller than the area of the PZT film, and if the area of the top electrode was larger than the PZT film. Then only a small dielectric separation layer would be required to electrically isolate the bottom electrode track from the top electrode. This type of design would be more useful when substrate space is an issue, for example in MEMS applications.

9.2.4 Replicating and measuring slip

Chapter 6 described the successful design and fabrication of three prototype fingertips, novel slip replication apparatus and software to allow slip signals to be collected and analysed. The results from experimentation showed that the slip replication apparatus worked well. However, the stiction caused between the nylon screws and the aluminium base was high and somewhat variable, causing the acceleration experienced between trials to differ. The stiction could be reduced by using a linear bearing attached to the horizontal or vertical face of the angle bracket, supporting the sliding block. To control the slip more repeatable it may also be advantageous to use a computer controlled motor to pull the sliding block, instead of the hanging mass system employed in this thesis.

References

[1] D. H. Plettenburg, *Upper extremity prosthetics current status and evaluation*, 1 edition, VSSD, 2006, ISBN 10 90-71301-75-3

[2] http://biomed.brown.edu/courses/BI108/BI108_2003_Groups/Hand_Prosthetics/history.html (Accessed on 18/9/2007).

[3] Bowers R. Technology in the human hand. In Motion 12[6], 40-47. 2002. Ref Type: Magazine Article

[4] http://www.amputeeresource.org/Changing%20Role%20of%20the%20Amputee.htm (Accessed on 18/9/2007).

[5] http://www.ispo.ca/about_ispo.html (Accessed on 18/9/2007).

[6] http://www.defenselink.mil/news/Feb2006/20060208_4146.html (Accessed on 21/2/2007).

[7] http://www.danishtechnology.dk/robot/20163 (Accessed on 4/9/2007).

[8] http://www.physicstoday.org/vol-59/iss-9/pdf/vol59no9p24_25.pdf (Accessed on 4/9/2007).

[9] http://www.touchbionics.com/news2.php?section=8&newsid=1&site=/professionals.php (Accessed on 3/9/2007).

[10] http://www.ottobock.com/cps/rde/xchg/ob_com_en/hs.xsl/3652.html (Accessed on 31/8/2007).

[11] http://www.utaharm.com/tds.htm#top (Accessed on 3/9/2007).

[12] http://www.vasi.on.ca/prosthetic/over1.htm (Accessed on 3/9/2007).

[13] P. H. Chappell, J. M. Nightingale, P. J. Kyberd, M. Barkhordar. "Control of a single degree of freedom artificial hand". *Journal of Biomedical Engineering*, 1987, 9(3), pp.273-277.

[14] J. M. Nightingale. "Microprocessor control of an artificial arm". *Journal of Microcomputer Applications*, 1985, 8(2), pp.167-173.

[15] I. D. Swain, J. M. Nightingale. "An adaptive control system for a complete hand/arm prosthesis". *Journal of Biomedical Engineering*, 1980, 2(3), pp.163-167.

[16] P. J. Kyberd, C. Light, P. H. Chappell, J. M. Nightingale, D. Whatley, M. Evans. "The design of anthropomorphic prosthetic hands: a study of the Southampton Hand". *Robotica*, 2001, 19, pp.593-600.

[17] P. J. Kyberd, O. E. Holland, P. H. Chappell, S. Smith, R. Tregidgo, P. J. Bagwell, M. Snaith. "MARCUS: a two degree of freedom hand prosthesis with hierarchical

grip control". *IEEE Transactions on Rehabilitation Engineering*, 1995, 3(1), pp.70-76.

[18] P. J. Kyberd, P. H. Chappell. "Characterization of an optical and acoustic touch and slip sensor for autonomous manipulation". *Measurement Science & Technology*, 1992, 3(10), pp.969-975.

[19] P. J. Kyberd, P. H. Chappell. "A force sensor for automatic manipulation based on the Hall effect". *Measurement Science & Technology*, 1993, 4(3), pp.281-287.

[20] P. J. Kyberd, P. H. Chappell. "Object-slip detection during manipulation using a derived force vector". *Mechatronics*, 1992, 2(1), pp.1-13.

[21] P. H. Chappell, J. A. Elliott. "Contact force sensor for artificial hands with a digital interface for a controller". *Measurement Science & Technology*, 2003, 14(8), pp.1275-1279.

[22] P. J. Kyberd, P. H. Chappell. "Characterization of an optical and acoustic touch and slip sensor for autonomous manipulation". *Engineering Optics*, 1993, 6(1), pp.17-23.

[23] C. M. Light, P. H. Chappell. "Development of a lightweight and adaptable multiple-axis hand prosthesis". *Medical Engineering and Physics*, 2000, 22(10), pp.679-684.

[24] C. M. Light. *An intellegent hand prosthesis and evaluation of pathological and prosthetic hand function* University of Southampton:PhD. 2000.

[25] C. M. Light, P. H. Chappell, P. J. Kyberd. "Establishing a standardized clinical assessment tool of pathologic and prosthetic hand function: Normative data, reliability, and validity". *Archives of Physical Medicine and Rehabilitation*, 2002, 83(6), pp.776-783.

[26] N. Dechev, W. L. Cleghorn, S. Naumann. "Multiple finger, passive adaptive grasp prosthetic hand". *Mechanism and machine theory*, 2001, 36(10), pp.1157-1173.

[27] N. Dechev, W. L. Cleghorn, S. Naumann. "Thumb design of an experimental prosthetic hand". in Proceedings of the 2nd international symposium on robotics and automation, 2000, pp. 7-12.

[28] N. Deechev, W. L. Cleghorn, S. Naumann. "Multi-segmented finger design of an experimental prosthetic hand". in Proceedings of the sixth national applied mechanisms and robotics conferenceCincinnati, OH pp. 99-033-01-99-033-08.

[29] http://www.cyberhand.org/ (Accessed on 3/9/2007).

[30] M. C. Carrozza, B. Massa, S. Micera, R. Lazzarini, M. Zecca, P. Dario. "The development of a novel prosthetic hand - Ongoing research and preliminary results". *IEEE/ASME Transactions on Mechatronics*, 2002, 7(2), pp.108-114.

[31] M. C. Carrozza, S. Micera, B. Massa, M. Zecca, R. Lazzarini, N. Canelli, P. Dario. "The development of a novel biomechatronic hand - Ongoing research and preliminary results". in *IEEE/ASME International Conference on Advanced Intelligent Mechatronics, Jul 8-12 2001* pp. 249-254.

[32] M. C. Carrozza, G. Cappiello, E. Cavallaro, S. Micera, F. Vecchl, P. Dario. "Design and control of an underactuated cybernetic artificial hand". in *Proceedings of the Sixth Biannual World Automation Congress, Robotics: Trends, Principles, and Applications, Jun 28-Jul 1 2004,* pp. 111-116.

[33] M. C. Carrozza, F. Vecchi, F. Sebastiani, G. Cappiello, S. Roccella, M. Zecca, R. Lazzarini, P. Dario. "Experimental analysis of an innovative prosthetic hand with proprioceptive sensors". *IEEE International Conference on Robotics and Automation, 2003,* pp. 2230-2235.

[34] B. Massa, S. Roccella, M. C. Carrozza, P. Dario. "Design and development of an underactuated prosthetic hand". *in IEEE International Conference on Robotics and Automation, 2002,* pp. 3374-3379.

[35] L. Zollo, S. Roccella, R. Tucci, B. Siciliano, E. Guglielmelli, M. C. Carrozza, P. Dario. "Biomechatronic design and control of an anthropomorphic artificial hand for prosthetics and robotic applications". in *EMBS International Conference on Biomedical Robotics and Biomechatronics, 20-22 Feb. 2006* pp. 6.

[36] M. C. Carrozza, C. Suppo, F. Sebastiani, B. Massa, F. Vecchi, R. Lazzarini, M. R. Cutkosky, P. Dario. "The SPRING Hand: Development of a Self-Adaptive Prosthesis for Restoring Natural Grasping". *Autonomous Robots*, 2004, 16(2), pp.125-141.

[37] D. S. Childress. "Historical aspects of powered limb prosthesis". *Clinical prosthetics and orthotics*, 1985, 9, pp.2-13.

[38] H. R. Nicholls, *Advanved tactile sensing for robotics*, World Scientific Publishing Co. Pte. Ltd, 1992,

[39] P. Dario, R. Lazzarini, R. Magni, S. R. Oh. "Integrated miniature fingertip sensor". in *Proceedings of the International Symposium on Micromechatronics and Human Science, Oct 2-4 1996* pp. 91-97.

[40] A. Mingrino, A. Bucci, R. Magni, P. Dario. "Slippage control in hand prostheses by sensing grasping forces and sliding motion". in *Proceedings of the IEEE/RSJ/GI International Conference on Intelligent Robots and Systems. Part 3 (of 3), Sep 12-16 1994,* pp. 1803-1809.

[41] M. R. Tremblay, M. R. Cutkosky. "Estimating friction using incident slip sensing during a manipulation task". in *Proceedings of the IEEE International Conference on Robotics and Automation, May 2-6 1993,* pp. 429-434.

[42] P. Ueberschlag. "PVDF piezoelectric polymer". *Sensor review*, 2001, 21(2), pp.118-125.

[43] R. D. Howe, M. R. Cutkosky. "Sensing skin acceleration for slip and texture perception". in *IEEE International Conference on Robotics and Automation, May 14-19 1989,* pp. 145-150.

[44] L. A. Jones, S. J. Lederman, *Human hand function*, Oxford university press, 2006, ISBN 0-19-517315-5

[45] L. Beccai, S. Roccella, A. Arena, F. Valvo, P. Valdastri, A. Menciassi, M. C. Carrozza, P. Dario. "Design and fabrication of a hybrid silicon three-axial force sensor for biomechanical applications". *Sensors and Actuators A: Physical*, 2005, 120(2), pp.370-382.

[46] C. M. Oddo, P. Valdastri, L. Beccai, S. Roccella, M. C. Carrozza, P. Dario. "Investigation on calibration methods for multi-axis, linear and redundant force sensors". *Measurement Science & Technology*, 2007, 18(3), pp.623-631.

[47] P. Dario, M. C. Carrozza, L. Beccai, C. Laschi, B. Mazzolai, A. Menciassi, S. Micera. "Design, fabrication and applications of biomimetic sensors in biorobotics". *in IEEE International Conference on Information Acquisition, 2005,* pp. 4.

[48] B. B. Edin, L. Beccai, L. Ascari, S. Roccella, J. J. Cabibihan, M. C. Carrozza. "Bio-inspired approach for the design and characterization of a tactile sensory system for a cybernetic prosthetic hand".*Robotics and Automation, 2006. ICRA 2006. Proceedings 2006 IEEE International Conference on* pp. 1354-1358.

[49] Puchhammer G. The tactile slip sensor: intergration of a miniturized sensory device on an myoelectric hand. Orthopädie-Technik Quarterly, English edition . 2000. Magazine Article

[50] W. Winkler, W. Bierwirth. "The use of a gliding detector for the control of prothseses-hand".*Proceedings of the seventh world congress of ISPO*Chicargo, Illinois USA 28 Jun 1992, pp. 188.

[51] B. Hudgins, P. Parker, R. N. Scott. "A new strategy for multifunction myoelectric control". *IEEE Transactions on Biomedical Engineering*, 1993, 40(1), pp.82-94.

[52] C. M. Light, P. H. Chappell, B. Hudgins, K. Engelhart. "Intelligent multifunction myoelectric control of hand prostheses". *Journal of Medical Engineering and Technology*, 2002, 26(4), pp.139-146.

[53] R. A. Normann, D. McDonnall, G. A. Clark, R. B. Stein, A. Branner. "Physiological activation of the hind limb muscles of the anesthetized cat using the Utah slanted electrode array". in *Proceedings of the International Joint Conference on Neural Networks, 31 July-4 Aug. 2005,* pp. 3103-3108.

[54] K. Horch, G. Dhillon. "Towards a neuroprosthetic arm". in *Proceedings of the IEEE/RAS-EMBS International Conference on Biomedical Robotics and Biomechatronics, Feb 20-22 2006,* pp. 1125-1128.

[55] M. Gasson, B. Hutt, I. Goodhew, P. Kyberd, K. Warwick. "Invasive neural prosthesis for neural signal detection and nerve stimulation". *International Journal of Adaptive Control and Signal Processing*, 2005, 19(5), pp.365-375.

[56] P. J. Kyberd, M. Evans, S. te Winkell. "An intelligent anthropomorphic hand with automatic grasp". *Robotica*, 1998, 16, pp.531-536.

[57] G. S. Dhillon, K. W. Horch. "Direct neural sensory feedback and control of a prosthetic arm". *IEEE Transactions on Neural Systems and Rehabilitation Engineering*, 2005, 13(4), pp.468-472.

[58] P. H. Chappell, A. Cranny, D. P. J. Cotton, N. M. White, S. P. Beeby. "Sensory motor systems of artificial and natural hands". *International Journal of Surgery,* In Press.

[59] M. M. Lowery, R. F. Weir, T. A. kuiken. "Simulation of intramuscular EMG signals detected using implantable myoelectric sensors (IMES)". *IEEE Transactions on Biomedical Engineering*, 2006, 53(10), pp.1926-1933.

[60] A. D. Glenn, R. T. Philip, A. K. Douglas, W. Richard. "An Implantable Myoelectric Sensor Based Prosthesis Control System". in *28th Annual International Conference of the IEEE Engineering in Medicine and Biology Society, 2006,* pp. 2970-2973.

[61] M. M. Lowery, R. F. Weir, T. A. kuiken. "Simulation of intramuscular EMG signals detected using implantable myoelectric sensors (IMES)". *IEEE Transactions on Biomedical Engineering*, 2006, 53(10), pp.1926-1933.

[62] R. F. Weir, P. R. Troyk, G. DeMichele, D. Kerns. "Technical Details of the Implantable Myoelectric Sensor (IMES) System for Multifunction Prosthesis Control". *in IEEE-EMBS. 27th Annual International Conference of the Engineering in Medicine and Biology Society, 2005,* pp. 7337-7340.

[63] R. F. Weir, P. R. Troyk, G. DeMichele, T. Kuiken. "Implantable myoelectric sensors (IMES) for upper-extremity prosthesis control- preliminary work". in *Proceedings of the 25th Annual International Conference of the IEEE Engineering in Medicine and Biology Society, 2003,* pp. 1562-1565.

[64] S. V. Notley, R. Turk, J. H. Burridge, G. Cosendai, A. M. Ripley. "Sensors for open loop control of reaching and grasping using the BION microstimulators".

[65] M. C. Carrozza, A. Persichetti, C. Laschi, F. Vecchi, P. Vacalebri, V. Tamburrelli, R. Lazzarini, P. Dario. "A novel wearable foot interface for controlling robotic hands". in *IEEE/RSJ International Conference on Intelligent Robots and Systems, 2-6 Aug. 2005,* pp. 2010-2015.

[66] M. C. Carrozza, P. Dario, F. Vecchi, S. Roccella, M. Zecca, F. Sebastiani. "The Cyberhand: on the design of a cybernetic prosthetic hand intended to be interfaced to the peripheral nervous system". in *Proceedings IEEE/RSJ International Conference on Intelligent Robots and Systems, 27-31 Oct. 2003,* pp. 2642-2647.

[67] T. A. kuiken, D. S. Childress, W. Z. Rymer. "The hyper-reinnervation of rat skeletal muscle". *Brain Surgery*, 1995, (676), pp.113-123.

[68] K. L. Moore, A. F. Dalley, *Clinically Orientated Anatomy*, Fifth Edition edition, Lippincott Williams & Wilkins, 2006, ISBN 0-7817-3639-0

[69] T. A. kuiken, G. A. Dumanian, R. D. Lipschutz, L. A. Miller, K. A. Stubblefield. "The use of targeted muscle reinnervation for improved myoelectric prosthesis control in a bilateral shoulder disarticulation amputee". *Prosthetics and Orthotics International*, 2004, 28(3), pp.245-253.

[70] Z. Ping, M. M. Lowery, J. P. A. Dewald, T. A. kuiken. "Towards improved myoelectric prosthesis control: high density surface EMG recording after targeted muscle reinnervation". in *27th Annual International Conference of the IEEE Engineering in Medicine and Biology Society, 31 Aug.-3 Sept. 2005,* pp. 4.

[71] Z. Ping, M. M. Lowery, R. F. Weir, T. A. kuiken. "Elimination of ECG artifacts from myoelectric prosthesis control signals developed by targeted muscle reinnervation". in *27th Annual International Conference of the IEEE Engineering in Medicine and Biology Society, 31 Aug.-3 Sept. 2005* pp. 4.

[72] http://www.morganelectroceramics.com/access-pzbook.html (Accessed on 26/10/2006).

[73] D. C. William, *Materials science and engineering an introduction*, Sixth edition, WILEY, 2003, ISBN 0-471-22471-5

[74] B. Xu, D. White, J. Zesch, A. Rodkin, S. Buhler, J. Fitch, K. Littau. "Characteristics of lead zirconate titanate ferroelectric thick films from a screen-printing laser transfer method". *Applied physics letters*, 2005, 87(19), pp.192902.

[75] B. Xu, D. White, J. Zesch, A. Rodkin, S. Buhler, J. Fitch, K. Littau. "Thick piezoelectric films from laser transfer process". in *Ceramic Transactions, 106th Annual Meeting of the American Ceramic Society, Apr 18-21 2004,* pp. 245-258.

[76] H. Baudry. "Screen-printing piezoelectric devices". in *Sixth European Microelectronics Conference Proceedings. 3-5 June 1987,* pp. 456-463.

[77] H. Baudry. "Screen printing piezoelectric devices". *Hybrid Circuits*, 1987, (14), pp.71-74.

[78] K. Tanaka, T. Konishi, M. Ide, Z. Meng, S. Sugiyama. "Fabrication of microdevices using bulk ceramics of lead zirconate titanate". *Japanese Journal of Applied Physics, Part 1*, 2005, 44(9B), pp.7068-7071.

[79] J. M. Hale, J. R. White, R. Stephenson, F. Liu. "Development of piezoelectric paint thick-film vibration sensors". *Journal of Mechanical Engineering Science, Part C,* 2005, 219(1), pp.1-9.

[80] F. Levassort, T. Bove, E. Ringgaard, L. P. Tran-Huu-Hue, J. Holc, M. Lethiecq. "A complete range of tape-cast piezoelectric thick films for high frequency ultrasonic transducers". in *2003 IEEE Ultrasonics Symposium, 5-8 Oct. 2003* pp. 2003-2006.

[81] W. W. Wolny. "Piezoceramic thick films - Technology and applications. State of the art in Europe". in *12th IEEE International Symposium on Applications of Ferroelectrics, Jul 21-Aug 2 2000,* pp. 257-262.

[82] M. Es-Souni, M. Kuhnke, A. Piorra, C. H. Solterbeck. "Pyroelectric and piezoelectric properties of thick PZT films produced by a new sol-gel route". *Journal of the European Ceramic Society*, 2005, 25(12), pp.2499-2503.

[83] P. J. Holmes, R. G. Loasby, *Hand book of thick-film technology*, elect, 1976,

[84] T. Papakostas. *Polymer thick-film sensors and their intergration with silicon: a route to hybrid microsystems, PhD,* University of Southampton. 2000.

[85] R. N. Torah. *Optimisation of the piezoelectric properties of thick-film piezoceramic devices, PhD,* University of Southampton. 2004.

[86] http://www.ferro.com/ (Accessed on 26/10/2006).

[87] R. Torah, S. P. Beeby, N. M. White. "An improved thick-film piezoelectric material by powder blending and enhanced processing parameters". *IEEE Transactions on Ultrasonics, Ferroelectrics and Frequency Control*, 2005, 52(1), pp.10-16.

[88] R. N. Torah, S. P. Beeby, N. M. White. "Improving the piezoelectric properties of thick-film PZT: The influence of paste composition, powder milling process and electrode material". in *Sensors and Actuators, A: Physical, 2002* pp. 378-384.

[89] http://www.ferroperm-piezo.com/ (Accessed on 26/10/2006).

[90] http://www.dek.com/web.nsf/dek/stencils_emulsion (Accessed on 15/1/2007).

[91] http://www.mcicambridge.co.uk/ie4/sp.htm (Accessed on 15/1/2007).

[92] www.bopp.ch (Accessed 15/9/2007).

[93] M. D. Herbst, N. Y. Binghampton, M. Jacobs. "How to control variables when setting up a screen printer". *Hybrib Circuit Technology*, 1989.

[94] P. Dargie, R. Sion, J. Atkinson, N. White. "An investigation of the effect of poling conditions on the characteristics of screen-printed piezoceramics". *Microelectronics International*, 1998, 15(2), pp.6-10.

[95] P. Glynne-Jones, S. P. Beeby, P. Dargie, T. Papakostas, N. M. White. "Investigation into the effect of modified firing profiles on the piezoelectric properties of thick-film PZT layers on silicon". *Measurement Science and Technology*, 2000, 11(5), pp.526-531.

[96] M. Guangtian, A. J. Jaworski, T. Dyakowski, J. M. Hale, N. M. White. "Design and testing of a thick-film dual-modality sensor for composition measurements in heterogeneous mixtures". *Measurement Science & Technology*, 2005, 16(4), pp.942-954.

[97] http://www.take-control.demon.co.uk/ (Accessed on 26/10/2006).

[98] J. E. Brignell, N. M. White, A. W. J. Cranny. "Sensor applications of thick-film technology ". *IEE Proceedings, Part I: Solid-State and Electron Devices*, 1988, 135(4), pp.77-84.

[99] N. White, A. Cranny. "Design and fabrication of thick film sensors". *Hybrid Circuits*, 1987, (12), pp.32-35.

[100] http://www.webelements.com/ (Accessed on 15/1/2007).

[101] R. Jenkins, *An Introduction to X-ray Spectrometry*, 1974, ISBN *085501 035 5*

[102] R. Tertian, F. Claisse, *Principles of X-ray quantitative X-ray fluorescence analysis*, 1982, ISBN 0-855-709-0

[103] http://www.bruker-axs.de/fileadmin/user_upload/xrfintro/author.html (Accessed on 14/7/2007).

[104] White EW, Johnson GG. X-ray and absorbtion wavelengths and two theta_tables. *second edition.* 1970. ASTM data series DS370. wall chart.

[105] http://www.electroscience.com/ (Accessed on 26/10/2006).

[106] O'dwyer, *The theory of electrical conduction and breakdown in solid dielectrics*, 1973,

[107] http://www.trstechnologies.com/Materials/piezoceramics.php (Accessed on 2/11/2006).

[108] T. V. Papakostas, N. M. White. "Polymer thick-films on silicon: A route to hybrid microsystems". *IEEE Transactions on Components and Packaging Technologies*, 2001, 24(1), pp.67-75.

[109] R. N. Torah, S. P. Beeby, M. J. Tudor, N. M. White. "Thick-film piezoceramics and devices". *Journal of Electroceramics*, 2007.

[110] R. S. Johansson, A. B. Vallbo. "Tactile sensory coding in the glabrous skin of the human hand". *Trends in Neurosciences*, 1983, 6, pp.27-32.

[111] J. Carvill, *Mechanical engineer's data handbook*, Elsevier, 2005, ISBN 0750619600

[112] N. M. White. "An assessment of thick-film piezoresistors on insulated steel substrates". *Hybrid Circuits*, 1989, (20), pp.23-27.

[113] N. M. White, J. E. Brignell. "Excitation of thick-film resonant sensor structures". *IEE Proceedings: Science, Measurement and Technology*, 1995, 142(3), pp.244-248.

[114] T. Yan, B. E. Jones, R. T. Rakowski, M. J. Tudor, S. P. Beeby, N. M. White. "Development of metallic digital strain gauges". *Measurement and Control*, 2004, 37(7), pp.214-216.

[115] T. Yan, B. E. Jones, R. T. Rakowski, M. J. Tudor, S. P. Beeby, N. M. White. "Metallic resonant strain gauges with high overload capability". *Sensor review*, 2005, 25(2), pp.144-147.

[116] T. Yan, B. E. Jones, R. T. Rakowski, M. J. Tudor, S. P. Beeby, N. M. White. "Design and fabrication of thick-film PZT-metallic triple beam resonators". *Sensors and Actuators, A: Physical*, 2004, 115(2-3 SPEC ISS), pp.401-407.

[117] T. Yan, B. E. Jones, R. T. Rakowski, M. J. Tudor, S. P. Beeby, N. M. White. "Thick-film PZT-metallic triple beam resonator". *Electronics Letters*, 2003, 39(13), pp.982-983.

[118] M. Lahdenpera. "Thick-film hybrid applications on stainless steel baseplate". *Hybrid Circuits*, 1991, (26), pp.26-29.

[119] A. Cranny, D. P. J. Cotton, P. H. Chappell, S. P. Beeby, N. M. White. "Thick-film force, slip and temperature sensors for a prosthetic hand". *Measurement Science and Technology*, 2005, 16(4), pp.931-941.

[120] A. Cranny, D. P. J. Cotton, P. H. Chappell, S. P. Beeby, N. M. White. "Thick-film force and slip sensors for a prosthetic hand". *Sensors and Actuators, A: Physical*, 2005, 123-124, pp.162-171.

[121] www.mecmesin.com/ucm/home/product_view.asp?proID=101&range=39 (Accessed on 23/8/2006).

[122] S. W. Smith, *The scientists and engineer's guide to digital signal processing*, 2nd edition, California Technical Publishing, 1999, ISBN 0-96601-6-8

[123] P. Horowitz, W. Hill, *The art of electronics*, 2nd edition, Cambridge University Press, 2001, ISBN 0-521-375095-7

[124] D. G. Robertson, G. E. Caldwell, J. Hamill, G. Kamen, S. N. Whittlesey, *Research methods in biomechanics*, Human Kinetics, 2004, ISBN 0-7360-3966-X

[125] http://www.noraxon.com/products/sensors/preampwires.php3 (Accessed on 23/8/2007).

[126] Otto Bock. MYOBOCK Arm Components. Catalogue, 2005.

[127] http://www.school-for-champions.com/science/friction_coefficient.htm (Accessed on 10/12/2007 A.D.).

[128] S. P. Beeby, R. N. Torah, N. Grabham, M. J. Tudor, N. M. White. "Thick-film piezoelectric materials for high temperature applications". *Ferroelectrics*, 2005, 313, pp.63-69.

[129] T. Papakostas. *Polymer thick-film sensors and their intergration with silicon: a route to hybrid microsystems* University of Southampton:PhD. 2000.

[130] T. V. Papakostas, N. M. White. "Influence of substrate on the gauge factor of polymer thick-film resistors". *Journal of physics D: applied physics*, 2000, 33(14), pp.73-75.

Appendix A: Publications

A1: Journal Papers

D. P. J. Cotton, A. Cranny, N. M. White, P. H. Chappell "A new binderless thick-film piezoelectric paste". *Journal of Materials Science: Materials in Electronics* <IN PRESS>

D. P. J. Cotton, A. Cranny, N. M. White, P. H. Chappell, S. P. Beeby, "A novel thick-film piezoelectric slip sensor for a prosthetic hand". *IEEE Sensors: Special Issue on Intelligent Sensors*, 2007, 7(5) pp. 752-761.

D. P. J. Cotton, A. Cranny, N. M. White, P. H. Chappell, S. P. Beeby "Control Strategies for a multiple degree of freedom prosthetic hand". *Measurement + Control The Journal of the Institute of Measurement and Control*, 2007, 40 pp. 24-27.

P. H. Chappell, A. Cranny, D. P. J. Cotton, N. M. White, S. P. Beeby "Sensory motor systems of artificial and natural hands". *International Journal of Surgery*. <IN PRESS>

A. Cranny, D. P. J. Cotton, P. H. Chappell, S. P. Beeby, N. M. White, "Thick-film force, slip and temperature sensors for a prosthetic hand". *Measurement Science and Technology*, 2005, 16 pp. 931-941.

A. Cranny, D. P. J. Cotton, P. H. Chappell, S. P. Beeby, N. M. White, "Thick-film force and slip sensors for a prosthetic hand". *Sensors and Actuators A: Physical*, 2005, pp. 162-171.

A2: Refereed Conference Proceedings

D. P. J. Cotton, A. Cranny, P. H. Chappell, N. M. White, "Thick-film piezoelectric slip sensors for automatic grip control in prosthetic hands". In *12th World Congress of the International Society for Prosthetics and Orthotics,* Vancouver, Canada, July 29 – August 3, 2007 pp. 83.

D. P. J. Cotton, A. Cranny, P. H. Chappell, N. M. White, S. P. Beeby, "Control strategies for a multiple degree of freedom prosthetic hand". In *Proceedings of UKACC Control 2006 Mini Symposia*, Glasgow, 2006, pp. 213-218.

D. P. J. Cotton, A. Cranny, P. H. Chappell, N. M. White, S. P. Beeby, "Thick-film piezoceramic "slip sensors" for a multifunctional prosthetic hand". In *Proceedings of MEC' 05, Intergrating prosthetics and medicine*, University of New Bruswick, Canada, 2005.

A. Cranny, D. P. J. Cotton, P. H. Chappell, N. M. White, "The use of design software in biomechanical engineering; the design of a force sensitive, single degree of freedom digit for a myoelectric prosthetic hand". In *Proceedings of Institute of Physics and Engineering in Medicine, Annual Scientific Meeting*, Glasgow, 2005, pp. 31.

D. P. J. Cotton, A. Cranny, N. M. White, P. H. Chappell, S. P. Beeby, "Design and development of integrated thick-film sensors for prosthetic hands". In *Proceedings of 7th Biennial ASME Conference Engineering Systems Design and Analysis*, Manchester, 2004, pp. 1-17, UK.

A. Cranny, D. P. J. Cotton, P. H. Chappell, N. M. White, "Thick film force and slip sensors for a prosthetic hand". In *Proceedings of EuroSensors 18,* Rome, 2004, pp. (C6.2),

A3: Non-refereed Conference Proceedings

D. P. J. Cotton, A. Cranny, N. M. White, P. H. Chappell, "Slip sensors for a prosthetic hand", *Postgraduate Research Showcase,* 2007, March 22nd, Southampton,

D. P. J. Cotton, A. Cranny, N. M. White, P. H. Chappell, "A thick-film piezoelectric slip sensor for a prosthetic hand". in *3rd Life Science Interface conference,* 2007, 15th March. Southampton.

D. P. J. Cotton, A. Cranny, N. M. White, P. H. Chappell, S. P. Beeby, "Finger-tip force, slip and temperature sensors for prosthetic hands". in *International Society of Prosthetics and Orthotics (ISPO) Trent Prosthetic Symposium*, 2005. 23-25 May, Nottingham, UK.

Appendix B: Labview™ Program

In order to collect data from the piezoelectric sensor and the motor encoder a Labview™ virtual instrument (VI) was created. The VI consists of three separate sub VI's, which are used for different tasks. One sub VI is used to collect the data, another to trim down the collected data and the third to produce FFT's of the piezoelectric sensors output. All of the data from each program is saved in a format compatible with Microsoft Excel. Figure B.0.1 illustrates the front panel of the VI. The top three buttons each activate one of the three sub VI's, the "Stop VI" button stops the VI and the "Exit Labview" button stops the VI and closes Labview.

Figure B.0.1: Program applications menu.

Figure B.0.2 illustrates the block diagram used to operate the VI and activate the sub VI's. The block diagram consists of a case structure within a while loop. The while loop is used to run the program continuously and the case structure is used to determine which of the three sub VI's is opened or whether the program is stopped or Labview is exited. When the VI is initially activated an input of -1 is entered into a shift register, this activates the case structure shown Figure B.0.3, and the applications menu in Figure B.0.1 is displayed. Each of the buttons on the front panel corresponds to a number and when a button is pressed the number is passed through the search 1D Array and into the shift register. The number is then input back into the case structure and the

content of the case structure is changed to one of those illustrated in Figure B.0.2 and Figure B.0.3-B.0.7.

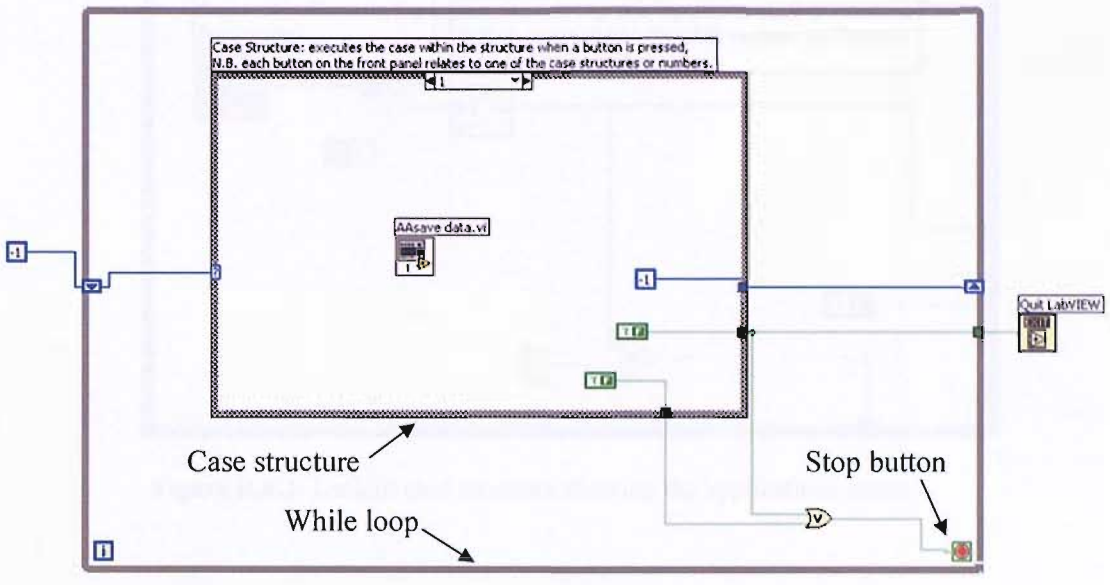

Figure B.0.2: Block diagram of program array VI showing case structure 1.

The -1 box on the right hand side of each case structure (with the exception of the -1 case structure) returns the program to the applications menu once the sub VI within the case structure has been stopped.

The little box with a circle in it, in the bottom right hand corner of the while loop is a stop button, which stops the program array VI if either of the two cases, (boxes marked "T F" in the bottom right hand side of the case structure) within the one of the case structures is true. If the top true or false button is set to true then the stop button is activated as well as the quit Labview sub VI, which closes the whole Labview program.

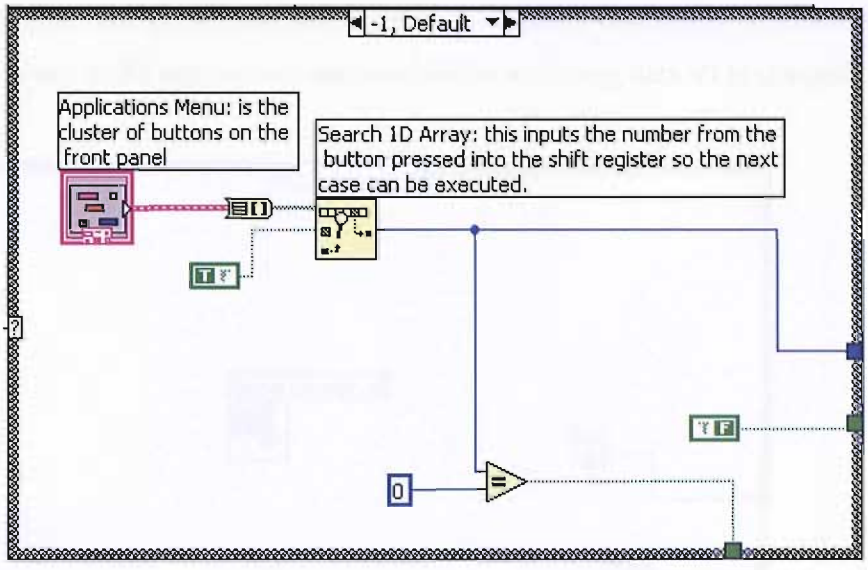

Figure B.0.3: Default case structure showing the applications menu.

Figure B.0.2 also shows an initial input into the while loop via a shift register, (left hand box outside the while loop marked with -1) this initial input is a -1 and activates the program applications menu. This is done by passing a number through the 1D search array and into the shift register (small arrow pointing upwards on the left hand side of the while loop in Figure B.0.2), which executes the -1 case structure.

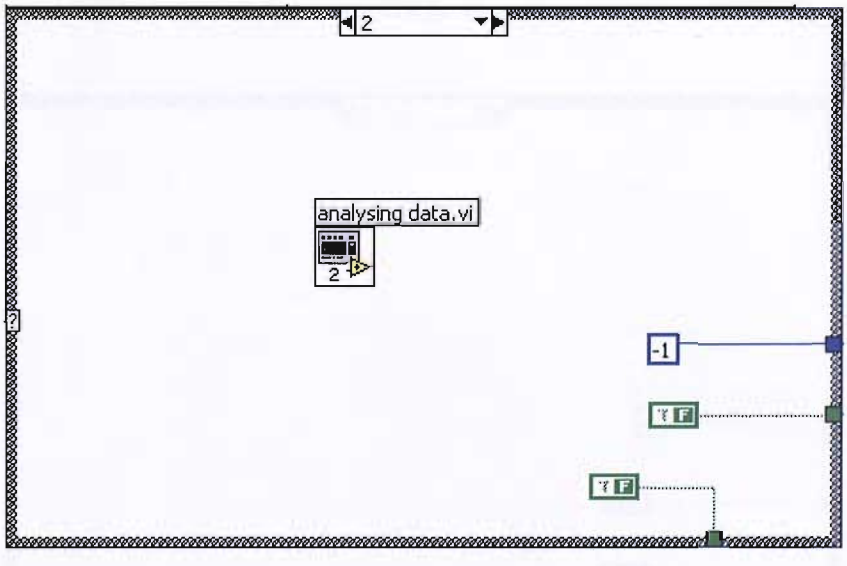

Figure B.0.4: Case structure 2, which activates the analysing data VI.

The analysing data VI shown in Figure B.0.4 is activated when the analyse data button is pressed on the applications menu. N.B. both of the true or false buttons (in the

right hand corner) are set to false and the box above them contains a -1 which means the VI will return to the applications menu when the analysing data VI is stopped.

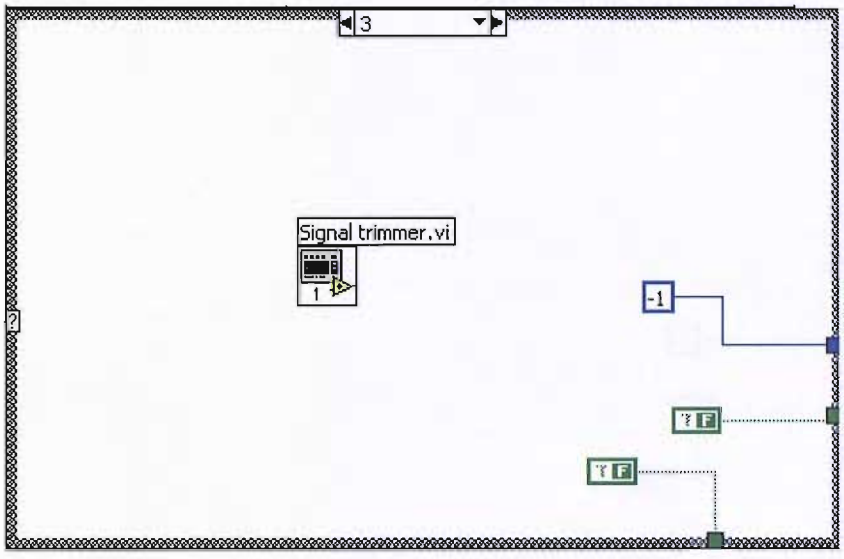

Figure B.0.5: Case structure 3, which activates the signal trimmer VI.

The signal trimmer VI, shown in Figure B.0.5, is activated when the trim signal button is pressed on the applications menu. N.B. both of the true or false buttons (in the right hand corner) are set to false and the box above them contains a -1 which means the VI will return to the applications menu when the analysing data VI is stopped.

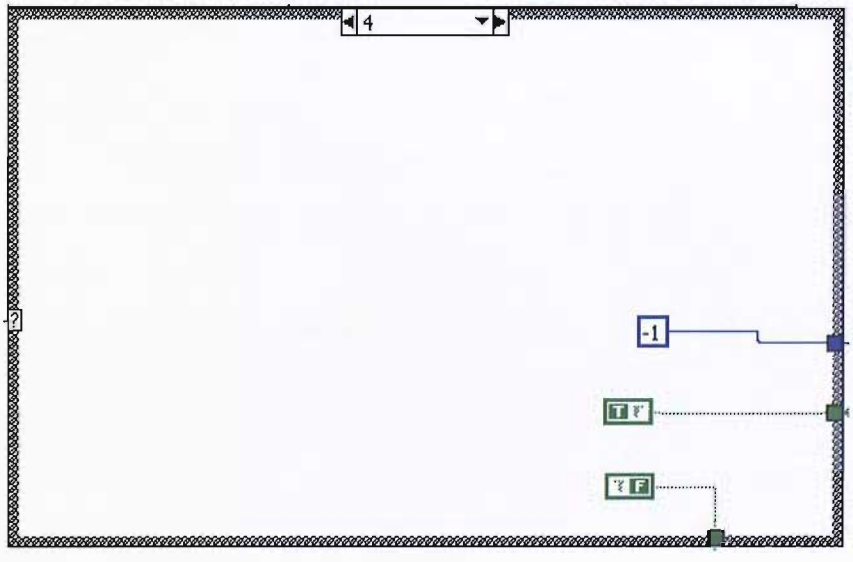

Figure B.0.6: Case structure 4, which stops the VI and exits Labview™.

Figure B.0.6 shows the top "true or false" button to be set to true, (cf. Figure B.0.2) this stops the VI and also exits Labview™.

Figure B.0.7: Case structure 0, which stops the program array but does not exit Labview.

Figure B.0.7 shows the bottom "true or false" button to be set to true, this stops the VI (cf. Figure B.0.2).

AAsave data VI

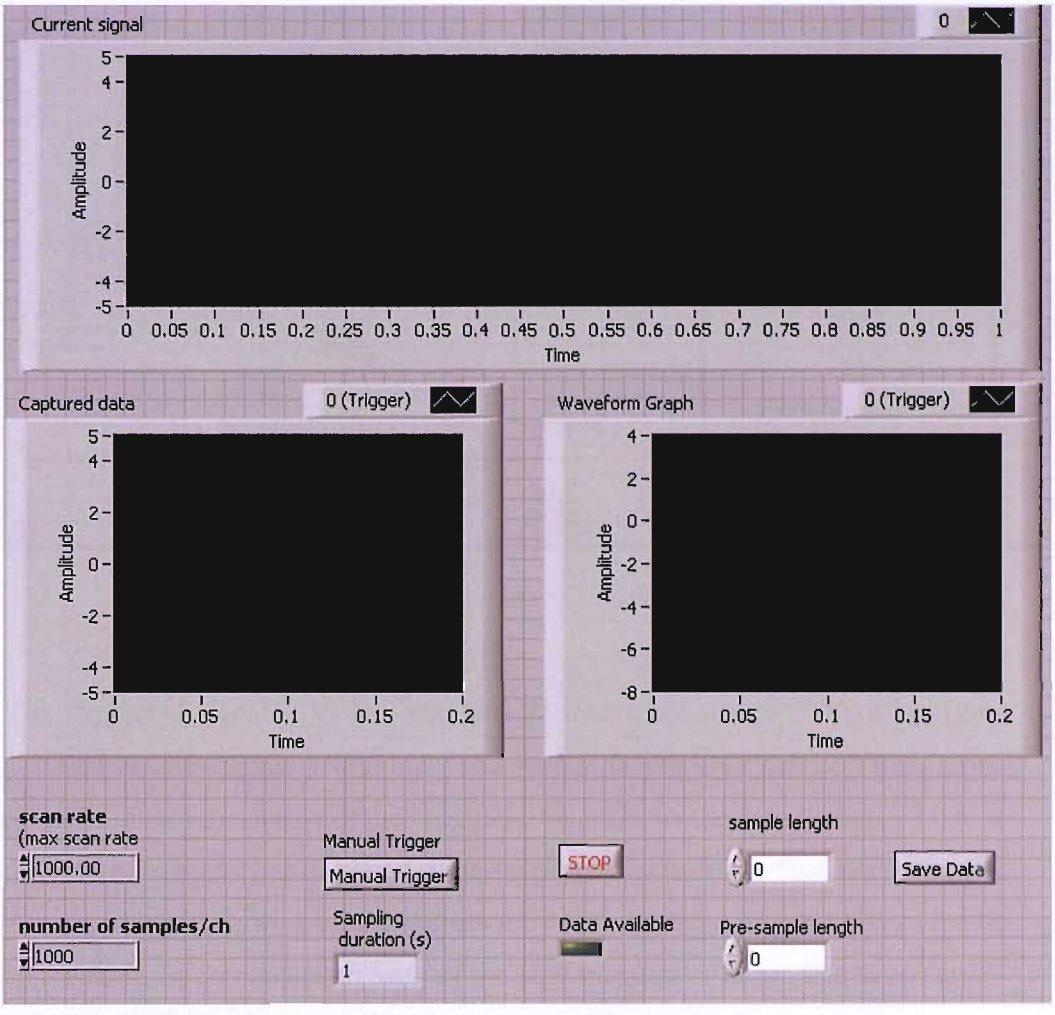

Figure B.0.8: Front panel of AAsave data VI.

Figure B.0.8 shows the front panel of the "AAsave" data sub VI. The top graph of this sub VI shows the current data coming from the sensor. The resolution or update time of this graph is controlled by the number of samples divided by the scan rate and is automatically displayed in the sampling duration box in seconds.

The bottom two graphs show a captured signal after the signal has been triggered either manually through the manual trigger button or if the PZT signal exceeds a preset trigger level from the preset "triggered signal2" VI. The duration of the triggered signal can also be set by entering the length of time required in the sample length box. It is also possible to pre-sample the data by entering a value in the pre-sample box.

To save the data displayed on the captured data graph the save data button is pressed, this then provides the option to enter a new file name or save to an old file.

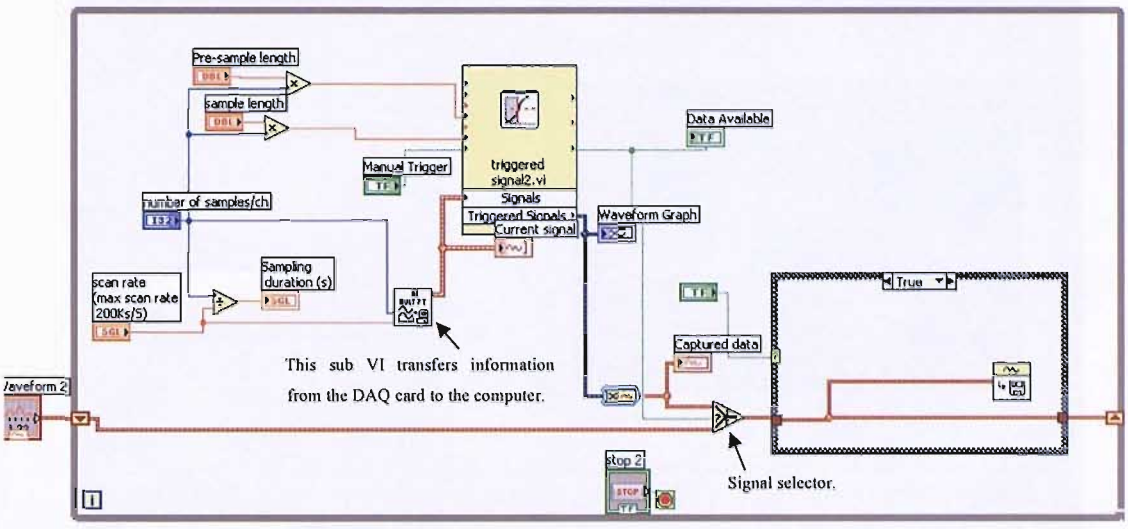

FigureB.0.9: Block diagram of the AAsave data VI.

The "triggered signal2" VI is a standard VI found in Labview 7.0 but has been altered so that the pre-sample length input and sample length input can be altered from the front panel. From the output of the "triggered signal2" VI the data is changed into a graph waveform so that it can be saved if the save button is pressed. The data then goes through a signal selector, which either passes the triggered data through to be stored in the shift memory, or connects both parts of the shift memory to allow data to be saved. This is essential to keep the data "alive" so that it can be saved. Pressing the save data button (on the front panel shown in Figure B.0.8) changes the case structure from that shown in Figure B0.10 to the case shown in FigureB.0.9, saving the data.

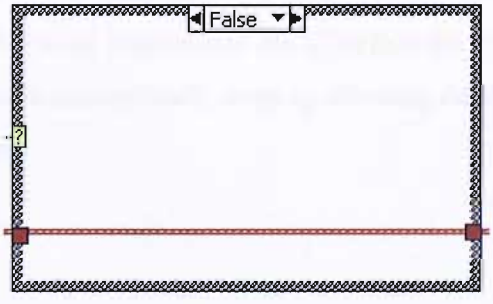

Figure B0.10: False case structure of AAsave data VI.

Analysing data VI

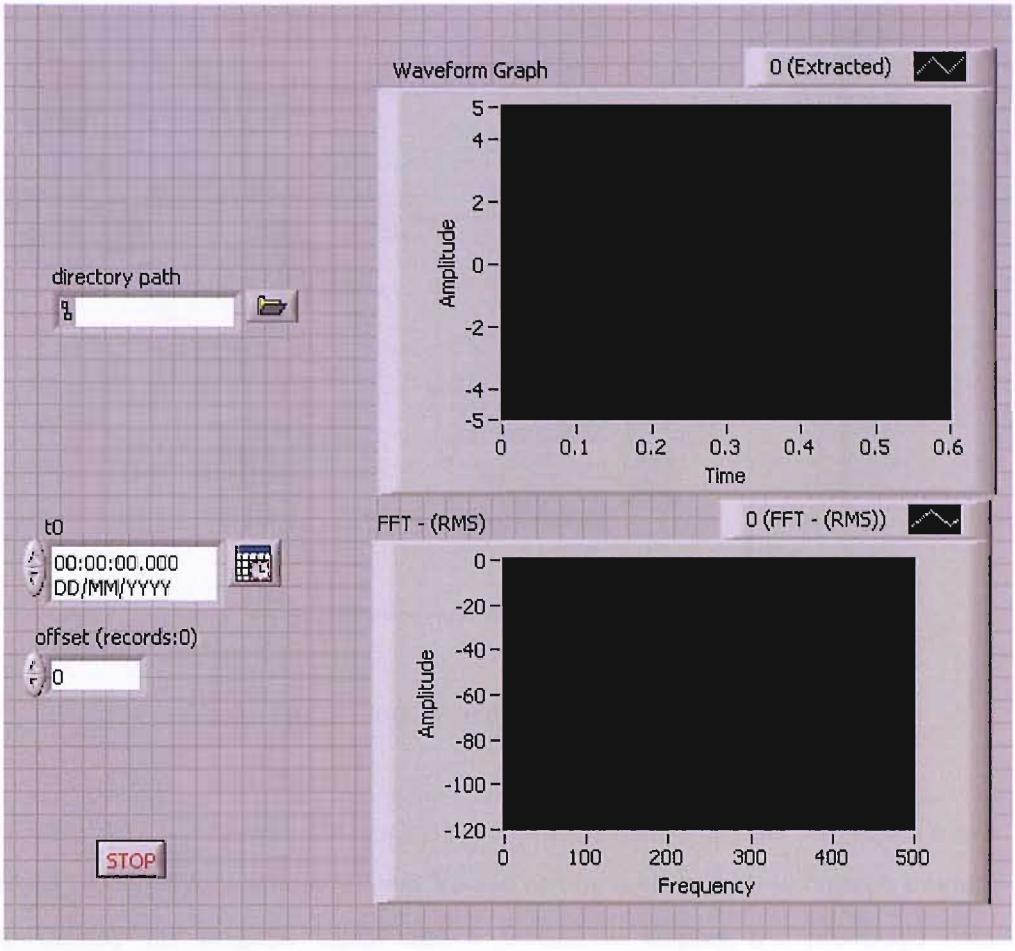

Figure B0.11: Front panel of Analysing data VI.

Figure B0.11 shows the front panel of the analysing data VI. The VI is used to create power spectrum FFT's from recorded data. The directory path box allows the directory of the signal file to be entered into the VI before the VI begins, or if the box is left empty then a file menu automatically pops up allowing data to be selected from any of the computers folders.

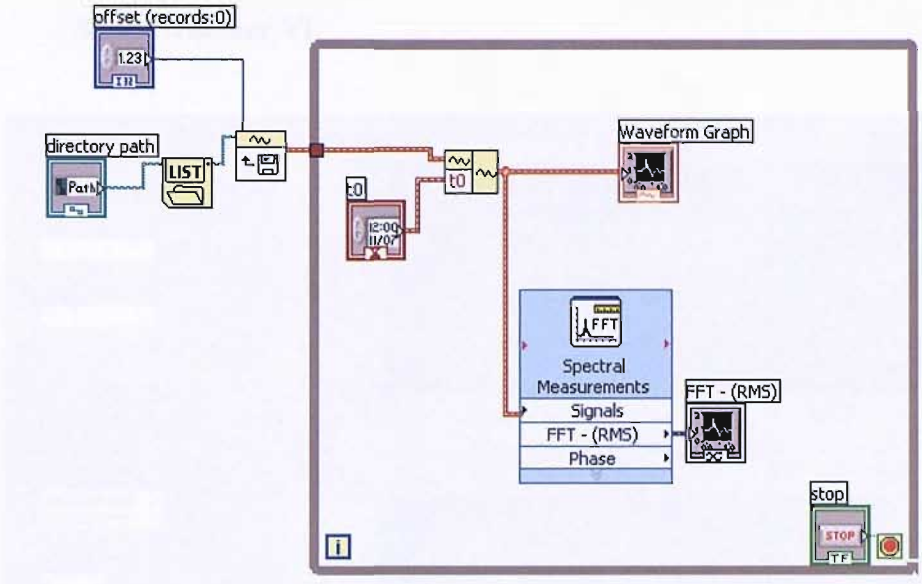

Figure B0.12: Block diagram of analysing data VI.

Figure B0.12 illustrates the block diagram of the analysing data VI. This VI uses a standard "spectral measurements" sub VI and can be seen to have two graph outputs, one to display the original signal and a second to display the processed data.

Signal trimmer VI

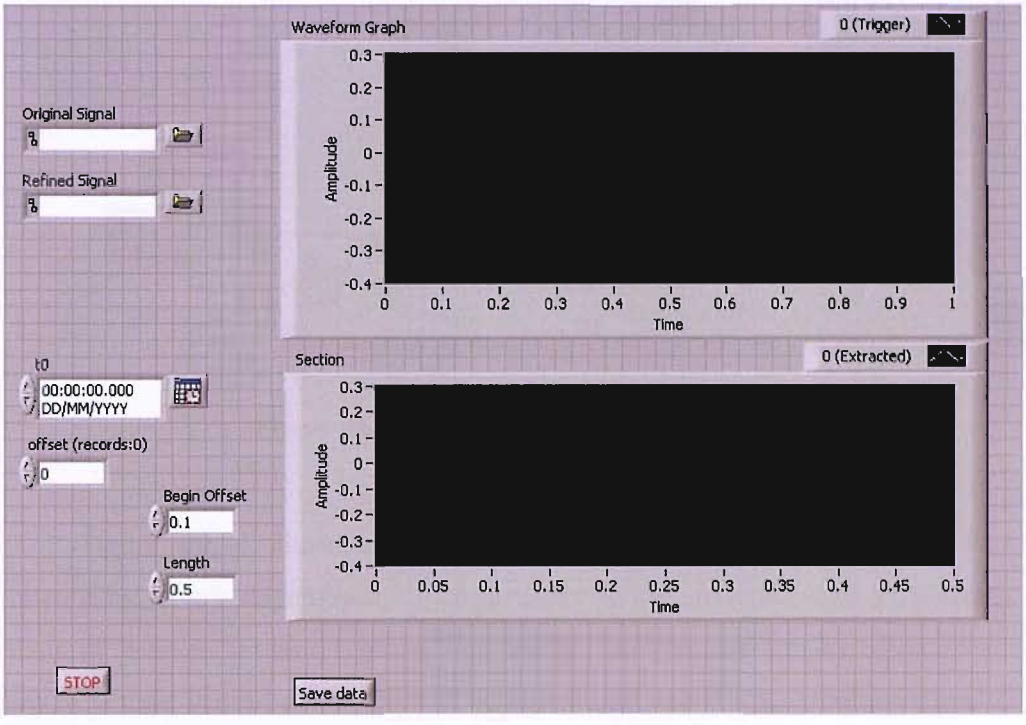

Figure B0.13: Front panel of signal trimmer VI.

Figure B0.13 shows the front panel of the signal trimmer VI. The top graph displays the original signal and the bottom graph shows the trimmed version of the signal. To trim the signal a time value must be entered in the length box to obtain that length of signal in seconds, if the section of signal is required from a point other than the beginning of the signal then an offset time must be entered in the begin offset box. The output of the graph is updated every two seconds.

When the VI first starts it allows you to select a file from all of the computer directories and when the save button is pressed the option to chose a directory is also available.

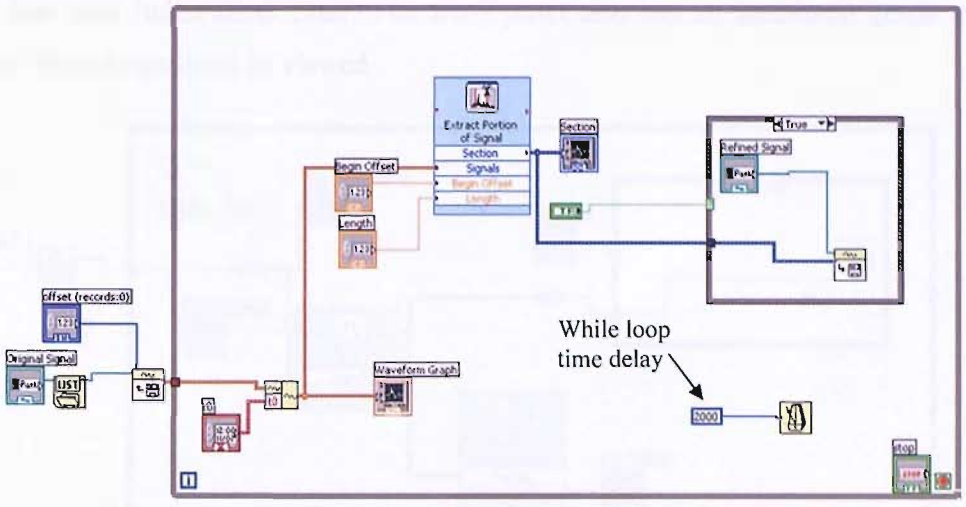

Figure B0.14: Block diagram of signal trimmer VI.

Figure B0.14 illustrates the block diagram of the signal trimmer VI. It is interesting to note its similarity in construction to the analysing data VI diagram. The main differences between the two VI's are that the standard sub VI extract portion of signal is used instead of the spectral measurements sub VI, the trimmed signal can be saved, (with the case structure) and the while loop has been limited to run (update inputs) every 2000ms.

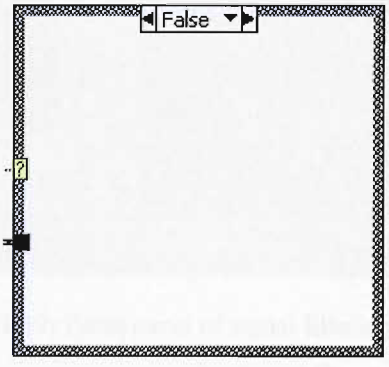

Figure B0.15: False case structure of signal trimmer VI.

Filtering data

Figure B0.16 and Figure B0.17 Show the block diagram and front panel of the program used to filter out frequencies from the slip signals. The program has been adapted from the analysis VI show in Figure B0- 12 and has the addition of a save function (shown in the case function). The filter sub VI can be used as an 8 pole high

pass or low pass Butterworth filter. The front panel also has an additional graph to allow the filtered signals to be viewed.

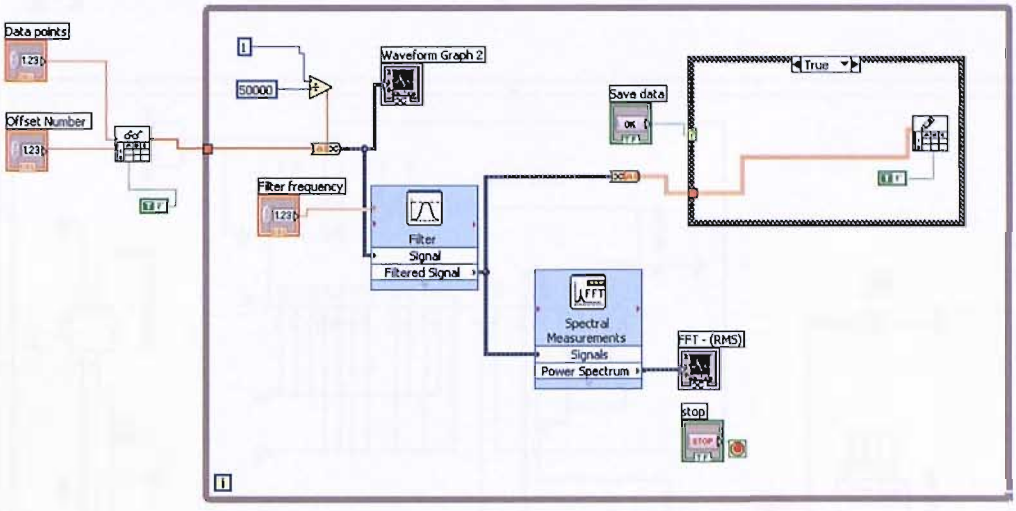

Figure B0.16: Block diagram of signal filtering program.

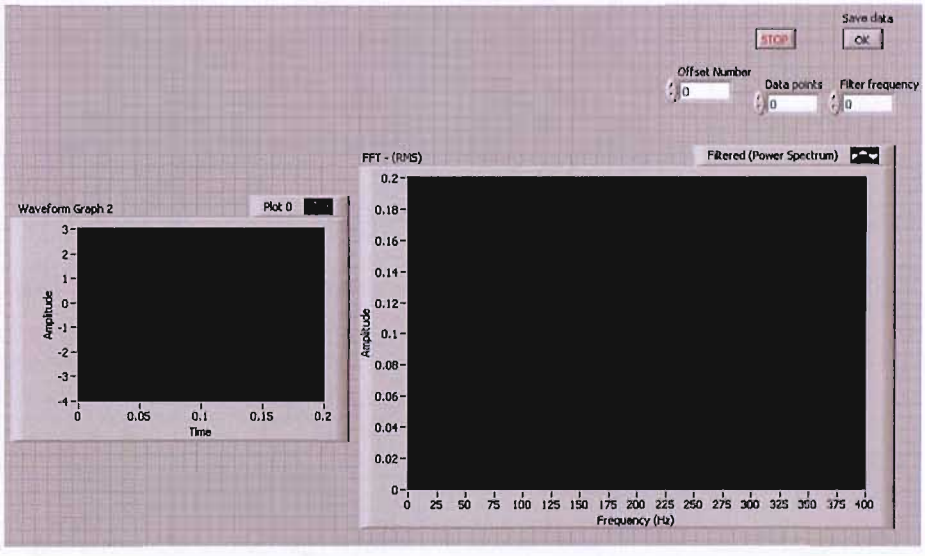

Figure B0.17: Front panel of signal filtering program.

Appendix C: Amplifier electronics

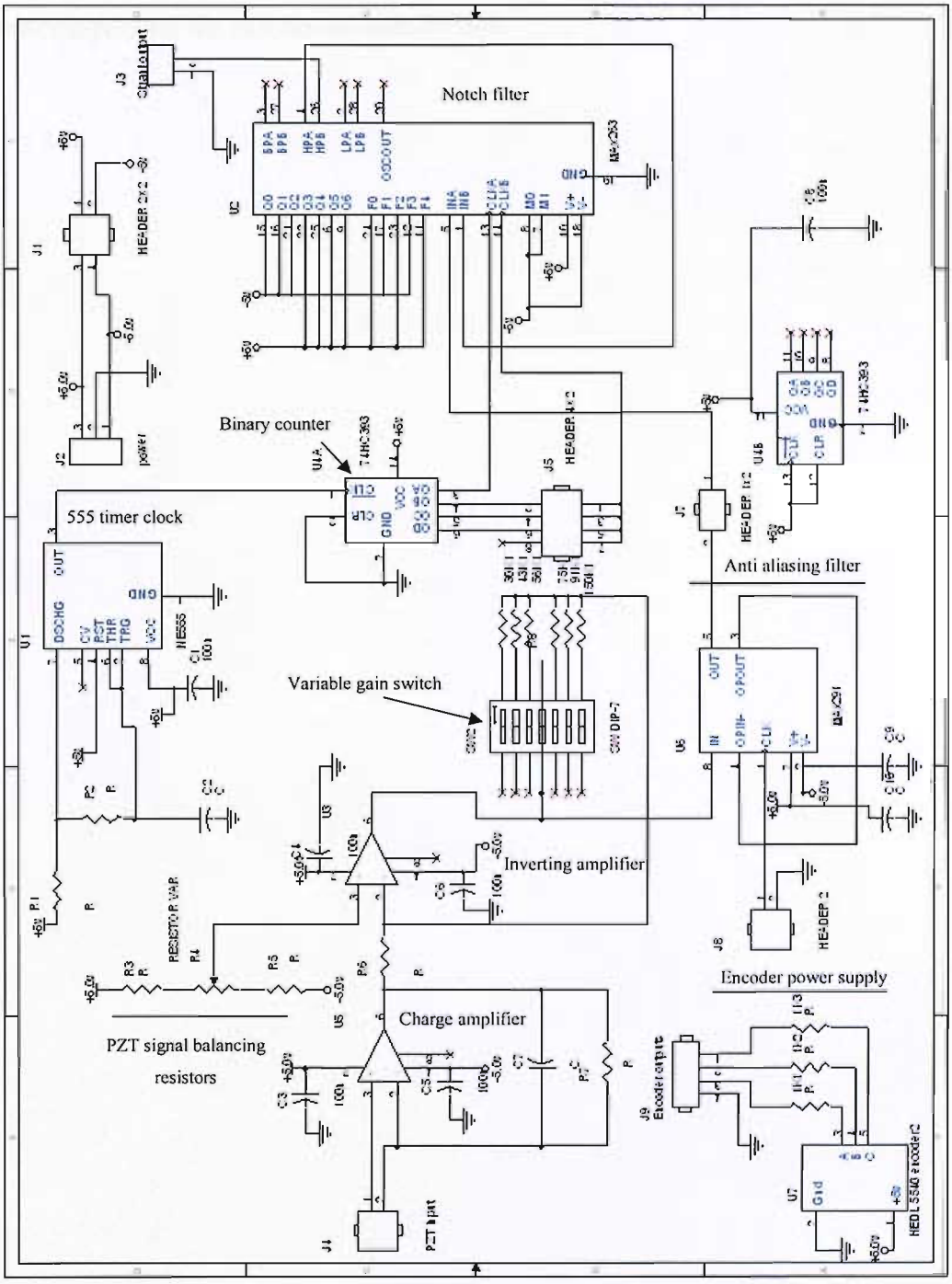

Figure C0.18: Schematic of amplifier and encoder electronics.

Figure C0.18 illustrates a schematic of the electronic circuits designed to collect and filter slip data. The circuit is made up of four separate circuits including an amplifier circuit, used to amplify PZT signals, a low pass filter to prevent aliasing of PZT signals (when collected with a DAQ card), a notch filter designed to remove 50Hz noise and a power supply for the HEDS5540 encoder unit.

Appendix D: Screen designs

Top design: Interdigitated electrodes.
Bottom design: Bottom electrode.

Top design: Dielectric layer.
Bottom design: Top electrode.

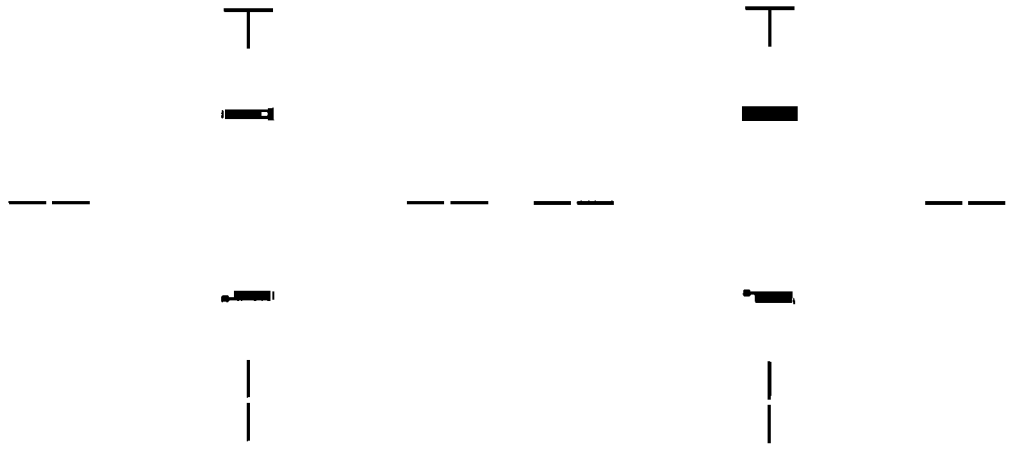

Top design: Interdigitated PZT layer.
Bottom design: PZT layer.

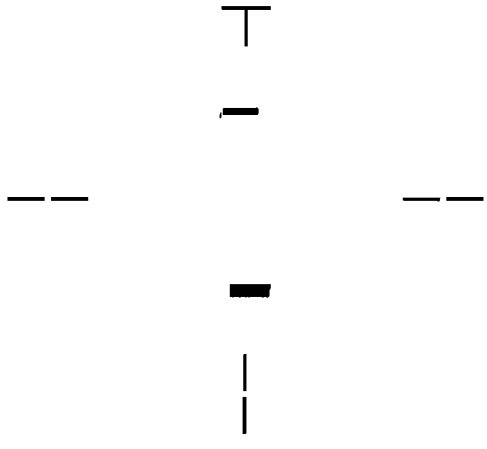

Figure 0.1: Screen designs for PZT finger linkage sensors (not to scale).

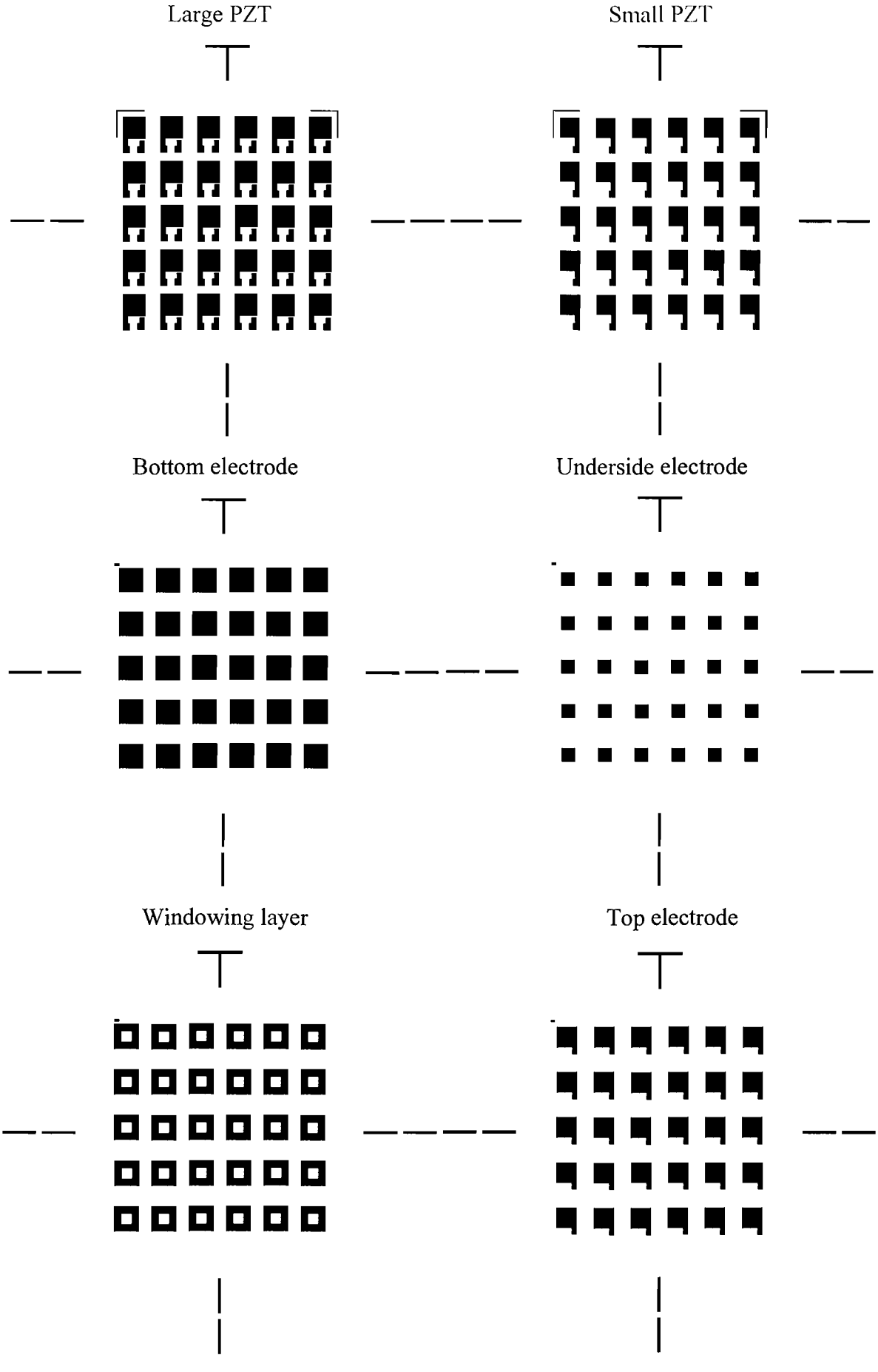

Figure 0.2: Screen designs for PZT test device layers (not to scale).

Appendix E: Technical drawings

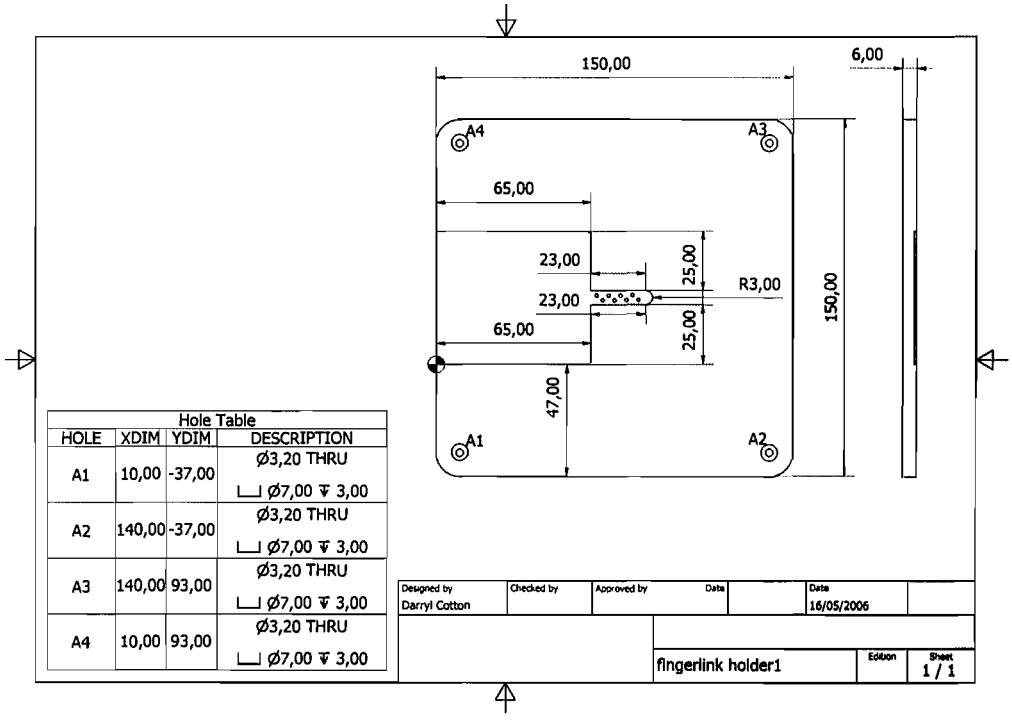

Figure E0.1: finger link holder.

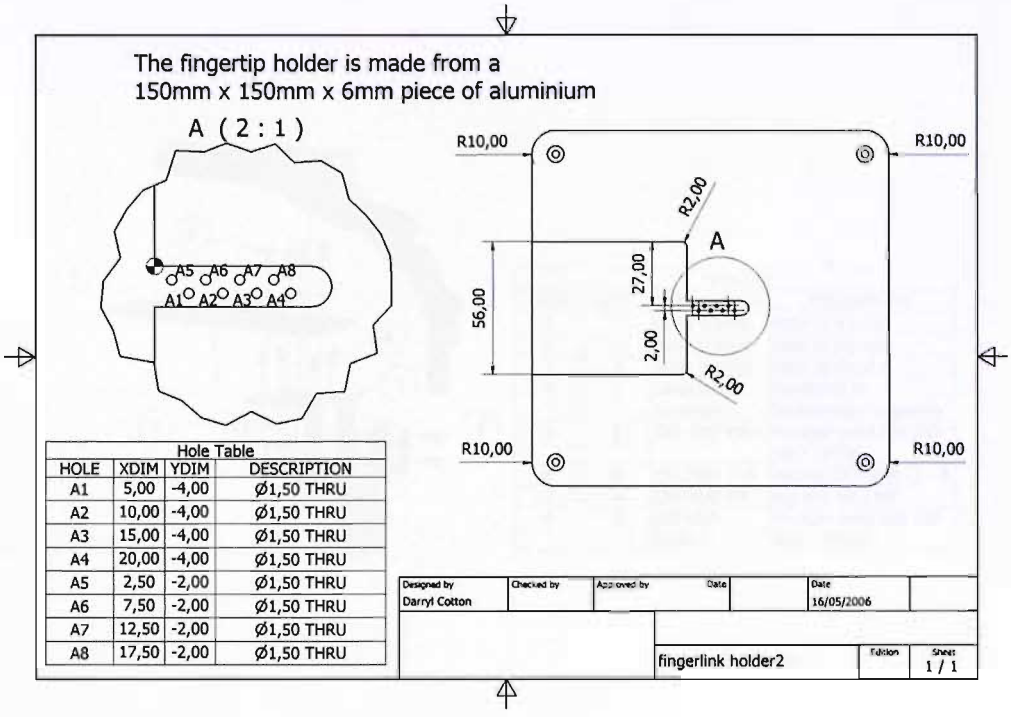

Figure E0.2: finger link holder2

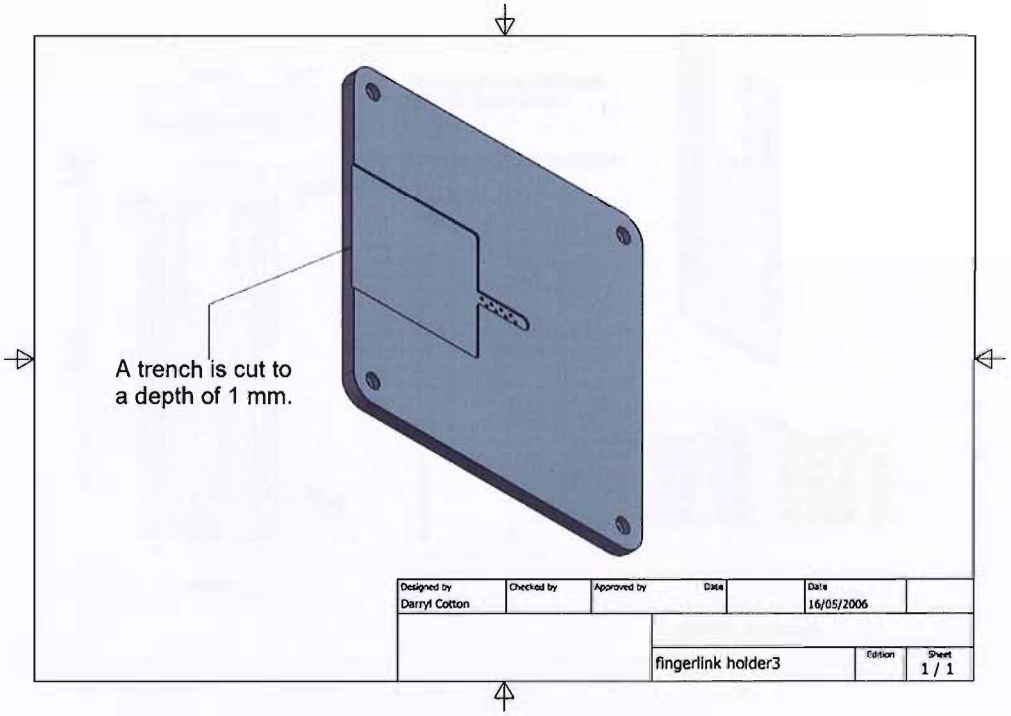

Figure E0.3: finger link holder3

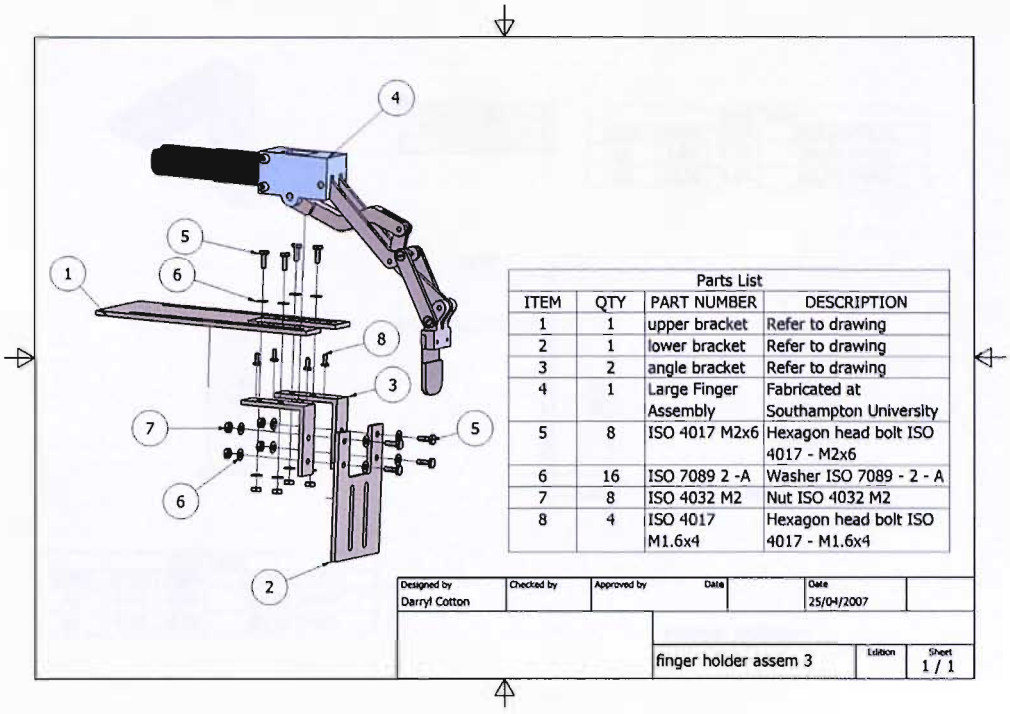

Figure E0.4: finger holder assem 3

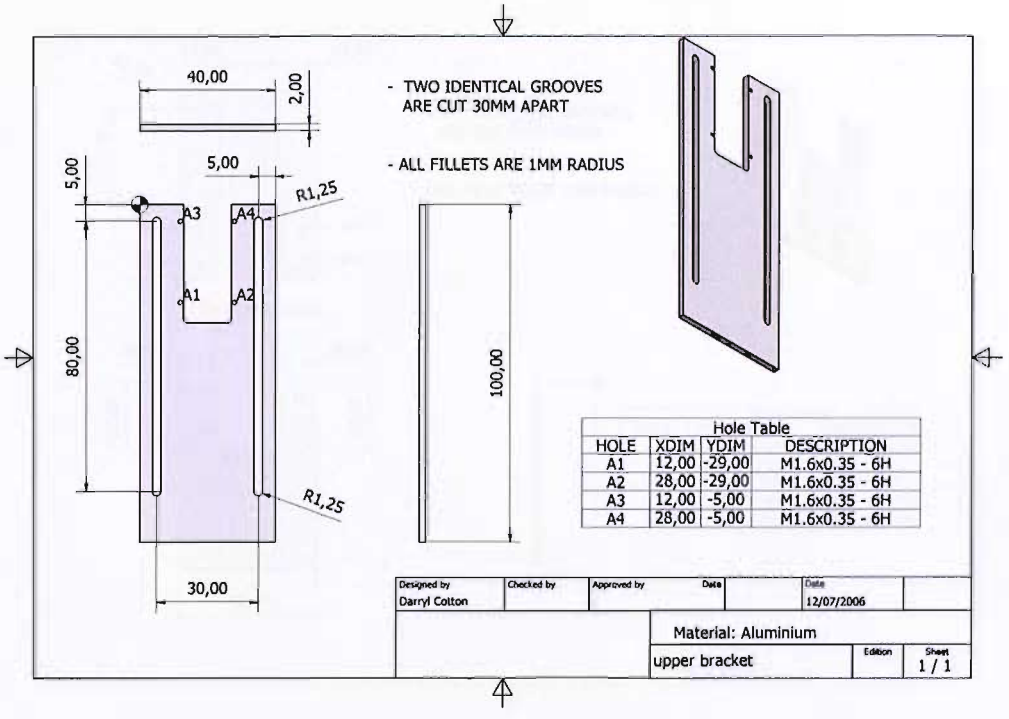

Figure E0.5: upper bracket.

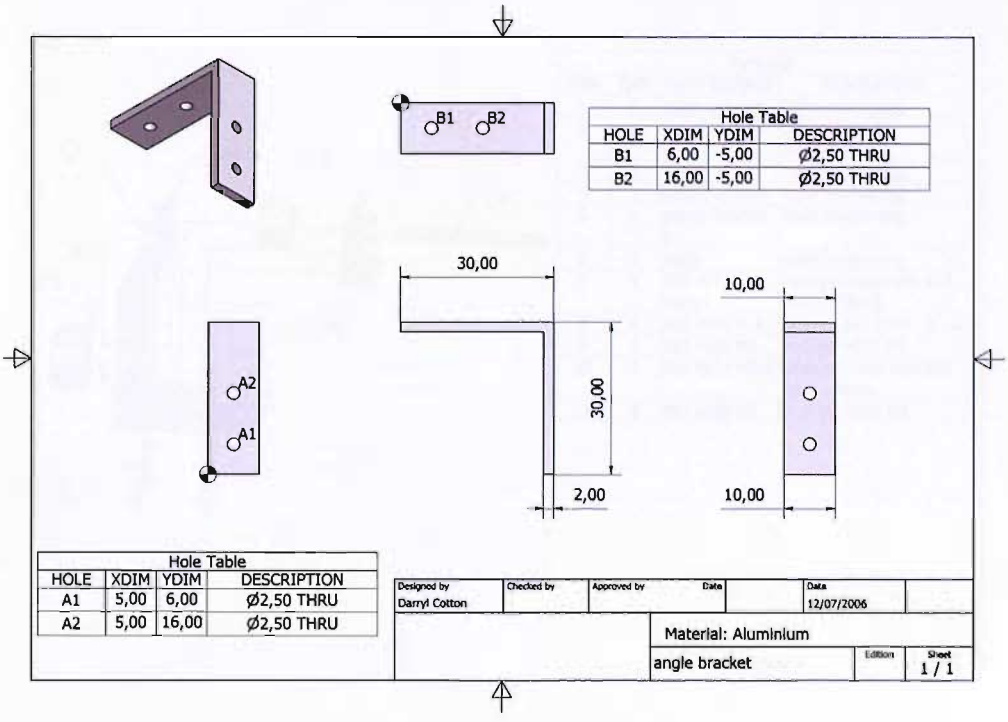

Figure E0.6: angle bracket.

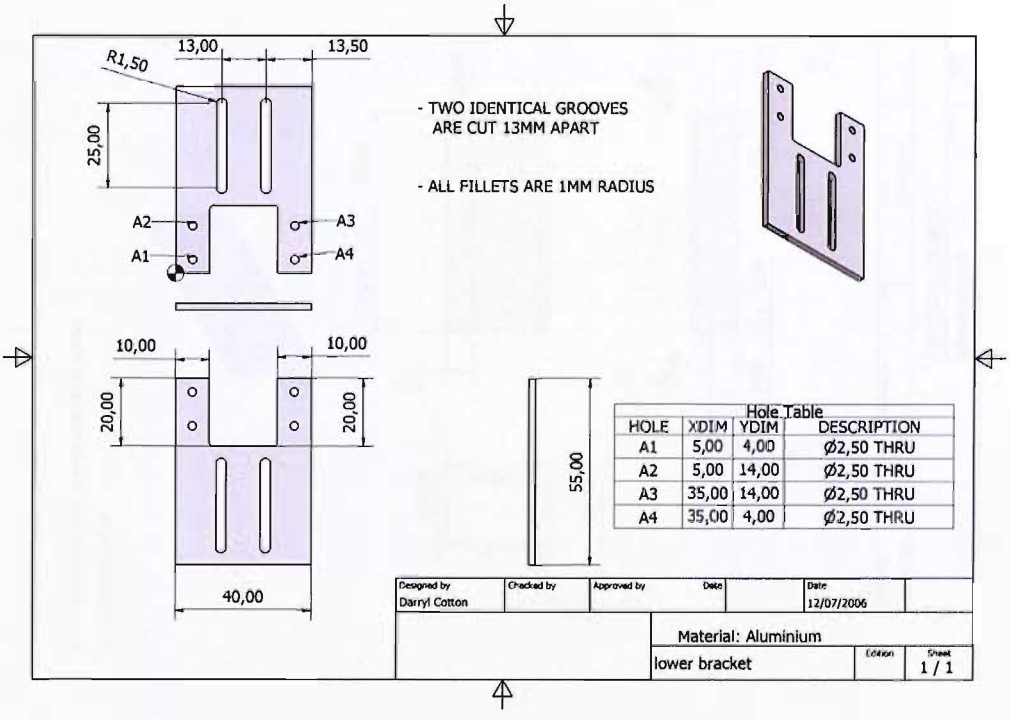

Figure E0.7: lower bracket.

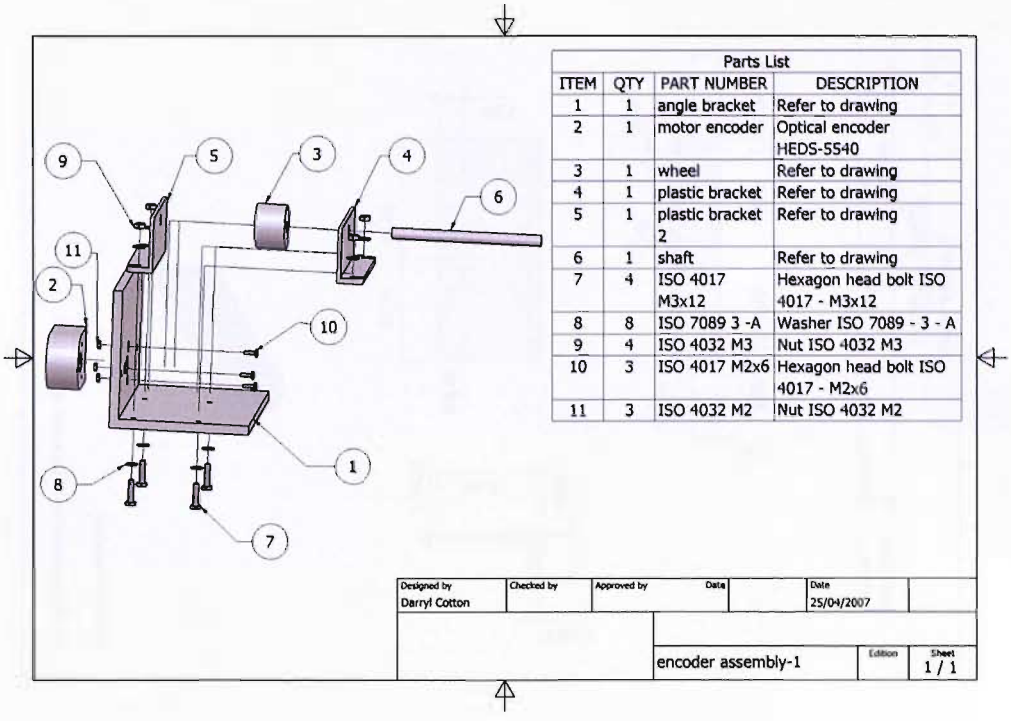

Figure E0.8: encoder assembly-1.

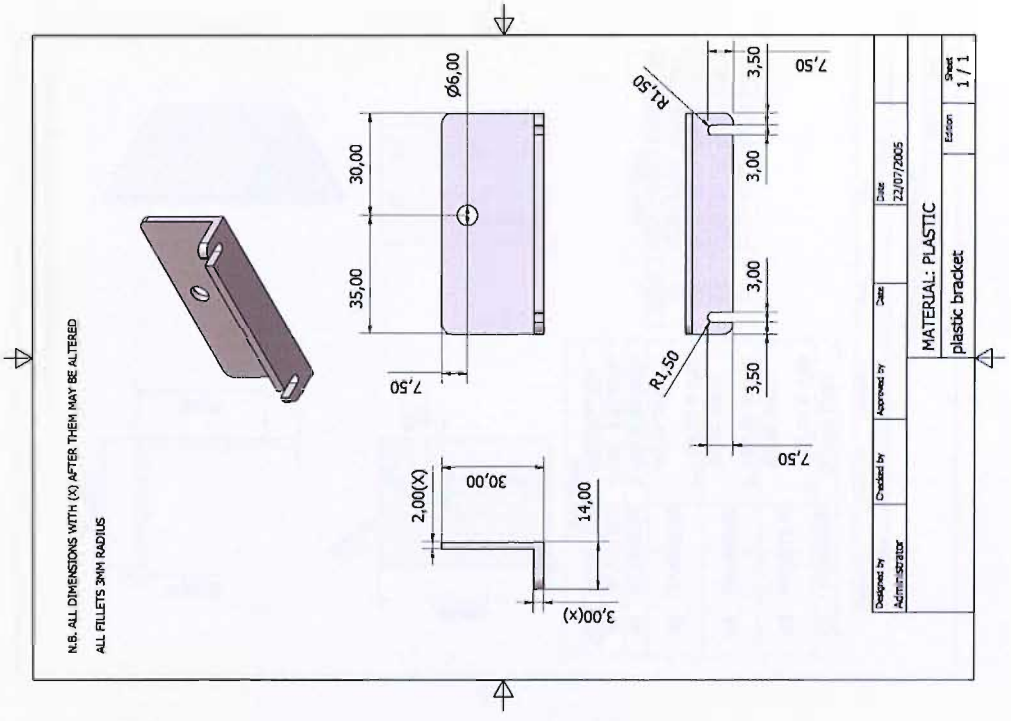

Figure E0.9: plastic bracket.

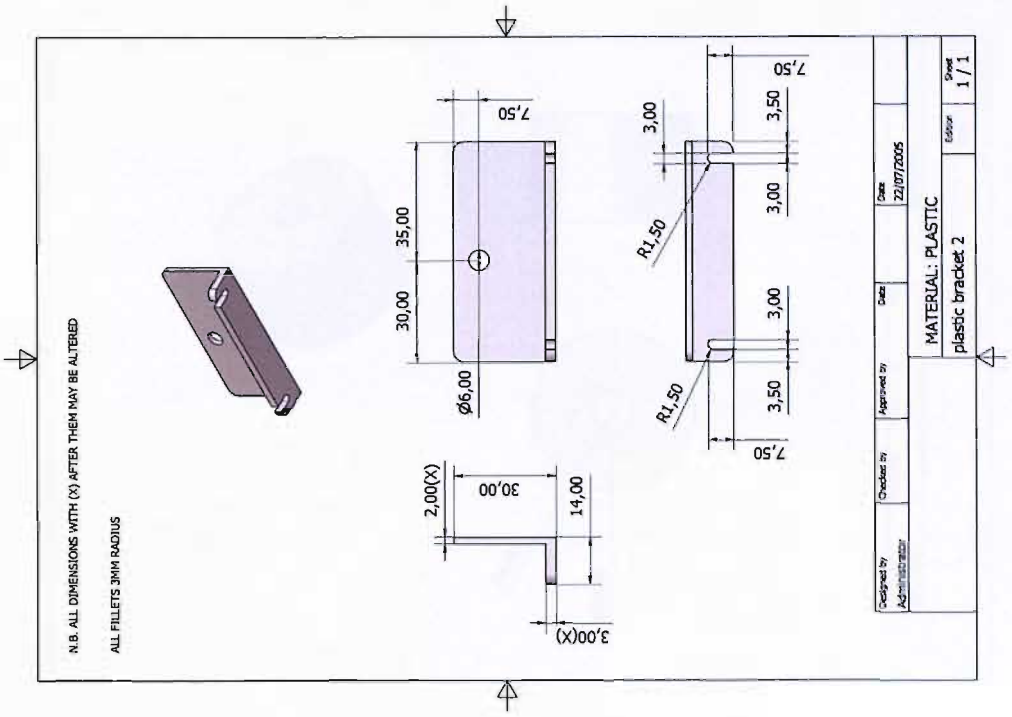

Figure E0.10: plastic bracket 2.

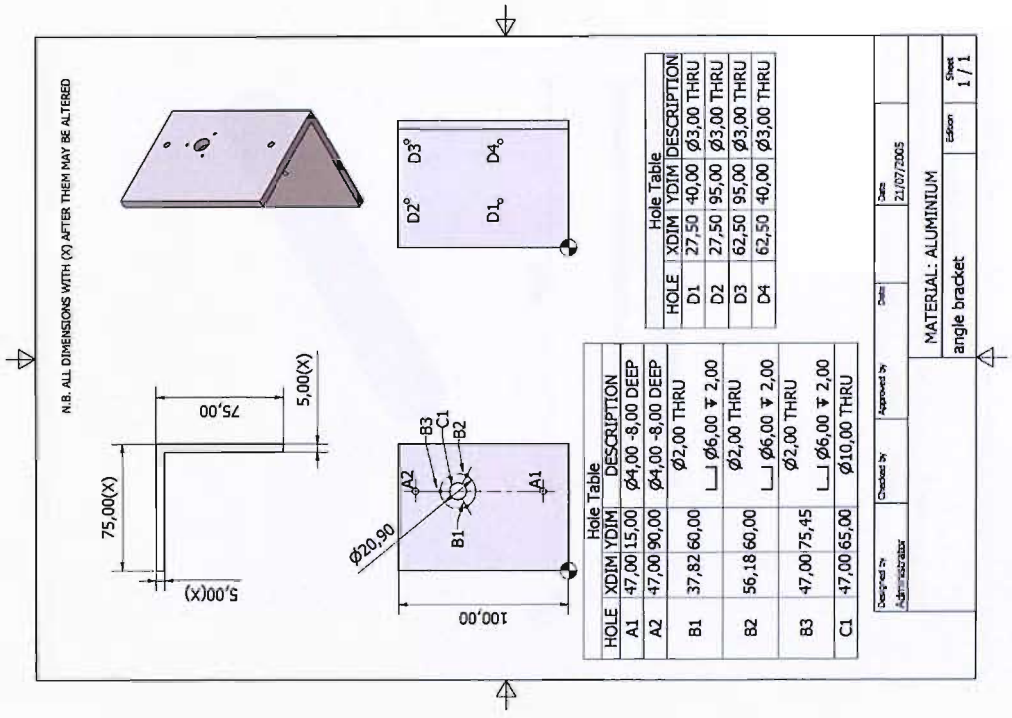

Figure E0.11: angle bracket.

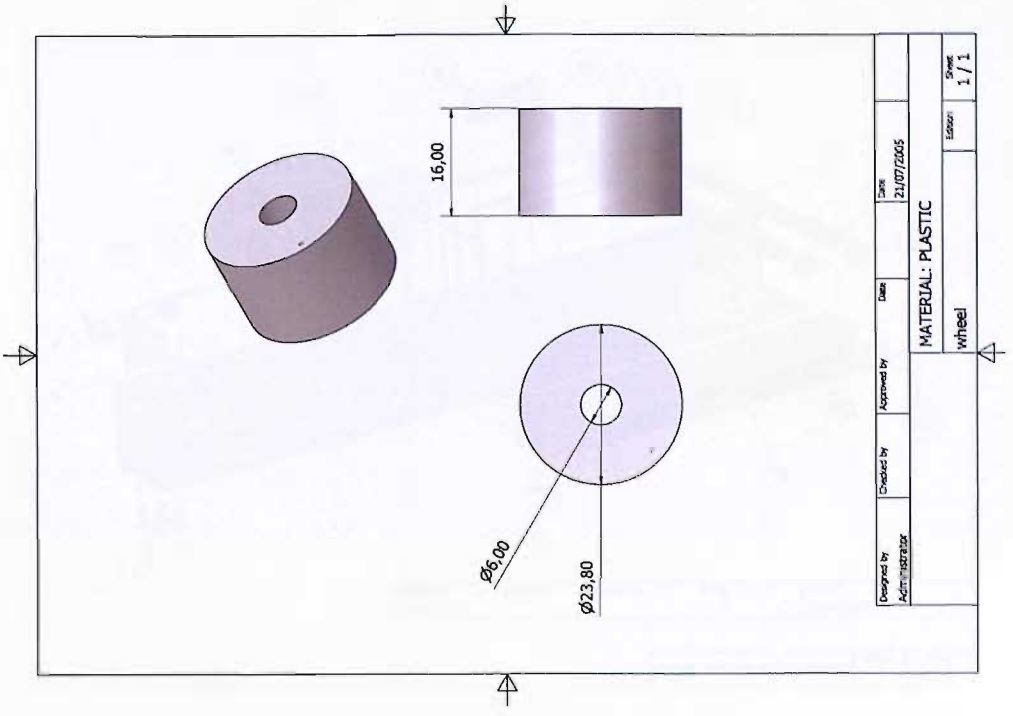

Figure E0.12: wheel.

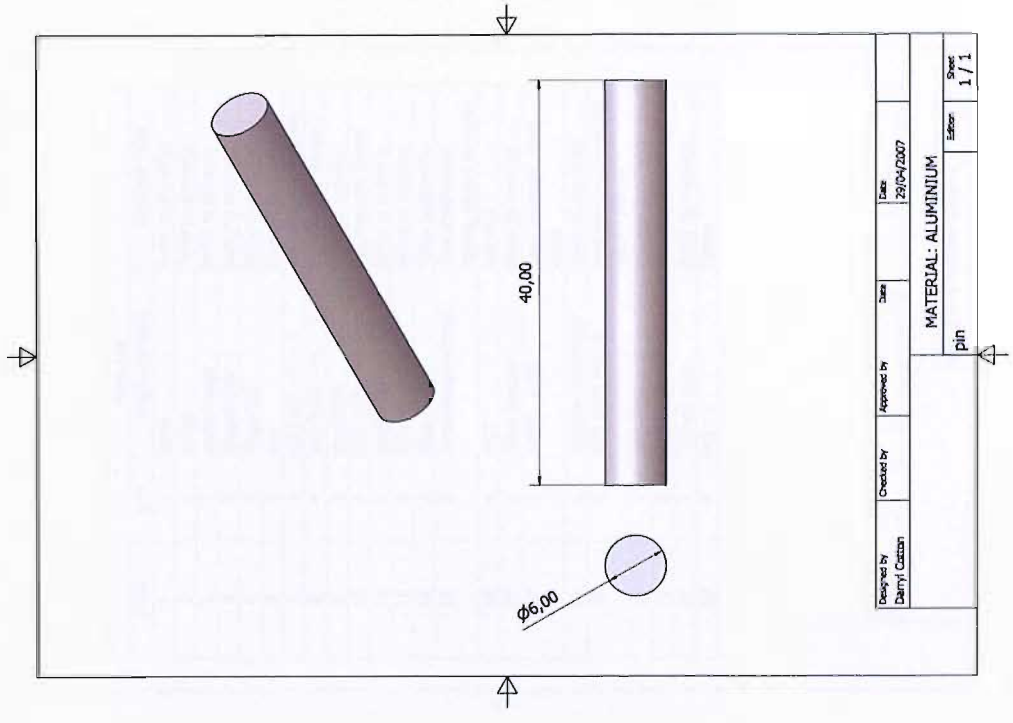

Figure E0.13: pin.

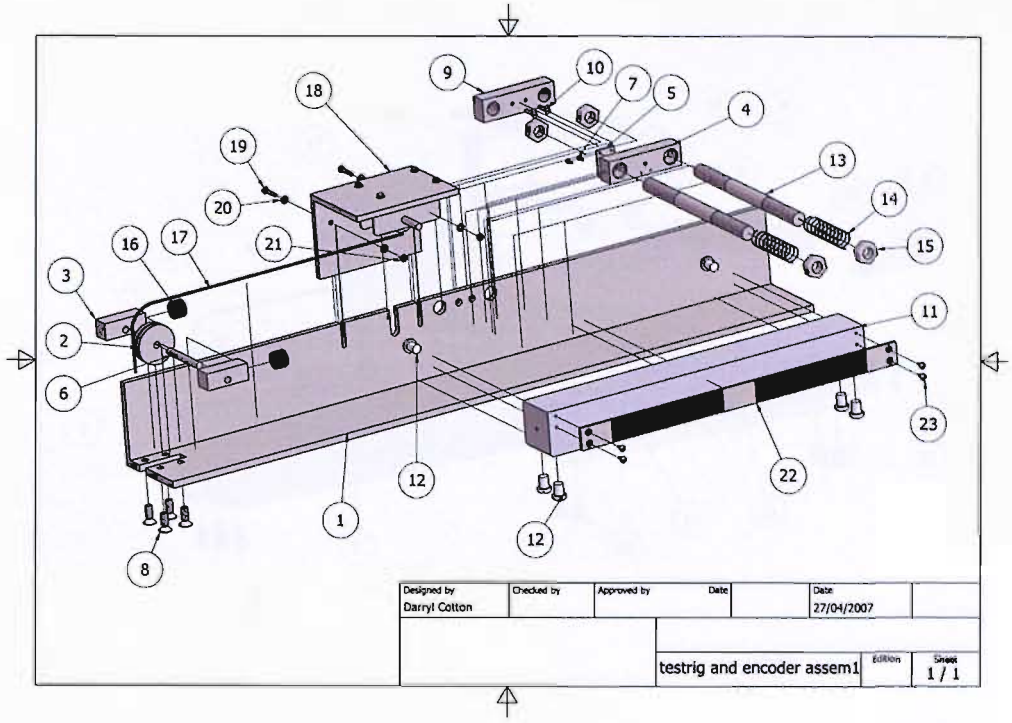

Figure E0.14: testrig and encoder assem1.

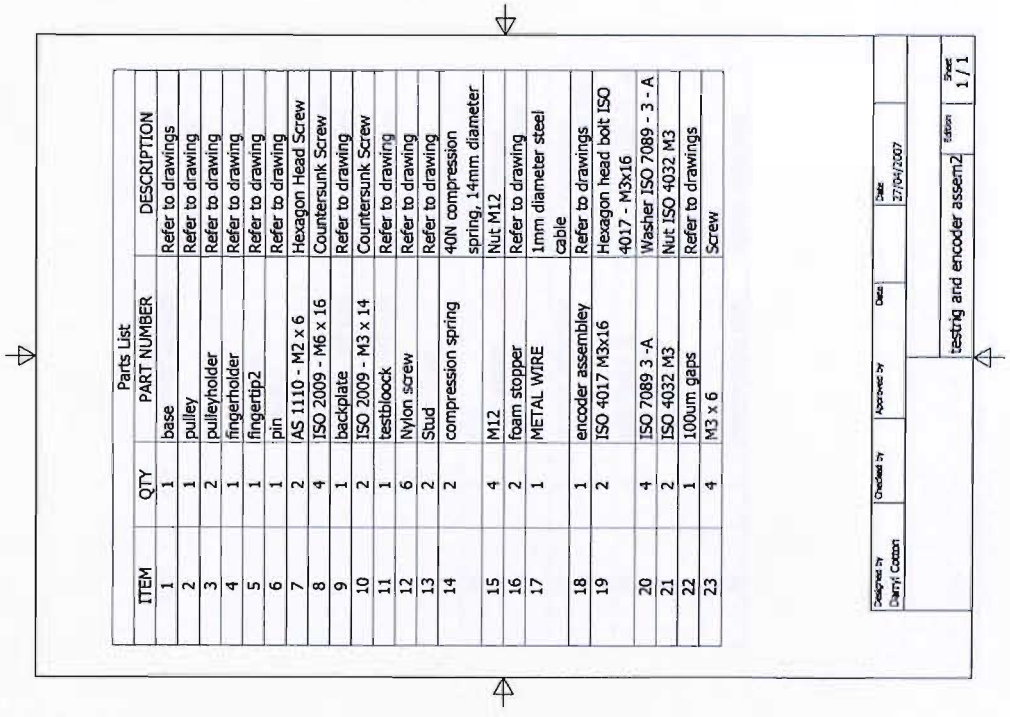

Parts List

ITEM	QTY	PART NUMBER	DESCRIPTION
1	1	base	Refer to drawings
2	1	pulley	Refer to drawing
3	2	pulleyholder	Refer to drawing
4	1	fingerholder	Refer to drawing
5	1	fingertip2	Refer to drawing
6	1	pin	Refer to drawing
7	2	AS 1110 - M2 x 6	Hexagon Head Screw
8	4	ISO 2009 - M6 x 16	Countersunk Screw
9	1	backplate	Refer to drawing
10	2	ISO 2009 - M3 x 14	Countersunk Screw
11	1	testblock	Refer to drawing
12	6	Nylon screw	Refer to drawing
13	2	Stud	Refer to drawing
14	2	compression spring	40N compression spring, 14mm diameter
15	4	M12	Nut M12
16	2	foam stopper	Refer to drawing
17	1	METAL WIRE	1mm diameter steel cable
18	1	encoder assembley	Refer to drawings
19	2	ISO 4017 M3x16	Hexagon head bolt ISO 4017 - M3x16
20	4	ISO 7089 3 -A	Washer ISO 7089 - 3 - A
21	2	ISO 4032 M3	Nut ISO 4032 M3
22	1	100um gaps	Refer to drawings
23	4	M3 x 6	Screw

Figure E0.15: testrig and encoder assem2.

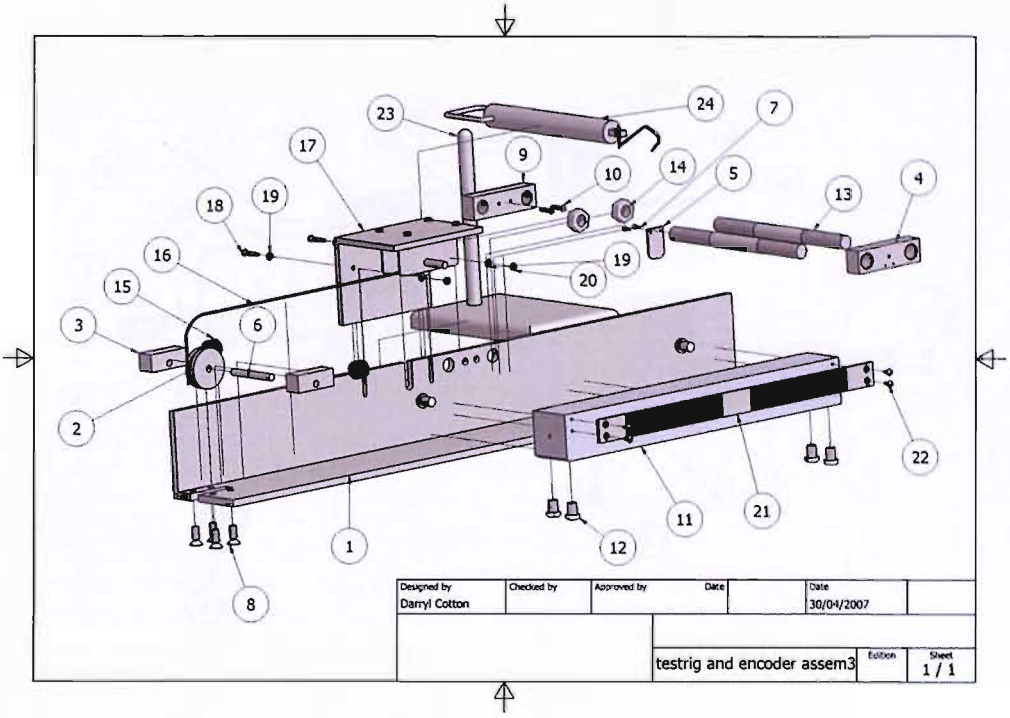

Figure E0.16: testrig and encoder assem3.

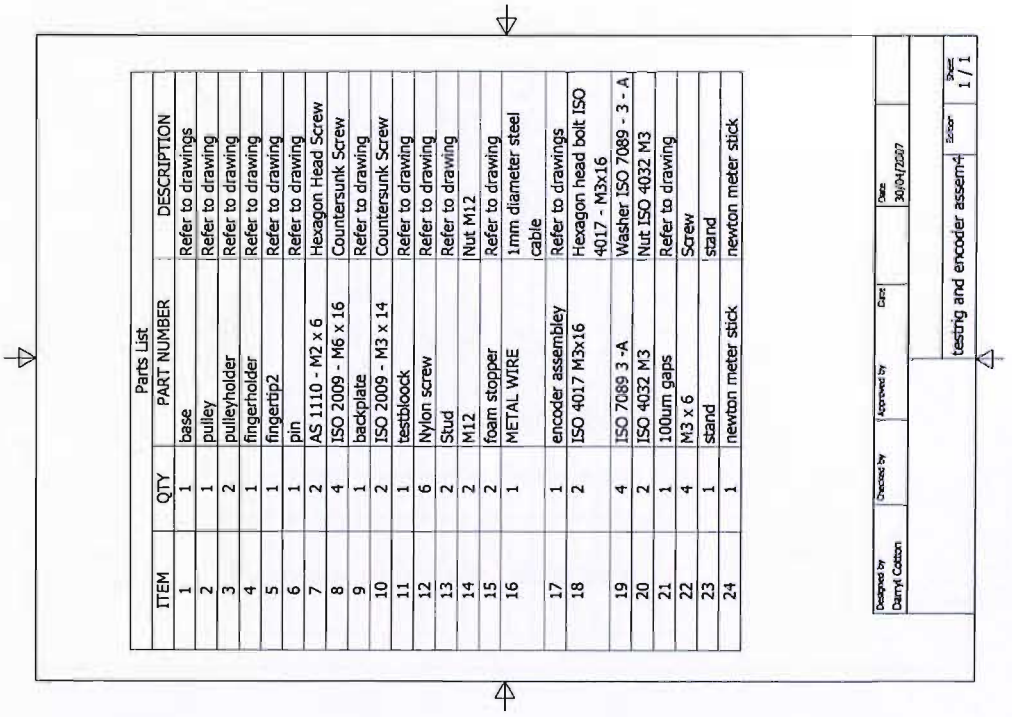

Parts List

ITEM	QTY	PART NUMBER	DESCRIPTION
1	1	base	Refer to drawings
2	1	pulley	Refer to drawing
3	2	pulleyholder	Refer to drawing
4	1	fingerholder	Refer to drawing
5	1	fingertip2	Refer to drawing
6	1	pin	Refer to drawing
7	2	AS 1110 - M2 x 6	Hexagon Head Screw
8	4	ISO 2009 - M6 x 16	Countersunk Screw
9	1	backplate	Refer to drawing
10	2	ISO 2009 - M3 x 14	Countersunk Screw
11	1	testbloock	Refer to drawing
12	6	Nylon screw	Refer to drawing
13	2	Stud	Refer to drawing
14	2	M12	Nut M12
15	2	foam stopper	Refer to drawing
16	1	METAL WIRE	1mm diameter steel cable
17	1	encoder assembley	Refer to drawings
18	2	ISO 4017 M3x16	Hexagon head bolt ISO 4017 - M3x16
19	4	ISO 7089 3 -A	Washer ISO 7089 - 3 - A
20	2	ISO 4032 M3	Nut ISO 4032 M3
21	1	100um gaps	Refer to drawing
22	4	M3 x 6	Screw
23	1	stand	stand
24	1	newton meter stick	newton meter stick

Figure E0.17: testrig and encoder assem4.

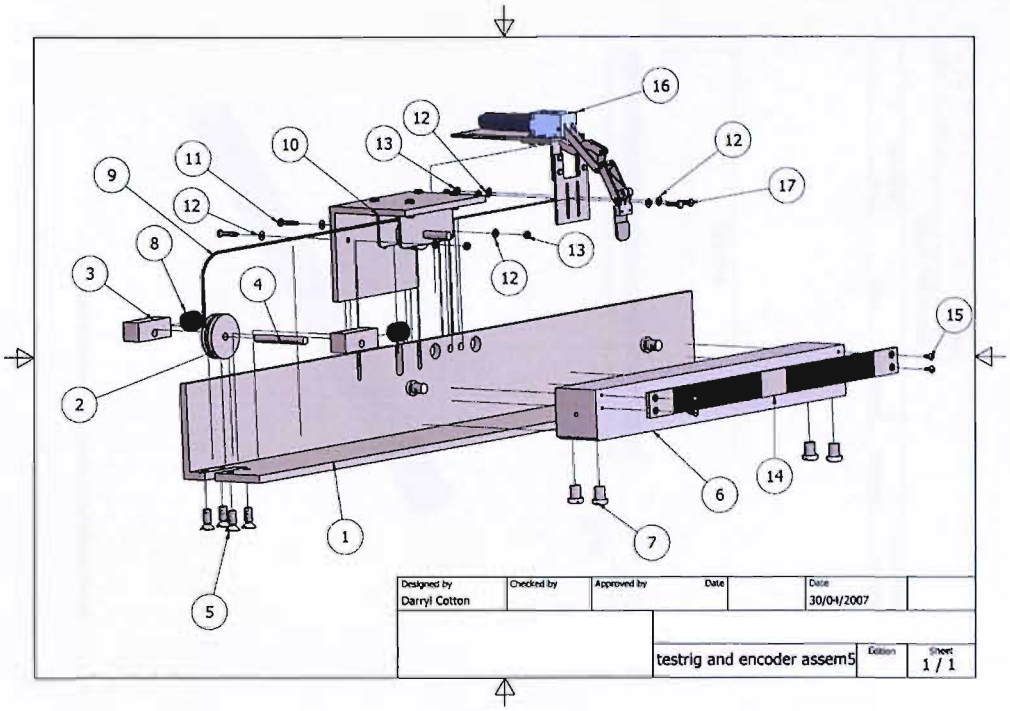

Figure E0.18: testrig and encoder assem5.

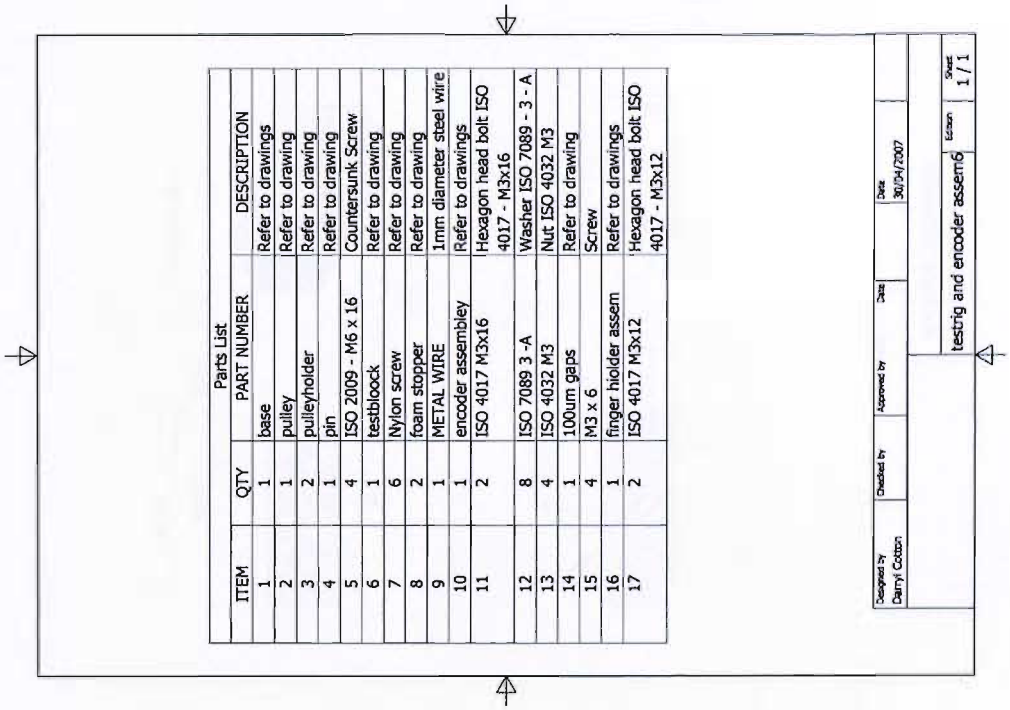

Parts List

ITEM	QTY	PART NUMBER	DESCRIPTION
1	1	base	Refer to drawings
2	1	pulley	Refer to drawing
3	2	pulleyholder	Refer to drawing
4	1	pin	Refer to drawing
5	4	ISO 2009 - M6 x 16	Countersunk Screw
6	1	testbloock	Refer to drawing
7	6	Nylon screw	Refer to drawing
8	2	foam stopper	Refer to drawing
9	1	METAL WIRE	1mm diameter steel wire
10	1	encoder assembley	Refer to drawings
11	2	ISO 4017 M3x16	Hexagon head bolt ISO 4017 - M3x16
12	8	ISO 7089 3 -A	Washer ISO 7089 - 3 - A
13	4	ISO 4032 M3	Nut ISO 4032 M3
14	1	100um gaps	Refer to drawing
15	4	M3 x 6	Screw
16	1	finger hiolder assem	Refer to drawings
17	2	ISO 4017 M3x12	Hexagon head bolt ISO 4017 - M3x12

Figure E0.19: testrig and encoder assem6.

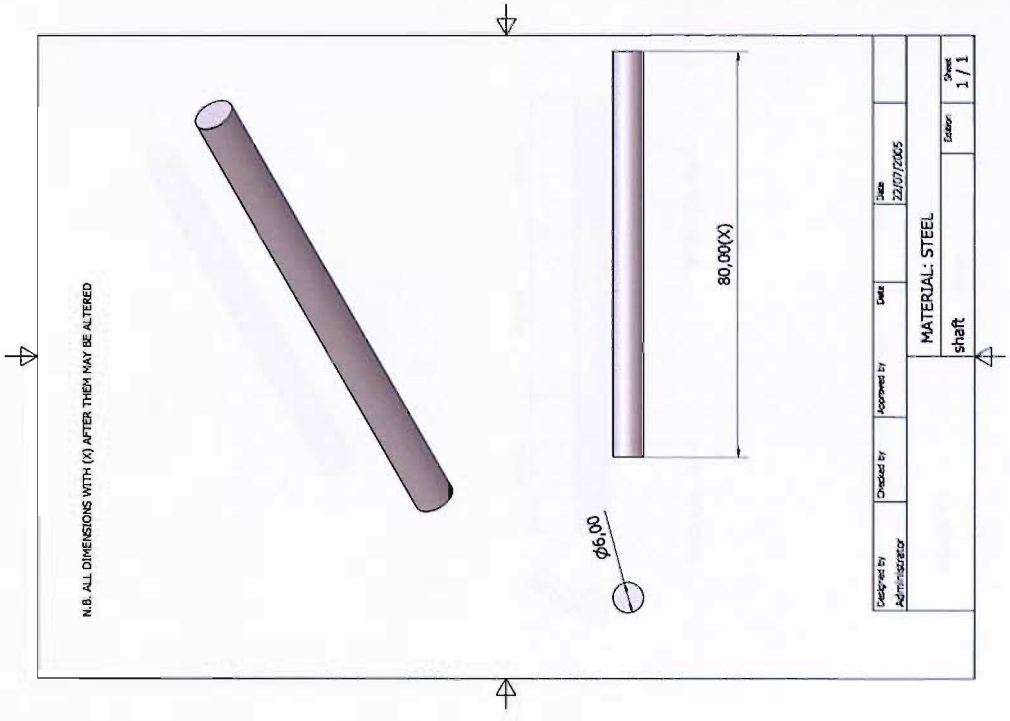

Figure E0.20: shaft.

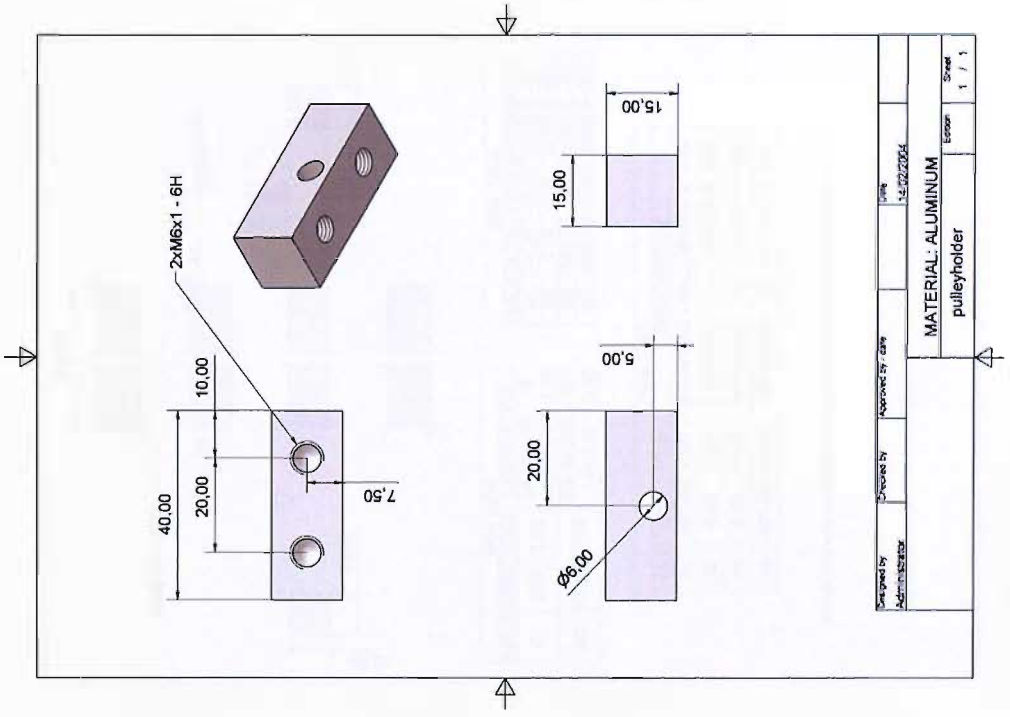

Figure E0.21: pulley holder.

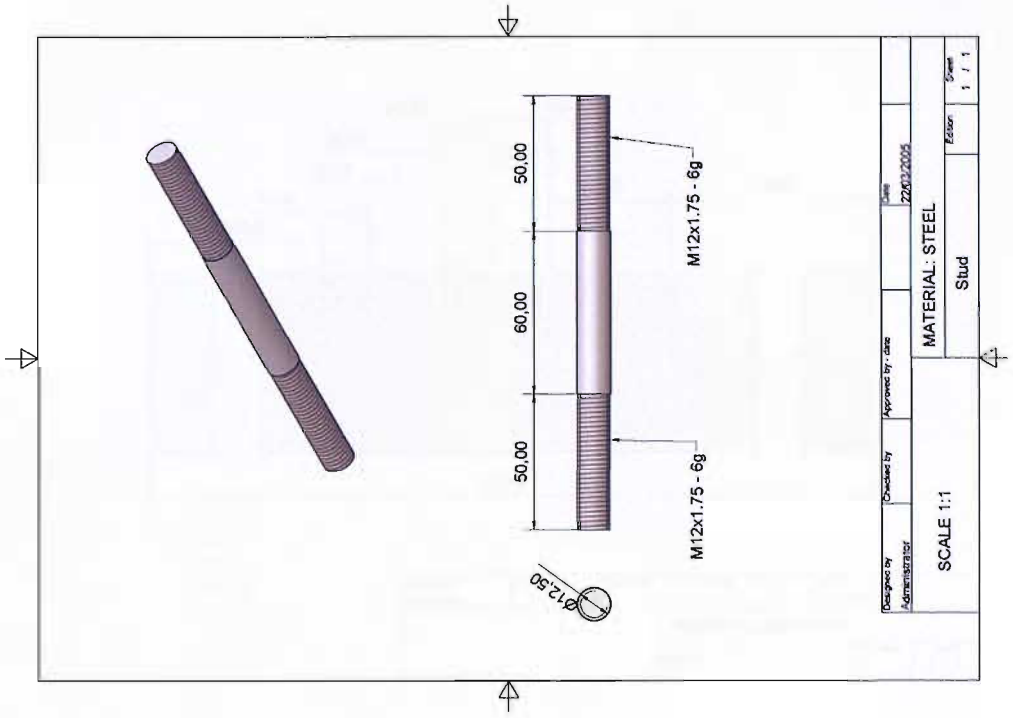

Figure E0.22: stud.

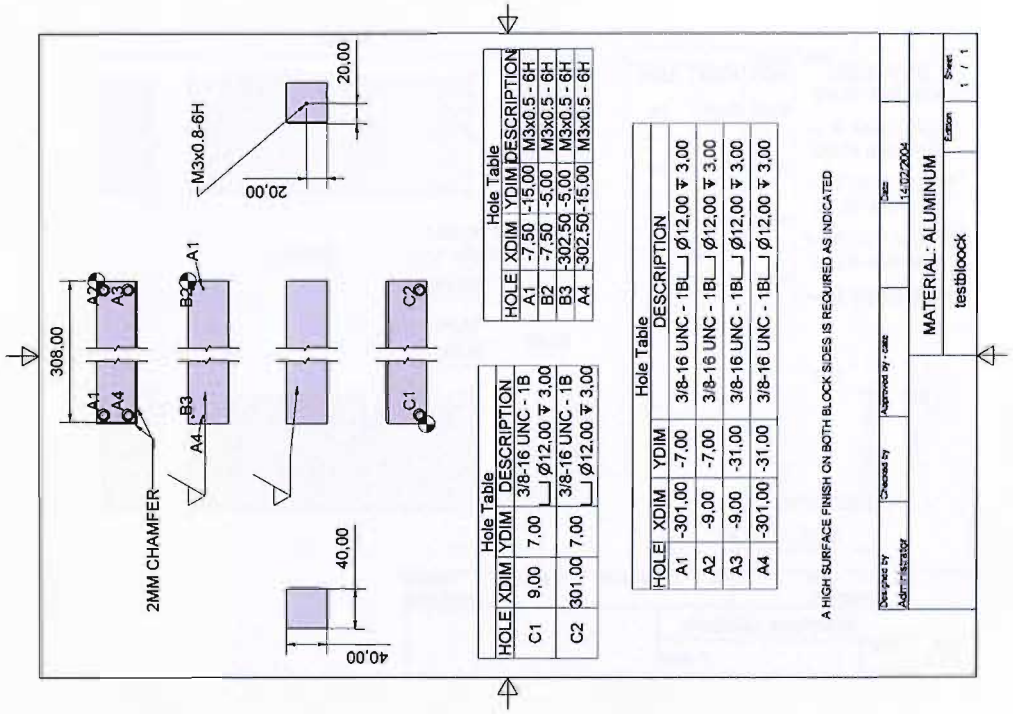

Figure E0.23: test block.

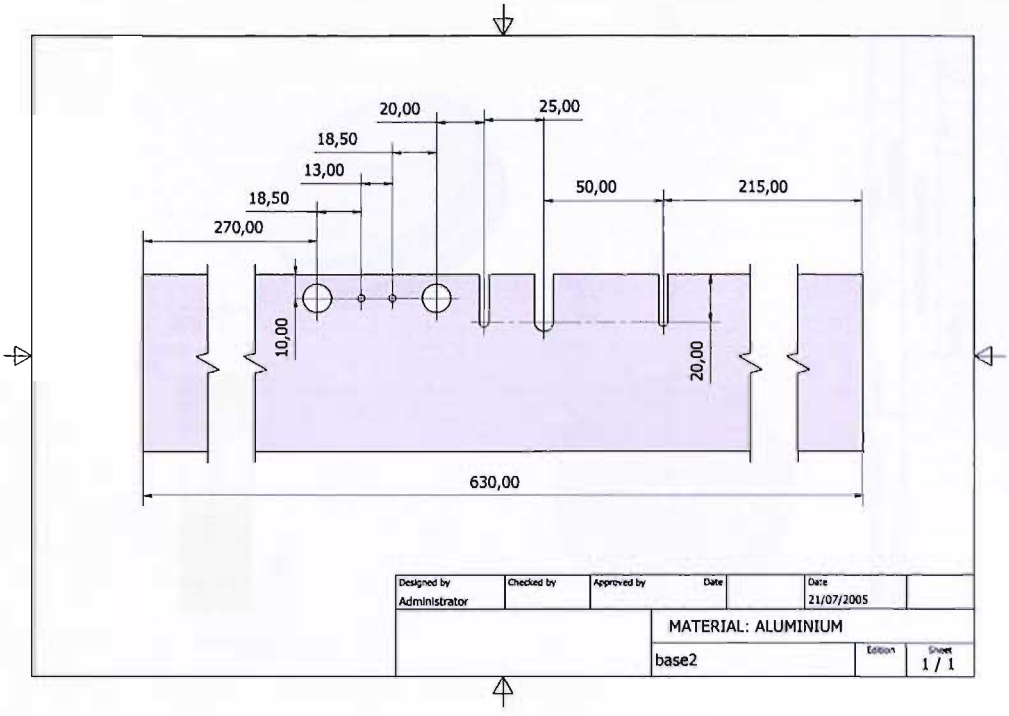

Figure E0.24: base2.

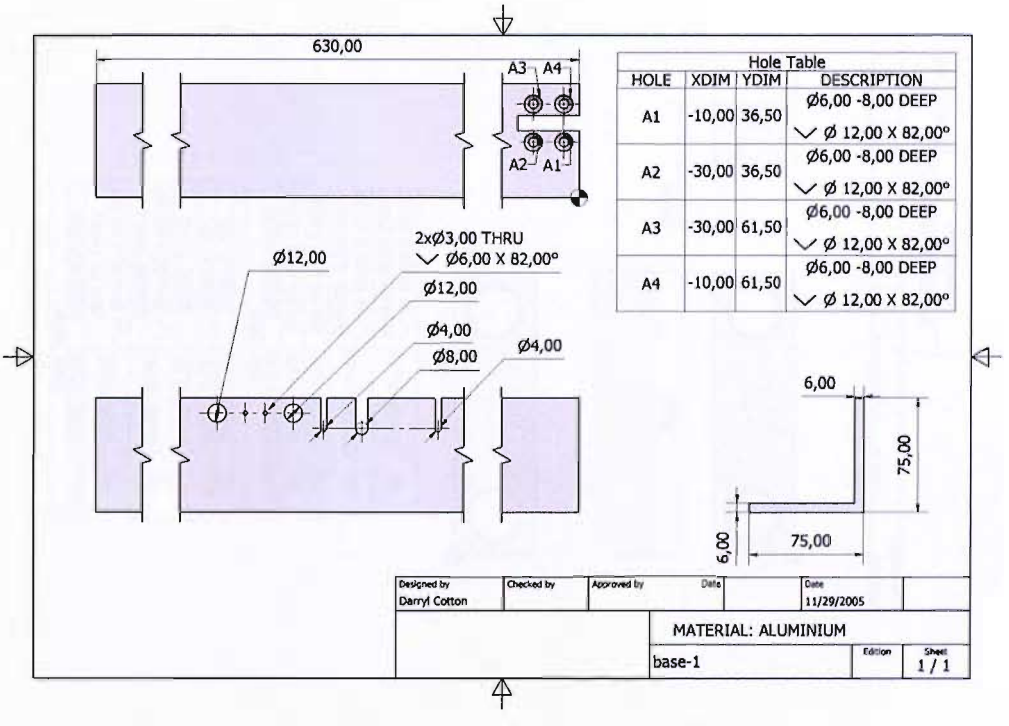

Figure E0.25: base 1.

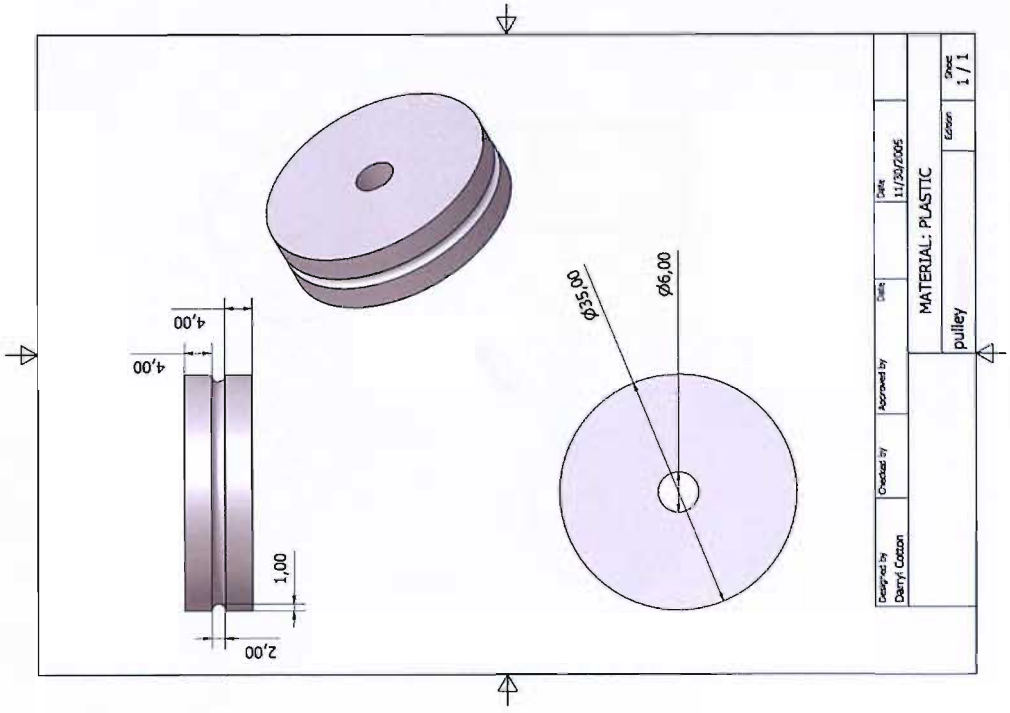

Figure E0.26: pulley.

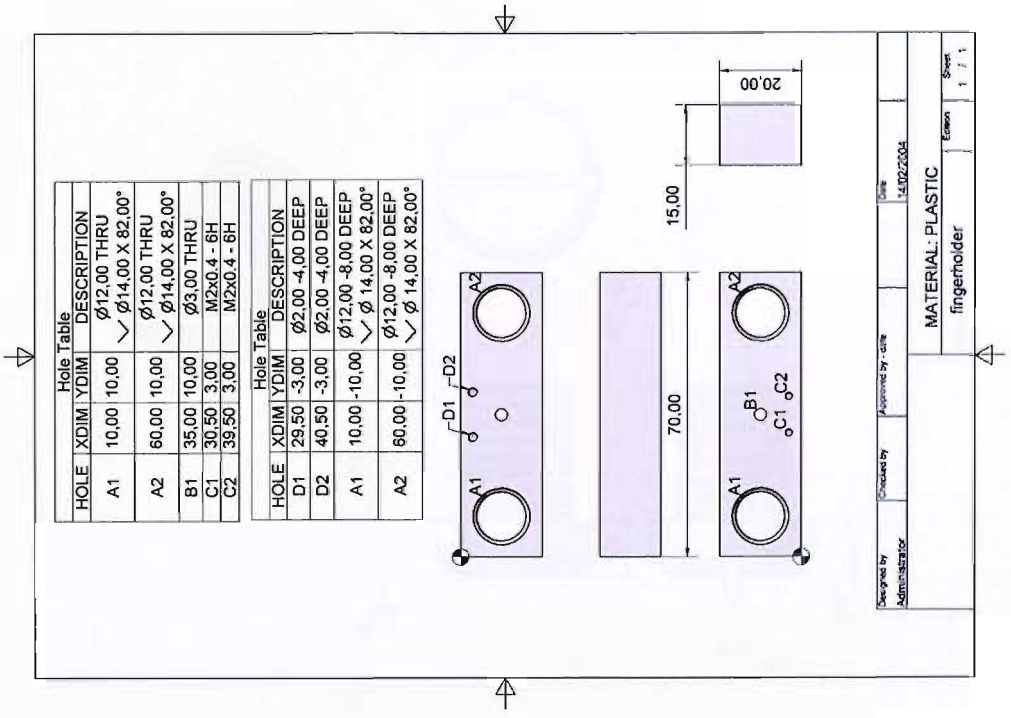

Figure E0.27: finger holder.

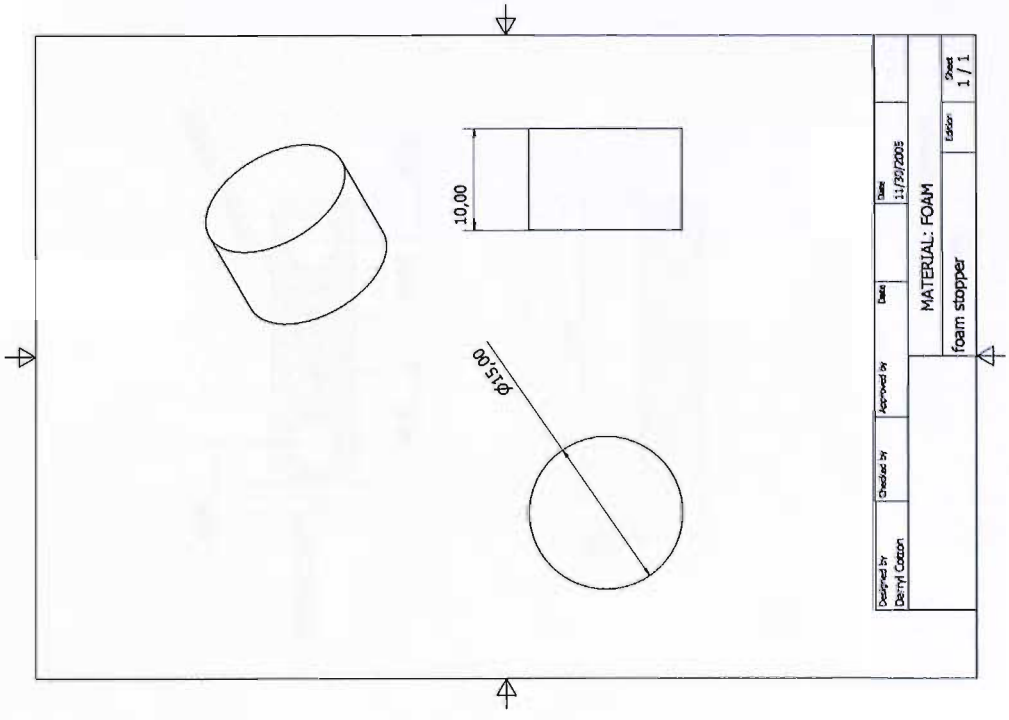

Figure E0.28: foam stopper.

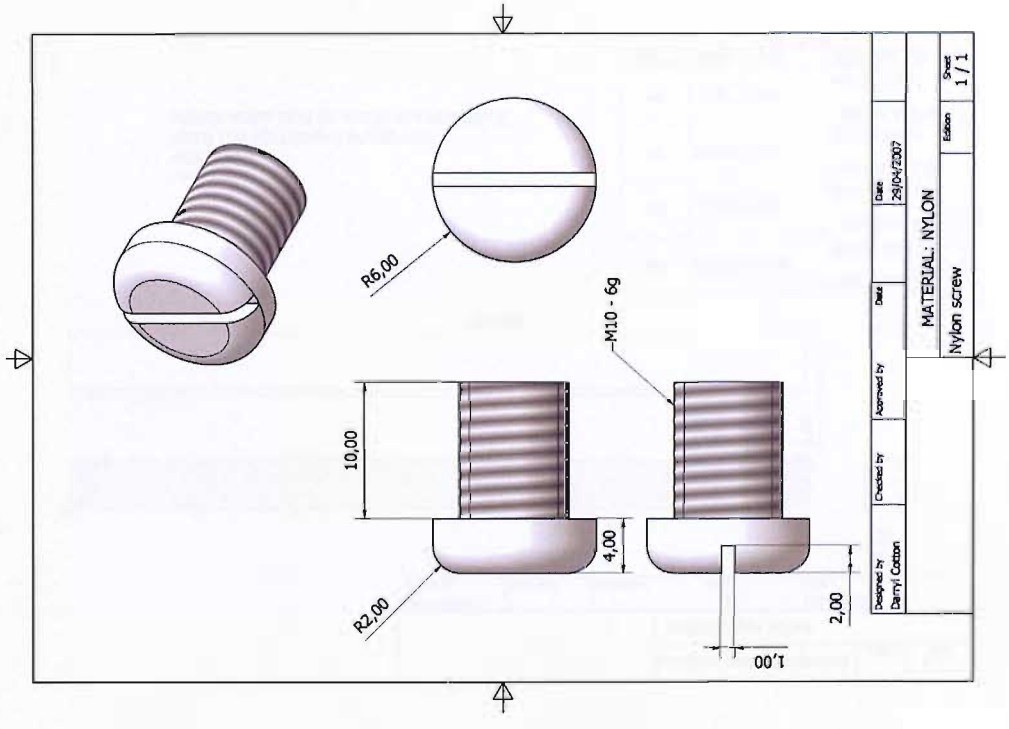

Figure E0.29: nylon screw.

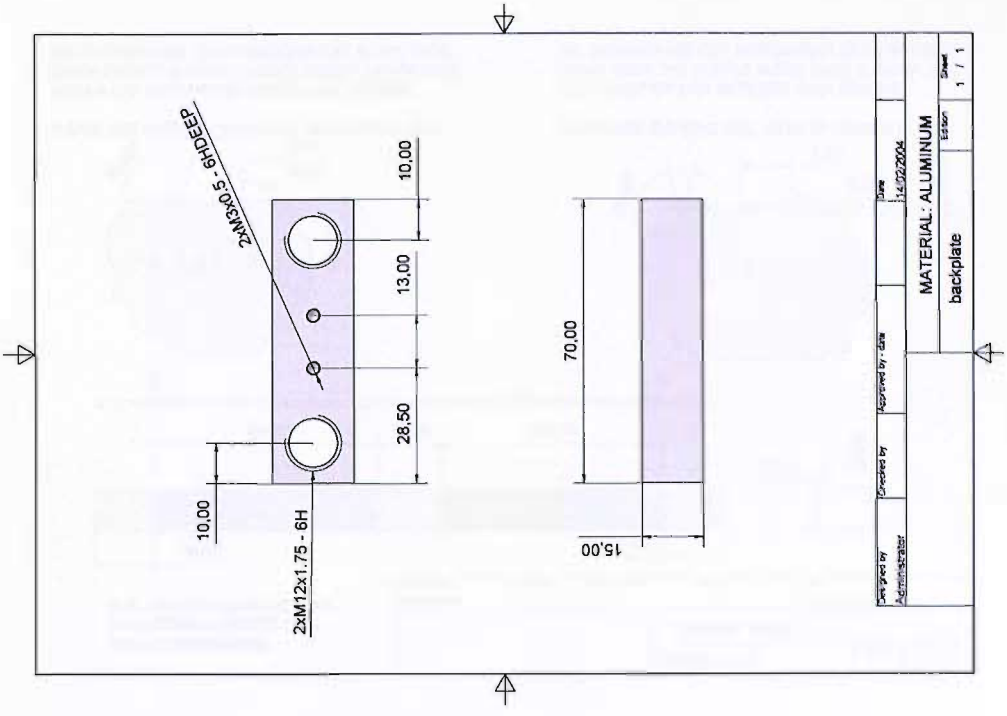

Figure E0.30: back plate.

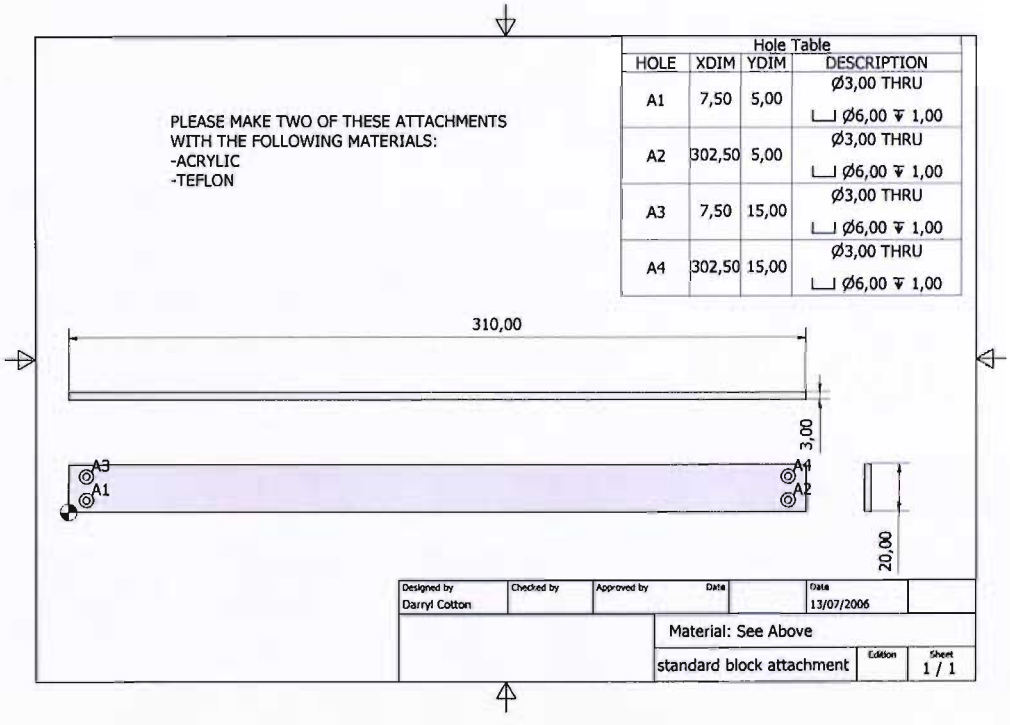

Figure E0.31: standard block attachment.

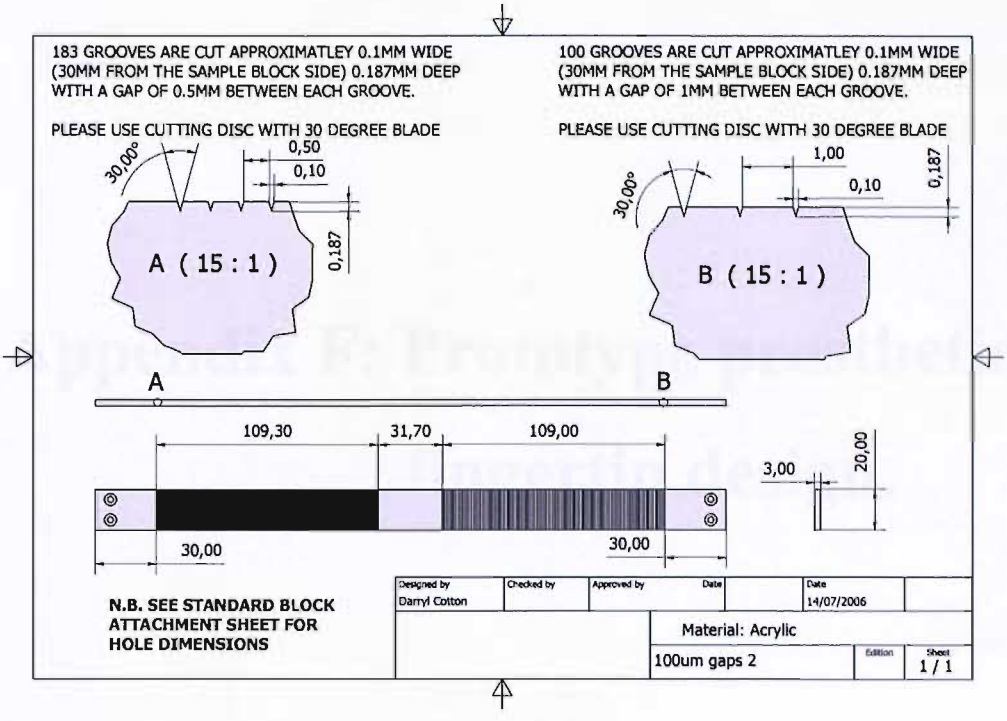

Figure E0.32: 100μm gaps 2.

Appendix F: Prototype prosthetic fingertip design.

F.1 Analysis of prototype fingertip 1 using ANSYS™

Figure F0.1 shows a diagram of the first prototype fingertip to be fabricated on 3mm thick type 304 stainless steel. The piezoresistive thick-film resistors that act as strain gauges are shown located to the left of the cantilever shape (A, B, C, D) and the piezoelectric sensor produced from PZT is shown located towards the tip of the fingertip (E). The location of the strain gauges was chosen as it was assumed that the fingertip would act similarly to a cantilever beam, producing the maximum strain at the clamped end and very little strain at the beam root.

For the purpose of the ANSYS™ modelling, the fingertip was divided into its lowest form of symmetry, as defined by the line X-X in Figure F0.1. Only half of the fingertip was then modelled; the other half being simulated using a symmetry function to reduce the processing time.

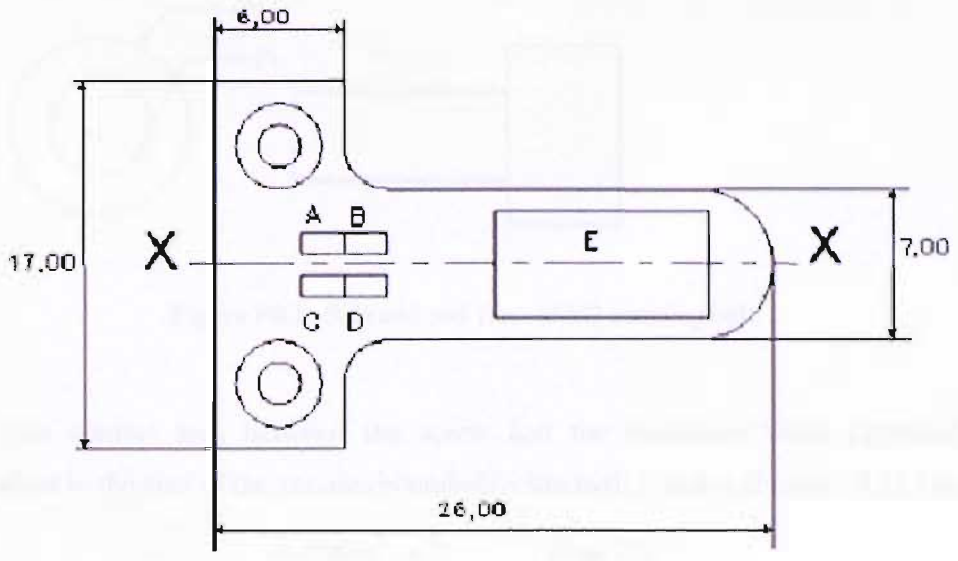

Figure F0.1: Diagram of fingertip prototype1, showing the line of symmetry X-X. (All dimensions in mm).

Three separate models were investigated, the first studying the effects of the bolt torque on the surface strain of the fingertip. For this analysis a comparison between a 400N and 500N force applied to the surface of the fingertip by each bolt was assumed (a total of 800N and 1000N respectively for the two bolts, 8 and 10 times the maximum load applied to the tip of the finger of 100N.) Equation F1 shows that the levels of torque required by the two securing M2 bolts to achieve these forces are approximately 0.15Nm and 0.19Nm respectively.

$$T \approx \frac{Fd}{5} \qquad \text{(Eqn F1)}$$

Where: T = torque (Nm), F = bolt tension load (N) and d = outer diameter of bolt (m).

In an ANSYS™ model it is necessary to consider a force being applied to a single node, so to simplify the model a displacement at the bolt reception hole was used to model the applied force. The bolts used to secure the fingertip are socket head cap screws and have a flat circular contact area (Figure F0.2). The contact area of the bolt can be calculated using Equation F2.

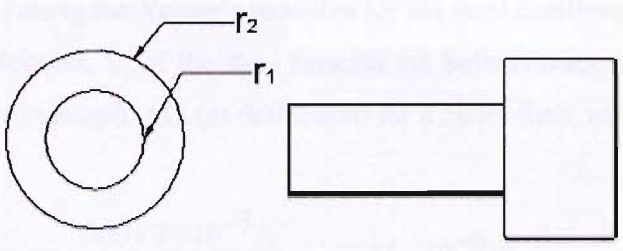

Figure F0.2: Side and end view of M2 securing bolt.

The contact area between the screw and the cantilever when tightened is equivalent to the area of the annulus bounded by the radii r_1 and r_2 (Figure F0.2) Thus:

$$A = \pi(r_2^2 - r_1^2) \qquad \text{(Eqn F2)}$$

Where r_1 = 1.92 mm and r_2 = 2.16 mm for a metric M2 socket head cap screw. Hence the contact area is:

$$\rightarrow A = 3.08 \times 10^{-6}\ m^2$$

The definition for Young's modulus, E, is:

$$E = \frac{\sigma}{e}\ Nm^{-2} \qquad \text{(Eqn F3)}$$

Where the stress, σ, is given by:

$$\sigma = \frac{F}{A}\ Nm^{-2} \qquad \text{(Eqn F4)}$$

and the strain ,e, by:

$$e = \frac{\Delta L}{L} \qquad \text{(Eqn F5)}$$

Substituting Equations (F3) and (F4) into (F5) yields an expression for the deflection in the surface of the steel caused by the bolt, thus:

$$\Delta L = \frac{FL}{EA} \qquad \text{(Eqn F6)}$$

Taking the Young's modulus for the steel cantilever, E, to be 190 x 10^9 Nm^{-2} and the thickness, L, of the steel beneath the bolts contact area to be 3 x 10^{-3} m gives the change in length, ΔL, (or deflection) for a 500N force to be:

$$= \frac{500 \times 3 \times 10^{-3}}{190 \times 10^9 \times 3.08 \times 10^{-6}} = 2.56 \times 10^{-6}\,\text{m}$$

$$\approx 2.6\mu\text{m}$$

For a 400N force applied to the bolt holes the change in length ΔL is:

$$= \frac{400 \times 3 \times 10^{-3}}{190 \times 10^9 \times 3.08 \times 10^{-6}} = 2.04 \times 10^{-6}\,\text{m}$$

$$\approx 2\mu\text{m}$$

These calculated values for deflection were subsequently used in the ANSYS™ model to simulate the strain distribution across the cantilever surface when the securing bolts were tightened to give force equivalents of 500N and 400N.

In this model the following assumptions and constraints were made:

1. The thick-film sensors have no contribution to the substrate stiffness.
2. The force is transmitted through the bolts to the surface of the finger tip.
3. The bottom surface of the fingertip is constrained in the Z-plane.
4. The bolt hole line "A" in Figure F0.3 is displaced by 2.6μm and 2μm in the z-plane simulating the forces applied by the bolt to the surface of the fingertip of 500N and 400N respectively.

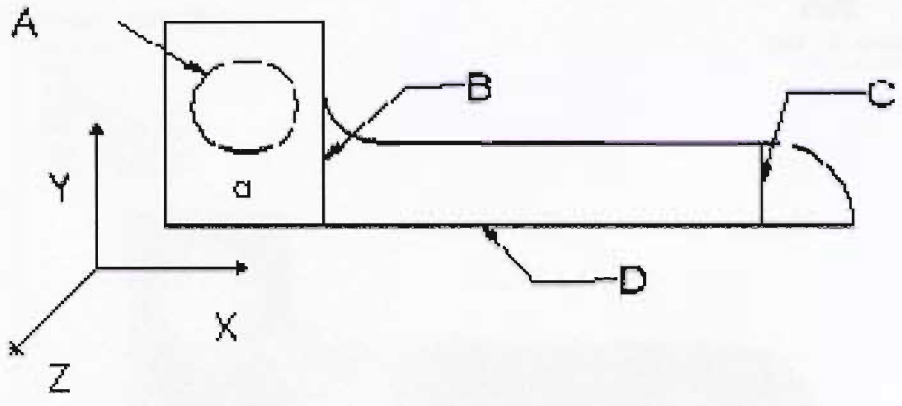

Figure F0.3: Fingertip model showing the location of constraints.

The second model concentrated on the effects of the fingertip being loaded whilst being firmly attached by the bolts. With reference to Figure F0.3, the following assumptions and constraints were made in this model:

1. The thick-film sensors have no contribution to the substrate stiffness.
2. The bolt hole line "A" is constrained on the top surface of the fingertip in the X,Y and Z planes with zero displacement.
3. The line "B" (beam pivot axis) is constrained on the bottom surface of the fingertip in all directions.
4. The line "C" is displaced on the top surface of the fingertip by 150μm in the Z-plane simulating the tip deflection for 200N load (calculations are shown in appendix G).

The third model compared the effects of the fingertip being loaded when it was securely clamped down instead of being bolted down. The following assumptions and constraints were made in this model (cf. Figure F0.3):

1. The thick-film sensors have no contribution to the substrate stiffness.
2. The area "a" is constrained on both the top and bottom of the fingertip with zero displacement in the X,Y and Z directions.
3. The line "C" is displaced by 150μm in the Z-plane simulating the tip deflection for a 200N load.

N.B. All of the code for the ANSYS™ models is shown in appendix E.

F.2 Model results

The strain concentration gradients were plotted using the Von Mises strain distribution model which simulates the strain contribution from the X, Y and Z directions. Results are shown in Figure F0.4 – Figure F0.7.

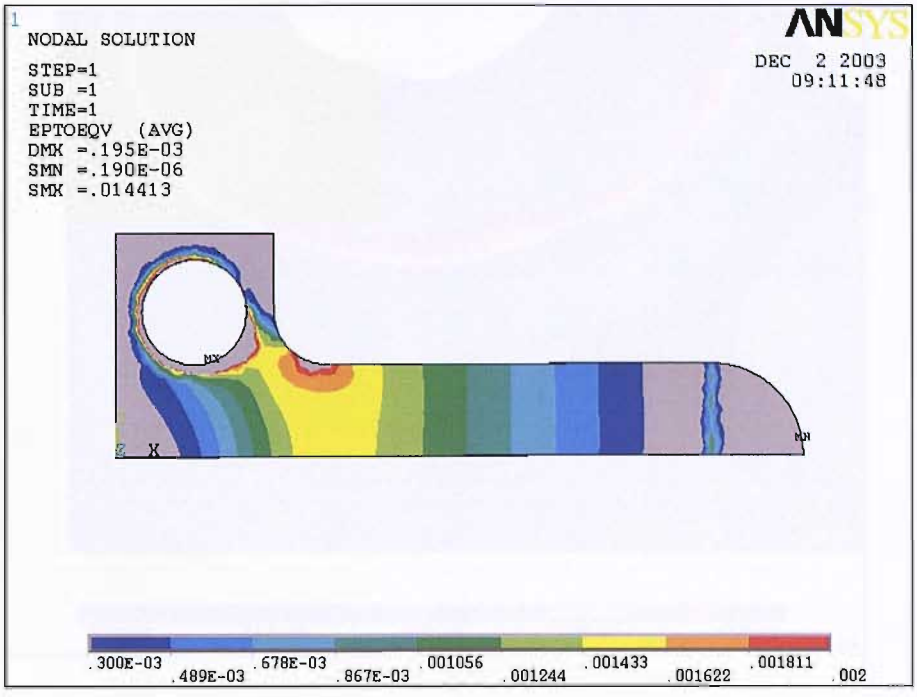

Figure F0.4: Von Mises Strain distribution when fingertip is constrained by the bolt holes and displaced across Line C.

From the Von Mises plot in Figure F0.4 it can be seen that there is a significant strain concentration around the chamfer of the finger exceeding 1.8 milli strain. This is 6% higher than that calculated using beam theory. Other strain raisers were not taken into account by beam theory such as the bolting fixture method and no allowance was made for the chamfer next to the strain gauges or curved beam tip. It is also evident that the strain concentrations below the bolt hole where the dummy strain gauges are to be placed are significantly large, ranging from approximately 1.2 milli strain to 0.5 milli strain. The average strain over the area occupied by the dummy gauge (approximately 0.85 milli strain) is about 60% of the maximum strain experienced by the active gauge. This configuration would therefore greatly reduce the sensitivity of the force sensor. The relatively uniform strain distribution shows that the use of bolts to fix the beam is a viable technique.

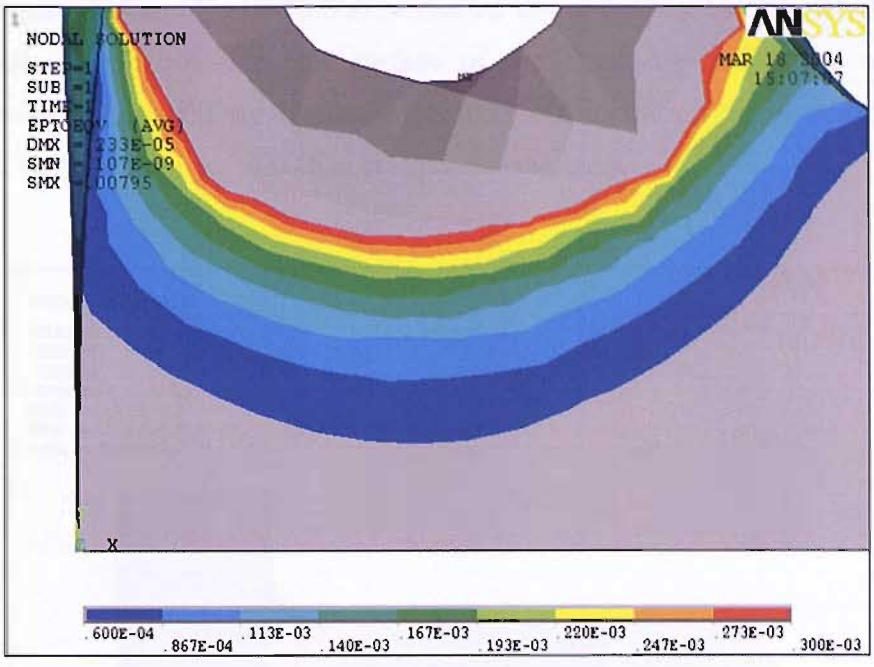

Figure F0.5: Von Mises Strain distribution of displacing the bolt hole (line "A") with the equivalent of a 400N force.

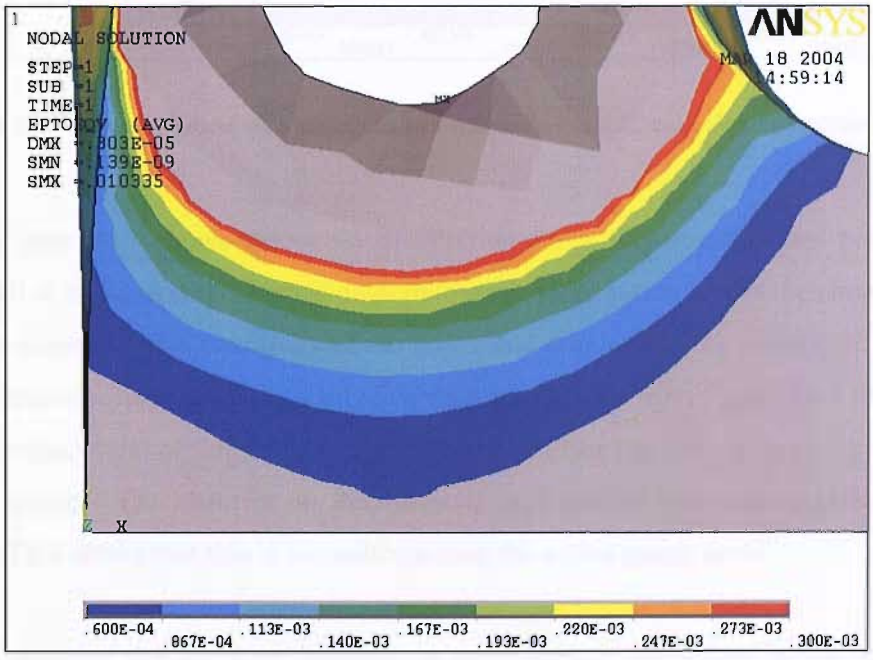

Figure F0.6: Von Mises Strain distribution of displacing the bolt hole (line "A") with the equivalent of a 500N force.

Figure F0.5 and Figure F0.6 show that the torque produced by the bolt will affect the strain distribution over the surface of the finger tip and hence offset the piezoresistive sensors. They also show that there is a significant change in strain when a small increase in torque of 0.4Nm is applied to the bolts.

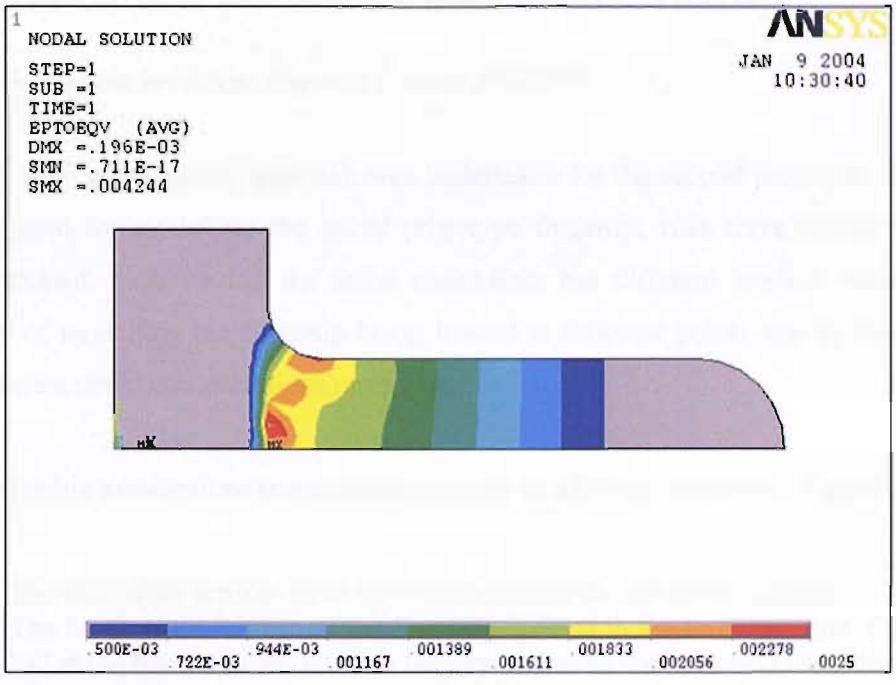

Figure F0.7: Detailed view of Von Mises strain distribution of beam clamped across area "a".

Figure F0.7 shows the strain distribution for a fingertip that has been firmly clamped at its fixed end. There is negligible strain distribution across the clamped area, thereby increasing the sensitivity of the finger and eliminating the problem of applying an accurate torque to the bolts. Furthermore it can be seen from Figure F0.4 that for the same displacement of fingertip, a larger strain is produced in the region occupied by the active gauges. The chamfer on the fingertip still affects the strain distribution and Figure F0.4 shows that this is not uniform over the active gauge areas.

Clamping the fingertip produces a more evenly distributed strain across the fingertip and eliminates any changes in strain where the dummy gauges are to be placed. However, clamping would produce a protrusion on the fingertip, which could increase the chance of loading occurring in a position where this device cannot measure the applied force.

F.2.1 Force sensor test results for prototype 1

Testing of the piezoresistive sensors showed a good linear response over a range of applied forces and deflections, however, the sensitivity could have been increased if a clamping method of fingertip attachment had been used. A detailed account of the methods used to test the force sensor and results can be found in [118].

F.2.2 Modelling prototype fingertip 2 using ANSYS™

A similar modelling approach was undertaken for the second prototype fingertip as that used for modelling the initial prototype fingertip, with three similar models being created, each having the same constraints but different loading points. The concept of modelling the fingertip being loaded at different points was to investigate the different strain concentrations produced.

The following assumptions and constraints apply to all three models (cf. Figure F0.9).

1. The thick-film sensors have no contribution to the substrate stiffness.
2. The block at the bottom of the fingertip is fixed in the same position. (The area "a" at the bottom of the block is constrained so as not to move in any direction.)
3. The strain around the edge of the bolt hole caused by the torque of the bolt is negligible but the bolt does constrain the fingertip in all directions. (Line "D" is constrained in the X, Y and Z planes with zero displacement.)
4. Line "C" is constrained by symmetry.
5. The fingertip is free to move away from the upper surface of the block. (Contact constraints between the surface of the block and the bottom of the fingertip were used.)

With reference to Figure F0.9, the following displacement constraints were applied to the separate models.

Model (a) A displacement of 120 microns was applied across line "B".
Model (b) A displacement of 120 microns was applied at point "F".
Model (c) A displacement of 120 microns was applied at point "E".

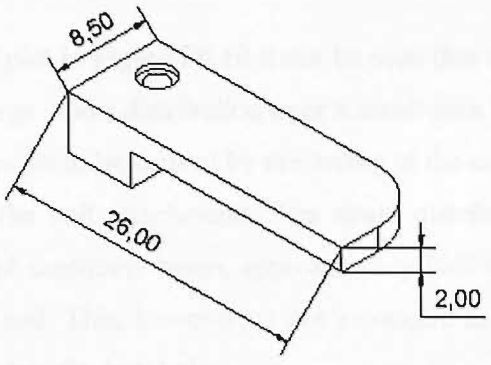

Figure F0.8: Cross-section through line of symmetry of 2nd fingertip with connecting block. All dimensions in mm.

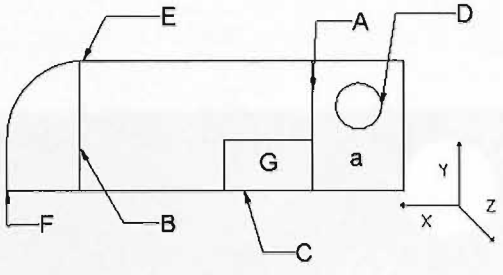

Figure F0.9: Diagram of the 2nd prototype fingertip.

F.2.3 Ansys results

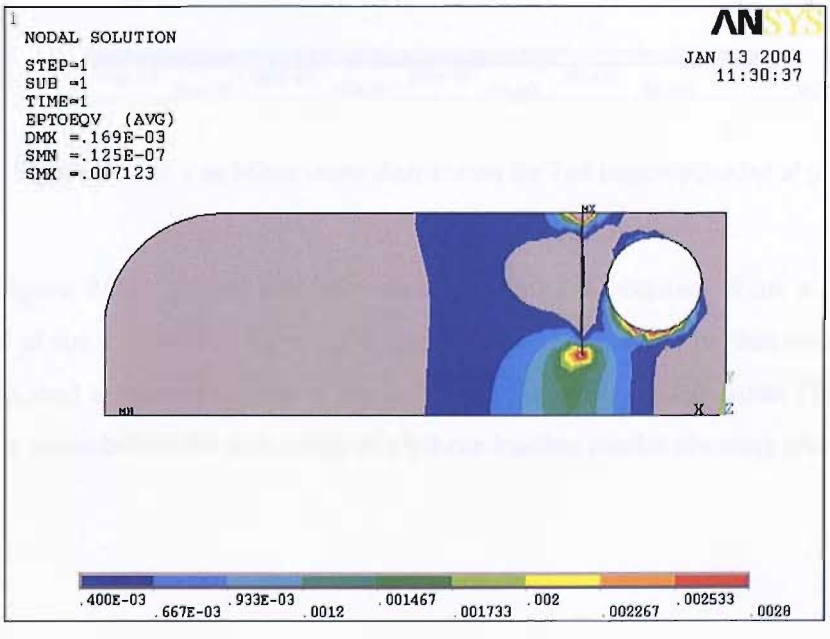

Figure F0.10: Concentrated view of Von Misses strain distribution of 2nd fingertip loaded across line B.

From the Von Mises plot in Figure F0.10 it can be seen that when the fingertip is loaded evenly there is a large strain distribution over a small area below the bolt hole. This is expected and is thought to be caused by the arcing at the centre of the fingertip due to the constraints of the bolt attachments. The strain distribution only becomes uniform, as with a standard cantilever beam, approximately half way up the fingertip length towards the loaded end. This, however, is not a concern as there is a relatively uniform change in strain below the bolt hole.

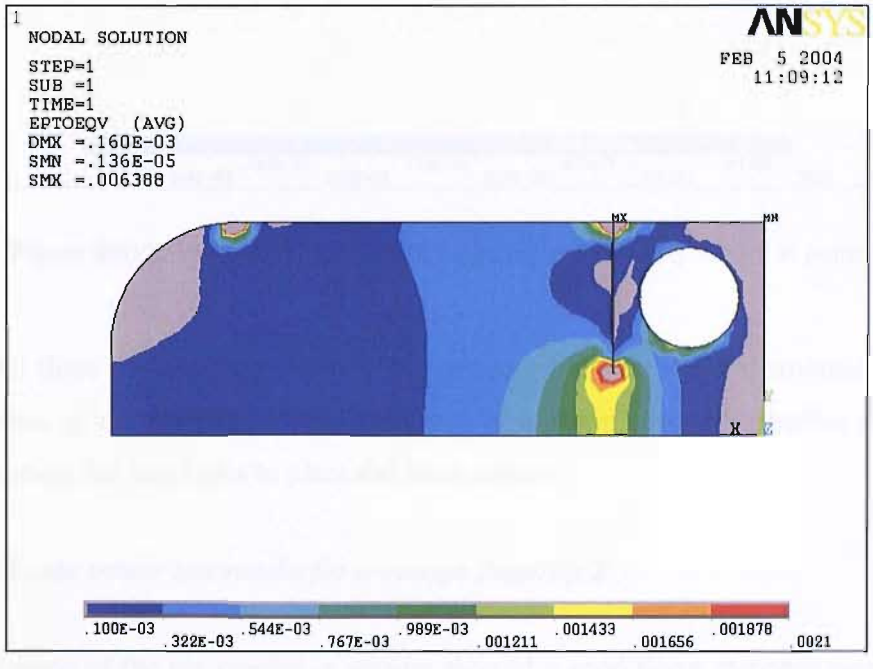

Figure F0.11: Von Mises strain distribution for 2nd fingertip loaded at point E.

Figure F0.11 shows that the strain distribution obtained from a displacement applied at the side of the fingertip is approximately the same as that obtained from a uniform load across the centre of the beam and the point loaded model (Figure F0.12), with the strain below the bolt holes of all three loading modes showing similar values.

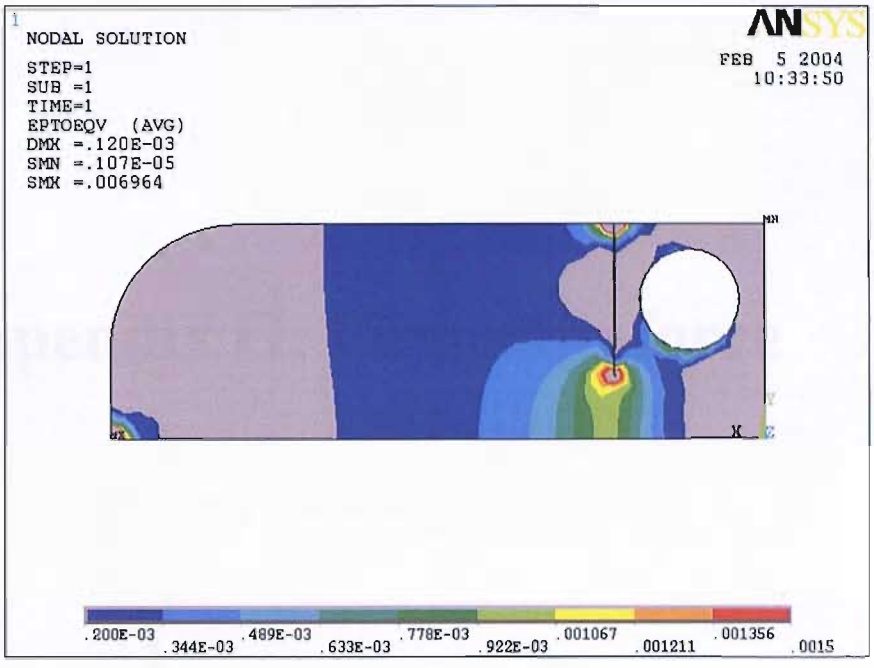

Figure F0.12: Von Mises strain distribution for 2nd fingertip loaded at point F.

All three different loading methods produced similar strain distributions across the surface of the fingertip. There is an area of uniform strain distribution with large strains below the bolt holes to place the force sensors.

F.2.4 Force sensor test results for prototype fingertip 2

Testing of the piezoresistive sensors showed a good linear response over a range of applied forces and deflections, independently of the position along the beam where the force was applied, using resistance ratios of any of the two piezoresistors. A detailed account of the methods used to test the force sensor and results can be found in [119].

Appendix G: Fingertip force calculations

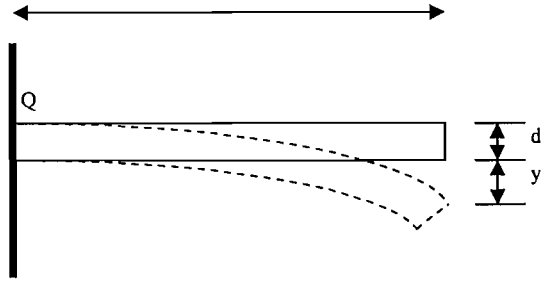

Figure G0.1: Cantilever beam.

Simulating the fingertip as a cantilever beam as shown in Figure G0.1 allows the following standard cantilever beam equations to be utilised to calculate the force applied for a set deflection.

$$y = \frac{ML^2}{2EI} \qquad \text{(Eqn G1)}$$

Where: y is the displacement in the beam tip, L is the length of the beam (to the point of displacement) (16.5×10^{-3} m for both prototype fingertips), E is the Young's modulus of the steel (taken to be 190×10^{9} Pa for both steel types), I is the second moment of area of the beam (defined by Equation G3) and M is the moment acting on the beam defined by Equation G2.

$$M = F \times L \qquad \text{(Eqn G2)}$$

Where F is the force applied at distance L from the root of the beam Q cf. Figure G0.1.

$$I = \frac{bd^3}{12} \qquad \text{(Eqn G2)}$$

Where b is the breadth of the beam and d is the depth of the beam.

Substituting equations G1 and G3 into G2 yields the equation for the equivalent force applied to the beam for a given deflection.

$$F = \frac{2yEI}{L^3} \qquad \text{(Eqn G4)}$$

G.1.1 First prototype fingertip

For the first prototype fingertip a deflection "y" of 150×10^{-6} m, a beam breadth "b" of 7×10^{-3} m and beam depth of 3×10^{-3}m were used as defined by the fingertips geometry in Figure F0.1.

$$F = \frac{2\times150\times10^{-6}\times190\times10^{9}\times7\times10^{-3}\times(3\times10^{-3})^3}{12\times(16.5\times10^{-3})^3} \approx 200N$$

G.1.2 Second prototype fingertip

For the second prototype fingertip a displacement "y" of 120×10^{-6}m, breadth of 17×10^{-3}m and a depth of 2×10^{-3}m (as defined in Figure F0.9) were used to calculate the equivalent force applied to the end of the beam for the set displacement.

$$F = \frac{2\times120\times10^{-6}\times190\times10^{9}\times17\times10^{-3}\times(2\times10^{-3})^3}{12\times(16.5\times10^{-3})^3} \approx 167N$$

Appendix E: ANSYS™ analysis program code

```
E1      Displacement around bolt hole

        /prep7

!Key point locations
        k,1,,,
        k,2,6e-3,,
        k,3,8e-3,,
        k,4,22.5e-3,,
        k,5,24.5e-3,,
        k,6,26e-3,,
        k,7,22.5e-3,3.5e-3,
        k,8,22.5e-3,2.5e-3
        k,9,8e-3,3.5e-3,
        k,10,8e-3,2.5e-3,
        k,11,6e-3,3.5e-3,
        k,12,6e-3,5.5e-3,
        k,13,6e-3,8.5e-3,
        k,14,3e-3,8.5e-3,
        k,15,,8.5e-3,
        k,16,,5.5e-3,
        k,17,8e-3,5.5e-3,
        k,18,3e-3,5.5e-3,
        k,19,3e-3,7.5e-3,
        k,20,5e-3,5.5e-3,
        k,21,3e-3,3.5e-3,
        k,22,1e-3,5.5e-3,
!Draw arcs to allow extra keypoints to be plotted.
        larc,19,20,18,2e-3
        larc,19,22,18,2e-3
!Plot extra keypoints along lines
        Kl,1,0.4,23,
        kl,2,0.4,24,
!Delete lines
        Ldele,all
!Copy all key points to a displacement of 3mm.
        Kgen,2,all,,,,,3e-3,100
!Generate arcs to allow volumes to be defined.
        larc,19,23,18,2e-3
        larc,23,20,18,2e-3
        larc,20,21,18,2e-3
!Circle arcs
        larc,21,22,18,2e-3
        larc,22,24,18,2e-3
        larc,19,24,18,2e-3
        larc,119,123,118,2e-3
        larc,123,120,118,2e-3
        larc,120,121,118,2e-3
!Circle arcs bottom layer
        larc,121,122,118,2e-3
        larc,122,124,118,2e-3
        larc,119,124,118,2e-3
!other arcs
        larc,106,107,104,3.5e-3
        larc,6,7,4,3.5e-3
        larc,12,9,17,2e-3
        larc,112,109,117,2e-3
!plot volumes
        V,1,21,11,2,101,121,111,102
        v,11,12,20,21,111,112,120,121
        v,2,3,10,11,102,103,110,111
        v,3,4,8,10,103,104,108,110
        v,4,5,8,104,105,108
        v,5,6,7,8,105,106,107,108
        v,7,9,10,8,107,109,110,108
        v,9,10,11,12,109,110,111,112,
        v,12,13,23,20,112,113,123,120
        v,23,13,14,19,123,113,114,119
        v,19,14,15,24,119,114,115,124
        v,15,24,22,16,115,124,122,116
        v,16,22,21,1,116,122,121,101
```

```
!Define temperature as linear
    MPTEMP,,,,,,,,
    MPTEMP,1,0
!Define material properties
    MPDATA,EX,1,,190e9
!Youngs modulus
    MPDATA,PRXY,1,,0.3
!Poissions ratio
!Define element types
    et,1,solid187
!define element size and mesh volumes
    lesize,all,5e-4
    vmesh,all
!apply displacements
    DA,1,ALL,
    DA,7,ALL,
    DA,38,ALL,
!constrained areas
    DA,43,ALL,
    DA,48,ALL,
    DA,53,ALL,
    DA,58,ALL,
    DL,7,47,UZ,-5e-6
!displacement on line
    DL,8,42,UZ,-5e-6
    DL,9,11,UZ,-5e-6
    DL,10,61,UZ,-5e-6
    DL,11,57,UZ,-5e-6
    DL,12,52,UZ,-5e-6
!simulate symmetry
    nsel,s,loc,y,0
    d,all,uy
    nall
!Solve
    fini
    /solu
    antype,static
    solve
    fini
!Postprocessing
    /POST1
    SET,FIRST
!read first set of results
    PLNSOL,S,EQV
!displays results as continous contours
    ANCNTR,20,0.1
!Animate contour deformed shape
```

E2 Model with bolt holes loaded across line "a"

```
    /prep7
!Key point locations
    k,1,,,
    k,2,6e-3,,
    k,3,8e-3,,
    k,4,22.5e-3,,
    k,5,24.5e-3,,
    k,6,26e-3,,
    k,7,22.5e-3,3.5e-3,
    k,8,22.5e-3,2.5e-3
    k,9,8e-3,3.5e-3,
    k,10,8e-3,2.5e-3,
    k,11,6e-3,3.5e-3,
    k,12,6e-3,5.5e-3,
    k,13,6e-3,8.5e-3,
    k,14,3e-3,8.5e-3,
    k,15,,8.5e-3,
    k,16,,5.5e-3,
    k,17,8e-3,5.5e-3,
    k,18,3e-3,5.5e-3,
    k,19,3e-3,7.5e-3,
    k,20,5e-3,5.5e-3,
    k,21,3e-3,3.5e-3,
    k,22,1e-3,5.5e-3,
!Draw arcs to allow extra keypoints to be ploted.
    larc,19,20,18,2e-3
    larc,19,22,18,2e-3
!Plot extra keypoints along lines
    Kl,1,0.4,23,
    kl,2,0.4,24,
!Delete lines
    Ldele,all
!Copy all key points to a displacement of 3mm.
    Kgen,2,all,,,,,3e-3,100
!Generate arcs to allow volumes to be defined.
    larc,19,23,18,2e-3
    larc,23,20,18,2e-3
    larc,20,21,18,2e-3
!Circle arcs
    larc,21,22,18,2e-3
    larc,22,24,18,2e-3
    larc,19,24,18,2e-3
    larc,119,123,118,2e-3
    larc,123,120,118,2e-3
    larc,120,121,118,2e-3
!Circle arcs bottom layer
    larc,121,122,118,2e-3
    larc,122,124,118,2e-3
    larc,119,124,118,2e-3
!other arcs
    larc,106,107,104,3.5e-3
    larc,6,7,4,3.5e-3
    larc,12,9,17,2e-3
    larc,112,109,117,2e-3
!plot volumes
    V,1,21,11,2,101,121,111,102
    v,11,12,20,21,111,112,120,121
    v,2,3,10,11,102,103,110,111
    v,3,4,8,10,103,104,108,110
    v,4,5,8,104,105,108
    v,5,6,7,8,105,106,107,108
    v,7,9,10,8,107,109,110,108
    v,9,10,11,12,109,110,111,112,
    v,12,13,23,20,112,113,123,120
    v,23,13,14,19,123,113,114,119
    v,19,14,15,24,119,114,115,124
    v,15,24,22,16,115,124,122,116
    v,16,22,21,1,116,122,121,101
```

```
!Define temperature as linear
    MPTEMP,,,,,,,,
    MPTEMP,1,0
!Define material properties
    MPDATA,EX,1,,190e9
!Youngs modulus
    MPDATA,PRXY,1,,0.3
!Poissions ratio
!Define element types
    et,1,solid187
!define element size and mesh volumes
    lesize,all,5e-4
    vmesh,all
!apply displacements
    Dl,19,1,ALL,
    Dl,29,7,ALL,
    Dl,67,38,ALL,
!constrained line on block
    DL,7,47,all,
!displacement on screw line
    DL,8,42,all,
    DL,9,11,all,
    DL,10,61,all,
    DL,11,57,all,
    DL,12,52,all,
!displacement of beam
    Dl,48,25,uz,-150e-6
    dl,61,30,uz,-150e-6
!simmulate symmetry
    nsel,s,loc,y,0
    d,all,uy
    nall
!SOLVE
    fini
    /solu
    antype,static
    solve
    fini
!Postprocessing
    /POST1
    SET,FIRST
!read first set of results
    PLNSOL,S,EQV
!displays results as continuous contours
    ANCNTR,20,0.1
!Animate contour deformed shape
```

E3 Clamped fingertip loaded across line "a"

```
    prep7
!Key point locations
    k,1,,,
    k,2,6e-3,,
    k,3,8e-3,,
    k,4,22.5e-3,,
    k,6,26e-3,,
    k,7,22.5e-3,3.5e-3,
    k,9,8e-3,3.5e-3,
    k,12,6e-3,5.5e-3,
    k,13,6e-3,8.5e-3,
    k,15,,8.5e-3,
    k,16,,5.5e-3,
    k,17,8e-3,5.5e-3,
!Copy all key points to a displacement of 3mm.
    Kgen,2,all,,,,,3e-3,100
!Generate arcs to allow volumes to be defined.
!other arcs
    larc,106,107,104,3.5e-3
    larc,6,7,4,3.5e-3
    larc,12,9,17,2e-3
    larc,112,109,117,2e-3
!plot volumes
    v,1,2,12,16,101,102,112,116
    v,12,13,15,16,112,113,115,116
    v,2,3,9,12,102,103,109,112
    v,3,4,7,9,103,104,107,109
    v,4,6,7,104,106,107
!Define temperature as linear
    MPTEMP,,,,,,,,
    MPTEMP,1,0
!Define material properties
    MPDATA,EX,1,,190e9
!Youngs modulus
    MPDATA,PRXY,1,,0.3
!Poissions ratio
!Define element types
    et,1,solid187
!define element size and mesh volumes
    lesize,all,10e-4
    vmesh,all
!apply displacements
    !Da,7,ALL,
    !da,2,all,
    !da,11,all,
!constrain areas
    !da,6,all,
!simmulate symmetry
    !nsel,s,loc,y,0
    !d,all,uy
    !nall
!displacement of beam
    !Dl,32,25,uz,-150e-6
!SOLVE
    !fini
    !/solu
    !antype,static
    !solve
    !fini
!Postprocessing
    !/POST1
    !SET,FIRST
!read first set of results
    !PLNSOL,S,EQV
!displays results as continuous contours
    !ANCNTR,20,0.1
!Animate contour deformed shape
```

E4 Prototype fingertip two with point load

(N.B. Some picking was used to constrain the block to the fingertip.)

```
/prep7
!Define keypoints
k,1,,,,
k,2,3e-3,,,
k,3,6e-3,,,
k,4,21e-3,,,
k,5,26e-3,,,
k,6,26e-3,3.5e-3,,
k,7,21e-3,3.5e-3,,
k,8,21e-3,8.5e-3,,
k,9,6e-3,8.5e-3,,
k,10,3e-3,8.5e-3,,
k,11,,8.5e-3,,
k,12,,5.5e-3,,
k,13,1e-3,5.5e-3,,
k,15,3e-3,7.5e-3,,
k,16,5e-3,5.5e-3,,
k,17,3e-3,3.5e-3,,
k,18,3e-3,5.5e-3,,
k,19,6e-3,2.5e-3,,
k,21,6e-3,5.5e-3,,
!Draw arcs to allow extra keypoints to be plotted.
larc,13,15,18,2e-3
larc,15,16,18,2e-3
!Plot extra keypoints along lines
Kl,1,0.5,14,
kl,2,0.5,20,
!Delete lines
Ldele,all
!Copy all keypoints down 2mm
Kgen,2,all,,,,,2e-3,100
!copy keypoints again 6mm down
Kgen,2,all,,,,,4e-3,200
!add keypoints to define block
!k,201,,6e-3
!k,203,6e-3,,6e-3
!k,209,6e-3,8.5e-3,6e-3
!k,211,,8.5e-3,6e-3
!Generate arcs to allow volumes to be defined.
larc,8,6,7,5e-3
larc,108,106,107,5e-3
larc,13,14,18,2e-3
larc,14,15,18,2e-3
larc,15,20,18,2e-3
larc,20,16,18,2e-3
larc,16,17,18,2e-3
larc,17,13,18,2e-3
larc,113,114,118,2e-3
larc,114,115,118,2e-3
larc,115,120,118,2e-3
larc,120,116,118,2e-3
larc,116,117,118,2e-3
larc,117,113,118,2e-3
!plot volumes of fingertip
V,1,2,17,101,102,117
v,1,17,13,12,101,117,113,112
v,12,13,14,11,112,113,114,111
v,11,14,15,10,111,114,115,110
v,10,15,20,9,110,115,120,109
v,9,21,16,20,109,121,116,120
v,2,3,19,17,102,103,119,117
v,3,4,7,19,103,104,107,119
v,19,7,8,9,119,107,108,109
v,4,5,6,7,104,105,106,107
v,6,7,8,106,107,108
v,16,17,19,21,116,117,119,121
!plot volumes of block
v,112,121,109,111,212,221,209,211
V,101,102,118,112,201,202,218,212
v,102,103,119,117,202,203,219,217
v,117,119,121,118,217,219,221,218
!Define temperature as linear
MPTEMP,,,,,,,,
MPTEMP,1,0
!Define material properties
MPDATA,EX,1,,190e9
!Youngs modulus
MPDATA,PRXY,1,,0.3
!Poissions ratio
!Define element types
et,1,solid187
!define element size and mesh volumes
lesize,all,7e-4
vmesh,all
dL,3,15,all,
!displacement on line screw hole
dl,4,20,all,
dl,5,25,all,
dl,6,30,all,
dl,7,57,all,
dl,8,10,all,
!displacement on line of 0
!dl,86,41,all,
!dl,51,41,all,
!dl,59,36,all,
! load on line
!Dl,63,50,uz,120e-6
!dl,70,53,uz,120e-6
! force on centre point
!f,5,fz,-100
!simmulate symmetry
nsel,s,loc,y,0
d,all,uy
nall
!numm,all,1e-6
!waves
!SOLVE
!fini
!/solu
!antype,static
!solve
!fini
!Postprocessing
!/POST1
!SET,FIRST
!read first set of results
```